Electron beam sizes and lifetimes at MAX II and MAX III

Rosborg, Anders

2012

Citation for published version (APA):
Rosborg, A. (2012). *Electron beam sizes and lifetimes at MAX II and MAX III*. [Doctoral Thesis (compilation), MAX IV Laboratory]. Department of Physics, Lund University.

Total number of authors:
1

Electron beam sizes and lifetimes at MAX II and MAX III

Anders Hansson

Doctoral Thesis
2012

Lund University

Electron beam sizes and lifetimes at MAX II and MAX III

Printed in Sweden by Media-Tryck, Lund, 2012.

MAX-lab
Lund University
P.O. Box 118
SE–221 00 Lund
Sweden

http://www.maxlab.lu.se

ISSN: 0284-1258
ISRN: LUNTDX/NTMX–1012–SE

ISBN: 978-91-7473-398-3

ABSTRACT

The MAX II and MAX III synchrotron light sources at MAX-lab provide synchrotron radiation for experiments in a wide variety of research fields. The synchrotron radiation is emitted by ultra-relativistic electrons circulating in electron storage rings. In this thesis the transverse and longitudinal electron beam sizes and the electron beam lifetime limitations in electron storage rings are discussed and the methods used at MAX-lab to measure them are described. The thesis describes how measurements of the electron beam sizes and lifetimes were used to investigate and improve the performance of MAX III and to evaluate a change in the MAX II vacuum system.

MAX II was the first synchrotron light source to install nonevaporable getter (NEG)-coated dipole vacuum chambers. They were installed in order to test the feasibility of the MAX IV 3 GeV storage ring vacuum design, where NEG-coated dipole chambers are an integral part of the design. From measurements of the lifetime limitations in MAX II it was concluded that NEG-coated dipole vacuum chambers do not appear to have any negative impact on the performance and operation of a synchrotron light source.

A diagnostic beam line was designed and installed in MAX III in order to determine the transverse electron beam profile. The performance of the beam line was investigated by conducting a series of measurements at different beam line settings. There was good agreement between the determined beam sizes for the different settings. The diagnostic beam line was used to determine the horizontal and vertical dispersion and emittance in MAX III at low currents, and an increase in the momentum spread from longitudinal instabilities at higher currents. By adding a second passive Landau cavity to the MAX III radio frequency (RF) system the instabilities were damped in the main window of operation. Measurements of the longitudinal beam size and the induced voltages in the passive cavities agreed well with computer simulations of the triple RF system of MAX III. At high Landau cavity voltages a stable overstretched bunch shape with two regions of phase stability was observed. The lifetime limitations and acceptances in MAX III were determined and the location of a horizontal aperture restriction was identified. Removing the aperture restriction increased the lifetime in MAX III by a factor of two.

POPULÄRVETENSKAPLIG SAMMANFATTNING

När elektroner som färdas i en hastighet nära ljusets hastighet böjs av i ett magnetfält genereras framåtriktad elektromagnetisk strålning. Denna strålning, som även kallas synkrotronljus, kan användas för att studera strukturer och egenskaper hos olika material. Vid en synkrotronljuskälla, som t.ex. MAX II eller MAX III vid MAX-lab i Lund, cirkulerar elektroner runt i vakuum i en lagringsring. Magneter utmed elektronbanan böjer av och fokuserar elektronstrålen. Synkrotronljuset som elektronerna sänder ut filtreras och fokuseras i strålrör och transporteras till experimentstationer placerade utmed lagringsringen. De flesta som bedriver forskning vid en synkrotronljuskälla kommer dit en kortare tid för att använda sig av synkrotronljuset. För att säkerställa att användarna får bra kvalitet på ljuset behövs goda kunskaper om elektronstrålen som genererar ljuset. I den här avhandlingen beskrivs studier relaterade till elektronstrålens egenskaper i MAX II och MAX III, med fokus på elektronstrålens storlek och livstid.

Ett diagnostikstrålrör har designats, byggts och installerats i MAX III för att bestämma elektronstrålens bredd och höjd. Strålröret använder sig av synligt synkrotronljus från en av böjmagneterna i MAX III för att skapa en bild av elektronstrålen. Prestandan hos strålröret testades genom att mäta elektronstrålens bredd och höjd för flera olika inställningar på strålröret och verifiera att den uppmätta bredden och höjden inte berodde på strålrörets inställningar. Den uppmätta bredden stämde överens med teoretiska förväntningar.

För att tillföra den energi som elektronerna tappar när de sänder ut synkrotronljus används mikrovågskaviteter. Det varierande fältet i kaviteterna får elektronerna att färdas runt i lagringsringen i separata ansamlingar av elektroner. I MAX III fanns sedan tidigare två olika sorters kaviteter, en aktiv kavitet för att tillföra energi till elektronerna och en passiv kavitet för att öka elektronansamlingarnas längd. Genom att installera en andra passiv kavitet kunde instabiliteter i elektronstrålens bredd och ansamlingarnas längd dämpas. Mätningar av ansamlingarnas längd och fältstyrkorna i kaviteterna visade god överensstämmelse med resultat från datorsimuleringar.

Om elektronerna i en lagringsring har fel energi eller avviker för långt från den ideala elektronbanan kan de slå i vakuumkammaren och förloras, vilket ger upphov till en begränsad livstid hos elektronstrålen. Livstiden i MAX III var lägre än förväntat. De livstidsbegränsande effekterna har mätts upp och den mest begränsande effekten har identifierats. Genom att flytta en felplacerad komponent i lagringsringen några millimeter fördubblades livstiden i MAX III.

Utöver studier av MAX III har mätningar även genomförts vid MAX II, där en ny sorts vakuumkammare har installerats. Mätningar av livstiden och trycket i MAX II före och efter installationen visade att de nya vakuumkamrarna fungerade bra. De positiva erfarenheterna från MAX II är viktiga inför den framtida synkrotronljuskällan MAX IV, där liknande teknik kommer att användas.

LIST OF PUBLICATIONS

This thesis is based on the following papers, which will be referred to by their Roman numerals in the text.

I **Experiences from nonevaporable getter-coated vacuum chambers at the MAX II synchrotron light source**
A. Hansson, E. Wallén, M. Berglund, R. Kersevan and M. Hahn.
J. Vac. Sci. Technol. A **28**, 220–225 (2010).

II **Transverse electron beam imaging system using visible synchrotron radiation at MAX III**
A. Hansson, E. Wallén, Å. Andersson.
Nucl. Instr. and Meth. A **671**, 94–102 (2012).

III **Imaging of the MAX III electron beam profile using visible synchrotron radiation**
A. Hansson, E. Wallén, Å. Andersson.
Proceedings of IPAC2011, San Sebastián, Spain, pp. 1332–1334 (2011).

IV **Electron beam stability and lifetime at the MAX III synchrotron light source**
A. Hansson, E. Wallén, Å. Andersson, J. Breunlin, G. Skripka.
Manuscript in preparation.

CONTENTS

Papers

PREFACE

The MAX IV laboratory is a Swedish national research infrastructure hosted by Lund University. It consists of the MAX IV project, constructing the new MAX IV facility, and MAX-lab, operating the present MAX I, MAX II and MAX III synchrotron light sources. The present facility at MAX-lab supports three distinct research areas: accelerator physics, nuclear physics and research based on the use of synchrotron radiation.

My PhD studies have been related to the research in accelerator physics performed at MAX-lab. The focus has been on the storage rings at the laboratory and the work has been performed on the MAX III storage ring as well as on the MAX II storage ring. Compared to many other synchrotron light sources, MAX-lab has a limited amount of staff and the staff often perform several different tasks. During my PhD studies I have been involved in everything from vacuum and diagnostics to RF and the daily operation of the storage rings, which has been a great way to learn how a synchrotron light source works.

Comments on the Papers

This thesis is based on four papers. They are briefly described below, stating the aim and the main results as well as my contribution to the papers. For all papers, the co-authors have assisted in the planning of the measurements, the interpretation of the results and in the revisions of the manuscripts.

Paper I

This paper describes the experiences from nonevaporable getter (NEG)-coated vacuum chambers at MAX II. NEG-coated vacuum chambers have been used in straight sections of synchrotron light sources for many years, but MAX II was the first to also install NEG-coated dipole vacuum chambers. For the MAX IV 3.0 GeV storage ring NEG-coated vacuum chambers, including dipole chambers, are an integral part of the design. The tests with NEG-coated vacuum chambers at MAX II were performed to test the feasibility of the MAX IV design. By determining the lifetime limitations in MAX II and by observing the bremsstrahlung from a dipole chamber, it was concluded that NEG-coated dipole vacuum chambers do not appear to have any negative impact on the performance and operation of a synchrotron light source.

The design of the NEG-coated dipole vacuum chambers and the NEG coating of the chambers, done at ESRF, were performed before I became involved in the project. My contribution consisted of setting up and performing the scraper and bremsstrahlung measurements, as well as performing the data analysis. I was also the main author of the manuscript.

Paper II

The MAX III diagnostic beam line utilizes the synchrotron radiation (SR) in the visible to ultraviolet (vis-UV) range to form images of the transverse electron beam profile in MAX III. The most common methods to determine the transverse beam sizes at synchrotron light sources are pinhole cameras using SR in the x-ray range and interferometers using SR in the visible range, but as shown at e.g. SLS the vis-UV imaging method is also a viable alternative. In the paper, the setup of the diagnostic beam line and the vis-UV imaging method is described in detail. The performance of the beam line was investigated by performing a series of measurements at 48 different beam line settings, showing a good agreement between the determined beam sizes. The large maximum horizontal opening angle of the measurement system made it possible to clearly observe a horizontal asymmetry in the measured images, as predicted by simulations using SRW. Utilizing these horizontal wave-optics features, the vis-UV imaging method can be used to measure future small horizontal beam sizes.

I participated in the design, construction and installation of the MAX III diagnostic beam line. I was responsible for the commissioning of the beam line and performed the measurements and the data analysis presented in the paper. I developed the computer model of the MAX III diagnostic beam line in SRW based on earlier models developed for the diagnostic beam lines at MAX II and SLS. I was the main author of the manuscript.

Paper III

This paper describes how the MAX III diagnostic beam line was used to determine the transverse electron beam sizes and emittances in MAX III at low currents. Whereas Paper **II** investigated the performance of the diagnostic beam line itself and the vis-UV imaging method, this paper is focused on the results for MAX III. The MATLAB LOCO software package was used to fit linear optics measurements to a computer model of MAX III. From the fitted computer model and measurements of the transverse beam size and dispersion using the diagnostic beam line, the horizontal and vertical emittance in MAX III was determined. The horizontal emittance was found to agree with the design value, whereas the vertical emittance and the emittance ratio was found to be smaller than design.

I performed the measurements and the data analysis presented in the paper, including the linear optics measurements and the MATLAB LOCO fits. I was the main author of the manuscript. The computer model of MAX III and the fit settings used in MATLAB LOCO were developed by Magnus Sjöström for an earlier paper on the commissioning of MAX III.

Paper IV

The aim of this paper was to investigate the increase in the horizontal beam size and bunch length at higher currents as well as the lower than design lifetime in MAX III. The increase in horizontal beam size was explained by an increase in the momentum spread from longitudinal instabilities. By installing and tuning in a second passive Landau cavity the instabilities were damped in the main window of operation for MAX III. Simulations of the triple RF system of MAX III, taking into account the measured momentum spread, reproduced the observed bunch lengths, bunch shapes and cavity voltages. The lifetime in MAX III was determined to be Touschek limited and the low Touschek lifetime was explained by the lower than design emittance ratio and momentum acceptance. A combination of local orbit distortions and horizontal scraper measurements pinpointed the location of a horizontal aperture restriction close to the center of the main cavity straight section. Moving the main cavity increased the lifetime in MAX III by a factor of two.

I was in charge of the measurements and performed some of them by myself and some together with Jonas Breunlin and Galina Skripka. I analyzed the data, did the calculations of the Touschek lifetimes in OPA and ZAP, and performed the simulations of the MAX III triple RF system based on a code developed by Åke Andersson. I was the main author of the manuscript.

Scope and outline of the thesis

This thesis is intended to be a complement to the papers. The main results and conclusions from the measurements can be found in the papers. The thesis will instead give an introduction to some of the concepts used in the papers and expand on parts of the measurements that were not included or only partially described in the papers. The aim is to include material that could be of interest for someone who wants to redo similar experiments. The papers cover a range of topics. Still, even though the topics studied have varied, most of the measurements have been related to studies of the transverse and longitudinal beam sizes or the lifetime limitations in the MAX II and MAX III storage rings. The focus of the thesis will thus be on these subjects.

Chapter 1 gives an introduction to synchrotron light sources in general and MAX-lab in particular. In Chapter 2 basic relations in accelerator physics are introduced. Chapter 3 briefly describes the measurement of the transverse beam size using the vis-UV imaging method and looks into the paraxial optics and Seidel abberations for the MAX III diagnostic beam line, topics that were only briefly mentioned in Paper **II**. Chapter 4 expands on aspects of the emittance measurement in Paper **III**, including the MATLAB LOCO fits and the dispersion measurement. The MAX III triple RF system is described in Chapter 5 along with a more detailed description of how the simulations of the triple RF system in Paper **IV** were performed and examples of simulation results. In Chapter 6 the measurement of the bunch length in Paper **IV** using a strip line and an optical sampling oscilloscope is described in more detail. Finally, Chapter 7 and Chapter 8 give a more general introduction to the lifetimes and lifetime measurements in Paper **I** and Paper **IV**. Chapter 7 describes the different lifetimes and acceptances of an electron storage ring. In Chapter 8 methods to measure the lifetimes and acceptances are described, focusing on vertical and horizontal scraper measurements and lifetime vs. main cavity voltage measurements.

Acknowledgements

It all started in Austria.

Late one evening in Linz, where I spent a year as an exchange student during my MSc studies, I was chatting with my friend Martin Pekkarinen on Skype. He had attended an oral exam held by Lennart Isaksson and had received information about the photonuclear research group at MAX-lab. Martin thought it sounded like something for me. Indeed it did. I didn't know much about MAX-lab, but I contacted Lennart and decided to do my MSc project in the photonuclear group. One MSc project later I had not found any signs of deeply bound pionic atoms from the (γ, p) reaction, but I had decided that I wanted to continue in the field of research and do a PhD at MAX-lab. Thanks to Martin for the tip and thanks to Lennart Isaksson, Kevin Fissum, Kurt Hansen, Magnus Lundin, Bent Schröder and all the other members of the photonuclear group for making the MSc project such an enjoyable time.

During the MSc project I took a course in accelerator technique given by Sverker Werin. It opened my eyes for the research in accelerator physics performed at MAX-lab. I applied for a PhD position in accelerator physics and got the position, the result of which is what you hold in your hands right now.

I would like to thank my main supervisor Erik Wallén and my assistant supervisor Åke Andersson, without whom the work presented in this thesis would not have been possible. Thanks to Erik for helping me to see the big picture and not getting bogged down in details and for trying to get things done in time. Thanks to Åke for all the fruitful discussions and tips and for encouraging me to look into and try to understand even the smallest details. Thanks also to Lars-Johan Lindgren, who was my assisting supervisor during the first two years.

I would also like to thank all the others in the accelerator physics group and at MAX-lab who helped me along the way. Thanks to Magnus Sjöström, Nino Čutić, Sara Thorin, Roderik Bruce and the other PhD students that finished before me, as well as Jonas Breunlin, Galina Skripka, Olivia Karlberg and the other PhD students that will finish after me, for the great research atmosphere and for sharing information and tips. Thanks to Per Lilja and Dionis Kumbaro for teaching me how to inject the rings and for making me feel at home in the control room. Thanks to Lars Malmgren, Robert Nilsson, Anders Månsson, Johan Thånell, Claes Lenngren, Filip Lindau, Magnus Lundin, Kurt Hansen, Håkan Svensson, Bengt Sommarin, Mikael Johansson, Martin Nilsson, Magnus Berglund and many others for helping out when I needed assistance with different things or when the machine didn't behave. Thanks to Simon Leemann, Mikael Eriksson, Pedro Fernandes Tavares and Sverker Werin for discussions about accelerator physics and measurement results.

Or maybe it all started in the library of Höör.

I was about 13 or 14 years old when I plowed through the popular science books in the library of Höör dedicated to elementary particle physics and large scale accelerators. Since it was Höör there were not that many books, but it was enough for me to decide that I wanted to study physics when I got older and that the dream job would be to one day work and do experiments at an accelerator facility. I would like to thank my father Lars, my late mother Gerd and my brothers Jonas and Magnus for supporting and encouraging my interests in the natural sciences and for making me who I am.

My thanks also goes out to my friends, and the student organizations I've been involved in during the years as a student at Lund University, for providing much needed diversions from work. Thanks to the members of Bleckhornen and especially to #365, #358 and #390 for the great year we had running the place.

During an interview for the PhD position I got a question if I had a girlfriend or children, since being a PhD student might mean a lot of time spent doing research. At the time the answer was no, but somehow I managed to find, and even hold on to, a great girl despite being a PhD student in physics. Thanks, Anna, for all the support and encouragement and my apologies for all the evenings, weekends and holidays spent at the lab.

ABBREVIATIONS

BESSY II	Berliner ElektronenSpeicherring-gesellschaft für SYnchrotronstrahlung II (synchrotron light source in Berlin, Germany)
BPM	Beam Position Monitor
ESRF	European Synchrotron Radiation Facility (synchrotron light source in Grenoble, France)
FBSF	Filament-Beam-Spread Function
FWHM	Full Width at Half Maximum
NEG	NonEvaporable Getter
RF	Radio Frequency
RMS	Root Mean Square
SLS	Swiss Light Source (synchrotron light source in Villigen, Switzerland)
SPEAR	Stanford Positron Electron Asymmetric Rings (former electron positron collider in Stanford, USA
SR	Synchrotron Radiation
UV	UltraViolet
vis-UV	Visible to UltraViolet

NOMENCLATURE

a_a	Aberration coefficient of astigmatism ($1/\mathrm{m}^3$)
a_c	Aberration coefficient of coma ($1/\mathrm{m}^3$)
a_d	Aberration coefficient of distortion ($1/\mathrm{m}^3$)
a_f	Aberration coefficient of field curvature ($1/\mathrm{m}^3$)
a_s	Aberration coefficient of spherical aberration ($1/\mathrm{m}^3$)
$a_x(s)$	Horizontal aperture (m)
$a_y(s)$	Vertical aperture (m)
A_a	Peak aberration coefficient of astigmatism (m)
A_c	Peak aberration coefficient of coma (m)
A_d	Peak aberration coefficient of distortion (m)
A_f	Peak aberration coefficient of field curvature (m)
A_s	Peak aberration coefficient of spherical aberration (m)
A_x	Horizontal acceptance (m)
A_y	Vertical acceptance (m)
B	Magnetic flux density (T)
c	Velocity of light in vacuum (m/s)
C	Ring circumference (m)
C_q	Quantum constant (m)
C_γ	Constant (m/eV^3)
d_l	Distance lens center to principal point (m)
d_p	Image displacement due to plane-parallel plate (m)
e	Elementary charge (C)
E_0	Nominal electron energy (eV)
f	Frequency (Hz)
f_0	Revolution frequency (Hz)
f_{RF}	Transmitter/main cavity radio frequency (Hz)
f_{res}	Cavity resonance frequency (Hz)

f_l	Effective focal length (m)
f_s	Synchrotron frequency (Hz)
F_n	Fourier component amplitude at harmonic n (1)
h	Object height (m)
h'	Image height (m)
h_{RF}	RF harmonic number (1)
$\hbar$	Reduced Planck constant (eV s)
$\mathcal{H}(s)$	$\mathcal{H}$ function (m)
I	Beam current (A)
I_1	First synchrotron radiation integral (m)
I_2	Second synchrotron radiation integral (1/m)
I_3	Third synchrotron radiation integral (1/m^2)
I_4	Fourth synchrotron radiation integral (1/m)
I_5	Fifth synchrotron radiation integral (1/m)
$I_{beam}(f)$	Beam current (A)
l_{strip}	Strip line length (m)
j_x	Horizontal damping partition number (1)
j_y	Vertical damping partition number (1)
j_z	Longitudinal damping partition number (1)
J_x	Horizontal action (m)
J_y	Vertical action (m)
$k(s)$	Quadrupole strength (1/m^2)
m	Magnification factor (1)
m_e	Electron rest mass (eV/c^2)
n	Higher harmonic order of Landau cavity (1)
n_g	Residual gas density (1/m^3)
n_l	Refractive index of lens (1)
n_p	Refractive index of plane-parallel plate (1)
N_b	Number of electrons per bunch (1)
N_e	Number of electrons (1)
p_l	Lens position factor (1)
$P_{att}(f)$	Relative cable attenuation (1)
$P_{signal}(f)$	Signal strength at spectrum analyzer (W)
q_l	Lens shape factor (1)
Q	Cavity quality factor (1)
Q_x	Horizontal betatron tune (1)
Q_y	Vertical betatron tune (1)
Q_z	Synchrotron tune (1)

r	Radial coordinate (m)
r_0	Radius of exit pupil (m)
r_e	Classical electron radius (m)
R_l	Radius of curvature of lens (m)
R_S	Cavity shunt impedance (Ω)
s	Coordinate along the ideal orbit (m)
S	Object distance (m)
S'	Image distance (m)
S_p	Distance plane-parallel plate to image (m)
t	Time (s)
t_l	Central thickness of lens (m)
t_p	Thickness of plane-parallel plate (m)
T_0	Revolution time (s)
$U(\delta)$	Energy loss per turn (eV)
U_0	Energy loss per turn from synchrotron radiation emission (eV)
U_{tot}	Total energy loss per turn (eV)
U_L	Energy loss per turn in Landau cavity (eV)
V_0	Peak voltage in the main cavity (V)
V_L	Peak voltage in Landau cavity (V)
$V_p(f)$	Induced voltage at strip line port (V)
$V_{RF}(\varphi)$	RF voltage (V)
$W(r, \theta; h')$	Primary aberration function (m)
$W(\rho_r, \theta)$	Primary aberration function (m)
x	Horizontal displacement coordinate (m)
x'	Horizontal angular deviation coordinate (1)
y	Vertical displacement coordinate (m)
y'	Vertical angular deviation coordinate (1)
z	Longitudinal displacement coordinate (m)
Z	Atomic number (1)
$Z_t(f)$	Transfer impedance of strip line (Ω)
α	Fine-structure constant (1)
α_c	Momentum compaction factor (1)
α_l	Angle optical axis – chief ray for lens (1)
α_p	Angle optical axis – chief ray for plane-parallel plate (1)
$\alpha_x(s)$	Horizontal alpha Twiss parameter (1)
$\alpha_y(s)$	Vertical alpha Twiss parameter (1)
$\beta_x(s)$	Horizontal beta function [beta Twiss parameter] (m)
$\beta_y(s)$	Vertical beta function [beta Twiss parameter] (m)

γ	Relativistic gamma factor (1)
$\gamma_x(s)$	Horizontal gamma Twiss parameter (1/m)
$\gamma_y(s)$	Vertical gamma Twiss parameter (1/m)
δ	Relative momentum deviation (1)
$\delta_{acc}(s)$	Relative momentum acceptance (1)
$\delta_{acc}^{L}(s)$	Lattice relative momentum acceptance (1)
δ_{acc}^{RF}	RF relative momentum acceptance (1)
$\delta_{bucket}(\varphi)$	RF bucket (1)
$\delta_{separatrix}(\varphi)$	Separatrix trajectory (1)
$\delta_{trajectory}(\varphi)$	Longitudinal phase space trajectory (1)
ϵ_x	Horizontal emittance (m)
ϵ_y	Vertical emittance (m)
$\eta_x(s)$	Horizontal dispersion function (m)
$\eta'_x(s)$	Derivative of horizontal dispersion function (1)
$\eta_y(s)$	Vertical dispersion function (m)
$\eta'_y(s)$	Derivative of vertical dispersion function (1)
θ	Angular coordinate (1)
θ_n	Fourier component phase at harmonic n (1)
$\lambda(\varphi)$	Electron density distribution (1)
$\mu_x(s)$	Horizontal betatron phase (1)
$\mu_y(s)$	Vertical betatron phase (1)
$\rho(s)$	Radius of curvature of the reference trajectory (m)
ρ_r	Normalized radial variable (1)
σ_δ	Relative RMS momentum spread (1)
$\sigma_x(s)$	Horizontal RMS beam size (m)
$\sigma_{x'}(s)$	Horizontal RMS beam divergence (1)
$\sigma_y(s)$	Vertical RMS beam size (m)
$\sigma_{y'}(s)$	Vertical RMS beam divergence (1)
σ_z	Longitudinal RMS bunch length (m)
$\tau_{elastic}$	Elastic scattering lifetime (s)
$\tau_{inelastic}$	Inelastic scattering lifetime (s)
$\tau_{quantum}$	Quantum lifetime (s)
τ_{tot}	Electron beam lifetime (s)
$\tau_{Touschek}$	Touschek lifetime (s)
τ_x	Horizontal damping time (s)
τ_y	Vertical damping time (s)
τ_z	Longitudinal damping time (s)
φ	Phase of the fundamental RF (1)

φ_L	Harmonic phase angle (1)
φ_s	Synchronous phase angle (1)
$\Phi_{RF}(\varphi)$	RF potential (1)
Ψ	Tuning angle (1)

CHAPTER 1

MAX-LAB

MAX-lab is a part of the MAX IV laboratory, which besides running the present facility at MAX-lab is also constructing the new MAX IV facility. The MAX IV facility will consist of a 3 GeV linear accelerator, a 96 m circumference 1.5 GeV synchrotron light source and a 528 m circumference 3 GeV synchrotron light source. The present facility consists of the MAX Injector and the MAX I, MAX II and MAX III synchrotron light sources. When the MAX IV facility is ready for operation, the present facility at MAX-lab will shut down. The work presented in this thesis was performed at MAX II and MAX III and the focus of this chapter is to introduce the present facility at MAX-lab. Section 1.1 gives a general introduction to synchrotron light sources. Section 1.2 introduces the MAX Injector and Secs. 1.3–1.5 introduce MAX I, MAX II and MAX III, respectively.

1.1 Synchrotron light sources

The purpose of synchrotron light sources is to provide electromagnetic radiation for experiments in a wide variety of research fields. The electromagnetic radiation is typically produced by high-energy electrons with an energy more than a thousand times larger than the rest mass energy. The emitted radiation, called synchrotron radiation, covers a large span of energies from the infrared and ultraviolet to the soft and hard x-ray regions. It can be used for material sciences, structural biology, energy research, condensed matter physics and many other fields of research.

Most synchrotron light sources are electron storage rings, where the electrons circulate around the storage ring for many hours and the nominal electron energy is kept constant. Dipole magnets steer the electrons to form a closed path and quadrupole magnets focus the electrons toward the ideal design orbit. Sextupoles, and sometimes octupoles, are used to compensate and correct chromatic and higher-order effects. The energy lost by the electrons due to the emission of synchrotron radiation is compensated by a corresponding energy gain in radio frequency (RF) cavities. The periodically varying electric fields in the RF cavities give rise to a discrete number of RF buckets that can be injected with electrons. At MAX-lab, all RF buckets are typically filled with electrons, which gives an even distribution of electron bunches circulating around the storage rings. It the case of MAX II that corresponds to 30 electron bunches and for MAX III 12 electron bunches.

The electrons in the storage ring are contained in a vacuum system with an ultra-high vacuum in order to reduce the scattering between the electrons and the atoms of the residual gas, which is essential for a long electron beam lifetime. Among the diagnostic equipment used to monitor the electrons in the storage ring are beam position monitors that determine the position of the electron bunches, current transformers to measure the beam current and lifetime, strip lines to study the frequency spectrum of the beam, and scrapers (variable aperture restrictions) to study the electron loss processes.

The first generation of synchrotron light sources parasitically used the synchrotron radiation emitted from bending magnets in storage rings used for elementary particle research. The second generation of synchrotron light sources were built specifically for the production of synchrotron radiation. They contained a few straight sections where insertion devices could be installed, but the synchrotron radiation primarily came from the bending magnets. Third generation synchrotron light sources are optimized from the outset to contain insertion devices, such as wigglers and undulators, in long straight sections between the magnet cells. Insertion devices are arrays of magnets with alternating polarity which cause the electrons to follow a undulating path and produce synchrotron radiation with a tunable energy and higher intensity than the bending magnet radiation. The synchrotron radiation from an insertion device or a bending magnet is filtered and focused in a beam line and transported to the experimental station where it interacts with the sample being studied. The different beam lines operate independently and at any given time many parallel experiments can take place on the different beam lines at a synchrotron light source.

1.2 MAX injector

An overview of the MAX-lab facility is shown in Fig. 1.1. The MAX Injector is located in the basement and the three synchrotron light sources MAX I, MAX II and MAX III are located on the ground floor.

The original injector at MAX-lab was a 100 MeV race-track microtron [1]. In 2002, after more than 20 years of operation, the race-track microtron was

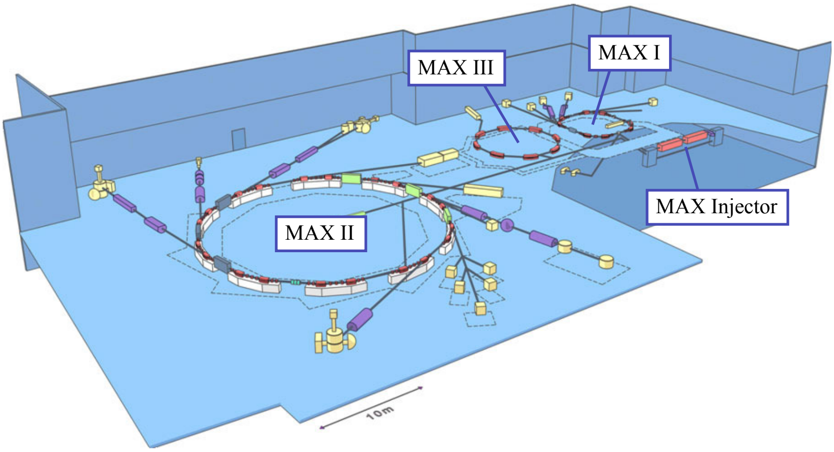

Figure 1.1: *Overview of the MAX-lab facility. In the basement the electron gun and the linear accelerators of the MAX Injector provide electrons for injections into the rings. On the ground floor the three synchrotron light sources MAX I, MAX II and MAX III provide synchrotron radiation for experiments at 13 different beam lines. MAX I is also operated as a pulse-stretcher for experiments in nuclear physics.*

replaced by a new injector system consisting of an electron gun and a linear accelerator [2]. The thermionic 3 GHz RF gun [3] injects the beam into two 5.2 m long linac structures that each gives an energy increase of approximately 100 MeV. After passing both linacs the electrons are either transported towards MAX I or turned around in a recirculator to pass through the linacs a second time. After the second pass the electrons, now with an energy of about 400 MeV, are transported to MAX II or MAX III.

The thermionic gun can also be operated as a photocathode gun [4]. This mode of operation is used for the MAX-lab test free-electron laser [5], located in center of the MAX II ring.

1.3 MAX I

At the early stages of development, the MAX accelerator system was envisaged as a project for experiments in photonuclear physics, with a race-track microtron, a pulse-stretcher and a photon tagging facility. In 1979, the project was modified to also include experiments using synchrotron radiation. MAX I [1, 6] was designed to work as a 100 MeV pulse-stretcher as well as a 550 MeV 2nd generation synchrotron light source. The first electrons were stored in 1985 and the first experiment using the synchrotron radiation took place in 1986. On the 30th of January 1987 MAX-lab was officially inaugurated.

MAX I has a circumference of 32.4 m, a 500 MHz RF system and four straight sections. At most, nine beam lines were in operation at MAX I. The majority of the beam lines have utilized the synchrotron radiation from dipole magnets, but two undulators have also been installed. Today the storage ring is effectively retired as a synchrotron light source. A beam line utilizing the infrared synchrotron radiation from one of the dipole magnets is still occasionally used. MAX I is operated as a pulse-stretcher [7] around 16 weeks per year for photonuclear experiments. The original photon tagging facility [8] used the stretched 100 MeV microtron electron beam. With the new linac injector the maximum electron energy injected into MAX I increased to about 200 MeV, and the photon tagging facility was upgraded to utilize the increase in electron energy [9].

1.4 MAX II

In 1991, four years after MAX I was inaugurated, MAX-lab got the go-ahead to build a second synchrotron light source. The MAX II [10, 11] storage ring is a 3rd generation synchrotron light source with an electron energy of 1.5 GeV. With a 90 m circumference, ten straight sections and a higher electron energy than previously available, MAX II increased the capacity of MAX-lab and allowed experiments using x-ray synchrotron radiation. The first electrons circulated around MAX II in 1994 and the storage ring was officially inaugurated by the King of Sweden in 1995.

Originally MAX II was injected using MAX I as a pre-accelerator and the storage ring had a 500 MHz RF system. With the new linac injector, electrons could be injected directly into MAX II from the 400 MeV injector. The RF system was changed from a 500 MHz system to a 100 MHz system [12] when two superconducting wigglers were installed. The RF system today consists of three 100 MHz main cavities and a 500 MHz Landau cavity.

MAX II is the main light source at MAX-lab and all ten straight sections in the storage ring are utilized. Three straight sections are used for the injection, the main RF cavities and for beam diagnostics. The remaining seven straight sections are equipped with insertion devices; three planar undulators, one elliptically polarizing undulator, one wiggler and two superconducting wigglers. Two additional beam lines use the synchrotron radiation from bending magnets.

1.5 MAX III

When the upgrade of the MAX injector was funded, MAX-lab also received funding for a third synchrotron light source. MAX III [13, 14] is a 3rd generation synchrotron light source with an electron energy of 700 MeV, a circum-

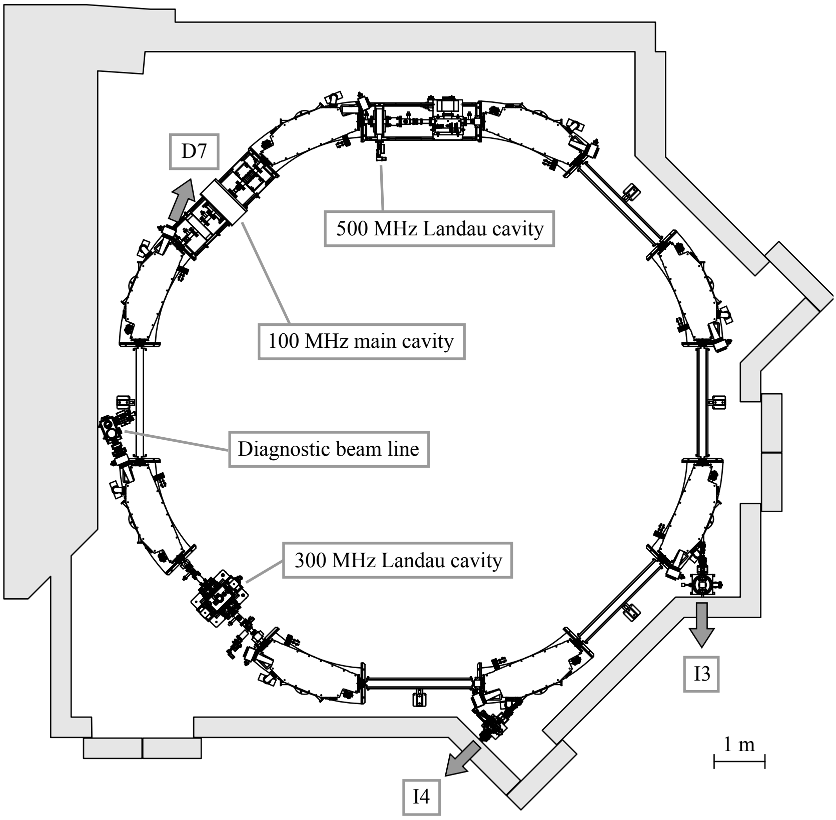

Figure 1.2: *Drawing of the MAX III synchrotron light source. The storage ring has a circumference of 36 m and an eightfold periodicity. Each unit cell contains a dipole with a defocusing gradient and two focusing quadrupoles with a sextupole component. An elliptically polarizing undulator and a planar undulator provides synchrotron radiation in the ultraviolet region to beam lines I3 and I4. A third beam line, D7, utilizes the infrared synchrotron radiation from the dipole magnet in cell 7.*

ference of 36 m and eight straight sections. One of the purposes of MAX III was to test new accelerator technology in preparation for MAX IV. The storage ring makes extensive use of combined function magnets and all magnets of the unit cell are machined into a common iron block. The first electrons were stored in 2005 and the first experiment using the synchrotron radiation took place in 2008. MAX III has, to the knowledge of the author, never been officially inaugurated.

Figure 1.2 shows a drawing of the MAX III ring. Five of the eight straight sections in MAX III are available for insertion devices. Two insertion devices have been installed, an elliptically polarizing undulator and a planar undulator, providing synchrotron radiation in the ultraviolet region. A third beam line utilizes the infrared synchrotron radiation from one of the dipole magnets. The RF system consists of a 100 MHz main cavity, a 300 MHz passive Landau cavity and a 500 MHz passive Landau cavity. The main cavity straight section also contains a skew quadrupole and the injection kicker. The 300 MHz cavity is located in the diagnostic straight section together with the horizontal and vertical scrapers, strip lines and two extra sets of beam position monitors. The 500 MHz cavity is located in the injection straight section, that also contains strip lines, a current transformer and the septum. The start of the injection straight section (slightly to the left of the 500 MHz cavity in Fig. 1.2) is chosen as the zero position for the figures in this thesis that refer to the position in MAX III.

Chapter 2

Basic relations in accelerator physics

This chapter introduces basic accelerator physics terms and relations that will be used later on in the thesis. For a more thorough treatment the reader is referred to the many textbooks that exist. A lot of excellent material is available free of charge on the Internet, such as the introduction to the physics of electrons storage rings by Sands [15] and the proceedings to the CERN Accelerator School (see e.g. [16]). Examples of introductory textbooks are the books by Wilson [17] and Wille [18] and examples of more comprehensive textbooks are the books by Wiedemann [19] and Lee [20]. The references for the material presented in this chapter are Refs. [15–20] mentioned above together with Ref. [21] and Ref. [22].

The material in this chapter is focused on electron storage rings. Section 2.1 introduces the coordinate system. In Sec. 2.2 and Sec. 2.3 basic relations from linear transverse dynamics and longitudinal dynamics are presented. Radiation damping and quantum excitation are introduced in Sec. 2.4 and in Sec. 2.5 the electron beam dimensions in the six phase space coordinates are given. The electrons are assumed to be ultra-relativistic and the deviations from the ideal orbit are assumed to be small. The horizontal and vertical subspaces are assumed to be uncoupled and the ideal orbit is assumed to be located in the horizontal plane.

2.1 Coordinate system

The motion of the electrons is described using a coordinate system related to the ideal orbit of the beam. The coordinate s describes the distance along this ideal orbit from an initial reference point. The origin of the coordinate system coincides with the position of an ideal particle with energy E_0 propagating along the ideal orbit. For small deviations from the ideal orbit the motion of the electrons can be described by the following six phase space coordinates. The transverse horizontal motion, perpendicular to the direction of the ideal particle, is described by the horizontal displacement x from the ideal particle and the horizontal angular deviation $x' = \mathrm{d}x/\mathrm{d}s$ from the ideal orbit. In a similar way, the transverse vertical motion is described by the vertical displacement y and the vertical angular deviation $y' = \mathrm{d}y/\mathrm{d}s$. The longitudinal motion, tangential to the direction of the ideal particle, is described by the longitudinal displacement z and the relative momentum deviation δ. The horizontal displacement x is positive in the outward direction, the vertical displacement y is positive in the upward direction and the longitudinal displacement z is positive in the forward direction.

Other choices for the phase space coordinates are common. The horizontal and vertical momentum normalized by the momentum of the ideal particle is often used instead of the horizontal and vertical angular deviation. Instead of the relative momentum deviation, the energy deviation or the relative energy deviation may be used. Also, the longitudinal coordinate is sometimes expressed in time or phase.

2.2 Linear transverse dynamics

For the linear approximation of the transverse dynamics, only the effects of the dipole and quadrupole terms in an expansion of the magnetic field are taken into account. The magnitude $B_0(s)$ of the magnetic field on the ideal orbit gives a radius of curvature $\rho(s)$ of the ideal orbit

$$\frac{1}{\rho(s)} = \frac{ec}{E_0} B_0(s) \tag{2.1}$$

where e is the elementary charge, c is the speed of light and E_0 is the nominal electron energy. Since the ideal orbit is located in the horizontal plane $\rho(s)$ describes the horizontal radius of curvature. The vertical radius of curvature of the ideal orbit is infinite.

The quadrupole field is zero on the ideal orbit but rises linearly with the transverse displacement from the ideal orbit. The horizontal quadrupole strength $k(s)$ is given by

$$k(s) = \frac{ec}{E_0} \left(\frac{\partial B_y}{\partial x} \right)_s \tag{2.2}$$

where $(\partial B_y/\partial x)_s$ is the horizontal gradient of the magnetic field at position s. A horizontally focusing quadrupole is a vertically defocusing quadrupole. The vertical quadrupole strength is thus $-k(s)$.

The radius of curvature and the quadrupole strength vary around the ring according to the placement of the magnets. After a complete turn in the ring the electrons will pass the same magnets again. The functions $\rho(s)$ and $k(s)$ are thus periodic functions with

$$\rho(s+C) = \rho(s) \tag{2.3}$$

$$k(s+C) = k(s) \tag{2.4}$$

where C is the circumference of the ring.

The magnets in the storage ring are designed so that the dipole fields and the focusing and defocusing quadrupole fields combined give a net focusing effect in both the horizontal and vertical direction. This is achieved by a suitable choice of strength and spacing of the magnets so that the electrons oscillating around the ideal orbit tend to be closer to the ideal orbit in the defocusing fields and further away from the ideal orbit in the focusing fields.

The linear equations of motion for the transverse motion are given by

$$\frac{\mathrm{d}^2x(s)}{\mathrm{d}s^2} + \left(\frac{1}{\left[\rho(s)\right]^2} - k(s)\right)x(s) = \frac{1}{\rho(s)}\delta \tag{2.5}$$

$$\frac{\mathrm{d}^2y(s)}{\mathrm{d}s^2} + k(s)\,y(s) = 0 \tag{2.6}$$

Starting with the vertical case, the vertical equation of motion in Eq. (2.6) resembles the equation of motion for a simple harmonic oscillator. If $k(s)$ would be constant the solution would be a harmonic oscillation with a constant amplitude and a linear phase advance. If $k(s)$ is periodic, which is the case for a storage ring, Eq. (2.6) has the form of Hill's equation and the general solution describes a vertical betatron oscillation about the ideal orbit given by

$$y(s) = \sqrt{2J_y\beta_y(s)}\cos\left(\mu_y(s) + \mu_{y0}\right) \tag{2.7}$$

where J_y and μ_{y0} are constants, $\beta_y(s)$ is a periodic function with the same periodicity as $k(s)$, and $\mu_y(s)$ is given by

$$\mu_y(s) = \int_0^s \frac{1}{\beta_y(s')}\mathrm{d}s' \tag{2.8}$$

The solution in Eq. (2.7) resembles a harmonic oscillation, but with an amplitude and a phase advance that depend on the position s. J_y is the vertical action or vertical single particle invariant, $\beta_y(s)$ is the vertical beta function and $\mu_y(s)$ is the vertical betatron phase.

For the horizontal case, the horizontal equation of motion in Eq. (2.5) contains an additional focusing term $(1/[\rho(s)]^2)$ because of the curvature of the ideal orbit. For a particle with a momentum deviation the curvature of the orbit will differ from the ideal orbit, which gives rise to a term in the right-hand side of the horizontal equation of motion that is non-zero for particles with a momentum deviation. The general solution of Eq. (2.5) is the sum of a homogeneous solution and a particular solution. The homogeneous solution is similar to the vertical solution and describes a horizontal betatron oscillation about the closed orbit. The particular solution defines a dispersion function that multiplied with the momentum deviation describes the off-momentum closed orbit. The general solution is given by

$$x(s) = \sqrt{2J_x\beta_x(s)}\cos\left(\mu_x(s) + \mu_{x0}\right) + \eta_x(s)\delta \tag{2.9}$$

where J_x is the horizontal action or horizontal single particle invariant, $\beta_x(s)$ is the horizontal beta function, μ_{x0} is a constant, $\eta_x(s)$ is the horizontal dispersion function, δ is the momentum deviation and $\mu_x(s)$ is the horizontal betatron phase given by

$$\mu_x(s) = \int_0^s \frac{1}{\beta_x(s')}\mathrm{d}s' \tag{2.10}$$

The phase advance during a complete revolution around the storage ring is given by 2π times the betatron tune. The betatron tune describes the number of betatron oscillations the particles perform during one revolution in the storage ring. The horizontal and vertical betatron tune is given by

$$Q_x = \frac{1}{2\pi}\oint \frac{1}{\beta_x(s)}\mathrm{d}s \tag{2.11}$$

$$Q_y = \frac{1}{2\pi}\oint \frac{1}{\beta_y(s)}\mathrm{d}s \tag{2.12}$$

where the integration symbol $\oint$ indicates the integral around the whole ring. Taking MAX III as an example, the horizontal tune is around 3.87 and the vertical tune is around 2.78.

The horizontal angular deviation $x'(s) = \mathrm{d}x(s)/\mathrm{d}s$ and vertical angular deviation $y'(s) = \mathrm{d}y(s)/\mathrm{d}s$ are given by the derivative of Eqs. (2.9) and (2.7) with respect to s

$$x'(s) = -\sqrt{\frac{2J_x}{\beta_x(s)}}\left[\sin\big(\mu_x(s)+\mu_{x0}\big)+\alpha_x(s)\cos\big(\mu_x(s)+\mu_{x0}\big)\right]+\eta_x'(s)\delta \tag{2.13}$$

$$y'(s) = -\sqrt{\frac{2J_y}{\beta_y(s)}}\left[\sin\big(\mu_y(s)+\mu_{y0}\big)+\alpha_y(s)\cos\big(\mu_y(s)+\mu_{y0}\big)\right] \tag{2.14}$$

where $\eta_x'(s)$ is the derivative of the dispersion function given by

$$\eta_x'(s) = \frac{\mathrm{d}\eta_x(s)}{\mathrm{d}s} \tag{2.15}$$

The beta functions $\beta_x(s)$ and $\beta_y(s)$ and the functions $\alpha_x(s)$, $\alpha_y(s)$, $\gamma_x(s)$ and $\gamma_y(s)$ given by

$$\alpha_x(s) = -\frac{1}{2}\frac{\mathrm{d}\beta_x(s)}{\mathrm{d}s} \tag{2.16}$$

$$\alpha_y(s) = -\frac{1}{2}\frac{\mathrm{d}\beta_y(s)}{\mathrm{d}s} \tag{2.17}$$

$$\gamma_x(s) = \frac{1+\big[\alpha_x(s)\big]^2}{\beta_x(s)} \tag{2.18}$$

$$\gamma_y(s) = \frac{1+\big[\alpha_y(s)\big]^2}{\beta_y(s)} \tag{2.19}$$

are sometimes called the Twiss parameters. Together with the dispersion functions $\eta_x(s)$ and $\eta_y(s)$ they are also called the optical functions (the vertical dispersion function $\eta_y(s)$ is zero since it is assumed that only quadrupole fields affect the vertical trajectory). The optical functions are all periodic functions of s with period C.

At a position s in the ring, the displacement and the angular deviation of the electron for each pass map out an ellipse in horizontal phase space $\{x,\, x'\}$ and in vertical phase space $\{y,\, y'\}$ given by

$$\begin{aligned}2J_x = {} & \gamma_x(s)\big[x(s)-\eta_x(s)\delta\big]^2 + 2\alpha_x(s)\big[x(s)-\eta_x(s)\delta\big]\big[x'(s)-\eta_x'(s)\delta\big] \\ & + \beta_x(s)\big[x'(s)-\eta_x'(s)\delta\big]^2\end{aligned} \tag{2.20}$$

$$2J_y = \gamma_y(s)\big[y(s)\big]^2 + 2\alpha_y(s)y(s)y'(s) + \beta_y(s)\big[y'(s)\big]^2 \tag{2.21}$$

The shape and orientation of the two ellipses change as the s-position vary and the electron moves along the ellipses in horizontal and vertical phase space. In the vertical phase space the ellipse at position s has its center at $y(s) = 0$ and $y'(s) = 0$. In the horizontal phase space the ellipse center at position s depends on the momentum deviation of the electron, and the ellipse has its center at $x(s) = \eta_x(s)\delta$ and $x'(s) = \eta_x'(s)\delta$. According to Liouville's theorem the area of phase space elements are conserved for a conservative system. On a short time scale non-conservative effects, such as the emission of synchrotron radiation, can be neglected. The area $2\pi J_x$ and $2\pi J_y$ of the phase space ellipses are conserved and the horizontal and vertical actions are invariants of the particle motion. On a longer time scale the average horizontal and vertical action, i.e. the horizontal and vertical emittance, in the storage ring will instead be determined by the equilibrium between radiation damping and quantum excitation (see Sect. 2.4).

2.3 Longitudinal dynamics

When the trajectories of the ultra-relativistic electrons in the storage ring are bent by the magnets the electrons will lose energy because of emission of synchrotron radiation. An electron with the nominal electron energy E_0 traveling around the ring on the ideal orbit will lose a certain amount of energy U_0 per turn. The energy loss is compensated by the cavities of the radio frequency (RF) accelerating system in the storage ring. If the electron regains the energy U_0 each turn it will continue to circulate on the ideal orbit. This electron is called the synchronous particle or the synchronous electron. The voltage in the RF cavities varies periodically. In order for the synchronous electron to regain the same energy each turn the RF frequency f_{RF} of the RF system must be an integer multiple of electron revolution frequency f_0

$$f_{RF} = h_{RF} f_0 \tag{2.22}$$

where h_{RF} is the harmonic number. For a sinusoidal RF voltage with a peak voltage larger than U_0/e, there are two possible locations per RF period where the voltage is equal to U_0/e and the synchronous particle can regain precisely the energy it has lost during the turn. One location is on the upward slope of the RF voltage and the other is on the downward slope of the RF voltage.

Since the electrons are ultra-relativistic a small momentum deviation will only negligibly affect the velocity of the electron. However, the momentum deviation will influence the electron orbit. An electron with a momentum deviation δ will follow the dispersive orbit instead of the ideal orbit, which will give a different path length around the ring. The ratio of the relative change in path length to the relative difference in momentum is given by the momentum compaction factor α_c according to

$$\frac{\Delta s}{C} = \alpha_c \delta \tag{2.23}$$

where Δs is the change in path length and C is the circumference of the ring. The momentum compaction factor is given by

$$\alpha_c = \frac{I_1}{C} \tag{2.24}$$

where I_1 is the first synchrotron radiation integral given by

$$I_1 = \oint \frac{\eta_x(s)}{\rho(s)} \mathrm{d}s \tag{2.25}$$

with $\eta_x(s)$ the horizontal dispersion function and $\rho(s)$ the radius of curvature of the ideal orbit. The momentum compaction factor is typically positive. An electron with a positive momentum deviation will thus travel a longer distance before it has completed a turn around the storage ring.

An electron that has the same momentum as the synchronous particle but arrives at the RF cavity earlier than the synchronous particle will, in case of a downward RF voltage slope, receive a larger energy gain than the synchronous particle. During the next turn it will travel a longer distance than the synchronous particle. In this chapter it is assumed that the electrons are ultra-relativistic. If that is the case the change in electron velocity is negligible and the turn will, because of the longer distance traveled, take a longer time than for the synchronous particle. During the next pass of the RF cavity the electron will be closer in time to the synchronous particle. After a number of turns the electron will overtake the synchronous particle and receive a smaller energy gain than the synchronous particle. This process will give rise to an oscillation in the longitudinal phase space $\{z, \delta\}$ around the synchronous particle. The oscillations are called synchrotron oscillations. In case of an upward slope of the RF voltage any deviation from the synchronous particle will grow in magnitude. For a sinusoidal RF voltage only one of the two possible locations of the synchronous particle per RF period is stable. In total there are h_{RF} stable synchronous locations in a storage ring.

The longitudinal equations of motion are given by

$$\frac{\mathrm{d}\delta}{\mathrm{d}t} = \frac{eV_{RF}(z) - U(\delta)}{E_0 T_0} \tag{2.26}$$

$$\frac{\mathrm{d}z}{\mathrm{d}t} = -\alpha_c c \delta \tag{2.27}$$

where e is the elementary charge, $V_{RF}(z)$ is the RF voltage, $U(\delta)$ is the energy loss per turn, T_0 is the revolution time (given by $T_0 = 1/f_0$) and c is the speed of light.

The energy loss $U(\delta)$ per turn depends on the momentum deviation. This dependency will give rise to a damping of the longitudinal phase space oscillations (see Sect. 2.4). In the remainder of this section and in Chapter 5 the radiation damping is neglected, since it is a comparatively slow process, and it is assumed that $U(\delta) = U_0$. From the equations of motion in Eqs. (2.26)–(2.27) the longitudinal motion can be described and studied via an RF potential. This is done in Chapter 5 for the triple RF system in MAX III.

For the special case of a single sinusoidal RF system and a small longitudinal displacement z from the synchronous particle the energy gain per turn from the RF system is given by

$$eV_{RF}(z) = eV_0 \sin\left(\varphi_s - \frac{2\pi h_{RF}}{cT_0} z\right) \approx U_0 - \frac{eV_0 2\pi h_{RF} \cos\varphi_s}{cT_0} z \tag{2.28}$$

where V_0 is the peak RF voltage seen by the beam and φ_s is the synchronous phase angle given by

$$\sin\varphi_s = \frac{U_0}{eV_0} \qquad \left(\frac{\pi}{2} < \varphi_s < \pi\right) \tag{2.29}$$

Inserting Eq. (2.28) into Eq. (2.26) (with $U(\delta) = U_0$) and combining it with Eq. (2.27) gives the longitudinal equation of motion

$$\frac{\mathrm{d}^2 z}{\mathrm{d}t^2} + (2\pi f_s)^2 z = 0 \tag{2.30}$$

where f_s is the synchrotron frequency given by

$$f_s = \sqrt{-\frac{eV_0}{E_0} \frac{\alpha_c h_{RF} \cos\varphi_s}{2\pi T_0^2}} \tag{2.31}$$

The equation of motion in Eq. (2.30) is the equation of motion of a simple harmonic oscillator. For a single RF system and small amplitude oscillations the electrons in longitudinal phase space $\{z, \delta\}$ will perform elliptical synchrotron oscillations around the synchronous particle with an oscillation frequency given by the synchrotron frequency. The number of synchrotron oscillations per turn is given by the synchrotron tune

$$Q_z = \frac{f_s}{f_0} = \sqrt{-\frac{eV_0}{E_0}\frac{\alpha_c h_{RF}\cos\varphi_s}{2\pi}} \tag{2.32}$$

For MAX III at normal operating conditions the synchrotron tune is around 0.003. Whereas the electrons in MAX III perform almost four horizontal betatron oscillations per turn and almost three vertical betatron oscillations per turn (see Sec. 2.2) it takes a few hundred turns before the electrons have completed a single synchrotron oscillation.

Further away from the synchronous phase the non-linearity of the RF voltage will become apparent and the oscillation frequency of the synchrotron oscillations will change. For large amplitudes the electron can escape the RF bucket. This gives a maximum momentum deviation, the RF momentum acceptance, above which the electron will be lost. The momentum acceptance is discussed further in Chapter 7.

2.4 Radiation damping

The energy loss per turn for the synchronous particle due to the emission of synchrotron radiation is given by

$$U_0 = \frac{C_\gamma}{2\pi} E_0^4 I_2 \tag{2.33}$$

where E_0 is the nominal electron energy, C_γ is a constant and I_2 is the second synchrotron radiation integral given by

$$I_2 = \oint \frac{1}{\left[\rho(s)\right]^2}\mathrm{d}s \tag{2.34}$$

with $\rho(s)$ the radius of curvature of the ideal orbit. The constant C_γ is given by

$$C_\gamma = \frac{4\pi}{3}\frac{r_e}{\left[m_e c^2\right]^3} \approx 8.846 \times 10^{-32}\ \mathrm{m/eV^3} \tag{2.35}$$

where r_e is the classical electron radius, m_e is the electron rest mass and c is the speed of light.

The energy loss per turn depends on the momentum deviation. During a longitudinal phase space oscillation the electron will lose more energy than U_0

per turn when the momentum deviation is positive and less energy than U_0 per turn when the momentum deviation is negative. After a synchrotron oscillation the amplitude of the phase space oscillation will have become slightly smaller. This effect is called radiation damping and the longitudinal damping time is given by

$$\tau_z = \frac{2}{j_z}\frac{E_0}{U_0}T_0 \tag{2.36}$$

where T_0 is the revolution time and j_z is the longitudinal damping partition number given by

$$j_z = 2 + \frac{I_4}{I_2} \tag{2.37}$$

with I_4 the fourth synchrotron radiation integral given by

$$I_4 = \oint \frac{\eta_x(s)}{\rho(s)}\left(\frac{1}{\left[\rho(s)\right]^2} + 2k(s)\right)\mathrm{d}s \tag{2.38}$$

where $\eta_x(s)$ is the horizontal dispersion function and $k(s)$ is the quadrupole strength.

If the emission of synchrotron radiation was a purely classical process the synchrotron oscillation amplitude would damp down to almost zero because of the radiation damping. However, the synchrotron radiation is emitted in discrete units. For example, an electron in MAX III emits on average around 90 photons per turn. The discrete emission of synchrotron radiation induces noise on the beam and causes the amplitude of the synchrotron oscillation to increase. The equilibrium between the quantum excitation and the radiation damping determines the distribution of the momentum deviations of the electrons. The equilibrium momentum spread, or natural momentum spread as it is also called, is the standard deviation of the Gaussian momentum deviation distribution. It is given by

$$\sigma_\delta^2 = C_q\gamma^2\frac{I_3}{j_z I_2} \tag{2.39}$$

where γ is the relativistic gamma factor given by

$$\gamma = \frac{E_0}{m_e c^2} \tag{2.40}$$

I_3 is the third synchrotron radiation integral given by

$$I_3 = \oint \frac{1}{\left|\rho(s)\right|^3} \mathrm{d}s \tag{2.41}$$

and C_q is the quantum constant given by

$$C_q = \frac{55}{32\sqrt{3}} \frac{\hbar}{m_e c} \approx 3.832 \times 10^{-13} \text{ m} \tag{2.42}$$

where $\hbar$ is the reduced Planck constant. The natural momentum spread takes the radiation damping and quantum excitation into account. If there are other excitation processes present, such as longitudinal instabilities in the case of MAX III, the momentum spread will be larger than the natural momentum spread.

The emission of synchrotron radiation also has a damping effect on the transverse betatron oscillations. The synchrotron radiation is emitted along the instantaneous direction of motion of the electron and the momentum of the electron is decreased along this direction. The RF cavity restores the momentum longitudinally, without any change in the transverse momentum. The net effect is a decrease in the transverse angular deviation and in the betatron oscillation amplitude. In the horizontal direction the effect of the dispersion must also be taken into account, which will also have an influence on the betatron oscillation amplitude. Combined, the horizontal damping time is given by

$$\tau_x = \frac{2}{j_x} \frac{E_0}{U_0} T_0 \tag{2.43}$$

where j_x is the horizontal damping partition number given by

$$j_x = 1 - \frac{I_4}{I_2} \tag{2.44}$$

The discrete emission of the synchrotron radiation introduces quantum excitations on the horizontal betatron oscillations. If the photon is emitted at a location with dispersion the electron will oscillate around a new off-momentum orbit which will on average increase the betatron oscillation amplitude. The equilibrium between the quantum excitation and the radiation damping gives a Gaussian distribution of the horizontal actions of the electrons. The horizontal emittance is defined as the average horizontal action of all the electrons in the storage ring. The horizontal equilibrium emittance, or the natural emittance as it is also called, is given by

$$\epsilon_x = \langle J_x \rangle = C_q \gamma^2 \frac{I_5}{j_x I_2} \tag{2.45}$$

where $\langle J_x \rangle$ is the average horizontal action and I_5 is the fifth synchrotron radiation integral given by

$$I_5 = \oint \frac{\mathcal{H}(s)}{\left|\rho(s)\right|^3} \mathrm{d}s \tag{2.46}$$

with $\mathcal{H}(s)$ the $\mathcal{H}$ function given by

$$\mathcal{H}(s) = \gamma_x(s)\left[\eta_x(s)\right]^2 + 2\alpha_x(s)\eta_x(s)\eta_x'(s) + \beta_x(s)\left[\eta_x'(s)\right]^2 \tag{2.47}$$

where $\alpha_x(s)$ is the horizontal alpha Twiss parameter, $\gamma_x(s)$ is the horizontal gamma Twiss parameter and $\eta_x'(s)$ is the derivative of the horizontal dispersion function.

As discussed above, the emission of synchrotron radiation has a damping effect on the transverse betatron oscillations. The vertical damping time is given by

$$\tau_y = \frac{2}{j_y} \frac{E_0}{U_0} T_0 \tag{2.48}$$

where j_y is the vertical damping partition number given by

$$j_y = 1 \tag{2.49}$$

Since the vertical dispersion is assumed to be zero, the quantum excitation process that increases the horizontal betatron oscillation amplitudes is not present for the vertical betatron oscillation amplitudes. Still, the vertical equilibrium emittance is not zero. The opening angle of the emitted synchrotron radiation will give a small excitation of the vertical betatron oscillations. The fundamental lower limit on the vertical emittance, from the opening angle of the synchrotron radiation, is given by [23]

$$\epsilon_y = \langle J_y \rangle = \frac{13}{55} \frac{C_q}{j_y I_2} \oint \frac{\beta_y(s)}{\left|\rho(s)\right|^3} \mathrm{d}s \tag{2.50}$$

where $\langle J_y \rangle$ is the average vertical action and β_y is the vertical beta function. Although the vertical emittance from the opening angle of the synchrotron radiation is not zero, it is a very small number. For MAX III it is more than four orders of magnitude smaller than the horizontal equilibrium emittance. In practice, it will be errors in the alignment of the magnets that will determine the vertical emittance in an electron storage ring. Vertically misaligned quadrupoles and roll errors of bending magnets introduce vertical dispersion. Vertically misaligned sextupoles and roll errors of quadrupole magnets cause linear coupling of the horizontal and vertical betatron motion. For MAX III, the combined errors give a vertical emittance that is around one percent of the horizontal emittance (see Paper **III**).

The total amount of radiation damping in the longitudinal, horizontal and vertical phase space is given by

$$\frac{1}{\tau_x}+\frac{1}{\tau_y}+\frac{1}{\tau_z}=\frac{U_0}{2E_0T_0}(j_x+j_y+j_z)=\frac{2U_0}{E_0T_0} \tag{2.51}$$

It is possible to shift the radiation damping between j_z and j_x but the sum of the damping remains constant. The condition in order to have damping in all directions is given by

$$-2<\frac{I_4}{I_2}<1 \tag{2.52}$$

If not fulfilled, either the horizontal betatron oscillations or the synchrotron oscillations will be antidamped. For a storage ring with separate function magnets I_4/I_2 is typically close to zero. For MAX III, where the dipole magnet contains a defocusing gradient, I_4/I_2 is around -0.768.

2.5 Electron beam dimensions

As seen in the previous section, the distribution of the momentum deviations of the beam electrons is Gaussian and the standard deviation of the distribution, the natural momentum spread, is given by

$$\sigma_\delta^2=C_q\gamma^2\frac{I_3}{j_zI_2} \tag{2.53}$$

where C_q is the quantum constant, γ is the relativistic gamma factor, I_3 is the third synchrotron radiation integral, j_z is the longitudinal damping partition number and I_2 is the second synchrotron radiation integral. For a single sinusoidal RF system and assuming small synchrotron oscillation amplitudes the longitudinal distribution will also be a Gaussian distribution if the momentum deviation distribution is a Gaussian distribution. The standard deviation of the distribution is called the bunch length and it is given by

$$\sigma_z = \frac{\alpha_c c}{2\pi f_s}\sigma_\delta \tag{2.54}$$

where α_c is the momentum compaction factor, c is the speed of light and f_s is the synchrotron frequency. If the bunch length is determined using the natural momentum spread it is called the natural bunch length. Eq. (2.54) is only valid for a single sinusoidal RF system. For a general shape of the RF voltage the longitudinal electron distribution will no longer be Gaussian. Instead, the distribution should be calculated using Eq. (5.13) in Sec. 5.4.

If the distribution of the horizontal actions and the distribution of the momentum deviations are both Gaussian distributions, the electron distributions for the horizontal displacements and the horizontal angular deviations will also be Gaussian. The standard deviation of the horizontal displacements of the electrons is called the horizontal beam size and it is given by

$$\sigma_x(s) = \sqrt{\epsilon_x \beta_x(s) + \left[\sigma_\delta \eta_x(s)\right]^2} \tag{2.55}$$

where ϵ_x is the horizontal emittance, $\beta_x(s)$ is the horizontal beta function, σ_δ is the momentum spread and $\eta_x(s)$ is the horizontal dispersion function. The standard deviation of the horizontal angular deviations of the electrons is called the horizontal beam divergence and it is given by

$$\sigma_{x'}(s) = \sqrt{\epsilon_x \gamma_x(s) + \left[\sigma_\delta \eta'_x(s)\right]^2} \tag{2.56}$$

where $\gamma_x(s)$ is the horizontal gamma Twiss parameter and $\eta'_x(s)$ is the derivative of the horizontal dispersion function. Whereas the momentum spread and the bunch length is constant around the ring, the horizontal beam size and the horizontal beam divergence depend on the position s in the ring.

In a similar way, the vertical electron beam size is given by

$$\sigma_y(s) = \sqrt{\epsilon_y \beta_y(s)} \tag{2.57}$$

where ϵ_y is the vertical emittance and $\beta_y(s)$ is the vertical beta function. The vertical beam divergence is given by

$$\sigma_{y'}(s) = \sqrt{\epsilon_y \gamma_y(s)} \tag{2.58}$$

where $\gamma_y(s)$ is the vertical gamma Twiss parameter. In Eqs. (2.57)–(2.58) it is assumed that the vertical dispersion function is zero. If the vertical dispersion function is non-zero, the vertical beam size and the vertical beam divergence is given by Eqs. (2.55)–(2.56) with x replaced by y.

CHAPTER 3

MEASURING THE BEAM SIZE

Several different methods are used at synchrotron light sources to determine the transverse electron beam sizes [24, 25]. The most common methods are pinhole cameras using synchrotron radiation (SR) in the X-ray range and interferometers using SR in the visible range. Other methods are imaging with visible to ultraviolet (vis-UV) SR and X-ray imaging using focusing optics, such as a Fresnel zone plate or compound refractive lenses.

The method used at MAX-lab to determine the transverse electron beam profile is imaging with vis-UV SR. This method was used already in the early 1970's to monitor the beam profile in SPEAR [26]. An updated version of the method, including near-field calculations of the emission, propagation and focusing of the SR wavefront, has been used to determine the beam sizes at MAX II [11, 27], SLS [28] and MAX III (see Paper **II** and Paper **III**).

The MAX III diagnostic beam line and the vis-UV imaging method is described in detail in Paper **II**. One aspect which was only briefly outlined in the paper was the geometrical optics calculations for the beam line. After a short introduction to the diagnostic beam line in Sec. 3.1, this chapter will expand on the geometrical optics. In Sec. 3.2 relevant formulas for plane-parallel plates and for lenses are given using the paraxial approximation. Section 3.3 introduces the concept of Seidel aberrations, estimates the aberrations in the MAX III diagnostic beam line and compares them to the fabrication errors of the optical components.

3.1 MAX III diagnostic beam line

The MAX III diagnostic beam line utilizes SR in the vis-UV region to image the transverse electron beam profile in MAX III. The source point of the

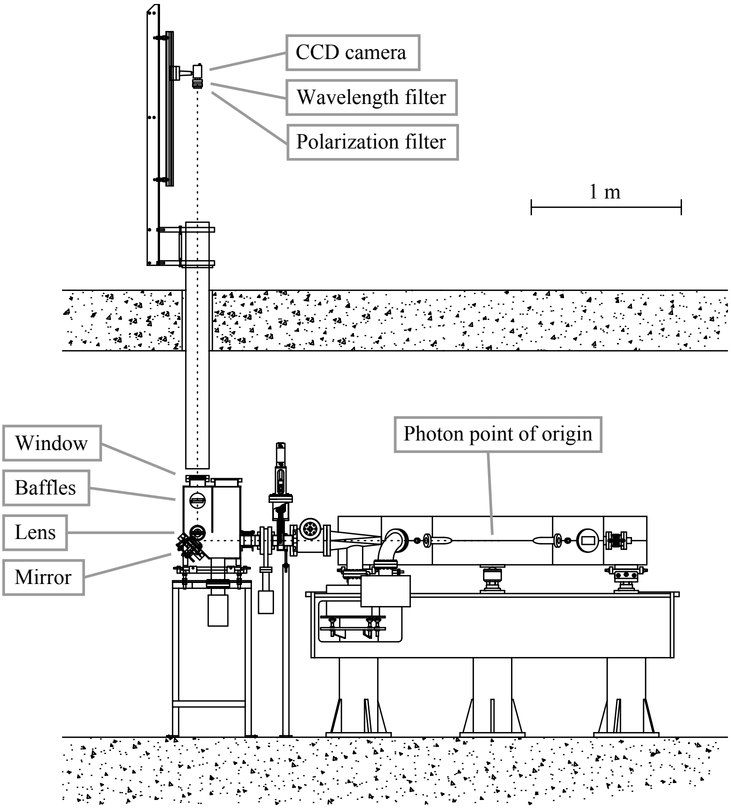

Figure 3.1: *Drawing of the MAX III diagnostic beam line and cell 6.*

beam line is the center of the bending magnet in cell 6 of MAX III. Figure 3.1 shows a side view drawing of the diagnostic beam line and cell 6. The vis-UV part of the SR is reflected 90 degrees upwards by a water-cooled silicon carbide mirror. The mirror determines the ±8.1 mrad vertical opening angle of the measurement system, which is sufficient to accept more than 99.8% of the vis-UV vertical light. A fused silica symmetric spherical lens focuses the SR, whereas movable aperture restrictions (baffles) determine the horizontal opening angle. The maximum horizontal opening angle used during measurements is ±13.6 mrad. The SR propagates out of the vacuum system through a fused silica vacuum window. Close to the image plane, narrow band-pass filters and a Glan-Taylor polarizer select the wavelength and polarization of the measurement. Measurements are typically performed at 364 nm, 488 nm or 633 nm wavelength using horizontally or vertically polarized SR. At the image plane a CCD camera (pixel size 3.75 µm) records the intensity distribution of the SR.

Ideally, the SR intensity distribution recorded by the beam line camera would correspond to the electron beam profile at the source point scaled by the magnification factor of the system. However, features such as the narrow vertical

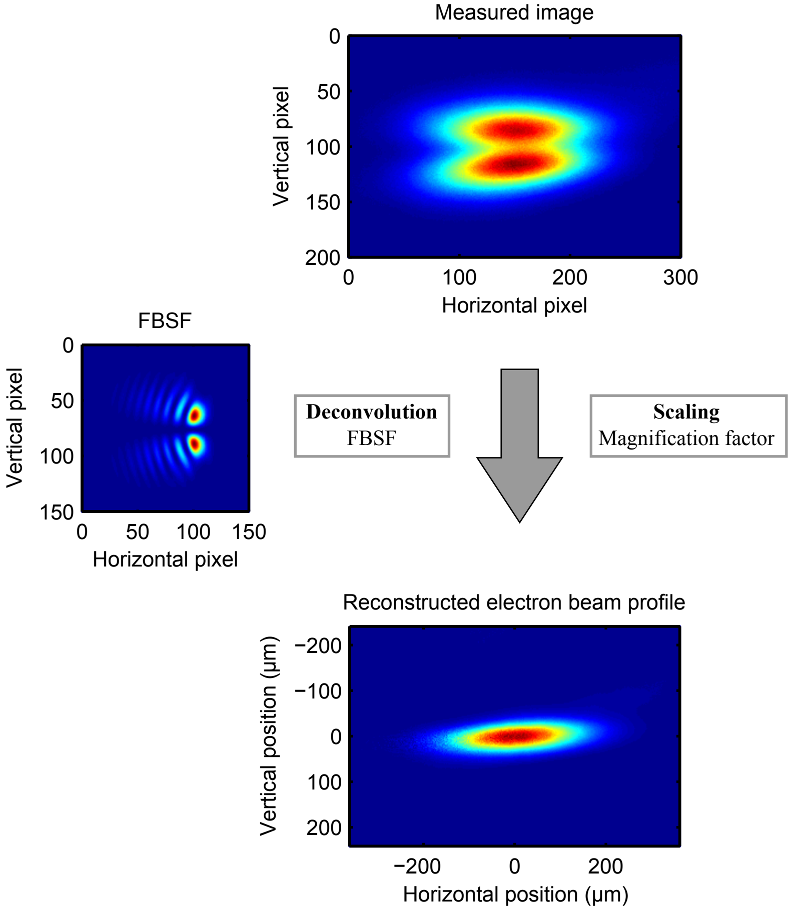

Figure 3.2: *Overview of the vis-UV imaging method. The CCD image measured by the MAX III diagnostic beam line is deconvoluted with the modeled filament-beam-spread function (single electron image) and scaled with the magnification factor of the measurement system in order to obtain the reconstructed electron beam profile.*

opening angle of SR and the longitudinally distributed SR generation cause the image to deviate from the scaled electron beam intensity distribution. In order to reconstruct this ideal image, the measured intensity profile is deconvoluted with the image a single electron passing through the bending magnet would give rise to at the camera. By scaling the deconvoluted image with the magnification factor the electron beam profile at the source point is reconstructed. Figure 3.2 shows an example of this process. The image a single electron passing through the bending magnet would give rise to at the camera is called the filament-beam-spread function (FBSF). It is calculated numerically using the software SRW [29]. The emission and subsequent propagation and focusing of the SR through the beam line is treated within the framework of classical electrodynamics, including in a natural way effects such as diffraction, the longitudinally distributed source point and the curvature of the electron orbit. Since no assumptions about the distribution of the electrons in the beam are made in the calculations, the full two-dimensional transverse electron beam profile is determined by the method.

The example image, FBSF and beam profile in Fig. 3.2 are taken from Fig. 7 and Fig. 8 in Paper **II**. The measurement was performed using vertically polarized light at 488 nm wavelength with a baffle aperture of 50 mm, corresponding to a horizontal opening angle of ±13.5 mrad.

3.2 Paraxial optics

The optical components in the MAX III diagnostic beam line consists of a mirror, a lens, a window, a polarizer and a wavelength filter. This section describes the geometrical optics properties of the components using the paraxial approximation. The window, the polarizer and the wavelength filter is discussed in Sec. 3.2.1 and the lens is discussed in Sec. 3.2.2. The mirror is not discussed further, since its only geometrical optics function is to reflect the synchrotron radiation.

3.2.1 Plane-parallel plate

A plane-parallel plate, such as a window or a filter, shifts the position of the image point for a converging beam. The image displacement is given by

$$d_p = t_p \left(1 - \frac{1}{n_p}\right) \tag{3.1}$$

where t_p is the thickness of the plate and n_p is the refractive index of the plate material.

The window in the diagnostic beam line is 20 mm thick and it is manufactured from UV-grade fused silica. The wavelength-dependent refractive index is around 1.46 in the wavelength region of the diagnostic beam line, which gives an image displacement of around 6.3 mm. The Glan-Taylor polarizer is manufactured from calcite, it is about 15 mm thick and has a wavelength-dependent extraordinary index of refraction at around 1.49 in the wavelength region of the diagnostic beam line, which gives an image displacement of around 4.9 mm. The wavelength laser-line filter is around 5 mm thick and consists of several different filters. Since the thickness and material of the individual filters are not specified by the manufacturer the image displacement from the wavelength filter is not included in the calculations. Combined, the image displacements

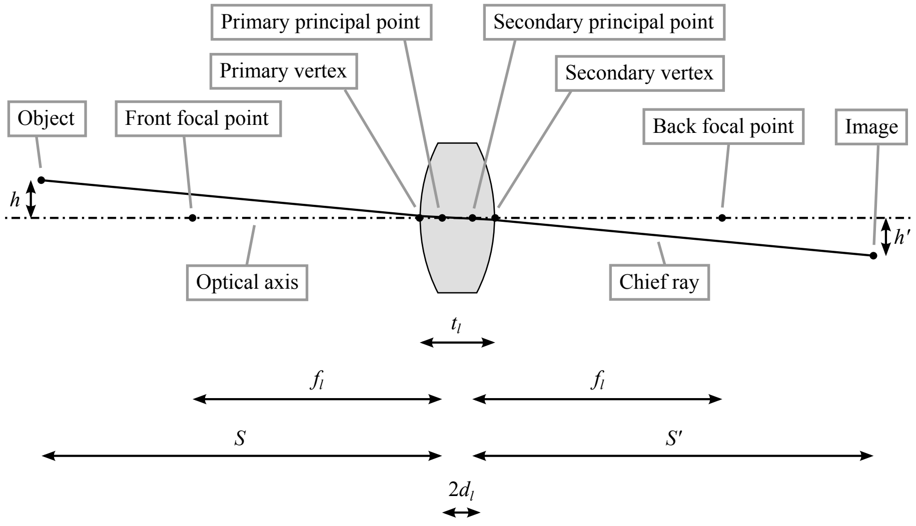

Figure 3.3: *Schematic drawing of a lens showing a selection of optical points and distances, including the object height h, the image height h', central lens thickness t_l, the effective focal length f_l, the object distance S, the image distance S' and the principal-point separation $2d_l$.*

from the window and the polarizer increase the distance between the lens and the image plane by almost 4%.

3.2.2 Lens

Figure 3.3 shows a selection of optical points and distances for a lens. The effective focal length of the lens, f_l, is related to the object distance S and the image distance S' via

$$\frac{1}{f_l} = \frac{1}{S} + \frac{1}{S'} \tag{3.2}$$

and the magnification factor of the imaging system is given by

$$m = \frac{h'}{h} = \frac{S'}{S} \tag{3.3}$$

where h' is the image height and h is the object height.

For the special case of a symmetrical spherical lens the effective focal length is given by

$$\frac{1}{f_l} = \frac{2(n_l - 1)}{R_l} - t_l \frac{(n_l - 1)^2}{n_l R_l^2} \tag{3.4}$$

where t_l is the central thickness of the lens, R_l is the radius of curvature of the lens surface and n_l is the refractive index of the lens material. From Eq. (3.4) the radius of curvature can be expressed as

$$R_l = (n_l - 1) f_l \left(1 + \sqrt{1 - \frac{t_l}{n_l f_l}} \right) \tag{3.5}$$

For a symmetrical spherical lens the distance between the center of the lens and the primary principal point is the same as the distance between the center of the lens and the secondary principal point. The distance is given by

$$d_l = \frac{t_l}{2} \cdot \frac{(n_l - 1)(2R_l - t_l)}{2n_l R_l - t_l(n_l - 1)} \approx \frac{t_l}{2} \left(1 - \frac{1}{n_l} \right) \tag{3.6}$$

Before installing the lens into the diagnostic beam line, the effective focal length of the lens was measured using Eq. (3.2) at 488 nm and 633 nm wavelength. The image distance and the object distance was measured taking the principal-point separation into account. The effective focal length was determined to be 1.204 m at 488 nm wavelength and 1.220 m at 633 nm wavelength. Based on the measured focal lengths, the radius of curvature of the spherical symmetric lens was determined, using Eq. (3.5), to be 1.112 m for both wavelengths. Including error estimations the radius of curvature was determined to be 1.112 ± 0.001 m (estimated maximum error).

After assembly and installation of the diagnostic beam line, the photon point of origin was determined using Eq. (3.2) for 364 nm, 488 nm and 633 nm wavelength. The image distance was determined for the three wavelengths taking the principal-point separation in the lens and the image displacement from the window and the polarizer into account. The diagnostic beam line image plane was assumed to be located halfway between the vertical image plane and the horizontal image plane (see discussion on astigmatism in Sec. 4.1 in Paper **II**). The photon point of origin was determined to be located 1.979 m from the center of the lens for the measurement at 364 nm wavelength and 1.980 m for the measurements at 488 nm and 633 nm wavelength. Including error estimations the photon point of origin was determined to be located 1.980 ± 0.007 m (maximum error) from the center of the lens .

From the determined photon point of origin and the measured image distance the magnification factor of the imaging system was determined using Eq. (3.3) for 364 nm, 488 nm and 633 nm wavelength. The magnification factor of the diagnostic beam line is 1.462 ± 0.011 at 364 nm, 1.556 ± 0.011 at 488 nm and 1.609±0.011 at 633 nm (maximum errors). As described in Sec. 3.1, the magnification factor of the imaging system is needed in order to determine the electron beam profile.

3.3 Seidel aberrations

In the paraxial approximation of geometrical optics, plane-parallel plates shift the position of the image plane and a lens focuses a point-like object to a point-like image. In a full geometrical treatment optical aberrations appear. To properly determine the aberrations ray-tracing can be performed, using Snell's law at each optical interface to determine the subsequent ray direction. This has not been done for the diagnostic beam line. Instead, an approximate approach has been used to estimate the aberrations and compare them to the fabrication errors of the optical components. In this section the approximate approach is described along with some of the results from the estimations.

In the paraxial approximation, the sine in Snell's law is approximated by

$$\sin x = x \tag{3.7}$$

If the sine is instead approximated by

$$\sin x = x - \frac{x^3}{3!} \tag{3.8}$$

five basic types of monochromatic third-order optical aberrations will appear. These are also called the primary aberrations or Seidel aberrations. The five Seidel aberrations are spherical aberration, coma, astigmatism, field curvature and distortion. All five aberrations depend on the size of the exit pupil and four of them depend on the image height.

The Seidel aberrations are described mathematically by the primary aberration function. It describes the wave aberration, i.e. the difference in optical path length between the wavefront under consideration and a reference sphere with its vertex at the center of the exit pupil and its center of curvature at the image point. The primary aberration function of a rotationally symmetric system is given by [30]

$$W(r,\theta;h') = a_s r^4 + a_c h' r^3 \cos\theta + a_a h'^2 r^2 \cos^2\theta + a_f h'^2 r^2 + a_d h'^3 r \cos\theta \tag{3.9}$$

where a_s, a_c, a_a, a_f and a_d are the aberration coefficients, h' is the image height and (r, θ) are the polar coordinates of a point in the plane of the exit pupil. The coefficients a_s, a_c, a_a, a_f and a_d represent the aberration coefficients of spherical aberration, coma, astigmatism, field curvature, and distortion, respectively. For an optical system with a circular pupil of radius r_0 a normalized radial variable

$$\rho_r = \frac{r}{r_0} \tag{3.10}$$

can be used to rewrite the primary aberration function in the form [30]

$$W(\rho_r, \theta) = A_s \rho_r^4 + A_c \rho_r^3 \cos\theta + A_a \rho_r^2 \cos^2\theta + A_f \rho_r^2 + A_d \rho_r \cos\theta \tag{3.11}$$

where A_s, A_c, A_a, A_f and A_d are the peak aberration coefficients of spherical aberration, coma, astigmatism, field curvature, and distortion, respectively. The peak aberration coefficients are given by

$$A_s = a_s r_0^4 \tag{3.12}$$

$$A_c = a_c h' r_0^3 \tag{3.13}$$

$$A_a = a_a h'^2 r_0^2 \tag{3.14}$$

$$A_f = a_f h'^2 r_0^2 \tag{3.15}$$

$$A_d = a_d h'^3 r_0 \tag{3.16}$$

3.3.1 Plane-parallel plate

The aberration coefficients (see Eq. (3.9)) for a plane-parallel plate, with a rotationally symmetric aperture stop at the front surface of the plate, are given by [30]

$$a_s = \frac{(n_p^2 - 1)t_p}{8 n_p^3 S_p^4} \tag{3.17}$$

$$a_c = -\frac{4(n_p^2 - 1)t_p}{8 n_p^3 S_p^4} \tag{3.18}$$

$$a_a = \frac{4(n_p^2 - 1)t_p}{8 n_p^3 S_p^4} \tag{3.19}$$

$$a_f = \frac{2(n_p^2 - 1)t_p}{8n_p^3 S_p^4} \tag{3.20}$$

$$a_d = -\frac{4(n_p^2 - 1)t_p}{8n_p^3 S_p^4} \tag{3.21}$$

where n_p is the refractive index of the plate material, t_p is the thickness of the plate and S_p is the distance along the optical axis between the front surface of the plane-parallel plate and the position of the image plane in the absence of the plate.

The image height can be described by the angle α_p between the chief ray and the optical axis of the plane-parallel plate, given by

$$\alpha_p = \arctan \frac{h'}{S_p} \approx \frac{h'}{S_p} \tag{3.22}$$

The peak aberration coefficients (see Eqs. (3.11)–(3.16)) for a plane-parallel plate, with a rotationally symmetric aperture stop with radius r_0 located at the front surface of the plate, can then be expressed as

$$A_s = \frac{(n_p^2 - 1)t_p r_0^4}{8n_p^3 S_p^4} \tag{3.23}$$

$$A_c = -\frac{4\alpha_p(n_p^2 - 1)t_p r_0^3}{8n_p^3 S_p^3} \tag{3.24}$$

$$A_a = \frac{4\alpha_p^2(n_p^2 - 1)t_p r_0^2}{8n_p^3 S_p^2} \tag{3.25}$$

$$A_f = \frac{2\alpha_p^2(n_p^2 - 1)t_p r_0^2}{8n_p^3 S_p^2} \tag{3.26}$$

$$A_d = -\frac{4\alpha_p^3(n_p^2 - 1)t_p r_0}{8n_p^3 S_p} \tag{3.27}$$

The vertical opening angle of the diagnostic beam line is determined by the mirror and the horizontal opening angle is determined by the baffles. Eqs. (3.23)–(3.27) assume that the aperture stop is rotationally symmetric and located at the front surface of the plate. To get an estimate on the Seidel aberrations for the window, the diagnostic beam line apertures can be projected on the window and the maximum radius of the projection can be defined as r_0. The angle α_p has not been measured, but it is probably smaller than 0.01 rad. Most of the measurements on the diagnostic beam line have been performed at 488 nm wavelength. As an example, the peak aberration coefficients have been calculated for the settings at 488 nm wavelength and 50 mm baffle aperture.

For spherical aberration the peak aberration is $A_s = 8 \times 10^{-12}$ m, for coma $A_c = -3 \times 10^{-11}$ m, for astigmatism $A_a = 3 \times 10^{-11}$ m, for field curvature $A_f = 2 \times 10^{-11}$ m and for distortion $A_d = -4 \times 10^{-11}$ m.

The fabrication error of the diagnostic beam line window was measured by the manufacturer. The measurement showed that the peak-to-valley error for the window at 633 nm was $\lambda/13.9$ when passing through both surfaces of the window, which corresponds to a total peak-to-valley error of 4.5×10^{-8} m. All the Seidel aberrations are at least three orders of magnitude smaller than the peak-to-valley fabrication error of the window. The Seidel aberrations can thus be neglected for the window. The situation is similar for the other plane-parallel plates.

3.3.2 Lens

The aberration coefficients (see Eq. (3.9)) for a thin lens, with a rotationally symmetric aperture stop at the lens, are given by [30]

$$a_s = -\frac{1}{32 n_l (n_l - 1) f_l^3} \left[\frac{n_l^3}{n_l - 1} + (3n_l + 2)(n_l - 1) p_l^2 + \frac{n_l + 2}{n_l - 1} q_l^2 + 4(n_l + 1) p_l q_l \right] \tag{3.28}$$

$$a_c = -\frac{1}{4 n_l f_l^2 S'} \left[(2n_l + 1) p_l + \frac{n_l + 1}{n_l - 1} q_l \right] \tag{3.29}$$

$$a_a = -\frac{1}{2 f_l S'^2} \tag{3.30}$$

$$a_f = -\frac{n_l + 1}{4 n_l f_l S'^2} \tag{3.31}$$

$$a_d = 0 \tag{3.32}$$

where n_l is the refractive index of the lens material, f_l is the effective focal length of the lens and S' is the image distance. The lens position factor p_l is given by

$$p_l = 1 - \frac{2 f_l}{S'} \tag{3.33}$$

and the lens shape factor q_l is given by

$$q_l = \frac{R_{l_2} + R_{l_1}}{R_{l_2} - R_{l_1}} \tag{3.34}$$

where R_{l_1} and R_{l_2} are the radii of curvature of the lens. For the special case of a symmetrical spherical lens the lens shape factor is zero.

The image height can be described by the angle α_l between the chief ray and the optical axis of the lens, given by

$$\alpha_l = \arctan \frac{h'}{S'} \approx \frac{h'}{S'} \tag{3.35}$$

The electron beam profile at the photon point of origin for the MAX III diagnostic beam line typically has a size in the order of a hundred µm. Since the magnification factor is around 1.5, the image size is also in the order of one or a few hundred µm. If the optical axis of the lens is properly aligned with the direction of propagation of the synchrotron radiation, the image height h' is determined by the image size. If the synchrotron radiation and the optical axis are not aligned, the image of the electron beam profile in the image plane will be displaced from the optical axis, and the image height h' and angle α_l will be affected by the misaligned image. To investigate the orientation of the optical axis a He-Ne laser was aligned with the direction of propagation of the synchrotron radiation. The laser light reflected on the surfaces of the lens gave rise to an interference pattern from which it was possible to determine the orientation of the optical axis. Measurements of the distance between the center of the interference pattern and the center of the beam profile image showed that $\alpha_l = 0.0024$ rad. Since the measured distance was much larger than the image size the contribution of the image size to the angle α_l can be neglected and α_l can be treated as a constant.

The peak aberration coefficients (see Eqs. (3.11)–(3.16)) for a symmetrical spherical lens, with a rotationally symmetric aperture stop with radius r_0 located at the lens, can be expressed as

$$A_s = -\frac{\left[n_l^3 + (3n_l + 2)(n_l - 1)^2 p_l^2\right] r_0^4}{32 n_l (n_l - 1)^2 f_l^3} \tag{3.36}$$

$$A_c = -\frac{\alpha_l (2n_l + 1) p_l r_0^3}{4 n_l f_l^2} \tag{3.37}$$

$$A_a = -\frac{\alpha_l^2 r_0^2}{2 f_l} \tag{3.38}$$

$$A_f = -\frac{\alpha_l^2 (n_l + 1) r_0^2}{4 n_l f_l} \tag{3.39}$$

$$A_d = 0 \tag{3.40}$$

In a similar way as in Sec. 3.3.1, r_0 can be estimated by projecting the diagnostic beam line apertures on the lens and defining r_0 as the maximum radius

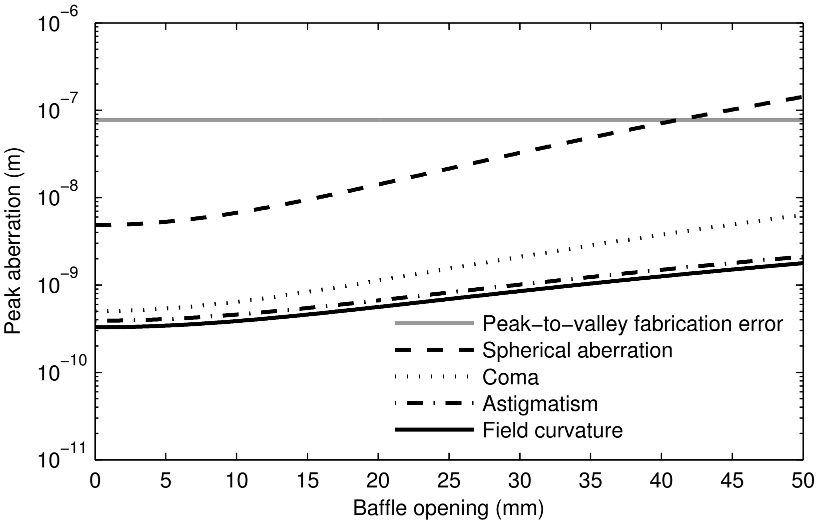

Figure 3.4: *Estimate of the absolute value of the peak aberration coefficients for the diagnostic beam line lens at 488 nm wavelength as a function of the baffle aperture. For comparison, the peak-to-valley fabrication error of the lens is shown as a gray line.*

of the projection. The value of r_0 depends on the baffle aperture. Figure 3.4 shows the absolute value of the peak aberration coefficients at 488 nm wavelength for the diagnostic beam line lens as a function of the baffle aperture. The figure also shows the fabrication error of the lens. The peak-to-valley fabrication error of the diagnostic beam line lens was measured by the manufacturer to be $\lambda/17.7$ for one of the sides and $\lambda/15.2$ for the other side at 633 nm. If the values are added linearly this corresponds to a total peak-to-valley error of 7.7×10^{-8} m. The peak aberration coefficients of coma, astigmatism and field curvature depend on the angle α_l. To minimize the optical aberrations it is thus essential to position the optical components carefully so that the optical axis is properly aligned with the direction of propagation of the synchrotron radiation. For the MAX III diagnostic beam line $\alpha_l = 0.0024$ rad and, as seen in Fig. 3.4, coma, astigmatism and field curvature are at least one order of magnitude smaller than the peak-to-valley fabrication error. Only spherical aberration has a peak aberration coefficient on the same scale as the peak-to-valley fabrication error. The spherical aberration was therefore added to the SRW computer model of the diagnostic beam line.

Chapter 4

Measuring the emittance

Chapter 3 and Paper **II** describes how the electron beam size in MAX III was determined using the diagnostic beam line. In Paper **III** the emittance in MAX III was determined based on measurements of the electron beam size. The main measurements and results of the experiment are given in Paper **III**. This chapter provides additional figures and background to the measurements in the paper. Section 4.1 presents the MATLAB LOCO fits, Sec. 4.2 describes the dispersion measurement using the diagnostic beam line and Sec. 4.3 discusses the relationship between the emittance and the beam size.

4.1 Linear optics from closed orbits

The MAX III storage ring has 16 corrector magnets that can apply kicks to the electron beam and 16 beam position monitors (BPMs) that measure the position of the electron beam. When engaged, the corrector magnets will affect the closed orbit of the electron beam. The measured change in the beam position at a BPM due to a kick from a corrector magnet depends, among other parameters, on the values of the beta function at the corrector and at the BPM as well as the phase advance between them. In a response matrix measurement the closed orbit distortion at the 16 BPMs is measured for a kick from each of the 16 correctors.

For the characterization of MAX III [14], a computer model of the storage ring was developed using MATLAB Accelerator Toolbox [31]. From the model of the storage ring the theoretical response matrix can be calculated. Using MATLAB LOCO [32], the difference between the theoretical response matrix and the measured response matrix is minimized by adjusting various model parameters. In this way the linear optics of the storage ring can be determined, such as the strengths of individual quadrupole magnets. In order to accurately

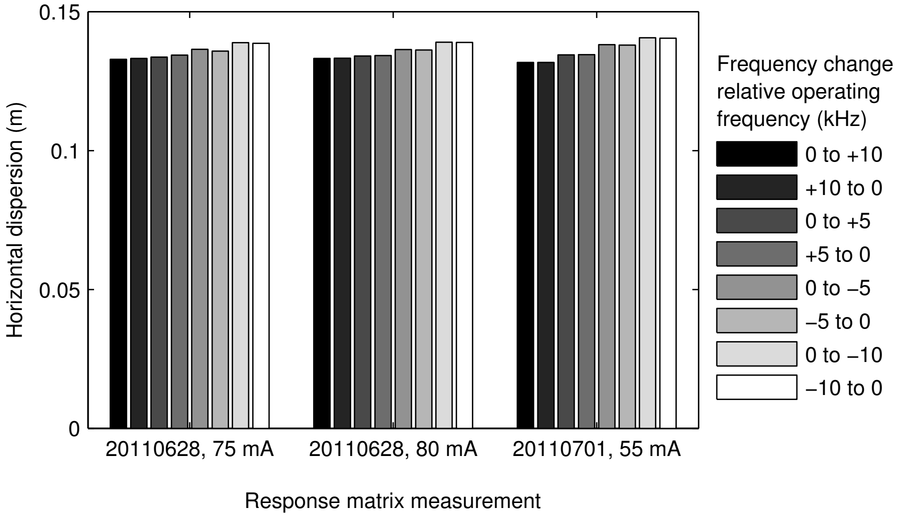

Figure 4.1: *Fitted horizontal dispersion in the center of the dipole magnet in cell 6 for 24 different* LOCO *fits. Three different response matrix measurements were each combined with eight different orbit change measurements.*

determine the dispersion function a measurement of the change in closed orbit from a change in RF frequency is also included in the fit. The model of the MAX III storage ring and the parameters fitted by LOCO are described in detail in Ref. [14] and Ref. [33].

For the determination of the emittance in Paper **III**, three different response matrix measurements were performed. For each response matrix measurement eight different changes in the closed orbit due to a change in the RF frequency were measured. Combined, this gave 24 different data sets for the LOCO fits. Figure 4.1 shows an example of the 24 different fit results for a certain parameter, in this case the horizontal dispersion in the center of the dipole magnet in cell 6. This particular value was also determined experimentally using the diagnostic beam line (see Sec. 4.2 and Paper **III**), which makes it possible to verify the results from the fitted models. Similar comparisons can also be made for other parameters, such as the horizontal and vertical betatron tune.

An updated model of MAX III was formed based of the average of the 24 different fitted models. Figure 4.2 shows the horizontal and vertical beta function and Fig. 4.3 shows the horizontal and vertical dispersion function around the ring for the fitted model of MAX III. For the design lattice, the machine functions are identical for the eight cells and the vertical dispersion is zero. Small errors in the strengths and alignments of the magnets give rise to the variations shown in Figs. 4.2–4.3. In the LOCO fit the vertical dispersion is the result of small tilts of the dipole magnets, but further investigations are needed in order to determine the origin of the vertical dispersion.

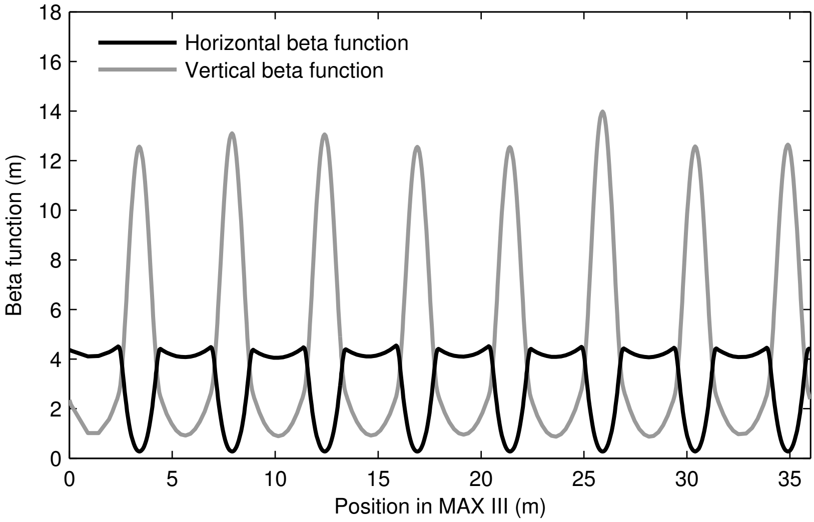

Figure 4.2: *Horizontal and vertical beta functions around the ring for the fitted model of MAX III. The fitted model is the average of the 24 individual* LOCO *fits.*

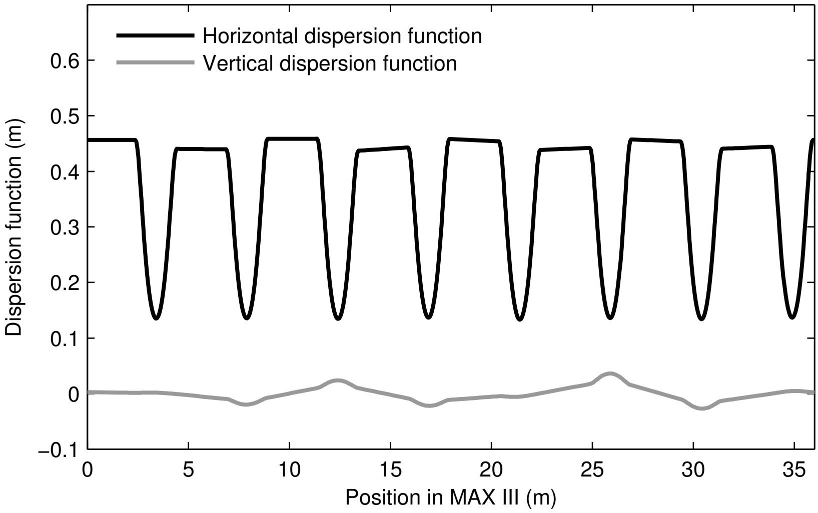

Figure 4.3: *Horizontal and vertical dispersion functions around the ring for the fitted model of MAX III. The fitted model is the average of the 24 individual* LOCO *fits.*

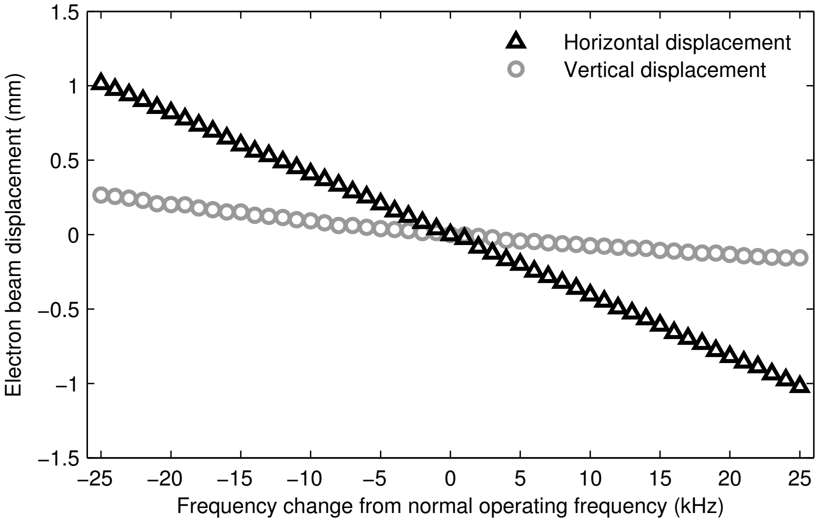

Figure 4.4: *Electron beam displacement in the center of the dipole magnet in cell 6 as a function of RF frequency change relative the normal operating frequency. The slopes of the curves were used in Paper **III** to determine the horizontal and vertical dispersion in the center of the dipole magnet in cell 6.*

4.2 Measuring the dispersion

The MAX III diagnostic beam line measures the transverse electron beam profile in the center of the dipole magnet in cell 6. A change in the RF frequency of the RF system will affect the energy of the beam electrons. Through dispersion the change in energy translates into a displacement of the electron beam. By measuring the beam displacement due to a change in RF frequency the horizontal dispersion can be determined via

$$\eta_x = -\alpha_c \frac{\Delta x}{\Delta f_{RF}} f_{RF} \tag{4.1}$$

where α_c is the momentum compaction factor, Δx is the horizontal beam displacement, Δf_{RF} is the change in RF frequency and f_{RF} is the RF frequency. The vertical dispersion is given by Eq. (4.1) with x replaced by y. Figure 4.4 shows the horizontal and vertical beam displacement in the center of the dipole magnet in cell 6 as a function of the change in RF frequency. The horizontal direction is defined as the bending plane of the dipole magnet. The horizontal displacement in Fig. 4.4 varies linearly with the change in RF frequency, whereas the vertical beam displacement also has a quadratic component. A possible explanation for the non-linear behavior of the vertical dispersion could be that the off-momentum beam samples additional skew components. For the determination of the dispersion in Paper **III** the slope at the normal operating frequency was used.

4.3 Emittance and beam size

The horizontal electron beam size is, as described in Sec. 2.5, given by

$$\sigma_x(s) = \sqrt{\epsilon_x \beta_x(s) + \left[\sigma_\delta \eta_x(s)\right]^2} \tag{4.2}$$

where ϵ_x is the horizontal emittance, $\beta_x(s)$ is the horizontal beta function, σ_δ is the momentum spread and $\eta_x(s)$ is the horizontal dispersion function. In a similar way, the vertical electron beam size is given by

$$\sigma_y(s) = \sqrt{\epsilon_y \beta_y(s) + \left[\sigma_\delta \eta_y(s)\right]^2} \tag{4.3}$$

where ϵ_y is the vertical emittance, $\beta_y(s)$ is the vertical beta function and $\eta_y(s)$ is the vertical dispersion function. The vertical dispersion is generally small and the vertical beam size mainly determined by the vertical emittance and the vertical beta function.

The horizontal and vertical beam sizes vary around the ring because of the position-dependent beta functions and dispersion functions. The momentum spread and the emittances are however approximately constant around the ring. The diagnostic beam line is used to determine the horizontal and vertical electron beam size in the center of the dipole magnet in cell 6 ($s = 25.9$ m). The value of the beta functions and dispersion functions at this position in the ring are given by the LOCO fits and the dispersion measurement. In order to determine the horizontal and vertical emittance using Eqs. (4.2)–(4.3) only the momentum spread in the storage ring remains to be determined. In Paper **III** the emittances in MAX III were determined by assuming that the momentum spread was equal to the natural momentum spread, since the beam size measurements were performed at low currents where the beam sizes are stable and unaffected by the longitudinal instabilities (see Paper **IV**). The natural momentum spread can be determined from the fitted model of the storage ring using Eq. (2.53).

With the horizontal and vertical emittances determined, Eqs. (4.2)–(4.3) can be used to determine the horizontal and vertical beam sizes around the ring. Figure 4.5 shows the horizontal and vertical electron beam sizes in MAX III as a function of the position in the ring. The momentum spread is assumed to be the natural momentum spread, which is valid at low currents. At higher currents, where longitudinal instabilities affect the momentum spread, the beam

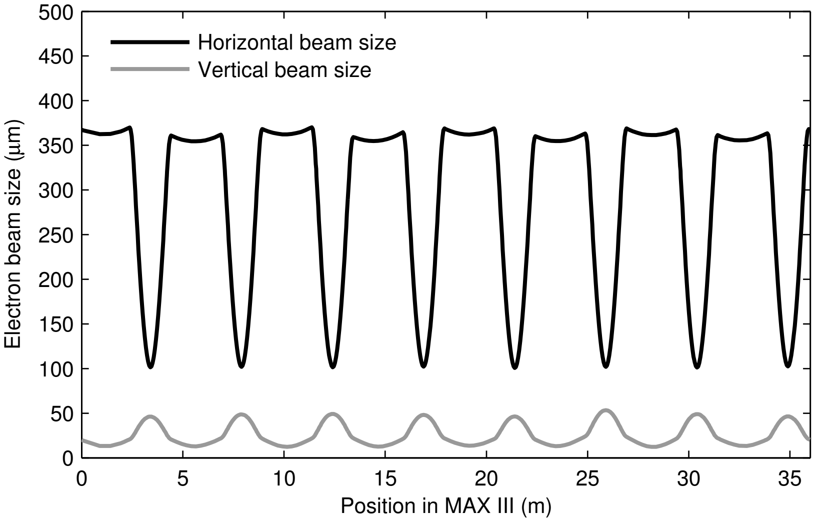

Figure 4.5: *The horizontal and vertical electron beam sizes in MAX III as a function of the position in the ring. The momentum spread is assumed to be the natural momentum spread.*

sizes will be somewhat larger than beam sizes presented in Fig. 4.5. In the center of the dipole magnets in MAX III the horizontal beta function and horizontal dispersion function have a minimum and the vertical beta function has a maximum. The horizontal beam size is only about twice as large as the vertical beam size at these locations. In the straight sections the horizontal beta function and the horizontal dispersion function are large and the vertical beta function is small, which gives a horizontal beam size around 20 times larger than the vertical beam size. Since the vertical dispersion is small, the vertical beam size around the ring is mainly determined by the vertical emittance and the vertical beta function. For the horizontal beam size the situation is different. The contribution of the horizontal dispersion and the momentum spread to the horizontal beam size around the ring is slightly larger than the contribution from the horizontal emittance and the horizontal beta function.

Chapter 5

The MAX III triple RF system

Electron storage rings are equipped with an RF system in order to replenish the energy lost by the electrons due to the emission of synchrotron radiation. The standard solution is a single RF system, with one or several RF cavities operating at the same RF frequency. Section 2.3 introduced the dynamics of a single RF system. At MAX II and MAX III the main RF system, operating at 100 MHz, is extended with an additional passive RF system, operating at a higher harmonic of the main RF system. In MAX II the higher harmonic cavity, or Landau cavity as it is also called, operates at 500 MHz. In MAX III two different types of Landau cavities are installed, one operating at 300 MHz and the other at 500 MHz, making the RF system in MAX III a triple RF system.

Higher harmonic RF systems are used to modify the shape of the RF potential. The number of buckets in the storage ring are generally not affected, but the shape of the buckets and the electron bunches inside them are. In MAX II and MAX III the Landau cavities are tuned to increase the length of the electron bunches in order to decrease the electron density. A lower electron density will increase the Touschek lifetime (see Sec. 7.5) and, since the Touschek lifetime is the limiting lifetime in MAX II and MAX III, the total lifetime. The modified potential will also increase the spread in the synchrotron frequencies, which can dampen longitudinal coupled-bunch instabilities through Landau damping (as seen in Paper **IV**). Landau cavities can also be used to shorten the bunches, which can be of interest for certain groups of users, but that mode of operation is not pursued at MAX-lab. The higher harmonic RF system can be actively powered by an external generator or passively powered by the beam itself. The cavities can also be normal conducting or superconducting.

At MAX II and MAX III the Landau cavities are passively powered and normal conducting. The effect of the MAX III Landau cavities on the beam stability and bunch length was investigated in Paper **IV**. In the paper, results from simulations of the MAX III triple RF system were presented and compared to measurements. This chapter will take a closer look at how the simulations were performed, a topic that was only briefly outlined in the paper. Section 5.1 gives a short introduction to the three different cavities in MAX III. In Sec. 5.2 the RF voltage as seen by the beam and the individual voltages in the Landau cavities are determined for the case of passive normal conducting Landau cavities. Section 5.3 describes how the RF potential and the height and shape of the RF buckets is determined and Sec. 5.4 describes the longitudinal electron distribution and the iterative process to find a self-consistent solution of the simulation. Finally, in Sec. 5.5 six examples of triple RF simulation results for different currents in MAX III are given and the obtained electron distributions are compared to measurement results.

5.1 The cavities

The RF system in MAX III consists of three RF cavities: one active cavity and two passive higher harmonic cavities. The main cavity operates at 100 MHz and is actively powered by a FM transmitter. A passive 500 MHz Landau cavity installed at the start-up of the ring never worked properly, possibly exciting a higher order mode when the cavity is tuned close to its operating point. It is thus detuned during normal operation. In October 2011 a new passive 300 MHz Landau cavity was installed. It is a prototype for the Landau cavities that will be used at MAX IV [34] and it is used during normal operation.

The 100 MHz main cavity is a capacitance loaded cavity located in the main cavity straight section of MAX III (see Fig. 1.2). An FM transmitter feeds power to the cavity through a coaxial line and a circulator is used to isolate the FM transmitter from the reflected power from the cavity. When there is beam in the storage ring, one part of the power sent to the cavity drives the electron beam and another part is lost in the cavity walls. The shunt impedance of the cavity, in this thesis defined as the square of the peak voltage in the cavity as seen by the beam divided by the cavity losses, is 3.4 MΩ [14]. More details are given in Appendix A.1 in Paper **IV**, where the calibration of the main cavity voltage is described.

The 300 MHz Landau cavity is a capacitance loaded cavity located in the diagnostic straight section of MAX III (see Fig. 1.2). The resonance frequency of the cavity is tuned by changing its temperature, by inserting a plunger or by changing the capacitance through mechanical deformation of the side walls. Under normal operating conditions it has a quality factor of 20400 and a shunt impedance of 5.4 MΩ. The calibration of the 300 MHz Landau cavity voltage is described in Appendix A.2 in Paper **IV**.

The 500 MHz Landau cavity is a pillbox type cavity located in the injection straight section of MAX III (see Fig. 1.2). The resonance frequency of the cavity is tuned by changing its temperature or by inserting a plunger. Under normal operating conditions it has a quality factor of 21700 and a shunt impedance of 3.1 MΩ. The calibration of the 500 MHz Landau cavity voltage is described in Appendix A.3 in Paper **IV**.

5.2 The RF voltage

The RF voltage seen by the beam with a triple RF system is given by

$$V_{RF}(\varphi) = V_0 \sin(\varphi + \varphi_s) + V_{L_1} \sin(n_1\varphi + \varphi_{L_1}) + V_{L_2} \sin(n_2\varphi + \varphi_{L_2}) \quad (5.1)$$

where φ is the phase of the fundamental RF and $\varphi = 0$ is the location of the synchronous particle. The first term on the right-hand side of Eq. (5.1) is the phase-dependent voltage in the main cavity, with V_0 the main cavity voltage and φ_s the synchronous phase angle. The second and third terms in Eq. (5.1) are the phase-dependent voltages in the Landau cavities of higher harmonic orders n_1 and n_2. V_{L_1} and V_{L_2} are the voltages in the Landau cavities and φ_{L_1} and φ_{L_2} are the harmonic phase angles.

For an even fill of the storage ring, the peak voltage seen by the beam in a passive Landau cavity of higher harmonic order n is given by

$$V_L = R_S I F_n \cos\Psi \quad (5.2)$$

where R_S is the transit-time corrected shunt impedance of the Landau cavity (defined as $R_S \equiv V_L^2/P_{cav}$, where P_{cav} is the cavity losses), I is the stored current, F_n is the amplitude of the Fourier component of the beam spectrum at higher harmonic n and Ψ is the tuning angle given by

$$\tan\Psi = Q\left(\frac{f_{res}}{nf_{RF}} - \frac{nf_{RF}}{f_{res}}\right) \approx \frac{2Q(f_{res} - nf_{RF})}{f_{res}} \quad (5.3)$$

where Q is the quality factor of the Landau cavity, f_{res} is the resonance frequency of the Landau cavity and f_{RF} is the RF frequency of the main cavity.

The harmonic phase angle for a passive Landau cavity of higher harmonic order n is given by

$$\varphi_L = \Psi - \frac{\pi}{2} - \theta_n \quad (5.4)$$

where θ_n is the phase of the Fourier component at higher harmonic n.

The voltage in a passive Landau cavity is induced by the beam. The electrons in the beam will thus on average suffer an energy loss when passing the cavity. For the synchronous particle the energy loss per turn in a Landau cavity is given by

$$U_L = eV_L \cos(\Psi - \theta_n) \tag{5.5}$$

The total energy loss per turn for the synchronous particle in a triple RF system is given by

$$U_{tot} = U_0 + U_{L_1} + U_{L_2} \tag{5.6}$$

where U_0 is the energy loss per turn due to emission of synchrotron radiation and U_{L_1} and U_{L_2} are the energy losses per turn in the Landau cavities. Other losses, such as parasitic energy losses, are neglected.

As described in Sec. 5.1 the main cavity is actively powered by an RF transmitter. The output power from the transmitter and the properties of the main cavity will determine the peak voltage V_0 in the main cavity (see Appendix A.1 in Paper **IV**).

The synchronous phase angle for a single RF system is given by Eq. (2.29). For the triple RF system the energy loss in the Landau cavities should also be included. The synchronous phase angle is thus given by

$$\sin\varphi_s = \frac{U_{tot}}{eV_0} \qquad \left(\frac{\pi}{2} < \varphi_s < \pi\right) \tag{5.7}$$

Figure 5.1 shows an example of the individual voltages in the three cavities as a function of the phase of the fundamental RF, where phase zero corresponds to the location of the synchronous particle. In the example the current is 300 mA, the main cavity voltage is 130 kV and the RF frequency is 99.925 MHz. The momentum spread is 0.00085, about 40% larger than the natural momentum spread in MAX III. The resonance frequencies in both Landau cavities are tuned so that they are larger than the frequency of the respective RF harmonic, in order to decrease the slope of the RF voltage at the location of the bunch center and lengthen the bunches. By adjusting the resonance frequency of a Landau cavity the induced field in the cavity can be increased or decreased. In the example the resonance frequency in the 300 MHz Landau cavity is 300.193 MHz, 418 kHz above the third RF harmonic. This is the frequency around which the 300 MHz Landau cavity is usually tuned to during MAX III injections. During normal operation the 300 MHz Landau cavity resonance

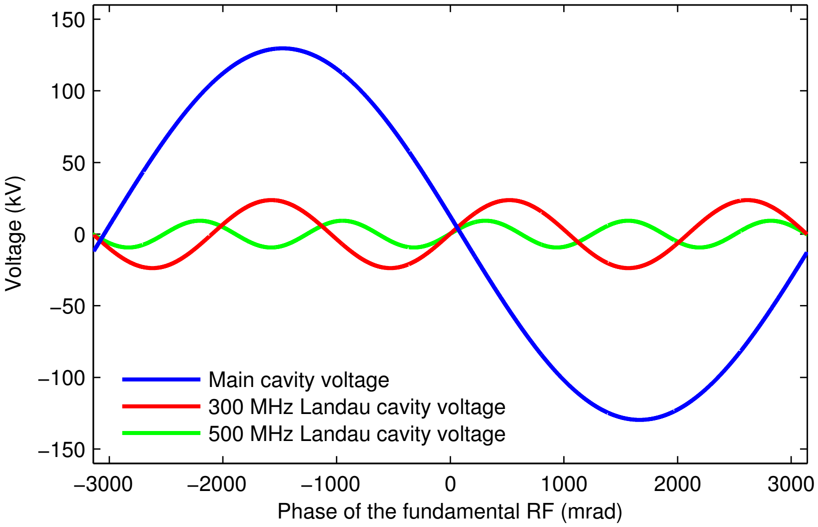

Figure 5.1: *Example of the cavity voltages in the MAX III triple RF system as a function of the phase of the fundamental RF (φ) for 300 mA stored current, 130 kV main cavity voltage and a momentum spread of 0.00085. The 300 MHz cavity is tuned 418 kHz above the third RF harmonic and the 500 MHz cavity is tuned 703 kHz above the fifth RF harmonic. Phase zero corresponds to the location of the synchronous particle.*

frequency is tuned closer to the third RF harmonic in order to increase the cavity voltage. As can be seen in Fig. 5.1 even the case of the tuned out cavity gives a significant voltage in the 300 MHz Landau cavity at 300 mA stored current. In the example the resonance frequency in the 500 MHz Landau cavity is 500.328 MHz, 703 kHz above the fifth RF harmonic. This is the resonance frequency at which the 500 mA Landau cavity is usually tuned to, both during injection and normal operation.

The example settings in Fig. 5.1 have not been chosen arbitrarily. They correspond to the settings of MAX III during the three vertical scraper measurements presented in Sec. 4.1 in Paper **IV**. The momentum spread used in the example was measured using the MAX III diagnostic beam line during one of the three vertical scraper measurements.

The RF voltage as seen by the beam is the combined voltages of the three cavities. Figure 5.2 shows the combined voltage for the three individual voltages in Fig. 5.1. Figure 5.2 also shows the RF voltage for the case of a single RF system with the same main cavity voltage V_0 as for the triple RF case and with the single RF synchronous phase angle. At the location of the synchronous particle (phase zero) the total RF voltage for both the triple RF system and the single RF system is equal to U_0/e, the voltage needed in order to replenish the energy loss of the synchronous particle due to the emission of synchrotron radiation.

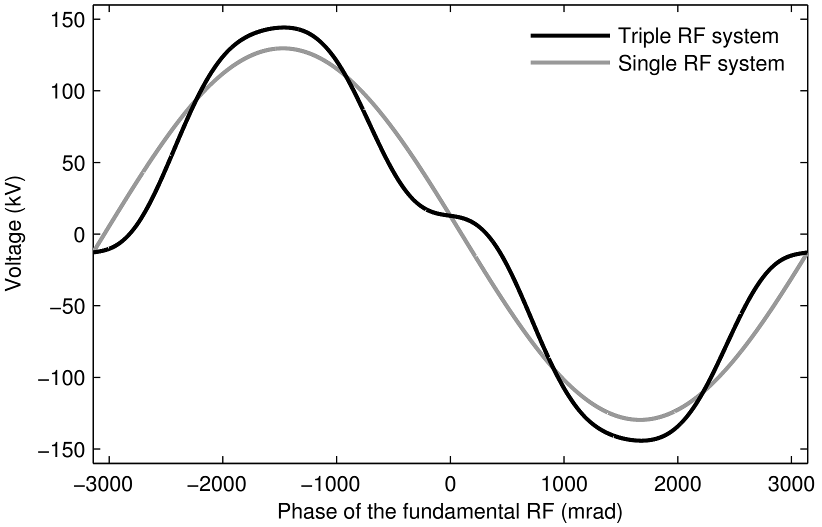

Figure 5.2: *Example of the total RF voltage as seen by the beam in MAX III for the triple RF system and for a single RF system with the same main cavity peak voltage. The simulation is performed with the same settings as in Fig. 5.1.*

The slope of the RF voltage in Fig. 5.2 around the synchronous particle is smaller for the triple RF system than for the single RF system. In the ideal case the amplitude and phase of the Landau cavity is adjusted so that the first and second derivative of the RF voltage is zero at the center of the bunch [35]. For a passive cavity with a fixed quality factor and shunt impedance, this can only be achieved at one specific beam current–tuning angle combination since the amplitude and the phase can not be adjusted independently [36]. Still, as seen in Paper **IV**, the Landau cavities will increase the bunch length and lifetime as well as dampen longitudinal instabilities even if the ideal shape of the RF voltage is not achieved.

5.3 The RF potential and bucket

The RF potential is given by [15]

$$\Phi_{RF}(\varphi) = -\frac{\alpha_c}{2\pi h_{RF} E_0}\left[\int_0^{\varphi} \{eV_{RF}(\varphi') - U_0\}\mathrm{d}\varphi' - \Phi_0\right] \tag{5.8}$$

where φ is the phase of the fundamental RF, α_c is the momentum compaction factor, h_{RF} is the harmonic number, E_0 is the nominal electron energy, e is the elementary charge, $V_{RF}(\varphi)$ is the RF voltage and U_0 is the energy loss per turn for the synchronous particle due to the emission of synchrotron radiation. The

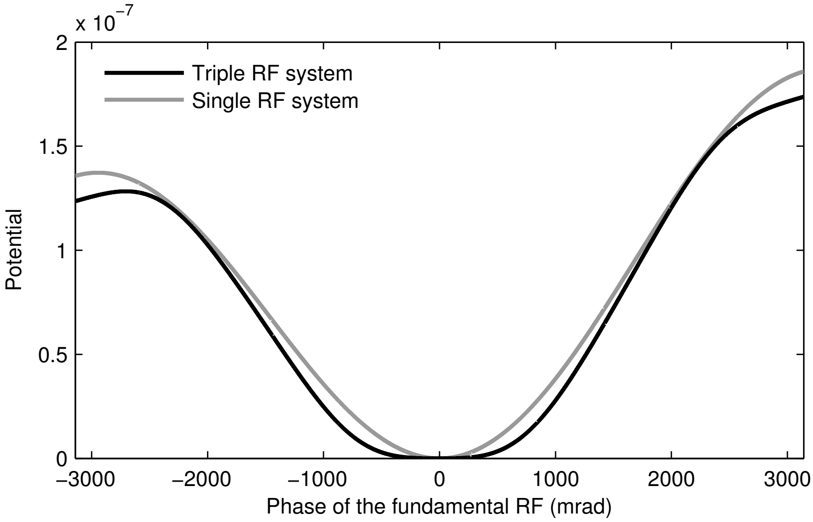

Figure 5.3: *Example of the RF potential in MAX III for the triple RF system and for a single RF system with the same main cavity peak voltage. The simulation is performed with the same settings as in Fig. 5.1.*

constant Φ_0 is chosen so that $\Phi_{RF}(\varphi) = 0$ at the potential minimum. For a single RF system the potential minimum is located at $\varphi = 0$ and the constant Φ_0 is zero. For a triple RF system the potential minimum is not necessarily located at $\varphi = 0$ and the constant Φ_0 may thus have a non-zero value.

Figure 5.3 shows an example, using the same settings as in Figs. 5.1–5.2, of the RF potential for the triple RF system and the single RF system. The potential minimum is located at phase zero for both RF systems. For a single RF system, assuming small displacements from phase zero, the potential shape is close to quadratic. For the triple RF system the potential is more shallow around phase zero. The largest value Φ_{peak} for the electron to stay inside the potential well is also different for the two RF systems.

The shape of the RF bucket as a function of the phase of the fundamental RF is given by [15]

$$\delta_{bucket}(\varphi) = \frac{\sqrt{2}}{\alpha_c}\sqrt{\Phi_{RF}(\varphi)} = \sqrt{-\frac{\int_0^{\varphi}\{eV_{RF}(\varphi') - U_0\}\mathrm{d}\varphi' - \Phi_0}{\pi h_{RF}\alpha_c E_0}} \tag{5.9}$$

Figure 5.4 shows an example, using the same settings as in Figs. 5.1–5.3, of the RF bucket as a function of the phase of the fundamental RF for the triple RF system and the single RF system. For an electron with a given momentum deviation, the electron excursion in phase is larger for the triple RF system than for the single RF system, which will give rise to a longer bunch length

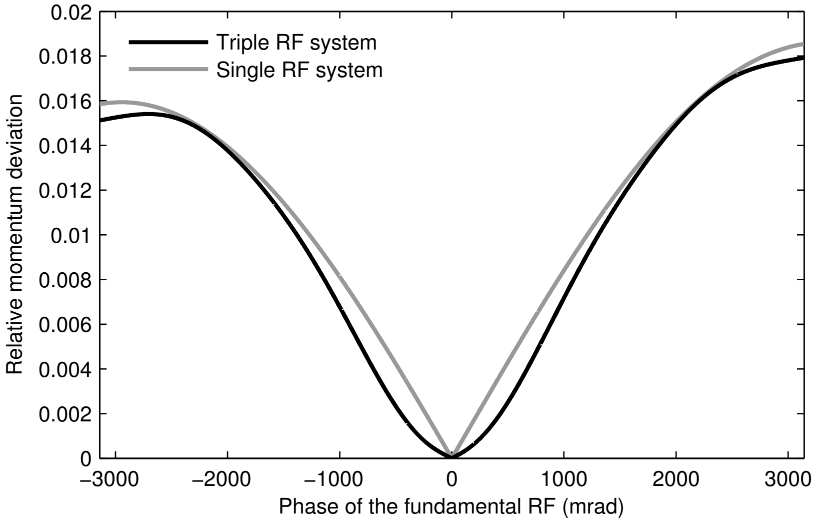

Figure 5.4: *Example of the RF bucket in MAX III for the triple RF system and for a single RF system with the same main cavity peak voltage. The simulation is performed with the same settings as in Fig. 5.1.*

for the triple RF system. The maximum momentum deviation for which the electron stays within the RF bucket defines the RF momentum acceptance of the storage ring. If the momentum deviation of an electron is larger than the RF momentum acceptance the electron will escape the RF bucket and eventually be lost. The RF momentum acceptance of the RF system is given by

$$\delta_{acc}^{RF} = \frac{\sqrt{2}}{\alpha_c}\sqrt{\Phi_{peak}} \tag{5.10}$$

where Φ_{peak} is the largest value of the RF potential for which the electrons stay inside the potential well. As can be seen in the left hand side of Fig. 5.4 the RF momentum acceptance is smaller for the triple RF system than for the single RF system. For the settings in Fig. 5.4 the triple RF momentum acceptance is around 3% smaller than the single RF momentum acceptance.

The electrons inside the RF bucket will perform oscillations in the longitudinal phase space. Neglecting the effect of the radiation damping, which is a slow process compared to the phase space oscillations, the longitudinal phase space trajectory for an electron with momentum deviation δ is given by [15]

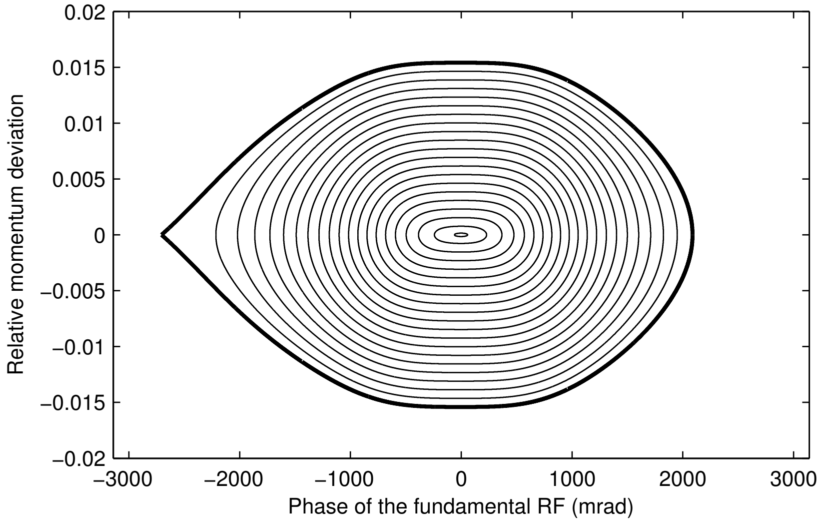

Figure 5.5: *Example of longitudinal phase space in MAX III for the triple RF system. The simulation is performed with the same settings as in Fig. 5.1. The thick line corresponds to the separatrix, the thin lines are examples of stable phase space trajectories.*

$$\begin{aligned}\delta_{trajectory}(\varphi) &= \pm\sqrt{\delta^2 - \frac{2\Phi_{RF}(\varphi)}{\alpha_c^2}} = \\ &= \pm\sqrt{\delta^2 + \frac{\int_0^{\varphi}\{eV_{RF}(\varphi') - U_0\}\mathrm{d}\varphi' - \Phi_0}{\pi h_{RF}\alpha_c E_0}}\end{aligned} \tag{5.11}$$

The special longitudinal phase space trajectory that limits the stable phase space oscillations inside the RF bucket and the unstable phase space trajectories outside the RF bucket is called the separatrix. The separatrix is the phase space trajectory for an electron with a momentum deviation identical to the RF momentum acceptance and it is given by

$$\delta_{separatrix}(\varphi) = \pm\sqrt{\left(\delta_{acc}^{RF}\right)^2 + \frac{\int_0^{\varphi}\{eV_{RF}(\varphi') - U_0\}\mathrm{d}\varphi' - \Phi_0}{\pi h_{RF}\alpha_c E_0}} \tag{5.12}$$

Figures 5.5 and 5.6 show examples, using the same settings as in Figs. 5.1–5.4, of the separatrix and a selection of stable longitudinal phase space trajectories for the triple RF system and single RF system, respectively. The phase space trajectories close to the center of the bucket, where most of the electrons are located, have significantly larger excursions in phase for the triple RF system than the corresponding trajectories for the single RF system.

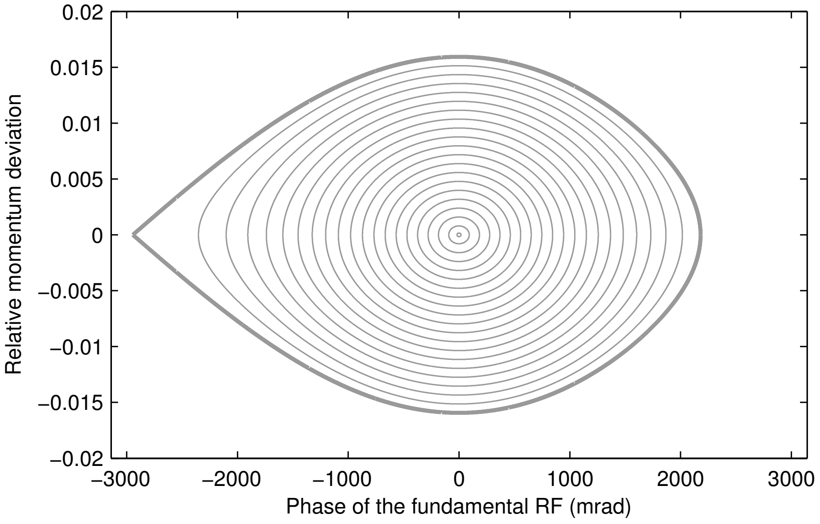

Figure 5.6: *Example of longitudinal phase space in MAX III for a single RF system with the same main cavity peak voltage as the main cavity in Fig. 5.5. The thick line corresponds to the separatrix, the thin lines are examples of stable phase space trajectories.*

5.4 The longitudinal electron distribution

The electron density distribution is given by [35, 36]

$$\lambda(\varphi) = \lambda_0 \exp\left(-\frac{\Phi_{RF}(\varphi)}{\alpha_c^2 \sigma_\delta^2}\right) = \lambda_0 \exp\left(\frac{\int_0^\varphi \{eV_{RF}(\varphi') - U_0\}\mathrm{d}\varphi' - \Phi_0}{2\pi h_{RF}\alpha_c E_0 \sigma_\delta^2}\right) \quad (5.13)$$

where φ is the phase of the fundamental RF, $\Phi_{RF}(\varphi)$ is the RF potential, α_c is the momentum compaction factor, σ_δ is the momentum spread, h_{RF} is the harmonic number, E_0 is the nominal electron energy, e is the elementary charge, $V_{RF}(\varphi)$ is the RF voltage and U_0 is the energy loss per turn for the synchronous particle due to the emission of synchrotron radiation. λ_0 is a normalization constant such that $\int \lambda(\varphi)\mathrm{d}\varphi = 1$.

Figure 5.7 shows an example, using the same settings as in Figs. 5.1–5.6, of the electron density distribution for the triple RF system and the single RF system. For the single RF system the electron density distribution is shown for the measured momentum spread (thick gray line) as well as for the natural momentum spread (thin gray line). The RMS bunch length in the example is about 2.0 times larger for the triple RF system than for the single RF system with the same momentum spread and about 2.8 times larger than for the single

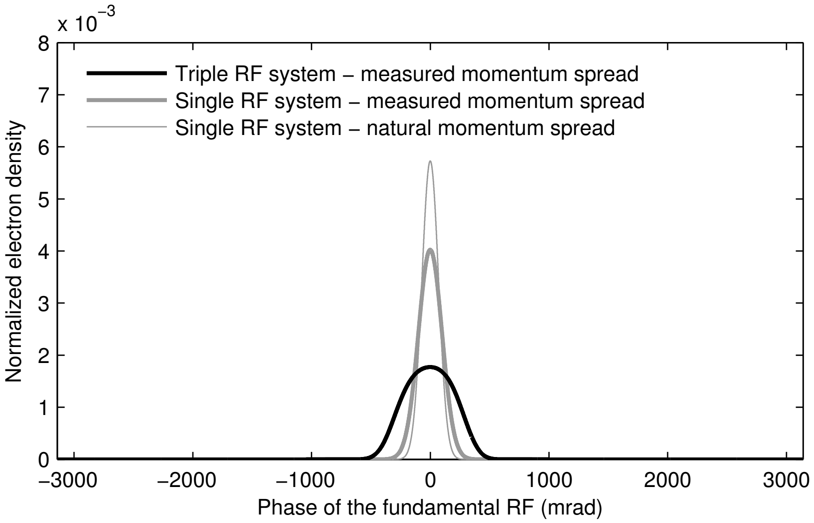

Figure 5.7: *Example of the electron density distribution in MAX III for the triple RF system and for a single RF system with the same main cavity peak voltage. The simulation is performed with the same settings as in Fig. 5.1. For the single RF system the electron density distribution is shown for the measured momentum spread (thick gray line) and for the natural momentum spread (thin gray line).*

RF system with the natural momentum spread.

From the electron density distribution, the Fourier component amplitude and phase can be determined for the third RF harmonic and the fifth RF harmonic. These can be compared to the values used in Eq. (5.2) and Eqs. (5.4)–(5.5) as an input when determining the peak voltages and harmonic phases in the Landau cavities. In order to be self-consistent the input values should be identical to the values calculated from the electron density distribution. For the simulations of the MAX III triple RF system the calculations are iterated until a self-consistent solution is found.

For a single RF system the RF voltage as well as the RF potential and the trajectories in the longitudinal phase space are independent of the electron distribution. The difference in appearance for the single RF electron distributions in Fig. 5.7 for different values of the momentum spread is due to the momentum spread appearing in Eq. (5.13). For the triple RF system the case is different. The voltages in the passive Landau cavities depend on the Fourier component amplitude and phase which in turn depend on the electron distribution. Different values for the momentum spread will thus give different iterative solutions in the simulation and the RF voltage, RF potential and longitudinal phase space trajectories will be affected. For example, in order to determine the electron distribution for the triple RF system with the same settings as in Figs. 5.1–5.7 but with the natural momentum spread, the iterative process would need to be redone in order to find a new self-consistent solution.

5.5 Examples of triple RF simulation results

Results from triple RF simulations were used in Paper **IV**. In this section six examples of simulations of the MAX III triple RF system used in Figs. 3–6 in Paper **IV** are shown in more detail. For each example the individual voltages, the combined voltage, the potential, the bucket, the electron density distribution, and the bunch shape in time and frequency domain is shown. The examples correspond to the situation for six different stored currents during one fill of MAX III in April 2012. During the fill the main cavity voltage was 108 kV and the RF frequency was 99.925 MHz. The 300 MHz Landau cavity resonance frequency was 299.972 MHz, 197 kHz above the third RF harmonic. The 500 MHz Landau cavity resonance frequency was 500.328 MHz, 703 kHz above the fifth RF harmonic. The 300 MHz Landau cavity was thus tuned closer to the third RF harmonic than it was for the example in Figs. 5.1–5.7, whereas the 500 MHz Landau cavity was tuned to the same distance from the fifth RF harmonic. The momentum spread in MAX III varied during the fill, depending on the severity of the longitudinal instabilities, and was determined from measurements using the MAX III diagnostic beam line (see Fig. 2 in Paper **IV**). In Fig. 5.8 the results of the triple RF simulation are shown for 2 mA stored current. Figure 5.9 shows the results for 35 mA stored current, Fig. 5.10 for 114 mA, Fig. 5.11 for 166 mA, Fig. 5.12 for 218 mA and Fig. 5.13 for 306 mA.

At 2 mA stored current (Fig. 5.8) the induced voltages in the Landau cavities are very small because of the low current. The momentum spread is close to the natural momentum spread, since the current is below the instability threshold (see e.g. Fig. 6.4). Combined this gives an almost Gaussian electron distribution with a bunch length close to the natural bunch length. In frequency domain, the bunch shape is also close to Gaussian.

At 35 mA stored current (Fig. 5.9) the current induce more voltage in the Landau cavities, but the triple RF system is still similar to a single RF system. The momentum spread, however, is almost 60% larger than the natural momentum spread because of longitudinal instabilities. The bunch shape is similar to a Gaussian distribution, but with a bunch length about twice as large as at 2 mA. The bunch shape is similar to a Gaussian distribution in the frequency domain as well.

At 114 mA stored current (Fig. 5.10) the voltage in the Landau cavities is higher and the total voltage is clearly affected by the Landau cavities. The longitudinal instabilities have almost been completely damped by the Landau cavities and the measured momentum spread is less than 10% larger than the natural momentum spread. The bunch shape is affected by the Landau cavities

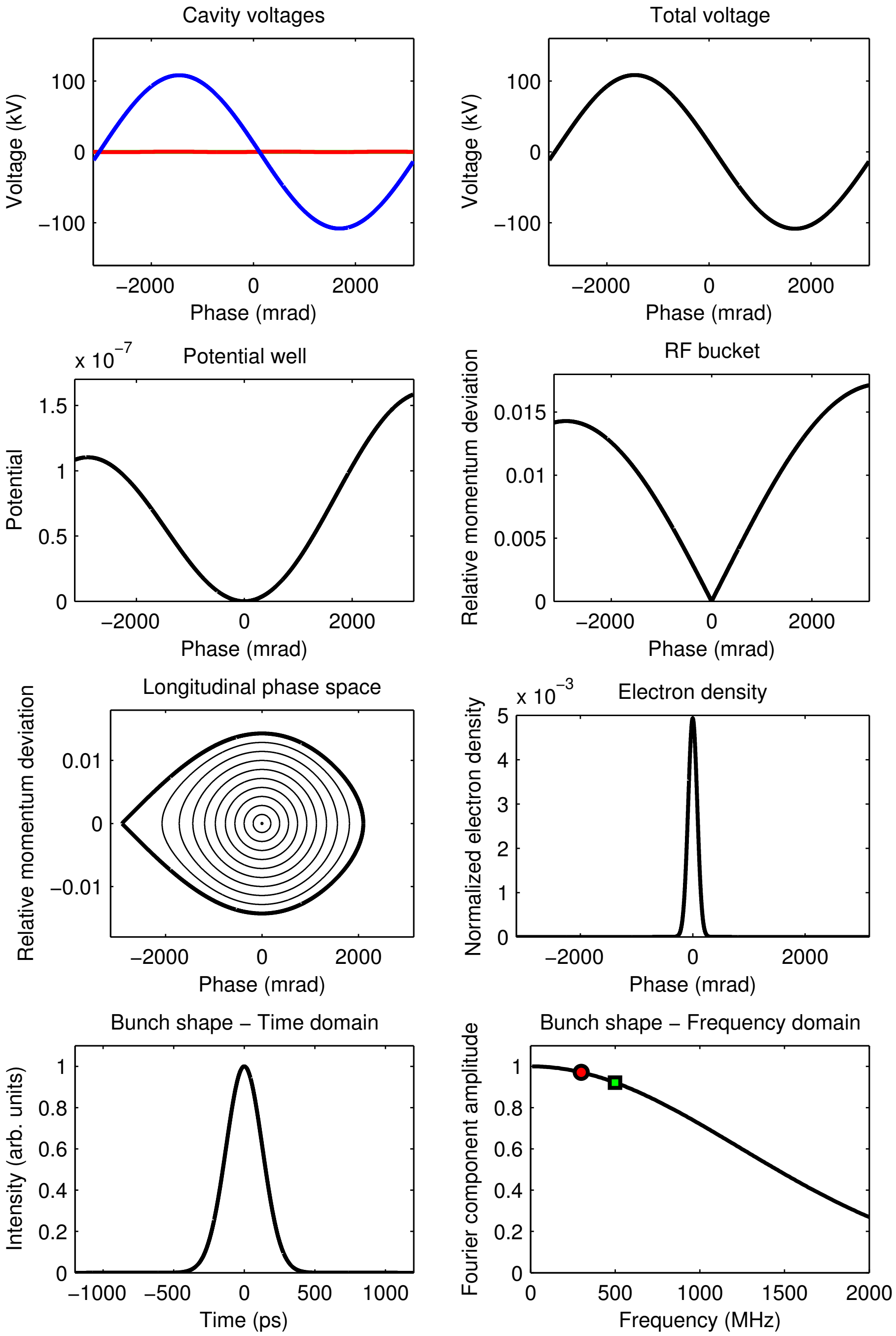

Figure 5.8: *Example of a MAX III triple RF simulation for 2 mA stored current, 108 kV main cavity voltage and the measured momentum spread. Blue is the main cavity, red is the 300 MHz Landau cavity and green is the 500 MHz Landau cavity. The Fourier component amplitudes for the third and fifth RF harmonic are marked in red and green. The results from the simulation were used in Figs. 3–6 in Paper* ***IV****.*

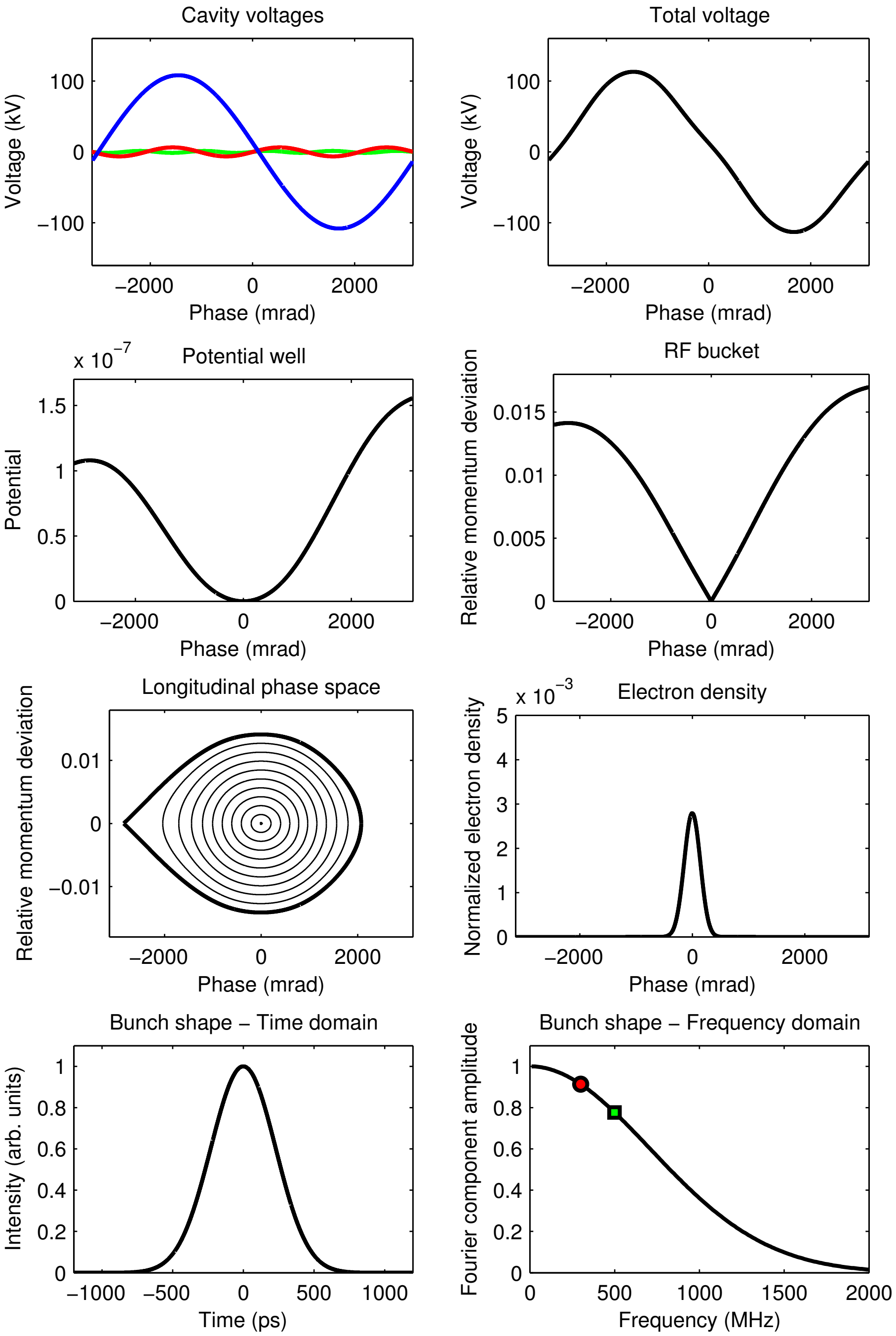

Figure 5.9: *Example of a MAX III triple RF simulation for 35 mA stored current, 108 kV main cavity voltage and the measured momentum spread. Blue is the main cavity, red is the 300 MHz Landau cavity and green is the 500 MHz Landau cavity. The Fourier component amplitudes for the third and fifth RF harmonic are marked in red and green. The results from the simulation were used in Figs. 3–6 in Paper* ***IV****.*

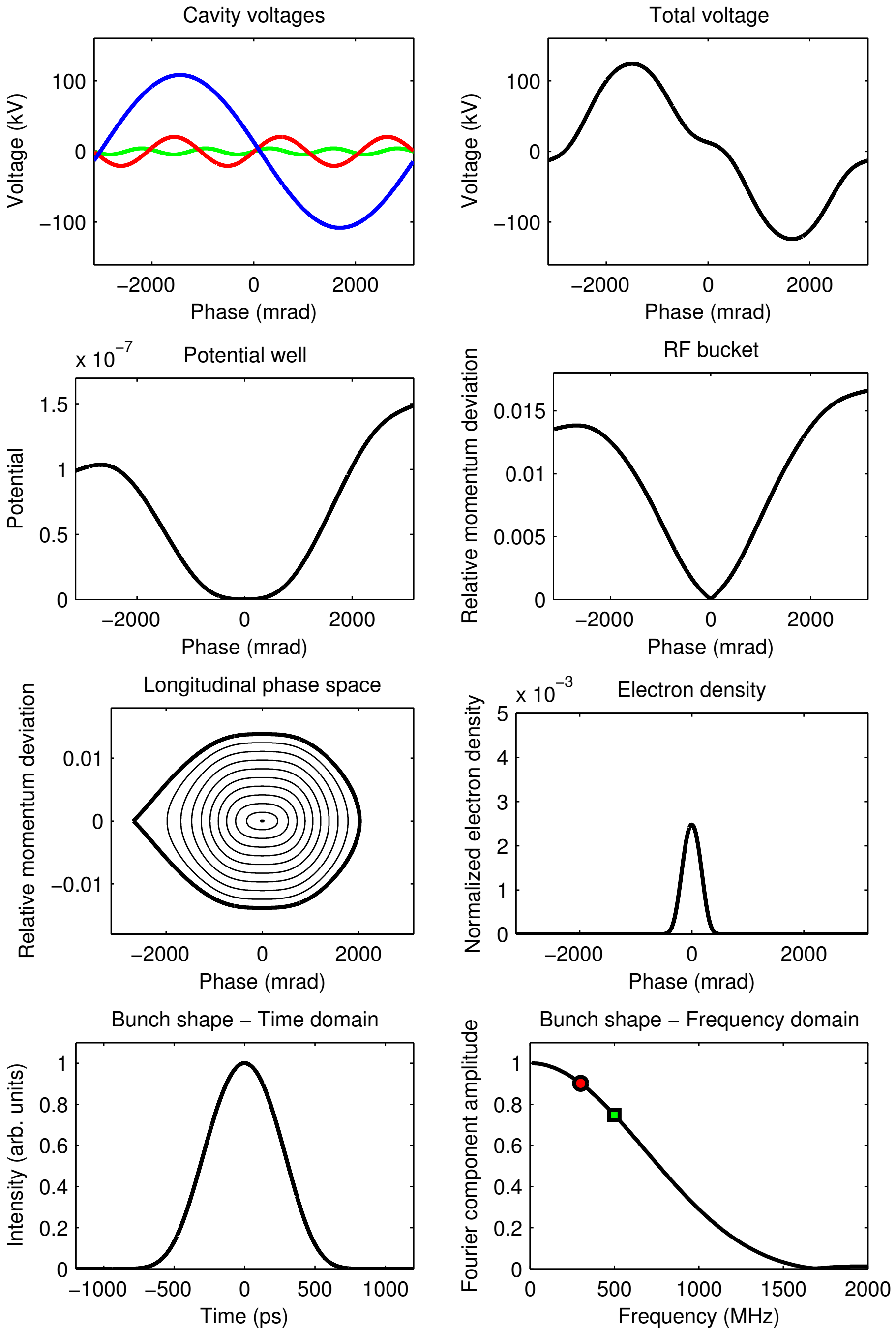

Figure 5.10: *Example of a MAX III triple RF simulation for 114 mA stored current, 108 kV main cavity voltage and the measured momentum spread. Blue is the main cavity, red is the 300 MHz Landau cavity and green is the 500 MHz Landau cavity. The Fourier component amplitudes for the third and fifth RF harmonic are marked in red and green. The results from the simulation were used in Figs. 3–6 in Paper* **IV***.*

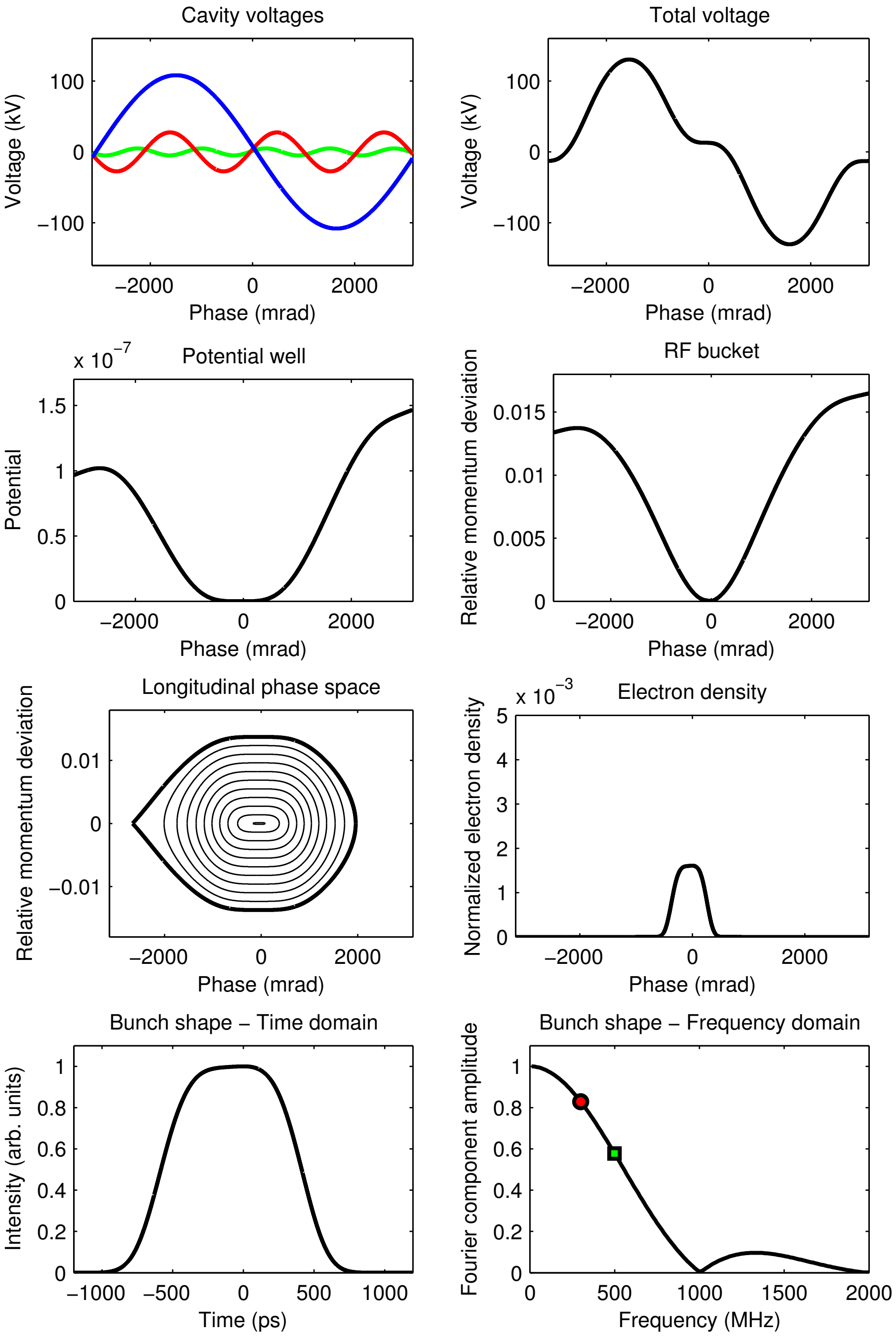

Figure 5.11: *Example of a MAX III triple RF simulation for 166 mA stored current, 108 kV main cavity voltage and the measured momentum spread. Blue is the main cavity, red is the 300 MHz Landau cavity and green is the 500 MHz Landau cavity. The Fourier component amplitudes for the third and fifth RF harmonic are marked in red and green. The results from the simulation were used in Figs. 3–6 in Paper* ***IV****.*

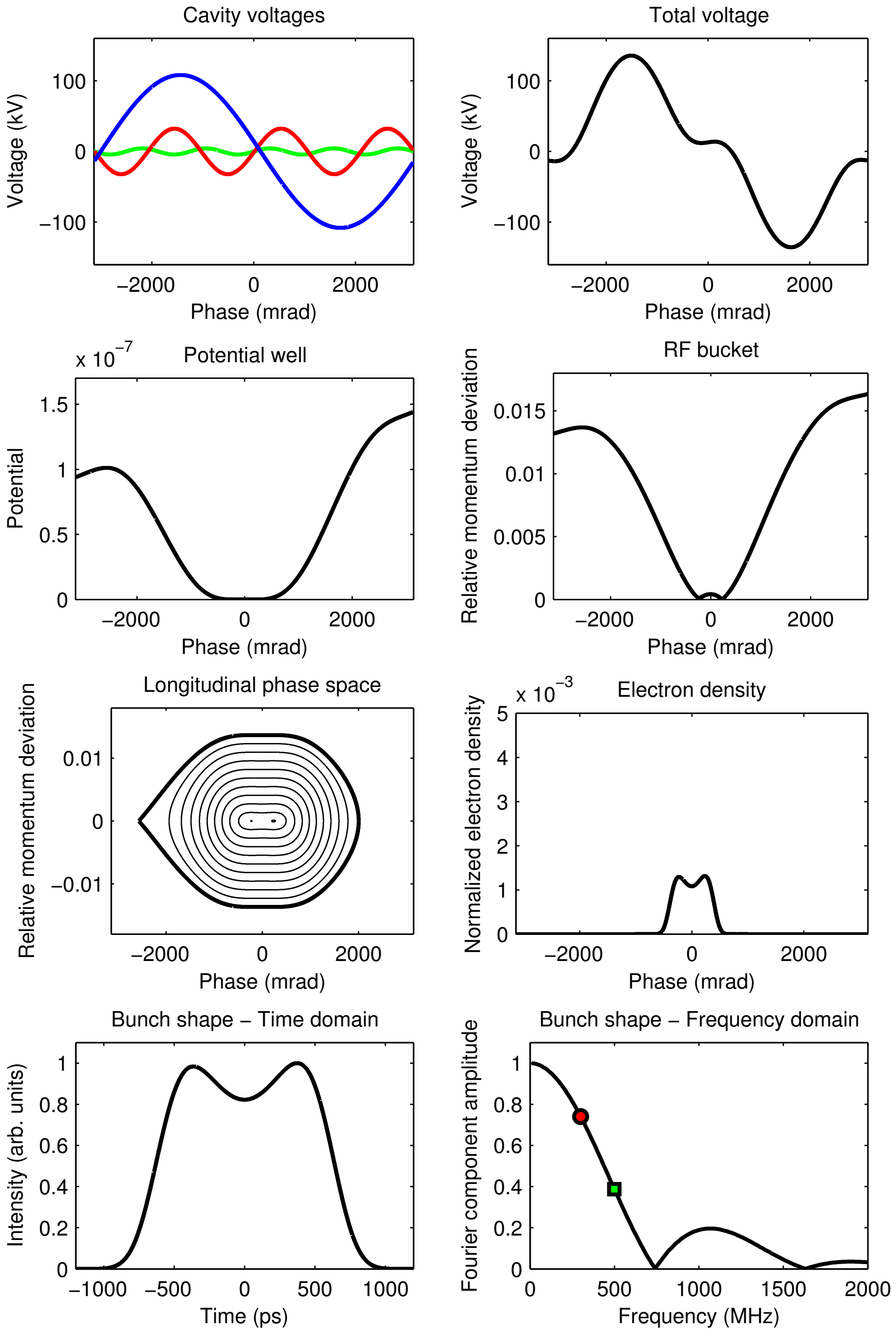

Figure 5.12: *Example of a MAX III triple RF simulation for 218 mA stored current, 108 kV main cavity voltage and the measured momentum spread. Blue is the main cavity, red is the 300 MHz Landau cavity and green is the 500 MHz Landau cavity. The Fourier component amplitudes for the third and fifth RF harmonic are marked in red and green. The results from the simulation were used in Figs. 3–6 in Paper* **IV**.

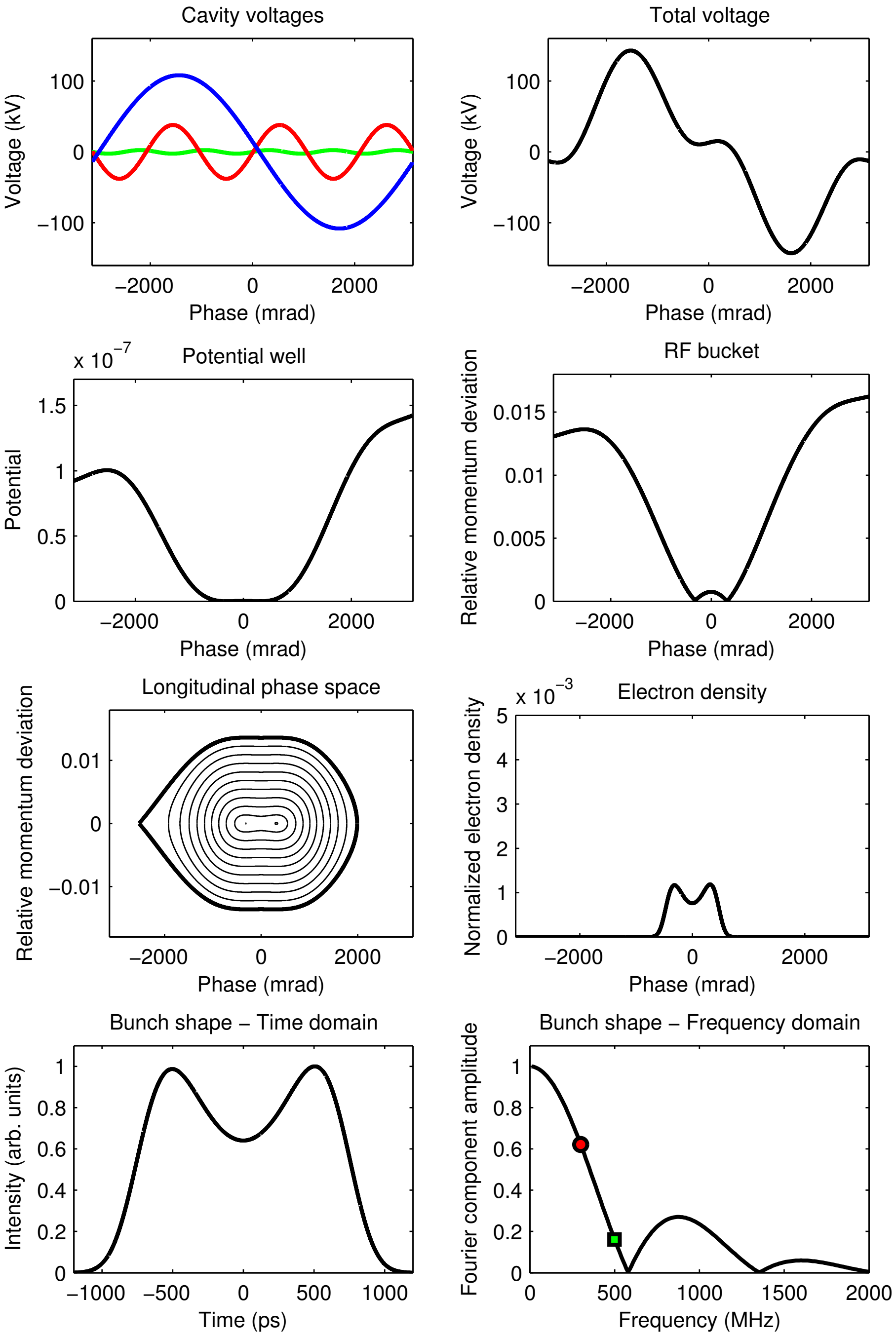

Figure 5.13: *Example of a MAX III triple RF simulation for 306 mA stored current, 108 kV main cavity voltage and the measured momentum spread. Blue is the main cavity, red is the 300 MHz Landau cavity and green is the 500 MHz Landau cavity. The Fourier component amplitudes for the third and fifth RF harmonic are marked in red and green. The results from the simulation were used in Figs. 3–6 in Paper* ***IV****.*

and it is wider than a normal Gaussian distribution. The bunch length is only slightly larger than at 35 mA, but whereas the bunch length increase at 35 mA was mainly caused by the increase in momentum spread from the longitudinal instabilities, the bunch length increase at 114 mA is mainly caused by the Landau cavities. In frequency domain the bunch shape no longer appears Gaussian, as it has a minimum around 1.6 GHz.

At 166 mA stored current (Fig. 5.11) the slope of the total voltage is almost zero at the center of the bunch. The longitudinal instabilities have been damped by the Landau cavities and the measured momentum spread is close to the natural momentum spread. The bunch shape is clearly distorted by the Landau cavities and it has an almost flat top in time domain and a clear minimum at around 1 GHz in frequency domain. The RMS bunch length is about two and a half times longer than at 2 mA.

At 218 mA stored current (Fig. 5.12) the slope of the total voltage has changed sign at the center of the bunch and the measured momentum spread is approximately 10% larger than the natural momentum spread. There are now three locations close to each other where a synchronous particle can be located. The central synchronous location is unstable and the two synchronous locations on either side are stable. There will thus be two regions of phase stability close to each other and the bunch shape has two distinct peaks. The calculations in the figure are performed for phase zero being the central synchronous location. The simulation would give the identical, but shifted, result if one of the other two synchronous locations would be selected as phase zero. In frequency domain, two minima can be observed below 2 GHz.

At 306 mA stored current (Fig. 5.13) the slope of the total voltage at the center of the bunch has increased and the measured momentum spread is approximately 25% larger than the natural momentum spread. The two peaks in the bunch shape are more distinct and separated. In frequency domain a third minimum is located close to 2 GHz and the first minimum is located close to 600 MHz. The amplitude of the Fourier component at the fifth RF harmonic is small and the peak voltage in the 500 MHz Landau cavity is only half of the peak voltage at 166 mA, despite the higher current. The RF momentum acceptance is also affected by the triple RF system. For the example at 306 mA the RF momentum acceptance is about 5% smaller than for a single RF system with the same peak voltage in the main cavity.

The bunch shape was measured by the optical sampling oscilloscope (see Sect. 6.2 and Paper **IV**) during the fill simulated in Figs. 5.8–5.13. In Fig. 5.14 the simulated bunch shapes are compared with the measured bunch shapes for the six different currents. Three of the comparisons were used in Fig. 4 in Paper **IV**. At 2 mA the intensity of the synchrotron radiation diverted to the optical sampling oscilloscope was low and the measured bunch shape is somewhat noisy. At 35 mA the top of the measured bunch shape is rugged and the tails do not agree fully with the simulated bunch shape. In Eq. (5.13) the momentum spread is assumed to have a Gaussian distribution. This is not

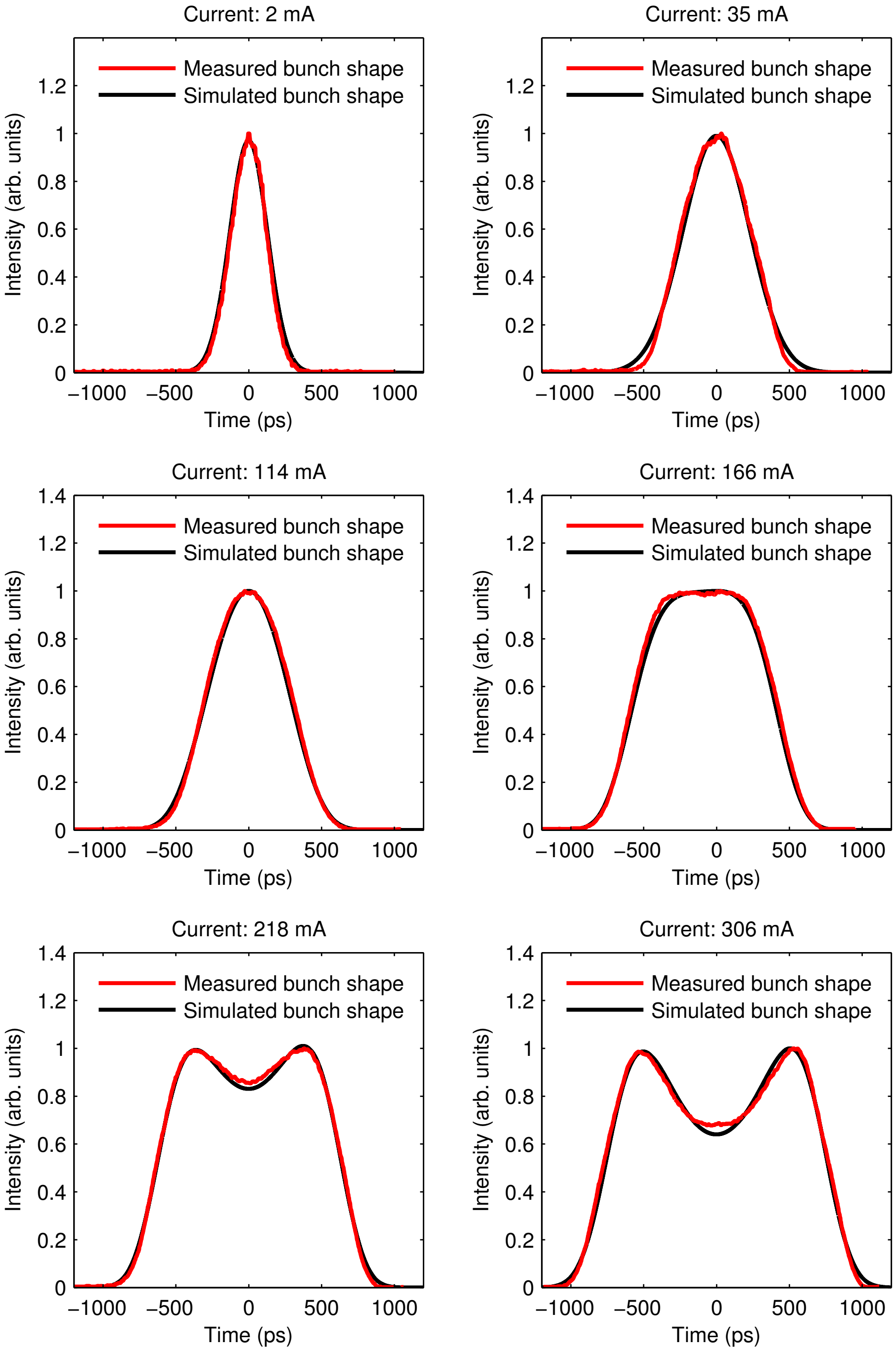

Figure 5.14: *Comparison between simulated and measured bunch shapes for the six simulations in Figs. 5.8–5.13. The measurements were performed with the optical sampling oscilloscope (see Sect. 6.2 and Paper* ***IV****). Three of the comparisons were used in Fig. 4 in Paper* ***IV****.*

necessarily valid when the momentum spread is affected by the longitudinal instabilities, which is the case at 35 mA. This discrepancy might explain the difference between the simulated bunch shape and the measured bunch shape at 35 mA. At higher currents the effect of the Landau cavities is apparent. The widening of the bunch shape at 114 mA, the almost flat top at 166 mA and the two distinct peaks in the bunch shapes at 218 mA and 306 mA can clearly be observed in the measured bunch shapes.

Chapter 6

Measuring the bunch length

In Chapter 5 the triple RF system in MAX III was described. The bunch length was simulated for different setting of the system. In order to compare the simulation results to the actual bunch length in the storage ring experimental observations are needed. This chapter describes two methods to determine the bunch length in a storage ring. Section 6.1 describes bunch length measurements using a strip line and Sec. 6.2 describes the optical sampling oscilloscope. There are several other methods to measure the bunch length in a storage ring, but this chapter will focus on the two methods used at MAX-lab.

6.1 Strip line

A strip line consists of a strip with a length l_{strip} located inside the vacuum chamber and connected, at each end, to a signal port outside of the vacuum chamber. In MAX III two sets of four strip lines are installed in the ring. For the bunch length measurement it is sufficient to use one strip line.

Figure 6.1 shows a schematic overview of the strip line signals induced by a passing electron bunch. In the example it is assumed that the impedance of the strip is matched to the impedance of the two ports. The electron velocity is approximated to be c, the speed of light. At the time $t = 0$ the electron bunch passes the front edge of the strip line. Since the impedance is matched the signal induced by the bunch is divided into two equal parts. One part follows the strip line and the other part exits through the upstream port. During $0 < t < l_{strip}/c$ the electron bunch and the signal travels along the strip line at the speed of light. At $t = l_{strip}/c$ the electron bunch passes the back edge of the strip line and a new signal is generated and divided into two equal parts. The new signals have the opposite sign as the previous signals. One part goes back along the strip line and the other part cancels the signal that was traveling

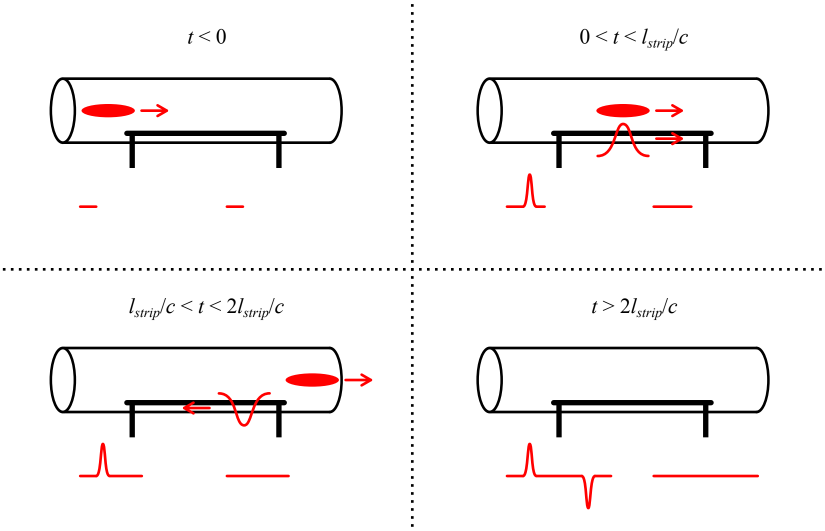

Figure 6.1: *Overview of the strip line signals induced by a passing electron bunch. At* $t = 0$ *the signal induced by the bunch at the front edge of the strip is split in two halves, where one signal exits the upstream port and the other signal travels along the strip. At* $t = l_{strip}/c$ *the signal induced by the bunch at the back edge of the strip (this time with opposite sign) is split in two halves, where one signal travels back along the strip and the other signal cancels the signal that was traveling along the strip. At* $t = 2l_{strip}/c$ *the second signal exits through the upstream port. In total two signals exit the upstream port whereas no signals exit the downstream port.*

along the strip line. During $l_{strip}/c < t < 2l_{strip}/c$ the second signal travels along the strip line and at $t = 2l_{strip}/c$ it exits through the upstream port. In this ideal case there is no voltage induced in the second port. In order to measure the bunch length using a strip line the measurement must thus be made on the upstream port.

For the bunch length measurement using a strip line a spectrum analyzer is connected to the upstream port of the strip line to measure the amplitude of the signal as a function of frequency. The downstream port is terminated. The amplitude of the induced voltage $V_p(f)$ in the upstream port is related to the electron beam current $I_{beam}(f)$ in the storage ring via the amplitude of the transfer impedance $Z_t(f)$. For the upstream port of a strip line the transfer impedance amplitude is given by [37, 38]

$$|Z_t(f)| \equiv \frac{|V_p(f)|}{I_{beam}(f)} = Z_0 \left| \sin\left(\frac{2\pi f l_{strip}}{c}\right) \right| \tag{6.1}$$

where Z_0 is a constant. The beam current for a single bunch with a Gaussian shape is given by

$$I_{beam}(f) = I_0 \exp\left(-2\pi^2 c^2 f^2 \sigma_z^2\right) \tag{6.2}$$

where I_0 is a constant and σ_z is the bunch length. The amplitude of the induced voltage in the upstream port is thus given by

$$|V_p(f)| = Z_0 \left| \sin\left(\frac{2\pi f l_{strip}}{c}\right) \right| I_0 \exp\left(-2\pi^2 c^2 f^2 \sigma_z^2\right) \tag{6.3}$$

Equation (6.3) describes the voltage amplitude at the port. The spectrum analyzer measures the amplitude of the signal power. A low-loss cable was connected between upstream port of the strip line and the spectrum analyzer. Taking the frequency-dependent attenuation $P_{att}(f)$ in the cable into account the signal strength P_{signal} measured by the spectrum analyzer at frequency f is given by

$$P_{signal}(f) = P_0 \sin^2\left(\frac{2\pi f l_{strip}}{c}\right) \exp\left(-4\pi^2 c^2 f^2 \sigma_z^2\right) P_{att}(f) \tag{6.4}$$

where P_0 is a constant.

Equation (6.4) assumes a single pass of a Gaussian bunch. For MAX III the bunches pass by the strip line at a frequency of approximately 100 MHz (the RF frequency). In frequency domain this corresponds to a multiplication of the frequency spectrum of a single bunch with the frequency spectrum of a sequence of point-like bunches passing at the RF frequency. The sequence of point-like bunches passing at the RF frequency will give rise to a line spectrum with lines at every integer multiple of the RF frequency (the "RF harmonics"). The single bunch frequency spectrum will define the envelope of the line spectrum. An introduction to the frequency spectrum of a stored beam can be found in Ref. [22].

Figure 6.2 and Fig. 6.3 show two examples of strip line measurements performed at MAX III with 108 kV main cavity voltage for a stored current of 1 and 20 mA, respectively. The signal strength was measured with the spectrum analyzer for the first 20 RF harmonics. The model in Eq. (6.4) was fitted to the measured signal strengths. The free parameters of the fit were the constant P_0, the strip length l_{strip} and the bunch length σ_z. The figures show the measurement data and the fitted signal strength as a function of the frequency. The figures also show the contribution to the signal strength from the frequency spectrum of the beam (note that the spectrum is squared since the amplitude of the power is the measured parameter), the contribution from the strip line modulation (proportional to the squared strip line transfer impedance) and the contribution from the attenuation in the cable between the strip line and the spectrum analyzer.

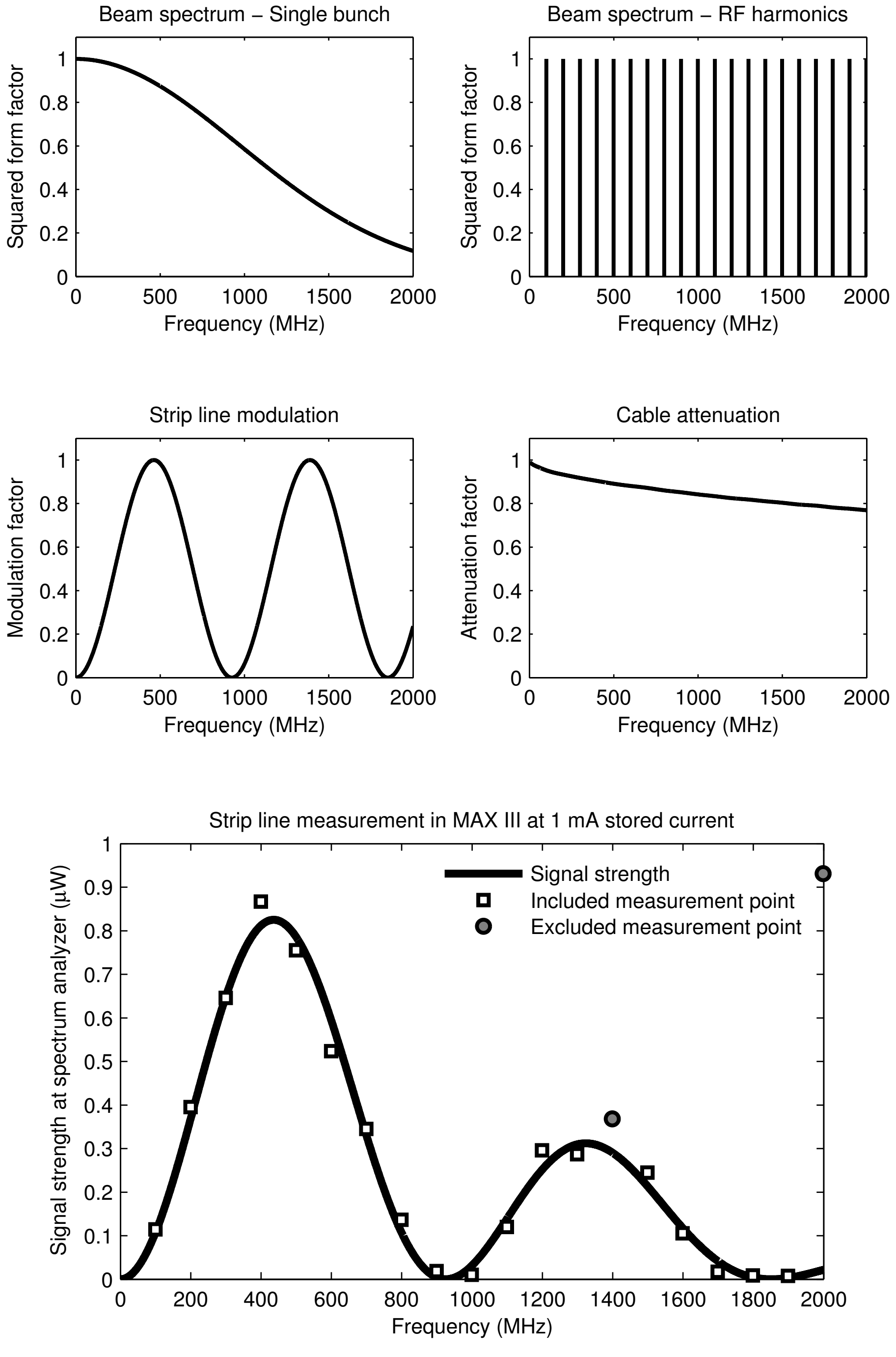

Figure 6.2: *Example of a strip line bunch length measurement performed at MAX III with 1 mA stored current and 108 kV main cavity voltage. The signal strength at the spectrum analyzer is given by multiplication of the squared frequency spectrum of the electron beam with the strip line modulation, the cable attenuation and a constant. The result of the measurement was used in Fig. 3 in Paper* ***IV****.*

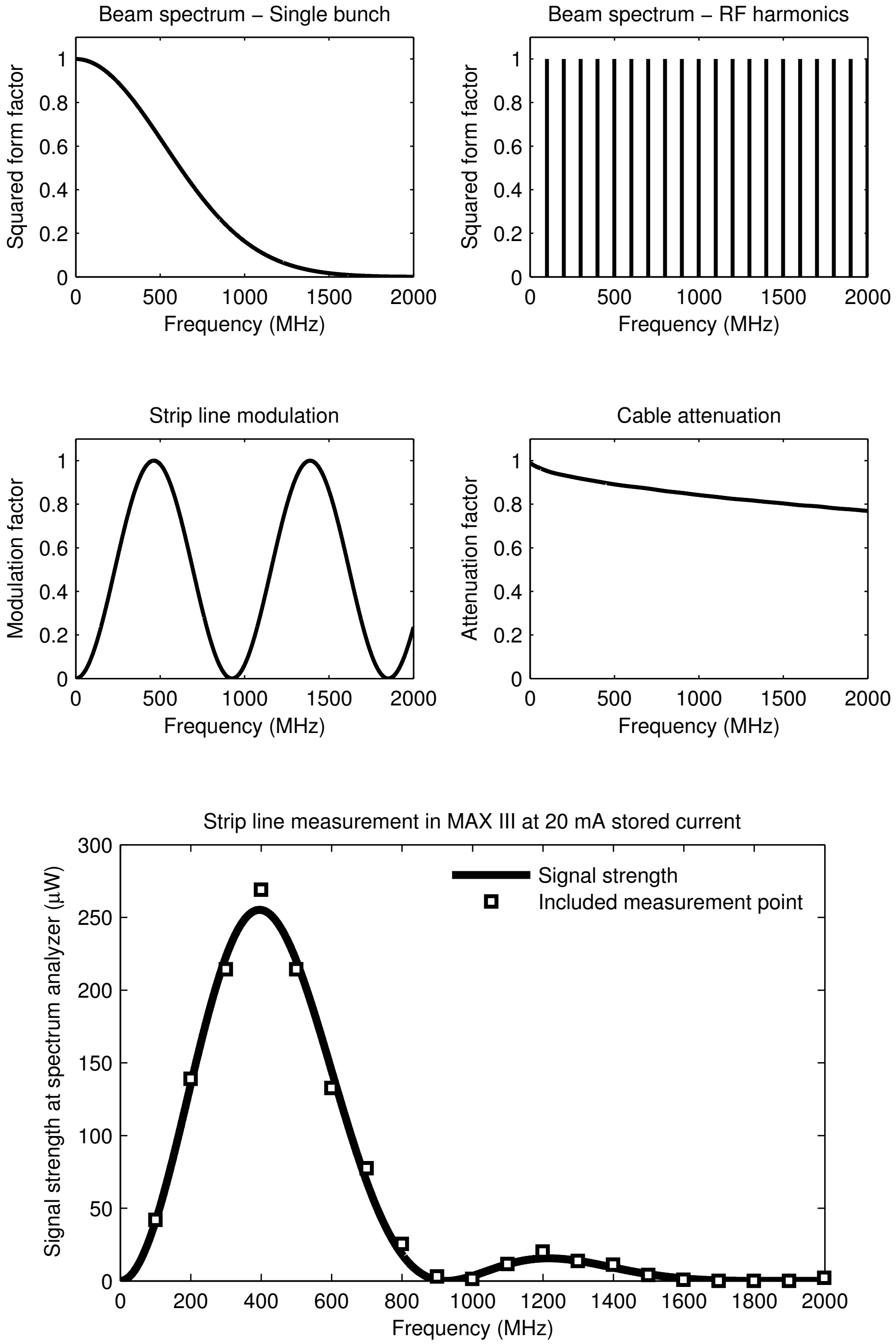

Figure 6.3: *Example of a strip line bunch length measurement performed at MAX III with 20 mA stored current and 108 kV main cavity voltage. The signal strength at the spectrum analyzer is given by multiplication of the squared frequency spectrum of the electron beam with the strip line modulation, the cable attenuation and a constant.*

For the measurement in Fig. 6.2, performed at 1 mA stored current, the fit result was 3.5 cm (RMS) for the bunch length and 16.3 cm for the strip length. Two of the measurement points were excluded from the fit. For these two measurement points the measured signal strengths have been observed to systematically deviate from the expected signal strengths for all measurements that have been performed at low currents. The cause of this deviation is unknown.

For the measurement in Fig. 6.3, performed at 20 mA stored current, the fit result was 6.4 cm (RMS) for the bunch length and 16.2 cm for the strip length. The bunch length is almost twice as long as in Fig. 6.2, mainly due to longitudinal instabilities (see Paper **IV**). A longer Gaussian bunch shape in time domain corresponds to a shorter Gaussian bunch shape in frequency domain, which can clearly be observed when comparing Fig. 6.3 and Fig. 6.2. All of the measurement points were included in the fit, since the systematical deviations observed at low currents did not appear at 20 mA stored current.

The fit to the model in Eq. (6.4) assumes a Gaussian bunch shape. This is valid for measurements at low currents, before the onset of the instabilities and before the Landau cavities start to noticeably lengthen the bunches. At high currents the assumption of a Gaussian bunch shape is not valid, as seen in Chapter 5. At 20 mA the longitudinal instabilities have a significant effect on the bunch length and the Gaussian approximation may not be valid. The strip line measurement as such does not require an initial assumption of the bunch shape, but without a simple assumption as in Eq. (6.4) it is more complicated to obtain a value for the bunch length from the measurement. The strip line has thus mainly been used for bunch length measurements at low currents where the bunch length is close to the natural bunch length and the bunch shape is Gaussian.

6.2 Optical sampling oscilloscope

Most of the bunch length measurements have been performed using the commercial optical sampling oscilloscope Hamamatsu OOS-001 from Hamamatsu Photonics. For the measurements in Paper **IV** the optical sampling oscilloscope was triggered by the MAX III RF frequency divided by the harmonic number, in order to do measurements on only one of the bunches in the storage ring. During the bunch length measurements, the synchrotron light from the diagnostic beam line was diverted from the optical rail of the diagnostic beam line using a mirror and focused with an additional lens in order to deliver light to the sampling head of the optical sampling oscilloscope.

Inside the sampling head of the Hamamatsu OOS-01 the incident light is focused and converted into photoelectrons at a photocathode. The electron path is deflected by deflection plates and swept over a sampling slit plate. The

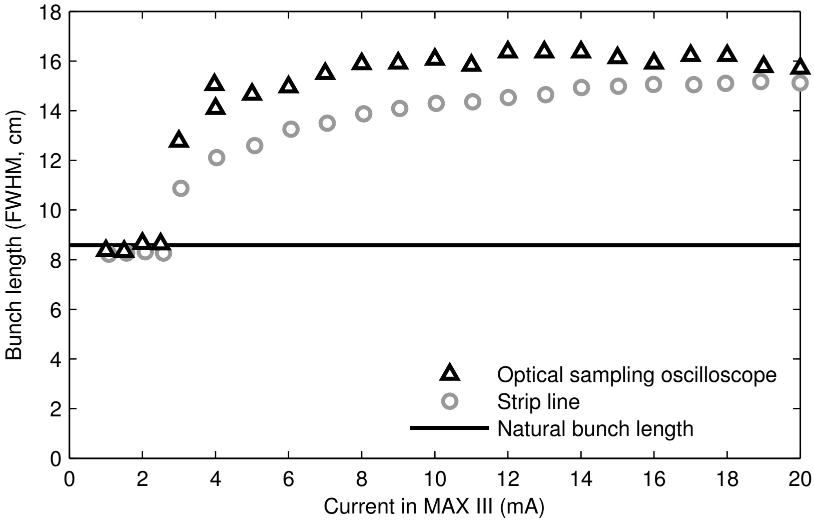

Figure 6.4: *Bunch length in MAX III as a function of stored current in February 2012. The FWHM bunch length is measured with an optical sampling oscilloscope as well as with a stip line. The solid line corresponds to the natural bunch length.*

photoelectrons passing the slit generate light on a phosphor screen which is transformed into an electric signal by a photomultiplier tube. For a typical measurement the signal was sampled with 2048 points on a 2.4 ns time axis and the data acquisition time was around 70 seconds.

Figure 6.4 compares measured full width at half maximum (FWHM) bunch lengths as a function of stored current for the optical sampling oscilloscope and the strip line. The bunch length measurements were performed in parallel during a single fill of MAX III in February 2012. The main cavity voltage was kept constant at 108 kV. The natural bunch length in MAX III for this voltage, calculated using Eq. (2.54), is added as a solid line in Fig. 6.4. The FWHM bunch length is presented instead of the RMS bunch length since the FWHM value is directly accessible from the optical sampling oscilloscope without the need for later offline data processing. Below the instability threshold at around 3 mA, the optical sampling oscilloscope and the strip line give similar values for the bunch length that agrees with the natural bunch length. Above the instability threshold the measured bunch length for the two methods differ by up to 25%. As discussed in Sec. 6.1 the assumptions of the strip line measurements are not necessarily valid above the instability threshold. The bunch length results from the optical sampling oscilloscope are thus more credible. This conclusion is supported by the observations in Sec. 5.5 and Paper **IV** that the bunch shape from the triple RF simulations agree well with the measurements using the optical sampling oscilloscope.

CHAPTER 7

THE LIFETIMES AND ACCEPTANCES OF AN ELECTRON STORAGE RING

The lifetime τ_{tot} in an electron storage ring containing N_e electrons is defined through the relative loss rate at a given time:

$$\frac{1}{\tau_{tot}} \equiv -\frac{\dot{N}_e}{N_e} \tag{7.1}$$

The lifetime is typically given in hours. A lifetime of e.g. 10 h should, however, not be interpreted as the time it would take for the current to decay to a particular value of e.g. half or a factor of 0.368 of its initial value. The lifetime is just a measure of the inverse relative loss rate at that particular moment.

With a long lifetime the heat load on the accelerator components and the beam lines remains more constant. A longer lifetime also means longer time before a new injection is needed. At MAX II a new injection is typically performed every 12 hours and at MAX III a new injection is typically performed every 4–6 hours. At MAX IV the injection will be done at full energy and with frequent small injections to top-up the current and keep it almost constant. Still, a fairly high lifetime is desired in order to keep the top-up interval reasonable, to reduce the radiation levels and to minimize the radiation-induced demagnetization of permanent magnets in undulators and wigglers.

There are several effects that limit the lifetime in an electron storage ring. The lifetime is usually determined by the elastic ($\tau_{elastic}$) and inelastic ($\tau_{inelastic}$) scattering of the beam electrons on the atoms of the residual gas, the electron-electron scattering within the bunch ($\tau_{Touschek}$) and the quantum excitation ($\tau_{quantum}$). The total lifetime τ_{tot} is given by

$$\frac{1}{\tau_{tot}} = \frac{1}{\tau_{elastic}} + \frac{1}{\tau_{inelastic}} + \frac{1}{\tau_{Touschek}} + \frac{1}{\tau_{quantum}} \tag{7.2}$$

The mechanism leading to an electron loss varies for the different lifetime limitations. For the elastic scattering on the residual gas nuclei the beam electrons are deflected and undergo large betatron oscillations. If the oscillation amplitude is sufficiently large the electron will be lost at the physical aperture of the vacuum chamber. Assuming linear dynamics it is the size of the vertical and horizontal physical acceptance of the storage ring that determines the maximum possible betatron amplitude. For the electron-electron scattering, i.e. the Touschek effect, it is instead the energy of the beam electrons that is affected. If the change in energy in larger than the RF momentum acceptance, i.e. the height of the RF bucket, the electron will be lost. Through dispersion a momentum deviation will also give rise to a transverse deviation, which defines a lattice momentum acceptance. The physical acceptance and the momentum acceptance is discussed further in Sec. 7.1. Section 7.2 takes a closer look at the quantum lifetime. The elastic and inelastic scattering lifetimes are discussed in Sec. 7.3 and Sec. 7.4, respectively. In Sec. 7.5 the Touschek lifetime is discussed.

7.1 Physical and momentum acceptance

The transverse beam sizes in a modern synchrotron light source are fractions of millimeters and the energy spread is around 10^{-3}. Still, the apertures of the vacuum chambers are typically several millimeters or centimeters and the momentum acceptance a few percent. In the horizontal direction, the aperture must be sufficiently large to accommodate the large betatron oscillations of the electrons when they are injected into the storage ring. The horizontal aperture as well as the RF momentum acceptance should be sufficiently large to contain a large part of the electrons that suffer energy changes from inelastic scattering on the residual gas or from scattering on the other electrons in the bunch. In the vertical direction, the aperture is often smaller because of the narrow insertion device vacuum chambers, but the aperture should still be sufficiently large to accommodate a large part of the betatron oscillations caused by elastic scattering on the residual gas.

The physical acceptances are determined by the dimensions of the vacuum chambers. It is assumed that the transverse dynamics are linear, which is the case for an ideal storage ring containing only dipoles and quadrupoles. But the storage ring also includes sextupoles, insertion devices and small errors in the position and rotation of the magnets, which gives rise to coupling and nonlinear dynamics. The onset of chaotic or unstable motion defines a dynamic acceptance, beyond which the electron is lost because of nonlinear resonances. The goal in the design of a storage ring is to have a dynamic acceptance larger than the physical acceptance. For off-momentum electrons the non-linear dynamics can give rise to a dynamic lattice momentum acceptance that is smaller than the linear lattice momentum acceptance. In this chapter the transverse motion is assumed to be linear.

The horizontal physical acceptance is given by [39]

$$A_x(\delta) = \min\left(\frac{(a_x(s) - |\eta_x(s)\delta|)^2}{\beta_x(s)}\right) \tag{7.3}$$

where $a_x(s)$ is the horizontal aperture, $\eta_x(s)$ is the horizontal dispersion function, δ is the momentum deviation and $\beta_x(s)$ is the horizontal beta function. The limiting horizontal aperture in a storage ring is not necessarily the same as the smallest horizontal aperture in the ring. Instead, it is the aperture that gives the minimum in Eq. (7.3). From the local projection of the horizontal acceptance, it is possible to determine the minimum and maximum x-values an electron can reach around the ring [39]:

$$x(s,\delta) = \pm\sqrt{A_x(\delta)\beta_x(s)} + \eta_x(s)\delta \tag{7.4}$$

When a reference is made to the horizontal acceptance, it is often the on-momentum horizontal physical acceptance that is implied. Unless otherwise specified, the horizontal acceptance means the on-momentum horizontal physical acceptance in this thesis and in Paper **I** and Paper **IV**. In Fig. 7.1 the design horizontal apertures in MAX III are shown. The design horizontal acceptance in MAX III is 73×10^{-6} m. The design limiting horizontal aperture is the absorber downstream the dipole magnet. Included in Fig. 7.1 is the maximum x-values an electron can reach around the ring for the design horizontal acceptance.

The vertical physical acceptance is given by Eq. (7.3) with x replaced by y. For most electron storage rings, the vertical dispersion is negligible and the vertical physical acceptance is given by [39]

$$A_y = \min\left(\frac{a_y(s)^2}{\beta_y(s)}\right) \tag{7.5}$$

where $a_y(s)$ is the vertical aperture and $\beta_y(s)$ is the vertical beta function. The minimum and maximum y-values an electron can reach is then given by [39]

$$y(s) = \pm\sqrt{A_y\beta_y(s)} \tag{7.6}$$

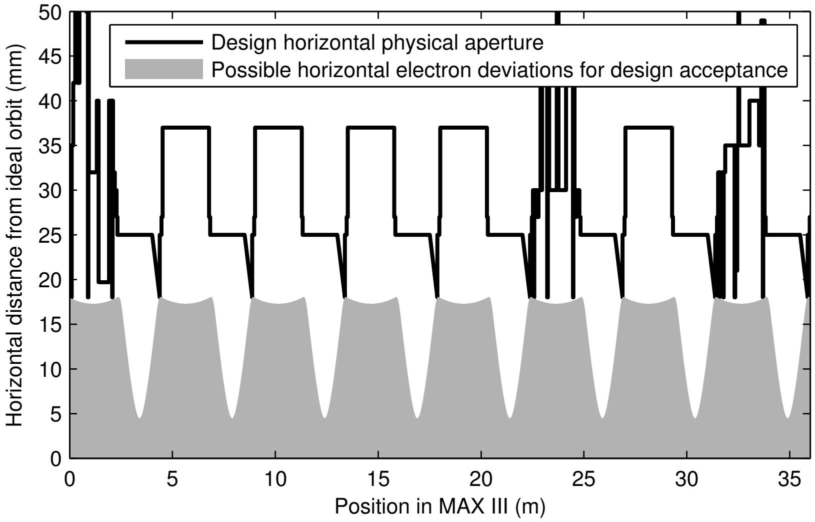

Figure 7.1: *Design horizontal apertures in MAX III and the x-values an electron can reach around the ring for the design horizontal acceptance. The calculations were performed for the design lattice and design horizontal beta function for on-momentum electrons. The smallest design horizontal apertures are the absorbers downstream of the dipole magnet and the absorbers in the straight sections. The design limiting horizontal apertures are the absorbers downstream the dipole magnets.*

In a similar way as for the horizontal acceptance, the vertical acceptance means the on-momentum vertical physical acceptance in this thesis and in Paper **I** and Paper **IV**. Figure 7.2 shows the design vertical apertures in MAX III and the maximum y-values an electron can reach around the ring for the design vertical acceptance. The design vertical acceptance of MAX III is 7.8×10^{-6} m and the design limiting vertical aperture is in the center of the dipole vacuum chamber.

An off-momentum electron will follow a dispersive closed orbit around the ring. From Eq. (7.3) it follows that for a momentum deviation $|\delta| > \min\bigl(a_x(s)/|\eta_x(s)|\bigr)$ the electron will collide with the vacuum chamber wall. All off-momentum electrons will follow a dispersive orbit. If the momentum is changed suddenly at a location with dispersion there will also be a betatron oscillation around the dispersive orbit. For an electron where the initial momentum deviation is close to zero and the momentum is changed suddenly at a certain location, which is e.g. the case for a Touschek scattering event, the dispersive orbit and betatron oscillation will determine a maximum momentum acceptance. This maximum momentum acceptance is called the lattice momentum acceptance. The lattice momentum acceptance at location s_0 is given by [39]

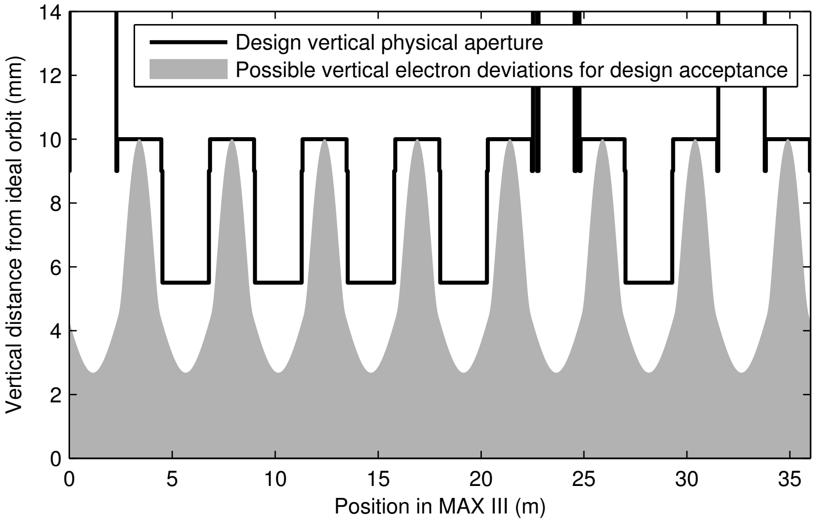

Figure 7.2: *Design vertical apertures in MAX III and the y-values an electron can reach around the ring for the design vertical acceptance. The calculations were performed for the design lattice and design vertical beta function. The smallest design vertical apertures are the insertion device vacuum chambers. The design limiting vertical apertures are in the center of the dipole vacuum chambers.*

$$\delta_{acc}^{L}(s_0) = \pm \min \left(\frac{a_x(s)}{\sqrt{\mathcal{H}(s_0)\beta_x(s)} + |\eta_x(s)|} \right) \tag{7.7}$$

where $\mathcal{H}(s_0)$ is the $\mathcal{H}$ function at location s_0. The lattice momentum acceptance in Eq. (7.7) is the linear lattice momentum acceptance. The non-linear dynamics will give rise to a dynamic lattice momentum acceptance. The total lattice momentum acceptance at a location in the ring is the smallest of the linear and the dynamic lattice momentum acceptances at that location.

The height of the RF bucket will also give a limit on the momentum acceptance of the storage ring. For a single sinusoidal RF system the RF momentum acceptance is given by [15]

$$\delta_{acc}^{RF} = \pm \sqrt{\frac{2U_0}{\pi \alpha_c h_{RF} E_0} \left[\sqrt{\frac{e^2 V_0^2}{U_0^2} - 1} - \arccos\left(\frac{U_0}{eV_0}\right) \right]} \tag{7.8}$$

where U_0 is the energy loss per turn, α_c is the momentum compaction factor, h_{RF} is the harmonic number, E_0 is the nominal electron energy, e is the elementary charge and V_0 is the main cavity voltage. The RF momentum acceptance is constant around the ring.

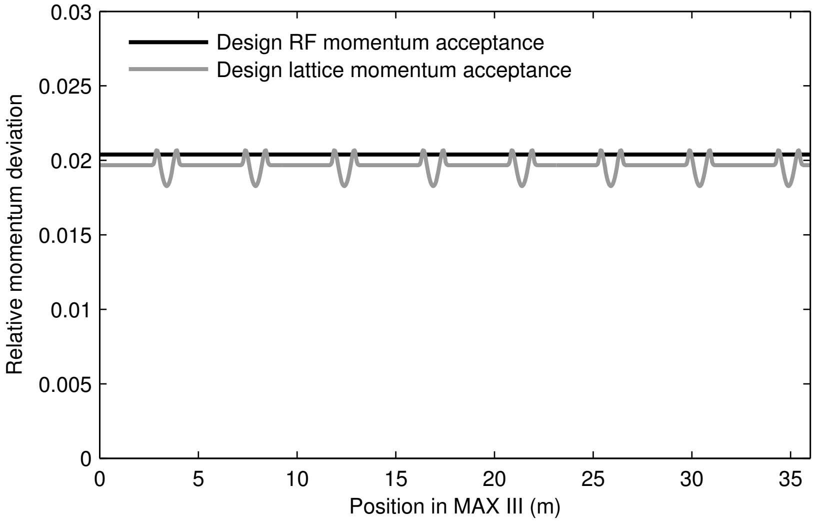

Figure 7.3: *Design RF momentum acceptance and design lattice momentum acceptance as a function of position in MAX III. The design RF momentum acceptance is for a main cavity voltage of 200 kV.*

Figure 7.3 shows the design lattice momentum acceptance of MAX III and the design RF momentum acceptance. For MAX III the lattice momentum acceptance is relatively flat since there is dispersion at all locations in the ring. The design main cavity voltage in MAX III is 200 kV. As can be seen in Fig. 7.3 the design lattice momentum acceptance and the design RF momentum acceptance are similar in magnitude. At most locations the lattice momentum acceptance is more restrictive than the RF momentum acceptance. At these locations a Touschek scattered electron with a sufficiently large momentum change will hit the vacuum chamber wall before it escapes the RF bucket. Figure 7.4 shows the average design lattice momentum acceptance and the RF momentum acceptance of MAX III as a function of the main cavity voltage. The lattice momentum acceptance is not affected by the main cavity voltage. The RF momentum acceptance, however, depends strongly on the main cavity voltage and is zero for $eV_0 \leq U_0$.

7.2 Quantum lifetime

The synchrotron radiation is emitted in discrete units. On average, an electron in MAX III emits around 90 photons per turn. The discrete emission of synchrotron radiation induces noise on the beam and cause the electrons to diffuse. The equilibrium between the quantum excitation and radiation damping determine the distribution of the electrons. In principle, the tails of the distribution will extend to infinity. The vacuum chamber and the momentum

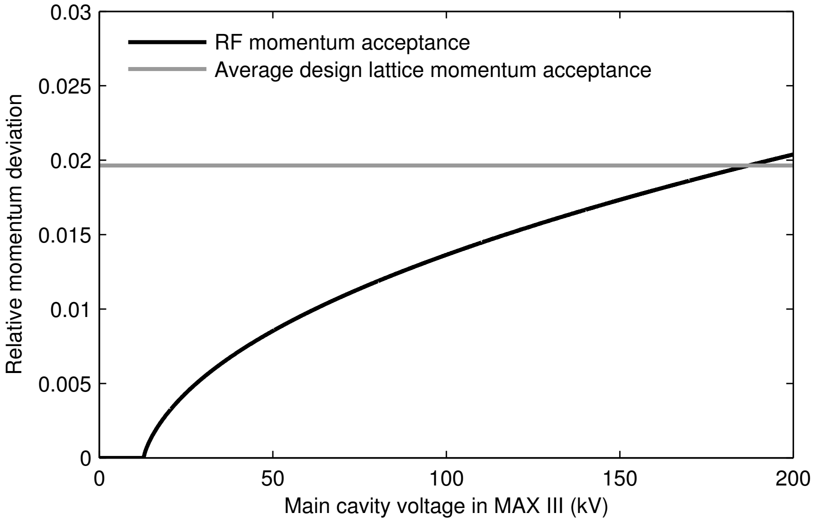

Figure 7.4: *RF momentum acceptance and average design lattice momentum acceptance as a function of the main cavity voltage in MAX III.*

Table 7.1: *Quantum lifetime for a vertical aperture in MAX III.*

a_y/σ_y	$\tau_{quantum}$
4	2.4 seconds
4.5	16 seconds
5	2.3 minutes
5.5	27 minutes
6	6.6 hours
6.5	5.4 days
7	135 days
10	≈ age of the universe

acceptance will however truncate the distribution, which leads to a constant loss of electrons. The resulting lifetime is called the quantum lifetime.

The quantum lifetime for a vertical aperture is given by [15, 40]

$$\tau_{quantum} = \tau_y \frac{\sigma_y^2}{a_y^2} \exp\left(\frac{a_y^2}{2\sigma_y^2}\right) \tag{7.9}$$

where τ_y is the vertical damping time, σ_y is the vertical beam size at the limiting vertical aperture and a_y is the limiting vertical aperture. In Table 7.1 the quantum lifetime is given for different values of a_y/σ_y using MAX III as an example. The vertical damping time in MAX III is 13.1 ms. As can be seen in Table 7.1 the quantum lifetime is several days as long as the limiting vertical aperture is further away than $6.5\sigma_y$. For smaller values of the limiting vertical aperture, the quantum lifetime decreases rapidly. At $4\sigma_y$ the lifetime is only a few seconds. This is a typical behavior for an electron storage ring, where the contribution of the quantum lifetime to the total lifetime is generally negligible as long as a_y/σ_y is 6–7 or larger. For MAX III in normal operating mode a_y/σ_y is 84 and the quantum lifetime for the limiting vertical aperture is practically infinite.

In Eq. (7.9) it is assumed that the vertical dispersion has a negligible influence on the vertical beam size, which is the case for MAX II, MAX III and most other storage rings. For a horizontal aperture the situation is different. At a location where the horizontal dispersion is zero or only has a minor influence on the horizontal beam size, the quantum lifetime for a horizontal aperture is given by Eq. (7.9) with y exchanged with x. At a location where the contribution of the horizontal dispersion and the momentum spread to the horizontal beam size is comparable to the contribution from the horizontal emittance and the horizontal beta function, the quantum lifetime for a horizontal aperture is instead given by [40]

$$\tau_{quantum} = \frac{\tau_x}{\sqrt{2\pi}} \frac{\sigma_x^3}{a_x^3} \exp\left(\frac{a_x^2}{2\sigma_x^2}\right) \frac{\tau_z}{[\tau_x r + \tau_z(1-r)]\sqrt{r(1-r)}} \tag{7.10}$$

where τ_x is the horizontal damping time, σ_x is the horizontal beam size at the limiting horizontal aperture, a_x is the limiting horizontal aperture, τ_z is the longitudinal damping time and

$$r = \frac{\eta_x^2 \sigma_\delta^2}{\sigma_x^2} \tag{7.11}$$

where η_x is the horizontal dispersion at the limiting horizontal aperture and σ_δ is the momentum spread. Sometimes the quantum lifetime for a horizontal aperture is stated as Eq. (7.9) with y exchanged with x irregardless of the value of the horizontal dispersion. The difference between the two equations is typically only relevant as long as a_x/σ_x is 6–7 or smaller. For larger horizontal apertures the quantum lifetime can generally be neglected when determining the total lifetime in an electron storage ring. For MAX III in normal operating mode a_x/σ_x is larger than 39.

For the longitudinal case the quantum lifetime is given by [15]

$$\tau_{quantum} = \tau_z \frac{\sigma_\delta^2}{\delta_{acc}^2} \exp\left(\frac{\delta_{acc}^2}{2\sigma_\delta^2}\right) \tag{7.12}$$

where δ_{acc} is the momentum acceptance. Again, the contribution of the quantum lifetime to the total lifetime is generally negligible as long as $\delta_{acc}/\sigma_\delta$ is 6–7 or larger. For MAX III in normal operating mode $\delta_{acc}/\sigma_\delta$ is 26. The contribution of the quantum lifetime to the total lifetime can thus be neglected for vertical, horizontal as well as longitudinal apertures in MAX III during normal operation. It is only if a vertical or horizontal aperture restriction is inserted close to the beam or if the main cavity voltage is decreased significantly that the quantum lifetime has to be taken into account. The situation in MAX II is similar.

7.3 Elastic scattering lifetime

The elastic scattering of a beam electron on the residual gas nuclei gives rise to a transverse deflection of the stored electron and increases the betatron oscillation amplitude. If the amplitude is larger than the transverse acceptance the scattered electron will be lost. The energy loss of the electron is negligible for elastic scattering on the residual gas nuclei. For elastic scattering on the electrons of the residual gas the situation is different, but as seen later in this section the contribution from elastic scattering on the residual gas electrons to the total elastic scattering lifetime can often be neglected. The elastic scattering lifetime is sometimes also referred to as the Coulomb lifetime.

The vertical acceptance of a storage ring is often smaller than the horizontal acceptance because of the narrow vertical gaps of the insertion device vacuum chambers. The lifetime due to elastic scattering on the residual gas nuclei for a one-dimensional vertically limiting aperture is given by [41]

$$\frac{1}{\tau_{elastic,nuclei}} = cn_g \frac{2\pi r_e^2 Z^2}{\gamma^2} \left[\frac{\langle \beta_y \rangle \beta_y}{a_y^2} \right] \tag{7.13}$$

where c is the speed of light, n_g is the residual gas density, r_e is the classical electron radius, Z is the atomic number of the residual gas, γ is the relativistic factor of the electrons in the stored beam, $\langle \beta_y \rangle$ is the vertical beta function averaged over the storage ring, β_y is the vertical beta function at the limiting vertical aperture and a_y is the limiting vertical aperture. For a one-dimensional horizontally limiting aperture Eq. (7.13) can be used if y is replaced by x.

If the vertical and horizontal acceptances are of comparable magnitude, Eq. (7.13) is not valid. For the case of an elliptical acceptance the lifetime due to elastic scattering on the residual gas nuclei is given by [42]

$$\frac{1}{\tau_{elastic,nuclei}} = cn_g \frac{2\pi r_e^2 Z^2}{\gamma^2} \left[\frac{\langle \beta_y \rangle \beta_y}{a_y^2} + \frac{\langle \beta_x \rangle \beta_x}{a_x^2} \right] \tag{7.14}$$

where $\langle\beta_x\rangle$ is the horizontal beta function averaged over the storage ring, β_x is the horizontal beta function at the limiting horizontal aperture and a_x is the limiting horizontal aperture. If the horizontal acceptance is infinitely large Eq. (7.14) becomes equal to Eq. (7.13), as expected.

For a rectangular acceptance the lifetime due to elastic scattering on the residual gas nuclei is given by [19]

$$\frac{1}{\tau_{elastic,nuclei}} = cn_g \frac{2\pi r_e^2 Z^2}{\gamma^2} \left[\frac{\langle\beta_y\rangle\beta_y}{a_y^2}\right] \frac{F(R)}{\pi} \tag{7.15}$$

where the function $F(R)$ is given by

$$F(R) = \pi + (R^2+1)\sin(2\arctan R) + 2(R^2-1)\arctan R \tag{7.16}$$

and R is given by

$$R = \sqrt{\frac{\langle\beta_x\rangle\beta_x a_y^2}{\langle\beta_y\rangle\beta_y a_x^2}} \tag{7.17}$$

In Eqs. (7.15)–(7.17) it is assumed that R is smaller than one, i.e. that the maximum allowed scattering angle is smaller in the vertical direction than in the horizontal direction. If this is not the case, Eqs. (7.15)–(7.17) can be used with exchanged y and x. If the horizontal acceptance is infinitely large $F(R)/\pi$ becomes equal to one and Eq. (7.15) becomes equal to Eq. (7.13), as expected.

Which of the three different equations for the elastic scattering on the residual gas nuclei should be used depends on the properties of the storage ring. For MAX II and Paper **I** the vertical and horizontal acceptances are rectangular and almost equal, which makes Eqs. (7.15)–(7.17) suitable. For MAX III and Paper **IV** the vertical acceptance is more than 30 times smaller than the horizontal acceptance and Eq. (7.13) can be used.

As mentioned above, the electrons in the beam do not only scatter elastically on the nuclei of the residual gas. They can also scatter on the electrons of the residual gas. The lifetime due to elastic scattering on the residual gas electrons is given by [41]

$$\frac{1}{\tau_{elastic,electrons}} = cn_g \frac{2\pi r_e^2 Z}{\gamma} \frac{1}{\delta_{acc}} \tag{7.18}$$

where δ_{acc} is the momentum acceptance. The cross section for elastic scattering on the residual gas electrons is typically much smaller than the cross section for elastic scattering on the residual gas nuclei and the lifetime is thus typically much longer. For MAX II and Paper **I** the lifetime from elastic scattering on the electrons is more than 30 times longer than the lifetime from elastic scattering on the nuclei. For MAX III and Paper **IV** the rest gas composition is unknown, but for a residual gas composition similar to MAX II the lifetime from elastic scattering on the electrons would be more than 100 times longer than the lifetime from elastic scattering on the nuclei. Even if the residual gas in MAX III would be only hydrogen, the lifetime from elastic scattering on the electrons would still be about 40 times longer than the lifetime from elastic scattering on the nuclei. The effect on the total elastic scattering lifetime from elastic scattering on the residual gas electrons can thus be neglected and the total elastic scattering lifetime is given by

$$\frac{1}{\tau_{elastic}} = \frac{1}{\tau_{elastic,nuclei}} + \frac{1}{\tau_{elastic,electrons}} \approx \frac{1}{\tau_{elastic,nuclei}} \tag{7.19}$$

7.4 Inelastic scattering lifetime

The inelastic scattering lifetime is sometimes also referred to as the bremsstrahlung lifetime, since a bremsstrahlung photon is emitted when the beam electron scatter inelastically on the residual gas nuclei. The transverse deflection of the stored electron is negligible for the inelastic scattering process, but the energy loss can be significant. If the energy loss exceeds the momentum acceptance of the storage ring the electron will be lost.

The lifetime due to inelastic scattering on the residual gas nuclei is given by [43]

$$\begin{aligned}\frac{1}{\tau_{inelastic,nuclei}} = cn_g 4\alpha r_e^2 Z^2 \Bigg\{ \ln\left(\frac{183}{Z^{1/3}}\right) \frac{4}{3} \left[\ln\left(\frac{1}{\delta_{acc}}\right) - \frac{5}{8} \right] \\ + \frac{1}{9} \left[\ln\left(\frac{1}{\delta_{acc}}\right) - 1 \right] \Bigg\}\end{aligned} \tag{7.20}$$

where c is the speed of light, n_g is the residual gas density, r_e is the classical electron radius, α is the fine-structure constant, Z is the atomic number of the residual gas and δ_{acc} is the momentum acceptance.

The electrons in the beam can also scatter inelastically on the electrons of the residual gas. The lifetime due to inelastic scattering on the residual gas electrons is given by [43]

$$\frac{1}{\tau_{inelastic,electrons}} = cn_g 4\alpha r_e^2 Z \left\{ \ln\left(\frac{1194}{Z^{2/3}}\right) \frac{4}{3}\left[\ln\left(\frac{1}{\delta_{acc}}\right) - \frac{5}{8}\right] + \frac{1}{9}\left[\ln\left(\frac{1}{\delta_{acc}}\right) - 1\right]\right\} \tag{7.21}$$

For the elastic scattering lifetime (see Sec. 7.3) the contribution from the scattering on the residual gas electrons was negligible. For the inelastic scattering, however, that is not the case. For MAX II and Paper **I** the lifetime from inelastic scattering on the electrons is only 1.9 times longer than the lifetime from inelastic scattering on the nuclei. For the case of a residual gas consisting of hydrogen the lifetime from inelastic scattering on the electrons is even 25% shorter than the lifetime from inelastic scattering on the nuclei. For a residual gas consisting of nitrogen the contribution from the scattering on the electrons is smaller and the lifetime from inelastic scattering on the electrons is approximately 5.5 times longer than the lifetime from inelastic scattering on the nuclei. For MAX II, where the residual gas in dominated by hydrogen (see Paper **I**) and MAX III, where the situation is believed to be similar, the contribution from the inelastic scattering on the residual gas electrons should thus be included. The total inelastic scattering lifetime is then given by

$$\begin{aligned}\frac{1}{\tau_{inelastic}} &= \frac{1}{\tau_{inelastic,nuclei}} + \frac{1}{\tau_{inelastic,electrons}} = \\ &= cn_g 4\alpha r_e^2 \left\{ \left[Z^2 \ln\left(\frac{183}{Z^{1/3}}\right) + Z \ln\left(\frac{1194}{Z^{2/3}}\right)\right] \frac{4}{3}\left[\ln\left(\frac{1}{\delta_{acc}}\right) - \frac{5}{8}\right] \right. \\ &\quad \left. + \frac{Z(Z+1)}{9}\left[\ln\left(\frac{1}{\delta_{acc}}\right) - 1\right]\right\}\end{aligned} \tag{7.22}$$

7.5 Touschek lifetime

If two electrons inside an electron bunch collide, some of the transverse momentum may be transferred into longitudinal momentum. If all of the transverse momentum would be transferred into longitudinal momentum, the longitudinal momentum would, in the laboratory frame, approximately be the transverse momentum multiplied by the relativistic factor γ. For MAX III γ is around 1370, which means the longitudinal momentum will receive a significant boost. The Touschek scattered electron can gain or lose longitudinal momentum from the scattering process. If the momentum deviation exceeds the momentum acceptance of the storage ring the electron will be lost.

Several different models exists that describe the Touschek lifetime. In order to be consistent with Paper **IV** the model described below is the model used by OPA [44] and ZAP [45] for the calculation of the linear Touschek lifetime. The transverse motion is in this approximation assumed to be non relativistic and the horizontal betatron motion is assumed to be the only source of Touschek scattering. The Touschek lifetime is then given by [45, 46]

$$\frac{1}{\tau_{Touschek}} = \frac{r_e^2 c N_b}{8\pi\gamma^3\sigma_z}\frac{1}{C}\oint \frac{F\left(\left[\frac{\delta_{acc}(s)}{\gamma\sigma_{x'}(s)}\right]^2\right)}{\sigma_x(s)\sigma_y(s)\sigma_{x'}(s)\left[\delta_{acc}(s)\right]^2}\mathrm{d}s \tag{7.23}$$

where r_e is the classical electron radius, c is the speed of light, N_b is the number of electrons per bunch, γ is the relativistic factor of the electrons in the stored beam, σ_z is the bunch length and C is the circumference of the ring. For the parameters that vary around the ring an integration is performed to obtain the Touschek lifetime. $\sigma_x(s)$ is the horizontal beam size given by

$$\sigma_x(s) = \sqrt{\epsilon_x\beta_x(s) + \left[\sigma_\delta\eta_x(s)\right]^2} \tag{7.24}$$

where ϵ_x is the horizontal emittance, $\beta_x(s)$ is the horizontal beta function, σ_δ is the momentum spread and $\eta_x(s)$ is the horizontal dispersion function. Since the beam is assumed to be flat there is no vertical dispersion and the vertical beam size $\sigma_y(s)$ is given by

$$\sigma_y(s) = \sqrt{\epsilon_y\beta_y(s)} \tag{7.25}$$

where ϵ_y is the vertical emittance and $\beta_y(s)$ is the vertical beta function. $\sigma_{x'}(s)$ is the horizontal beam divergence for $x \approx 0$ given by

$$\sigma_{x'}(s) = \frac{\epsilon_x}{\sigma_x(s)}\sqrt{1 + \frac{\mathcal{H}(s)\sigma_\delta^2}{\epsilon_x}} \tag{7.26}$$

where $\mathcal{H}(s)$ is the $\mathcal{H}$ function. $\delta_{acc}(s)$ is the momentum acceptance given by

$$\delta_{acc}(s) = \min\left(\delta_{acc}^{RF},\ \delta_{acc}^{L}(s)\right) \tag{7.27}$$

where δ_{acc}^{RF} is the RF momentum acceptance and $\delta_{acc}^{L}(s)$ is the lattice momentum acceptance. $F(\zeta)$ is a special function defined by

$$F(\zeta) = \int_0^1 \left(\frac{1}{u} - \frac{1}{2} \ln \frac{1}{u} - 1 \right) \exp\left(-\frac{\zeta}{u} \right) \mathrm{d}u \tag{7.28}$$

In the OPA calculations of the Touschek lifetime the horizontal and vertical emittance is given by the natural horizontal emittance and the emittance coupling factor. The momentum spread is given by the natural momentum spread and the bunch length is given by the natural bunch length. The RF momentum acceptance is given by Eq. (7.8) and the lattice momentum acceptance by Eq. (7.7).

For the calculation of the Touschek lifetime in ZAP the user specifies the values of the horizontal and vertical emittance, the momentum spread and the bunch length. The RF momentum acceptance is given by Eq. (7.8), but the user can specify a fixed momentum acceptance to be used in the calculations. ZAP however uses a different definition of the lattice momentum acceptance than the standard relation given in Eq. (7.7). In ZAP, the lattice momentum acceptance at location s_0 is given by [45]

$$\delta_{acc}^{L,\text{ZAP}}(s_0) = \pm \min \left(\frac{a_x(s)}{\sqrt{\mathcal{H}(s_0)\beta_x(s) + \left[\eta_x(s)\right]^2}} \right) \tag{7.29}$$

where $a_x(s)$ is the horizontal aperture and $\mathcal{H}(s_0)$ is the $\mathcal{H}$ function at location s_0. As long as the momentum acceptance is given by the RF momentum acceptance or a constant momentum acceptance, ZAP provides more freedom in the input parameters and will give a better estimate of the Touschek lifetime. But to study the influence on the Touschek lifetime from the lattice momentum acceptance OPA is better equipped. In Chapter 8 and in Paper **IV** the Touschek lifetime calculations are primarily performed using OPA.

The approximate expression in Eq. (7.23) is sufficient for most applications. If a more precise estimate is needed a Monte Carlo simulation can be performed. No such simulation has been performed for MAX II or MAX III, but simulations have been performed at other synchrotron light sources. For BESSY II the Touschek lifetime calculated using a relativistic Monte Carlo simulation was about 10% shorter than the lifetime calculated using ZAP [47].

CHAPTER 8

MEASURING THE LIFETIMES AND ACCEPTANCES

The lifetimes and acceptances of an electron storage ring were described in Chapter 7. This chapter will look into how the individual lifetime limiting effects and the acceptances can be determined from measurements of the total lifetime. In order to separate the lifetime limiting effects measurements are performed where the total lifetime is measured while keeping all parameters in the storage ring, except one, constant. In Sec. 8.1 vertical scraper measurements are described, where the total lifetime is measured for different positions of the vertical scraper. Section 8.2 describes horizontal scraper measurements, where it is instead the effect on the total lifetime from the position of the horizontal scraper that is studied. Finally, Sec. 8.3 describes measurements of the total lifetime as a function of the main cavity voltage in the storage ring.

Other common methods to determine the lifetimes are by studying the total lifetime for different values of the stored current or for different filling patterns. The vacuum lifetime, i.e. the combined elastic and inelastic scattering lifetimes, is inversely proportional to the residual gas density, and the residual gas density generally depend on the total stored current in the storage ring. The Touschek lifetime, on the other hand, is inversely proportional to the stored current per bunch. This difference can be used to separate the Touschek lifetime from the vacuum lifetime. For example, if the total stored current is kept constant but the filling pattern, and thus the current per bunch, is varied the vacuum lifetime should in principle be constant while the Touschek lifetime should vary inversely with the current per bunch. However, measurements of this kind assume that the bunch volume is independent of the stored current and the filling pattern. If that is not the case the Touschek lifetime will also be affected by the change in bunch volume, which will complicate the measurements. For MAX II and MAX III the Landau cavities give rise to a current-dependent bunch volume. For MAX III the situation is further complicated by the longitudinal instabilities, which have been observed to be current-dependent and vary for different filling patterns and even from fill to fill. Additionally, the standard operation of the MAX-lab injection system does not allow a detailed control of the filling pattern of the storage rings. Because of these complications, lifetime measurements for varying stored current or filling patterns have not been pursued for MAX II and MAX III.

8.1 Lifetime vs. vertical scraper position

A vertical scraper is a movable vertical aperture restriction. During normal operation, the scraper is positioned far from the beam so that it does not limit the total lifetime or the vertical acceptance. In a vertical scraper measurement the total lifetime in the storage ring is studied for different positions of the vertical scraper. Ideally, the variation of the stored current in the storage ring during the measurement should be small in order not to introduce current-dependent lifetime effects.

Figure 8.1 shows an example of a vertical scraper measurement. The measurement data is taken from Fig. 7 in Paper **IV**. The quantum lifetime, the elastic scattering lifetime, the inelastic scattering lifetime, the Touschek lifetime and the total lifetime in MAX III are shown as a function of the distance between the vertical scraper and the beam center. The main cavity voltage is kept constant at 130 kV. The stored current is around 300 mA. In the example it is assumed that vertical scraper does not affect the lattice momentum acceptance of MAX III, that the current is constant and the residual gas composition is identical to the residual gas composition in MAX II, i.e. 94.6% H_2, 2.2% H_2O, 2.6% CO and 0.6% CO_2 (see Paper **I**).

The quantum lifetime in Fig. 8.1 is calculated using Eq. (7.9). At the location of the vertical scraper the vertical beam size is around 16 µm. As long as the vertical scraper is further than 0.1 mm from the beam center the contribution from the quantum lifetime to the total lifetime is negligible.

The elastic scattering lifetime for a one-dimensional vertically limiting aperture is given by Eq. (7.13). For an elliptical acceptance the elastic scattering lifetime is given by Eq. (7.14), and for a rectangular acceptance it is given by Eqs. (7.15)–(7.17). For MAX III the vertical acceptance is more than 30 times smaller than the horizontal acceptance. In Fig. 8.1 the elastic scattering lifetime is shown for the three different models. The residual gas density is assumed to be constant. Since the vertical acceptance is significantly smaller than the horizontal acceptance all three models give similar results. The elastic lifetime increases quadratically, or close to quadratically for the elliptical and rectangular model, up until the point where the vertical scraper is about 1.3 mm away from the beam center. At this point the vertical scraper is no longer the limiting vertical aperture, and for scraper positions further away than about 1.3 mm

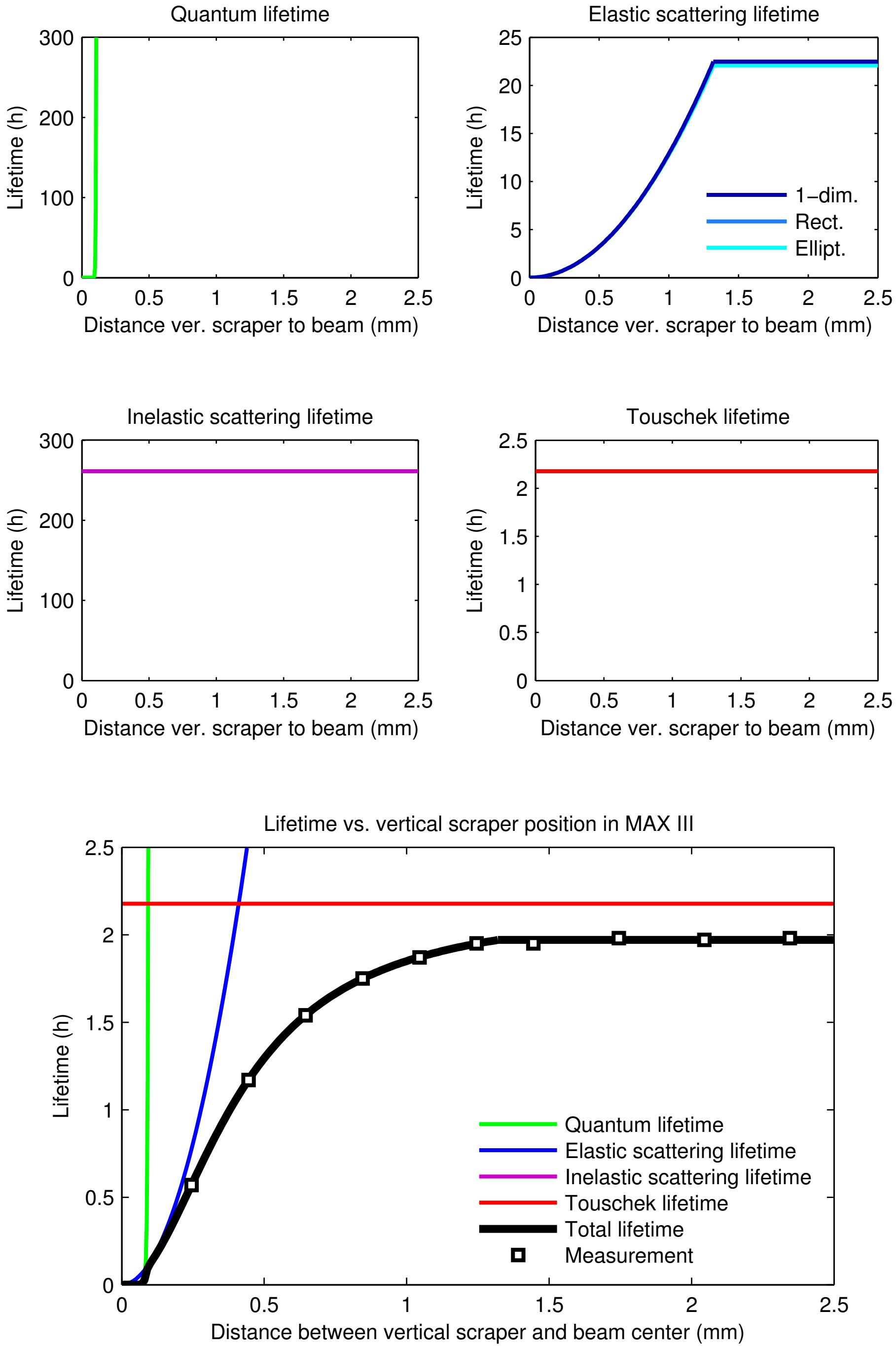

Figure 8.1: *Example of a vertical scraper measurement. The quantum lifetime, elastic and inelastic scattering lifetimes, Touschek lifetime and the total lifetime in MAX III are shown as a function of the distance between the vertical scraper and the beam center. The measurement data is taken from Fig. 7 in Paper* ***IV****. For the example the vertical scraper is assumed not to influence the momentum acceptance.*

from the beam center the vertical acceptance and thus the elastic scattering lifetime remains constant.

The inelastic scattering lifetime is given by Eq. (7.22). In Fig. 8.1 it is assumed that the vertical scraper does not affect the lattice momentum acceptance and that the residual gas density is constant. As long as that is valid the inelastic scattering lifetime will remain constant during a vertical scraper measurement.

The Touschek lifetime in Fig. 8.1 is independent of the position of the vertical scraper. For this to be valid the vertical scraper should not affect the lattice momentum acceptance. In order to keep the Touschek lifetime constant, the main cavity voltage should be kept constant during a vertical scraper measurement in order not to affect the RF momentum acceptance and the bunch length. Other parameters such as the current and the transverse beam sizes are also assumed to be constant.

The total lifetime in Fig. 8.1 is given by Eq. (7.2), i.e. the combination of the four different lifetime limitations. Figure 8.1 also shows measurement data taken from Fig. 7 in Paper **IV**. Since the total lifetime in MAX III at 300 mA is relatively short the measurement only consists of 10 measurement points in order to keep the current variation during the measurement as low as possible. The smallest distance between the vertical scraper and the beam center was about 0.25 mm. If the vertical scraper is moved closer than 0.25 mm away from the beam center, measurements of the lifetime as a function of the main cavity voltage have shown that the vertical scraper influences the lattice momentum acceptance of MAX III. As long as the vertical scraper is 0.25 mm or further away from the beam center it is only the elastic scattering lifetime that is affected by the vertical scraper. Since the three models for the elastic scattering lifetime give similar results for MAX III, the simple one-dimensional model can be used. The total lifetime for a vertical scraper measurement is then given by

$$\frac{1}{\tau_{tot}} = C_1 + C_2 \frac{\beta_y}{a_y^2} \tag{8.1}$$

where C_1 and C_2 are constants. The vertical acceptance a_y^2/β_y is constant until the scraper becomes the limiting aperture. When the scraper is the limiting aperture, a_y is the distance between the vertical scraper and the beam center and β_y is the vertical beta function at the scraper location. Since the lattice momentum acceptance is not influenced by the vertical scraper (for $a_y > 0.25$ mm) the position where the scraper starts to influence the total lifetime can be used to determine the vertical acceptance of the storage ring. By performing a fit to Eq. (8.1) for the measurement data the constants C_1 and C_2 can be determined. The elastic scattering lifetime when the scraper is far out is then given by the vertical acceptance divided by C_2. The constant C_2 determined by the fit is given by

$$C_2 = cn_g \frac{2\pi r_e^2 Z^2 \langle \beta_y \rangle}{\gamma^2} \tag{8.2}$$

where c is the speed of light, n_g is the residual gas density, r_e is the classical electron radius, Z is the atomic number of the residual gas, $\langle \beta_y \rangle$ is the vertical beta function averaged over the storage ring and γ is the relativistic factor of the electrons in the stored beam. If the residual gas composition is known the residual gas density can be determined from Eq. (8.2). The residual gas density can then be used to determine the inelastic scattering lifetime from Eq. (7.22). The constant C_1 determined by the fit is given by

$$C_1 = \frac{1}{\tau_{inelastic}} + \frac{1}{\tau_{Touschek}} \tag{8.3}$$

where $\tau_{inelastic}$ is the inelastic scattering lifetime and $\tau_{Touschek}$ is the Touschek lifetime. If the inelastic scattering lifetime has been determined using the residual gas density the Touschek lifetime can then be determined using Eq. (8.3).

In summary, a vertical scraper measurement can thus by itself in principle be used to determine the elastic scattering lifetime, the vertical acceptance and the combined inelastic scattering and Touschek lifetime in a storage ring. If the residual gas composition is known the inelastic scattering lifetime and the Touschek lifetime can also be determined.

Figure 8.2 shows two examples of vertical scraper measurements performed at MAX II at different vacuum conditions. The examples are from MAX II before and after the vacuum system was vented for the installation of a NEG-coated dipole vacuum chamber. For the measurement with bad vacuum conditions the elastic scattering lifetime has a larger effect on the total lifetime. The total lifetime increases more slowly as the vertical scraper moves away from the beam and the position where the vertical scraper no longer influences the elastic scattering lifetime, and thus the total lifetime, can clearly be seen about 4.5 mm away from the beam center. For the measurement with good vacuum conditions the total lifetime increases faster as the vertical scraper moves away from the beam and it is hard to locate the position where the scraper no longer affects the lifetime.

8.2 Lifetime vs. horizontal scraper position

The principle of a horizontal scraper measurement is similar to a vertical scraper measurement, but because of the horizontal dispersion the lifetimes are influenced differently by a horizontal scraper than by a vertical scraper. During normal operation, the horizontal scraper is positioned far from the beam so

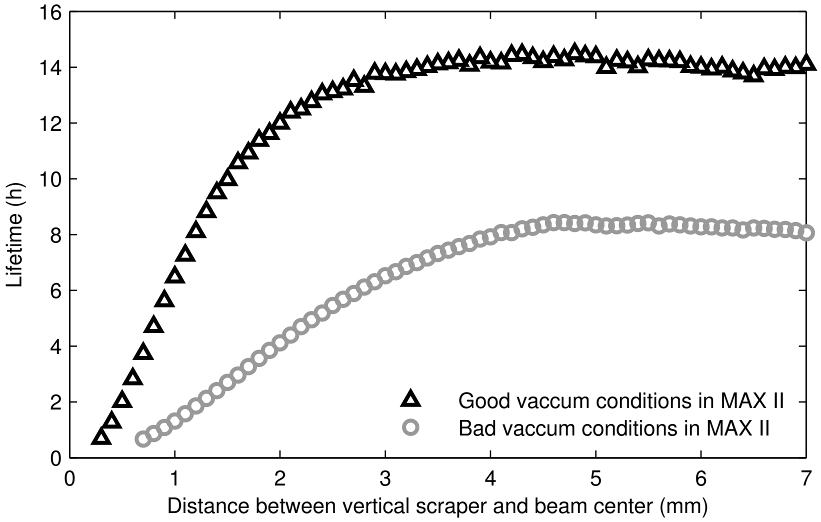

Figure 8.2: *Two examples of vertical scraper measurements used for Fig. 3 and Fig. 4 in Paper* ***I****. The total lifetime in MAX II is shown as a function of the distance between the vertical scraper and the beam center. The measurements were performed at similar stored currents in April 2009 before and after the vacuum system of MAX II was vented.*

that is does not limit the total lifetime, the horizontal acceptance or the lattice momentum acceptance. As for the vertical scraper measurement, the variation of the stored current in the storage ring during the a horizontal scraper measurement should be small in order not to introduce current-dependent lifetime effects.

Figure 8.3 shows an example of a horizontal scraper measurement. The measurement data is taken from Fig. 12 in Paper **IV**. The quantum lifetime, the elastic scattering lifetime, the inelastic scattering lifetime, the Touschek lifetime and the total lifetime in MAX III are shown as a function of the distance between the vertical scraper and the beam center. The main cavity voltage is kept constant at 108 kV. The stored current is around 300 mA. In the example it is assumed that the cavity absorber determines the horizontal acceptance and the lattice momentum acceptance and that it is located 10.6 mm from the center of the beam. It is also assumed that the current is constant, that the residual gas composition is identical to the residual gas composition in MAX II, i.e. 94.6% H_2, 2.2% H_2O, 2.6% CO and 0.6% CO_2 (see Paper **I**) and that the residual gas density is the same as for the example in Fig. 8.1.

The quantum lifetime in Fig. 8.3 is calculated using Eq. (7.10). At the location of the horizontal scraper the horizontal beam size is around 350 µm. The contribution of the horizontal dispersion and the momentum spread to the horizontal beam size at the location of the horizontal scraper is almost the same as the contribution from the horizontal emittance and the horizontal

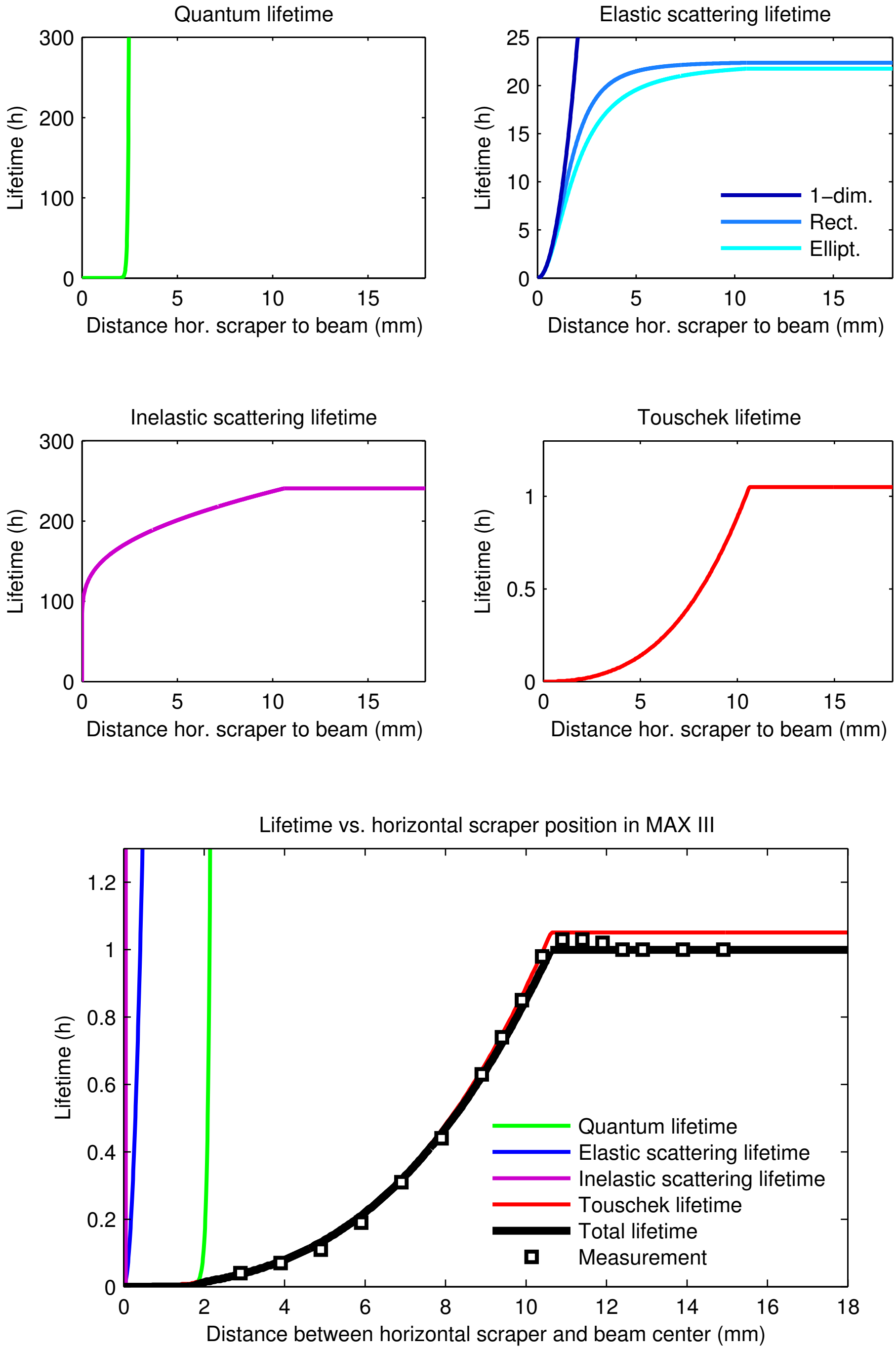

Figure 8.3: *Example of a horizontal scraper measurement. The quantum lifetime, elastic and inelastic scattering lifetimes, Touschek lifetime and the total lifetime in MAX III are shown as a function of the distance between the horizontal scraper and the beam center. The measurement data is taken from Fig. 12 in Paper* **IV***. The cavity absorber is assumed to be located 10.6 mm from the center of the beam.*

beta function. As long as the horizontal scraper is further away than 2 mm from the beam center the contribution from the quantum lifetime to the total lifetime is negligible.

The elastic scattering lifetime for a one-dimensional horizontally limiting aperture is given by Eq. (7.13) if y is replaced by x. For an elliptical acceptance the elastic scattering lifetime is given by Eq. (7.14). For a rectangular acceptance it is given by Eqs. (7.15)–(7.17) as long as the maximum allowed scattering angle is smaller in the vertical direction than in the horizontal direction, and by Eqs. (7.15)–(7.17) with exchanged y and x when the maximum allowed scattering angle is smaller in the horizontal direction than in the vertical direction. In Fig. 8.3 the elastic scattering lifetime is shown for the three different models. The residual gas density is assumed to be constant. For MAX III the horizontal acceptance is more than 30 times larger than the vertical acceptance. Since the horizontal acceptance is much larger than the vertical acceptance the three models give results that differ significantly from each other. The assumption of a one-dimensional horizontally limiting aperture is not valid except when the horizontal scraper is so close to the beam that all the electrons have already been lost from the low quantum lifetime. The elliptical and rectangular models both asymptotically approach the elastic lifetime as given by a one-dimensional vertically restricting aperture. When the horizontal scraper is further away than about 10.6 mm from the beam center the cavity absorber is the limiting horizontal aperture. For scraper positions further away than about 10.6 mm from the beam center the horizontal acceptance and thus the elastic scattering lifetime remains constant.

The inelastic scattering lifetime in Fig. 8.3 is calculated using Eq. (7.22). In the calculation the momentum acceptance is assumed to be equal to the average momentum acceptance around the ring. When the horizontal scraper is far from the beam, the lattice momentum acceptance is determined by the cavity absorber. The RF momentum acceptance at 108 kV main cavity voltage is larger than the lattice momentum acceptance, and the momentum acceptance around the ring is thus only given by the lattice momentum acceptance. For scraper positions further away than about 10.6 mm from the beam center the momentum acceptance is determined by the cavity absorber and the inelastic scattering lifetime remains constant. For scraper positions closer than about 10.6 mm away from the beam center the horizontal scraper determines the momentum acceptance, and the inelastic scattering lifetime decreases if the scraper is moved closer to the beam. The lifetime decrease is slow until the scraper is about 1 mm away from the beam center, by which time all the electrons have already been lost from the low quantum lifetime.

The Touschek lifetime in MAX III was determined in Paper **IV** based on vertical scraper measurements. Calculations of the Touschek lifetime using OPA gave a Touschek lifetime 2.7 times smaller than the measured Touschek lifetime (the OPA calculation does not take the bunch lengthening from the Landau cavities and the increased momentum spread from the instabilities into account). The Touschek lifetime in Fig. 8.3 was determined by multiplication of Touschek

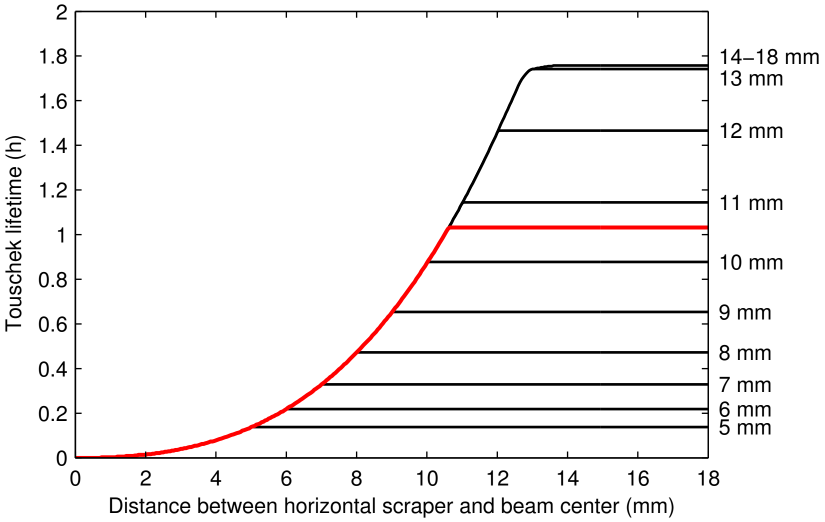

Figure 8.4: *Calculations of the Touschek lifetime in MAX III as a function of the distance between the horizontal scraper and the beam center for different positions of the cavity absorber. The main cavity voltage for the calculations is 108 kV. The red line line corresponds to the cavity absorber at 10.6 mm.*

lifetime calculations using OPA with the scaling factor 2.7. In a similar way as for the inelastic scattering lifetime, the momentum acceptance is determined by the cavity absorber for scraper positions further than about 10.6 mm from the beam center and the Touschek lifetime is constant. For scraper positions closer than about 10.6 mm from the beam center the horizontal scraper determines the momentum acceptance, and the Touschek lifetime decreases if the scraper is moved closer to the beam. The lifetime decrease when the horizontal scraper starts to limit the momentum acceptance creates a sharp edge in the Touschek lifetime curve.

The total lifetime in Fig. 8.3 is given by Eq. (7.2), i.e. the combination of the four different lifetime limitations. Figure 8.3 also shows measurement data taken from Fig. 12 in Paper **IV**. All four lifetime limitations are affected by the horizontal scraper. It is thus not possible to fit a simple model to the measurement data, as was the case for the vertical scraper measurement (see Sec. 8.1). However, for MAX III the Touschek lifetime is the dominating lifetime limitation, which makes horizontal scraper measurements a possible method to study the Touschek lifetime.

Figure 8.4 shows an example of the Touschek lifetime as a function of the horizontal scraper position for several different positions of the cavity absorber. The Touschek lifetime is calculated with OPA using the same settings as in Fig. 8.3, except the location of the cavity absorber, and scaled with the scaling factor 2.7. The red line corresponds to the cavity absorber at 10.6 mm,

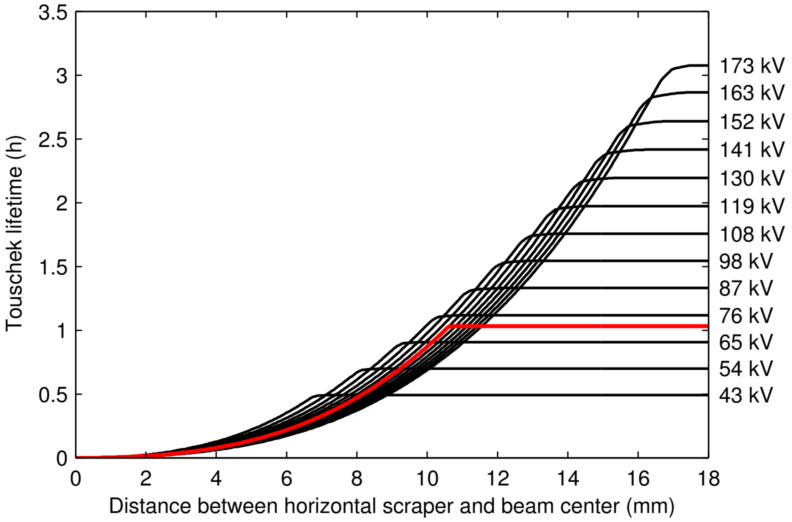

Figure 8.5: *Calculations of the Touschek lifetime in MAX III as a function of the distance between the horizontal scraper and the beam center for different main cavity voltages. The horizontal apertures are assumed to be the design apertures for the black lines. The red line corresponds to a main cavity voltage of 108.3 kV and the cavity absorber at 10.6 mm.*

i.e. the same calculation as shown in Fig. 8.3. The RF momentum acceptance is assumed to be given by Eq. (7.8), i.e. the influence from the Landau cavities is neglected. If the cavity absorber is around 12 mm away from the beam or closer the momentum acceptance is given by the lattice momentum acceptance only. There is a sharp edge in the horizontal scraper measurements when the horizontal scraper is moved towards the beam center and it abruptly starts to limit the momentum acceptance instead of the cavity absorber. The sensitivity of the lattice momentum acceptance and the Touschek lifetime to a horizontal aperture restriction was used in Paper **IV** to pinpoint where in MAX III the aperture restriction was located. The main cavity voltage in the example is 108 kV. If the cavity absorber is around 14 mm or further away from the beam it does not influence the momentum acceptance, since the RF momentum acceptance is more limiting. The edge in the horizontal scraper measurement is noticeably softer, since the momentum acceptance is RF limited until the scraper starts to influence it through the lattice momentum acceptance. For scraper positions between 14 and 12 mm away from the beam center, the momentum acceptance is given by the lattice momentum acceptance in certain parts of the ring and the RF momentum acceptance in other parts of the ring.

Figure 8.5 shows an example of the Touschek lifetime as a function of the horizontal scraper position for the design apertures and several different main cavity voltages. The Touschek lifetime is calculated with OPA using the same settings as in Fig. 8.3, except the main cavity voltage and the location of the cavity absorber, and scaled with the scaling factor 2.7. The red line corresponds to 108 kV main cavity voltage and the cavity absorber at 10.6 mm, i.e. the same calculation as shown in Fig. 8.3. The design position of the cavity absorber is 18 mm away from the beam center. The RF momentum acceptance is assumed to be given by Eq. (7.8). As seen in Fig. 8.5 the main cavity voltage has a large influence on the horizontal scraper measurement. A larger main cavity voltage will give a shorter bunch length and a shorter Touschek lifetime. A larger main cavity voltage will also give a larger RF momentum acceptance and, as long as the lattice momentum acceptance is sufficiently large, a longer Touschek lifetime. The effect of the main cavity voltage on the total lifetime is discussed in Sec. 8.3.

The horizontal scraper position that starts to influence the lattice momentum acceptance, and thus the Touschek lifetime if the momentum acceptance is not RF limited, is not necessarily the same scraper position that starts to influence the horizontal (on-momentum) acceptance, and thus the elastic scattering lifetime. For the example in Fig. 8.3 it was the cavity absorber in the main cavity straight section (at 10.6 mm) that determined the lattice momentum acceptance around the ring as well as the horizontal acceptance. The horizontal beta function and the horizontal dispersion function are similar at the location of the cavity absorber and at the location of the horizontal scraper. The scraper will start to limit both the lattice momentum acceptance and the horizontal acceptance at around 10.6 mm. For the present settings in MAX III, after moving the main cavity and the cavity absorber, it is unknown where the new horizontal restriction is located. Figure 14 in Paper **IV** shows the horizontal apertures around the ring that would give the same average lattice momentum acceptance as the horizontal scraper when it is 14.2 mm away from the beam center. As an example, an aperture in the middle of the dipole in cell 4 ($s = 16.9$ m) would need to be 4.0 mm away from the beam center to give the same average lattice momentum acceptance. Such an aperture in the middle of dipole 4 would give a horizontal acceptance of 58×10^{-6} m. The horizontal scraper would start to limit the horizontal acceptance 15.6 mm away from the beam center and the lattice momentum acceptance 14.2 mm away from the beam center. Since the vertical acceptance is so small in MAX III, the effect on the elastic scattering lifetime from a horizontal scraper located 15.6 mm away from the beam center is small and the effect on the total lifetime would be difficult to detect. From a horizontal scraper measurement in MAX III it is thus not possible to conclude what the horizontal acceptance is as long as the Touschek lifetime is the dominating lifetime limitation.

In summary, a horizontal scraper measurement affects the quantum lifetime, the elastic and inelastic scattering lifetimes as well as the Touschek lifetime. When the horizontal scraper is the limiting horizontal aperture, it will affect the horizontal acceptance and thus the elastic scattering lifetime and the quantum lifetime. When the horizontal scraper limits the lattice momentum acceptance, it might (depending on the RF momentum acceptance) also affect the momentum acceptance and thus the inelastic scattering lifetime and the Touschek lifetime. The scraper position where the scraper becomes the limiting horizontal aperture is not necessarily the same as the position where is starts to influence the lattice momentum acceptance. Still, as seen in Paper **IV**, horizontal scraper measurements can be a useful tool in investigating the properties of a storage ring, but a careful analysis should be done to determine which lifetimes and acceptances are mainly affected by the horizontal scraper.

8.3 Lifetime vs. main cavity voltage

The lifetime limitations can also be studied by varying the main cavity voltage. Ideally, the variation of the stored current in the storage ring during the measurement should be small in order not to introduce current-dependent lifetime effects. When the main cavity voltage is changed, the RF momentum acceptance will be affected. The lattice momentum acceptance as well as the vertical and horizontal acceptances will however not be affected. If the dynamic lattice momentum acceptance is smaller than the linear lattice momentum acceptance, it will influence the results. In this chapter, only the linear lattice momentum acceptance (as given by Eq. (7.7)) is considered. The RF momentum acceptance is assumed to be given by Eq. (7.8), i.e. the influence from the Landau cavities is neglected.

Figure 8.6 shows an example of a lifetime vs. main cavity voltage measurement. The measurement data is taken from the measured total lifetime used for Fig. 13 in Paper **IV**. The quantum lifetime, the elastic scattering lifetime, the inelastic scattering lifetime, the Touschek lifetime and the total lifetime in MAX III are shown as a function of the main cavity voltage. The stored current is around 300 mA. In the example it is assumed that the cavity absorber determines the lattice momentum acceptance and that it is located 10.6 mm away from the center of the beam. It is also assumed that the current is constant, that the residual gas composition is identical to the residual gas composition in MAX II, i.e. 94.6% H_2, 2.2% H_2O, 2.6% CO and 0.6% CO_2 (see Paper **I**) and that the residual gas density is the same as for the examples in Fig. 8.1 and Fig. 8.3.

The quantum lifetime in Fig. 8.6 is calculated using Eq. (7.12). The momentum acceptance is given by the RF momentum acceptance and the momentum spread is assumed to be the natural momentum spread. As long as the main cavity voltage is larger than 23 kV the contribution from the quantum lifetime to the total lifetime is negligible.

The elastic scattering lifetime is affected by the vertical and horizontal acceptance, but not by the momentum acceptance. Since the main cavity voltage only affects the momentum acceptance the elastic scattering lifetime in Fig. 8.6 is constant.

The inelastic scattering lifetime is given by Eq. (7.22). In the calculation

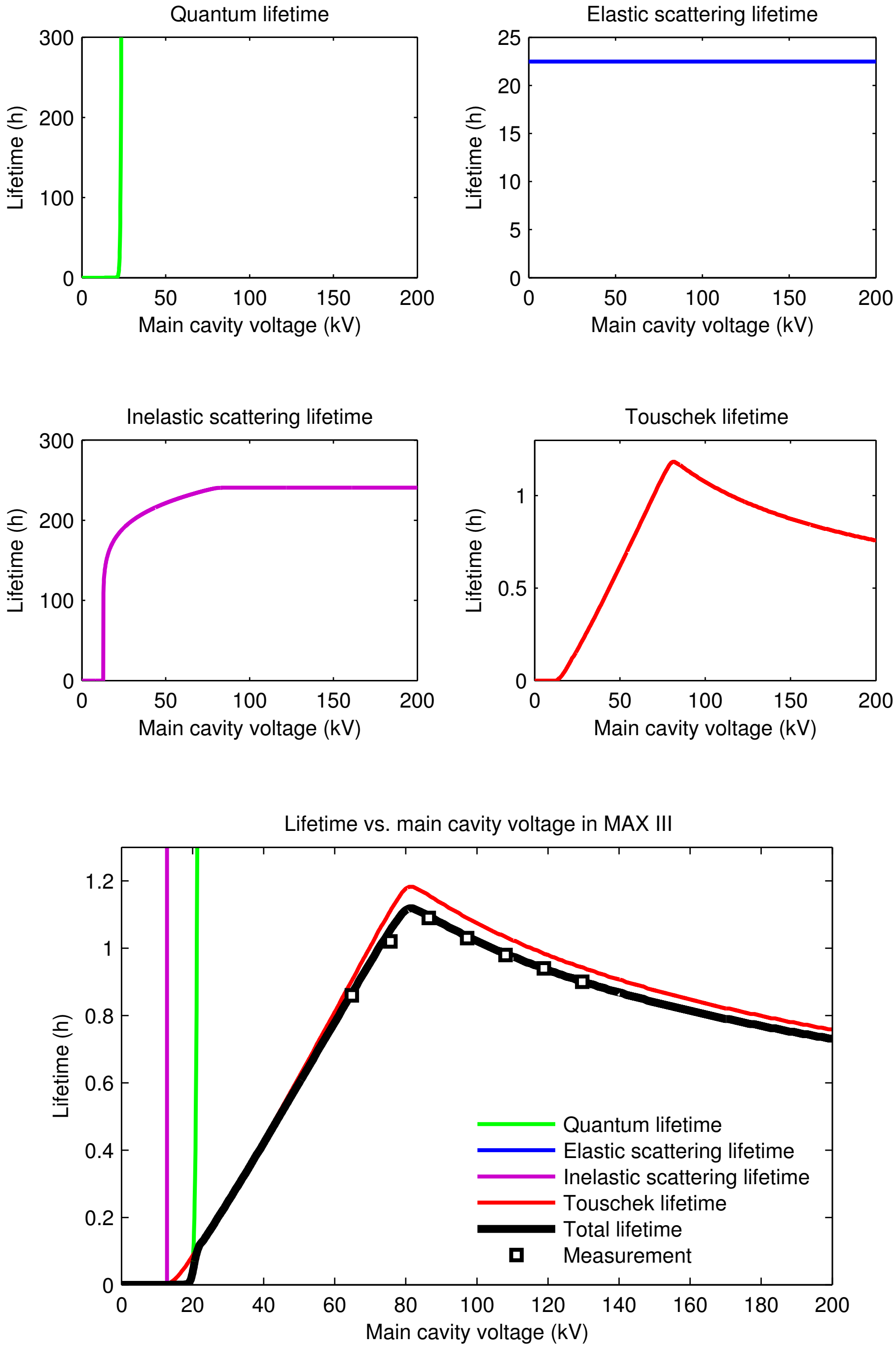

Figure 8.6: *Example of a lifetime vs. main cavity voltage measurement. The quantum lifetime, elastic and inelastic scattering lifetimes, Touschek lifetime and the total lifetime in MAX III are shown as a function of the main cavity voltage. The measurement data is taken from the measured total lifetime used for Fig. 13 in Paper* **IV**. *The cavity absorber is assumed to be located 10.6 mm from the beam center.*

the momentum acceptance is assumed to be equal to the average momentum acceptance around the ring. For main cavity voltages above 89 kV the inelastic scattering lifetime in Fig. 8.6 is constant since the momentum acceptance is limited by the lattice momentum acceptance. For main cavity voltages below 89 kV the inelastic scattering lifetime decreases with the main cavity voltage since the momentum acceptance is partly or completely limited by the RF momentum acceptance. The lifetime decrease is slow until the main cavity voltage is approximately 15 kV, by which time all the electrons have already been lost from the low quantum lifetime.

The Touschek lifetime in Fig. 8.6 was determined by multiplication of the Touschek lifetime calculations using OPA with the scaling factor 2.7 (see Paper **IV** and Sec. 8.2 for details on the scaling factor). For the calculations of the Touschek lifetime in Fig. 8.6 the cavity absorber is assumed to be located 10.6 mm from the beam center. The average lattice momentum acceptance is 0.0119, the minimum lattice momentum acceptance is 0.0109 and the maximum lattice momentum acceptance is 0.0126. The momentum acceptance is RF limited as long as the main cavity voltage is below 72 kV and lattice limited as long as the main cavity voltage is above 89 kV. For the intermediate region (72–89 kV) the momentum acceptance is given by the lattice momentum acceptance in certain parts of the ring and the RF momentum acceptance in other parts of the ring. For a main cavity voltage of about 80 kV the RF momentum acceptance has the same value as the average lattice momentum acceptance. The main cavity voltage affects the bunch length. A larger main cavity voltage will give a shorter bunch length and a shorter Touschek lifetime. A larger main cavity voltage will also give a larger RF momentum acceptance and, as long as the lattice momentum acceptance is sufficiently large, a longer Touschek lifetime. The combined effect for an increase in the main cavity voltage is an increase in the Touschek lifetime when the momentum acceptance is RF limited and a decrease in the Touschek lifetime when the momentum acceptance is lattice limited. The maximum Touschek lifetime in Fig. 8.6 is for a main cavity voltage of about 81 kV, close to the main cavity voltage where the the RF momentum acceptance has the same value as the average lattice momentum acceptance.

The total lifetime in Fig. 8.6 is given by Eq. (7.2), i.e. the combination of the four different lifetime limitations. Figure 8.6 also shows measurement data taken from the measured total lifetime used for Fig. 13 in Paper **IV**. The main cavity voltage affects the quantum lifetime, the inelastic scattering lifetime and the Touschek lifetime. Above 23 kV the contribution from the quantum lifetime to the total lifetime is negligible. When the momentum acceptance is limited by the lattice momentum acceptance, it is only the Touschek lifetime that is affected by a change in the main cavity voltage through the variation in bunch length. For MAX III, the inelastic lifetime is significantly longer than the Touschek lifetime, which makes lifetime vs. main cavity voltage measurements a possible method to study the Touschek lifetime.

Figure 8.7 shows an example of the Touschek lifetime in MAX III as a function of the main cavity voltage for different positions of the cavity absorber. The

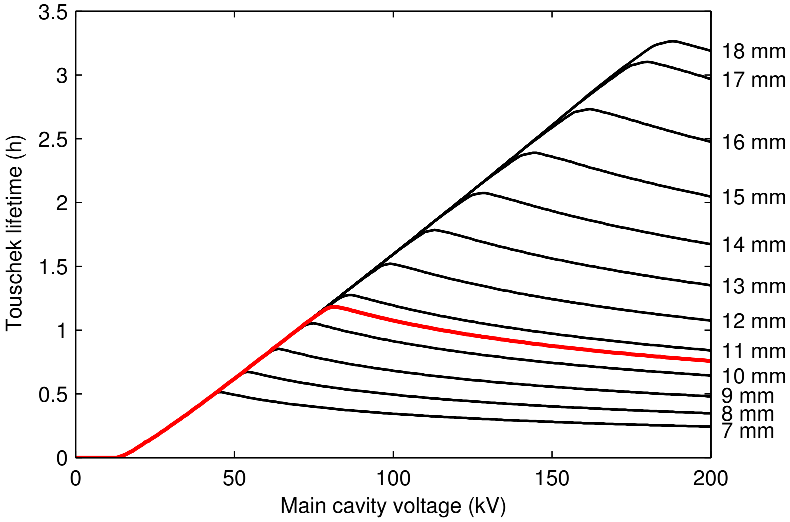

Figure 8.7: *Calculations of the Touschek lifetime in MAX III as a function of the main cavity voltage for different positions of the cavity absorber. The red line corresponds to the cavity absorber at 10.6 mm*

Touschek lifetime is calculated with OPA using the same settings as in Fig. 8.6, except the location of the cavity absorber, and scaled with the scaling factor 2.7. The red line corresponds to the cavity absorber at 10.6 mm, i.e. the same calculation as shown in Fig. 8.6. The RF momentum acceptance is assumed to be given by Eq. (7.8), i.e. the influence from the Landau cavities is neglected. Since the lattice momentum acceptance of MAX III varies little around the ring, the transition from a mostly lattice limited momentum acceptance to a mostly RF limited momentum acceptance is sharp. This was used in Paper **IV** to determine the distance between the cavity absorber and the beam center as well as to determine the average lattice momentum acceptance of MAX III. For a certain average lattice momentum acceptance of MAX III, the ideal main cavity voltage from a lifetime point of view is where the Touschek lifetime has a maximum. This roughly corresponds to the main cavity voltage where the RF momentum acceptance is equal to the average lattice momentum acceptance.

In summary, a lifetime vs. main cavity voltage measurement affects the RF momentum acceptance and thus the inelastic scattering lifetime and the Touschek lifetime. For low main cavity voltages the quantum lifetime is also affected. A lifetime vs. main cavity voltage measurement can be used to study the transition from a lattice limited momentum acceptance to a RF limited momentum acceptance.

REFERENCES

1. M. Eriksson. *The accelerator system MAX.* Nucl. Instr. and Meth. **196**, 331–340 (1982).
2. Å. Andersson, M. Eriksson, S. Werin, S. Biedron and H. Freund. *An RF-gun-driven recirculated linac as injector and FEL driver.* Nucl. Instr. and Meth. A **445**, 413–421 (2000).
3. B. Anderberg, Å. Andersson, M. Demirkan, M. Eriksson, L. Malmgren and S. Werin. *The design of a 3 GHz thermionic RF-gun and energy filter for MAX-lab.* Nucl. Instr. and Meth. A **491**, 307–313 (2002).
4. S. Thorin, N. Čutić, F. Lindau, S. Werin and F. Curbis. *Photocathode operation of a thermionic RF gun.* Nucl. Instr. and Meth. A **606**, 291–295 (2009).
5. N. Čutić, F. Lindau, S. Thorin, S. Werin, J. Bahrdt, W. Eberhardt, K. Holldack, C. Erny, A. L'Huillier and E. Mansten. *Vacuum ultraviolet circularly polarized coherent femtosecond pulses from laser seeded relativistic electrons.* Phys. Rev. ST Accel. Beams **14**, 030706 (2011).
6. L.-J. Lindgren and M. Eriksson. *Injection and extraction at MAX.* Nucl. Instr. and Meth. **214**, 179–187 (1983).
7. L.-J. Lindgren and M. Eriksson. *Experiences with the MAX accelerator system in the pulse-stretcher mode.* Nucl. Instr. and Meth. A **294**, 10–14 (1990).
8. J.-O. Adler, B.-E. Andersson, K. I. Blomqvist, B. Forkman, K. Hansen, L. Isaksson, K. Lindgren, D. Nilsson, A. Sandell, B. Schröder and K. Ziakas. *The photon tagging facility at the MAX accelerator system in Lund.* Nucl. Instr. and Meth. A **294**, 15–25 (1990).
9. W. J. Briscoe, Jason Brudvik, K. G. Fissum, K. Hansen, L. Isaksson, M. Lundin, B. Nilsson and B. Schröder. *Nuclear physics program at MAX-lab.* Chinese Physics C **33**, 1159–1166 (2009).
10. Å. Andersson, M. Eriksson, L.-J. Lindgren, P. Röjsel and S. Werin. *The MAX II synchrotron radiation storage ring.* Nucl. Instr. and Meth. A **343**, 644–649 (1994).
11. M. Sjöström, H. Tarawneh, E. Wallén and M. Eriksson. *Characterisation of the MAX II storage ring lattice.* Nucl. Instr. and Meth. A **577**, 425–436 (2007).
12. Å. Andersson, M. Bergqvist, M. Eriksson, L. Malmgren and L. Thånell. *The 100 MHz RF system for MAX-II and MAX-III.* In *Proceedings of the 2002 European Particle Accelerator Conference, Paris* pages 2118–2120 (2002).

13. G. LeBlanc, Å. Andersson, M. Eriksson, M. Georgsson, L.-J. Lindgren and S. Werin. *MAX III, a 700 MeV Storage Ring for Synchrotron Radiation.* In *Proceedings of the 2000 European Particle Accelerator Conference, Vienna* pages 643–644 (2000).

14. M. Sjöström, E. Wallén, M. Eriksson and L.-J. Lindgren. *The MAX III storage ring.* Nucl. Instr. and Meth. A **601**, 229–244 (2009).

15. M. Sands. *The Physics of Electron Storage Rings, an Introduction.* SLAC-121 (1970).

16. S. Turner, editor. *Proceedings of the 1992 CERN Accelerator School, Jyväskylä, Finland* (1994). CERN-94-01.

17. E. J. N. Wilson. *An Introduction to Particle Accelerators.* Oxford University Press (2001).

18. K. Wille. *The Physics of Particle Accelerators.* Oxford University Press (2001).

19. H. Wiedemann. *Particle Accelerator Physics.* Springer (2007).

20. S. Y. Lee. *Accelerator Physics.* World Scientific (2012).

21. A. Wolski. *Low Emittance Rings. Part 1: Beam Dynamics with Synchrotron Radiation.* Lecture notes from the 2011 CERN Accelerator School, Chios, Greece. Available at http://cas.web.cern.ch/cas/Greece-2011/Lectures/Wolski1.pdf.

22. S. Khan. *Collective Phenomena in Synchrotron Radiation Sources.* Springer (2006).

23. T. Raubenheimer. *The generation and acceleration of low emittance flat beams for future linear colliders.* SLAC-R-387 (1991).

24. G. Kube. *Review of synchrotron radiation based diagnostics for transverse profile measurements.* In *Proceedings of the eighth European Workshop on Diagnostics and Instrumentation for Particle Accelerators, Venice* pages 6–10 (2007).

25. S. Takano. *Beam diagnostics with synchrotron radiation in light sources.* In *Proceedings of the 2010 International Particle Accelerator Conference, Kyoto* pages 2392–2396 (2010).

26. A. P. Sabersky. *Monitoring the beams in SPEAR with synchrotron light.* IEEE Transactions on Nuclear Science **20**, 638–641 (1973).

27. Å. Andersson, M. Eriksson and O. Chubar. *Beam profile measurement with visible synchrotron light on MAX-II.* In *Proceedings of the 1996 European Particle Accelerator Conference, Sitges* pages 1689–1691 (1996).

28. Å. Andersson, M. Böge, A. Lüdeke, V. Schlott and A. Streun. *Determination of a small vertical electron beam profile and emittance at the Swiss Light Source.* Nucl. Instr. and Meth. A **591**, 437–446 (2008).

29. O. Chubar and P. Elleaume. *Accurate and efficient computation of synchrotron radiation in the near field region.* In *Proceedings of the 1998 European Particle Accelerator Conference, Stockholm* pages 1177–1179 (1998).

30. V.N. Mahajan. *Aberration Theory Made Simple.* SPIE Press (2011).

31. A. Terebilo. *Accelerator Toolbox for MATLAB.* SLAC-PUB-8732 (2001).

32. J. Safranek, G. Portmann, A. Terebilo and C. Steier. *MATLAB-based LOCO.* In *Proceedings of the 2002 European Particle Accelerator Conference, Paris* pages 1184–1186 (2002).

33. M. Sjöström. *Accelerator physics studies of the MAX-lab storage rings.* PhD thesis Lund University (2009).

34. S. C. Leemann, Å. Andersson, M. Eriksson, L.-J. Lindgren, E. Wallén, J. Bengtsson and A. Streun. *Beam dynamics and expected performance of Sweden's new storage-ring light source: MAX IV.* Phys. Rev. ST Accel. Beams **12**, 120701 (2009).

35. A. Hofmann and S. Myers. *Beam dynamics in a double RF system.* CERN-ISR-TH-RF-80-26 (1980).

36. J. M. Byrd and M. Georgsson. *Lifetime increase using passive harmonic cavities in synchrotron light sources.* Phys. Rev. ST Accel. Beams **4**, 030701 (2001).

37. A. Chao and M. Tigner. *Handbook of Accelerator Physics and Engineering.* World Scientific (1999).

38. P. Forck, P. Kowina and D. Liakin. *Beam position monitors.* In *Proceedings of the 2008 CERN Accelerator School, Dourdan, France* pages 187–228. CERN-2009-005 (2009).

39. A. Streun. *Lattices for light sources.* In *Proceedings of the 2003 CERN Accelerator School, Brunnen, Switzerland* pages 55–82. CERN-2005-012 (2005).

40. A. Chao. *Equations for multiparticle dynamics.* In *Lecture Notes in Physics, Vol. 296* pages 51–86. Springer (1988).

41. J. Le Duff. *Current and current density limitations in existing electron storage rings.* Nucl. Instr. and Meth. A **239**, 83–101 (1985).

42. J. Murphy. *Synchrotron Light Source Data Book.* BNL 42333 (1996).

43. A. Wrulich. *Single-beam lifetime.* In *Proceedings of the 1992 CERN Accelerator School, Jyväskylä, Finland* pages 409–435. CERN-94-01 (1994).

44. A. Streun. Code and documentation available at http://people.web.psi.ch/streun/opa.

45. M. S. Zisman, S. Chattopadhyay and J. J. Bisognano. *ZAP User's Manual.* LBL-21270 (1986).

46. A. Streun. *Momentum acceptance and Touschek lifetime.* SLS 18/97 (1997).

47. S. Kahn. *Simulation of the Touschek effect for BESSY II - A Monte Carlo approach.* In *Proceedings of the 1994 European Particle Accelerator Conference, London* pages 1192–1194 (1994).

PAPERS

Paper I

Experiences from nonevaporable getter-coated vacuum chambers at the MAX II synchrotron light source

A. Hansson, E. Wallén, M. Berglund, R. Kersevan and M. Hahn.

J. Vac. Sci. Technol. A **28**, 220–225 (2010).

Experiences from nonevaporable getter-coated vacuum chambers at the MAX II synchrotron light source

A. Hansson,[a] E. Wallén, and M. Berglund
MAX-lab, P.O. Box 118, SE-221 00 Lund, Sweden

R. Kersevan and M. Hahn
ESRF, BP 220, FR-38043 Grenoble Cedex, France

(Received 18 September 2009; accepted 7 December 2009; published 20 January 2010)

Vacuum chambers coated with nonevaporable getter (NEG) materials have been used in straight sections of synchrotron light sources for the past 10 years. The MAX II storage ring, where four NEG-coated insertion device vacuum chambers and three NEG-coated dipole vacuum chambers have been installed, is the first synchrotron light source to also use NEG-coated dipole vacuum chambers. In connection with the installation of the latest two NEG-coated dipole chambers in April 2009, the evolution of the pressure and lifetime-limiting effects in MAX II has been determined from measurements with movable scrapers. The results have been compared with results from scraper measurements done in 2003, before any NEG-coated vacuum chambers were installed in the storage ring. Less than three months after the installation of the latest dipole chambers the vacuum system in MAX II was performing well with a pressure already lower than the pressure measured in 2003. © *2010 American Vacuum Society.* [DOI: 10.1116/1.3281432]

I. INTRODUCTION

Throughout the past 10 years, the use of vacuum chambers coated with thin films of nonevaporable getter (NEG) materials in particle accelerators and storage rings has steadily increased. To a large extent the NEG material used for these ultrahigh vacuum (UHV) applications has been a ternary alloy of titanium, zirconium, and vanadium. An overview of the properties of thin films of the Ti–Zr–V NEG alloy is given by Chiggiato and Costa Pinto.[1] In short, NEG improves the vacuum in the chambers both by direct pumping of the residual gas and by reducing the electron and photon-induced desorption. Active gases such as CO, CO_2, H_2O, N_2, and O_2 are chemisorbed on the NEG surface whereas H_2 diffuses into the getter bulk. Noble gases and CH_4 are not pumped by NEG materials. To activate the NEG it is heated to a temperature where the native oxide layer on the surface is dissolved into the bulk.

Up until the 1970s, the vacuum levels in accelerator and storage ring vacuum systems was achieved by pumps connected to the vacuum chambers by means of flanges. As the vacuum chamber apertures got smaller and the machines got longer new linear pumping technologies, such as distributed sputter-ion pumps and NEG strips, were developed. For the large electron-positron collider (LEP) at CERN NEG strips made from St101, a commercial NEG alloy from SAES Getters was used for about 22 km of the 27 km long LEP.[2] St101 is a Zr–Al alloy with a composition of 84% Zr and 16% Al by weight (Zr 61 Al 39 at. %) activated by heating to 740 °C for 45–60 min.[3,4] Another SAES Getters NEG alloy, St707, was also found to be suitable for UHV conditions. The Zr–V–Fe alloy (Zr 70 V 24.6 Fe 5.4 wt %, Zr 57 V 36 Fe 7 at. %) had the advantage of being activated at temperatures of 350–400 °C, allowing passive activation during bakout.[5,6] NEG strips from St707 have been used at synchrotron light sources, e.g., at SPring-8 (Ref. 7) and TLS.[8] By covering most of a test vacuum chamber with NEG strips pressures in the 10^{-14} Torr range was obtained.[6] To lower the degassing from the chamber walls and further decrease the obtainable pressures, a method to sputter coat the inner vacuum chamber walls with NEG material was developed.[9] A suitable NEG alloy, Ti–Zr–V, with an activation temperature of 200 °C and properties suitable for particle accelerators and storage rings was developed.[10,11] The low activation temperature made it possible to use vacuum chambers made of aluminum and copper alloys.

The first storage ring to install a NEG-coated vacuum chamber was ESRF, where a narrow-gap aluminum insertion device (ID) vacuum chamber was installed in 1999.[12] Today, a majority of the ID vacuum chambers in ESRF are NEG coated[13] and NEG-coated vacuum chambers are used at several light sources, e.g., at ELETTRA,[14] Diamond,[15] SOLEIL,[16] and MAX III.[17] At SOLEIL 56% of the ring circumference is NEG coated, including the quadrupole and sextupole straight sections. For the upgrade of the heavy ion synchrotron SIS 18 at GSI, NEG-coated dipole vacuum chambers will be used.[18] For synchrotron light sources however, NEG-coated dipole vacuum chambers have so far not been tested. This article reports on the first experience with NEG-coated dipole vacuum chambers in a synchrotron light source.

II. NEG AT MAX II

The MAX II synchrotron light source[19] was commissioned in 1996. It is a 1.5 GeV third generation storage ring with a circumference of 90 m. It has a tenfold periodicity

---

[a] Author to whom correspondence should be addressed; electronic mail: anders.hansson@maxlab.lu.se

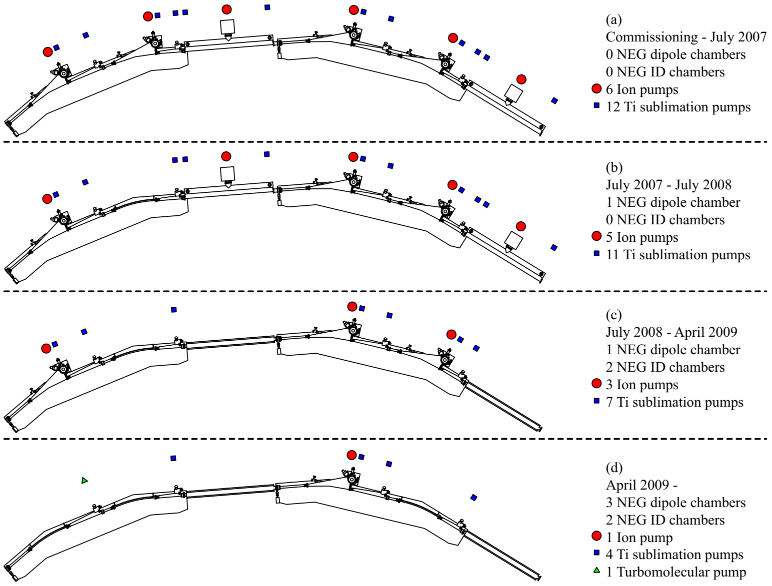

FIG. 1. (Color online) Vacuum system of cells 2 and 3 in the MAX II storage ring from (a) commissioning to July 2007, (b) July 2007 to July 2008, (c) July 2008 to April 2009, and (d) from April 2009 onward.

with two dipole magnets in each cell. The original vacuum system in MAX II was made of stainless steel. To allow smaller gaps for the insertion devices, NEG-coated aluminum ID vacuum chambers were installed in the straight section between cells 4 and 5 and in the straight section between cells 9 and 10. The experience with the NEG-coated ID vacuum chambers was positive and together with reports from other synchrotron radiation facilities, this fueled an interest in extended use of NEG-coated vacuum chambers. For the future synchrotron light source MAX IV, currently being designed at MAX-lab,[20] the vacuum system is proposed to be almost entirely made up of NEG-coated vacuum chambers. To examine the feasibility of this design, NEG-coated dipole vacuum chambers were manufactured for installation into MAX II with the goal to evaluate how NEG-coated dipole chambers influence the operation of the storage ring.

Besides the two NEG-coated ID chambers mentioned above, five more NEG-coated chambers have been installed in MAX II. All of them have been installed in cells 2 and 3 of the storage ring. Figure 1 depicts the vacuum system of cells 2 and 3 in MAX II from commissioning to its current arrangement. Added to the figure are circles (corresponding to ion pumps), squares (corresponding to titanium sublimation pumps), and triangles (corresponding to turbomolecular pumps) showing how the distribution of pumps has changed during the years. In July 2007 a NEG-coated copper dipole vacuum chamber was installed in the second dipole of cell 2. In July 2008 the straight sections between cells 2 and 3 and between cells 3 and 4 were exchanged with NEG-coated aluminum ID vacuum chambers. Finally, in April 2009 two NEG-coated copper dipole vacuum chambers were installed in the first dipole in cell 2 and in the second dipole of cell 3. During this time the total amount of pumps in cells 2 and 3 (including the ID vacuum chambers) decreased from six ion pumps and twelve titanium sublimation pumps to only one ion pump, four titanium sublimation pumps, and a turbomolecular pump. The turbomolecular pump was connected to the vacuum system for the initial pumping from atmospheric pressure but has been kept running for most of the time since April 2009.

III. NEG-COATED COPPER DIPOLE VACUUM CHAMBERS

The standard dipole vacuum chambers of the MAX II storage ring are made of stainless steel. They are connected to two pumps each, one ion pump and one titanium sublimation pump. The new NEG-coated copper dipole vacuum chambers on the other hand have no additional pumps. They are made of 1 mm thick oxygen-free high thermal conductivity (OFHC) copper tubes with an inner diameter of 31 mm. An additional 1 mm thick copper tube, with an inner diameter of 10 mm, is spot welded and soldered outside the larger tube and it is used for the cooling water supplying the necessary cooling of the vacuum chamber. The top part of Fig. 2 shows a drawing of the standard stainless steel dipole vacuum chamber. The bottom part of Fig. 2 shows a drawing of the new NEG-coated copper dipole vacuum chamber.

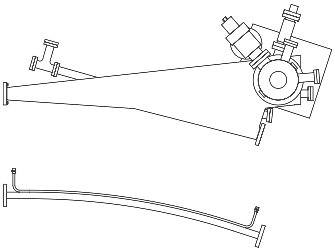

FIG. 2. Drawings of the standard stainless steel dipole vacuum chamber (top) and the new NEG-coated copper dipole vacuum chamber (bottom).

The NEG coating of the copper chambers was done at ESRF NEG coating facility's tower No. 2, using a 1 m long solenoid producing a maximum field on axis of about 500 G, and with a flat-out field length of around 80 cm. The 1.3 m long copper chamber and sections of transition chambers made for the purpose were therefore coated in two passes. The NEG material was sputtered onto the copper using a single Ti–Zr–V intertwisted cathode made up of 0.5 mm wires. The total sputtering time was 60 h, giving a film thickness of 1 μm. Due to the curvature of the chamber (radius of 3.33 m) and in order to keep the cathode close to the chamber's axis, four ceramic spacers were evenly spaced along the chamber, plus two adaptors at either end. The rectangular ceramic spacers covered a negligible part of the circular chamber, resulting in a surface coverage of the sputtered film above 99%. The process gas and pressure were krypton at around 0.1 mbar, and the chamber temperature was around 110 °C. The composition of the NEG material has not been measured for the dipole chambers, but in July 2009 measurements were done at ESRF on the composition of the NEG material in an aluminum chamber sample coated using the same coating procedure as for the dipole chambers. The sample composition was 27.6% Ti, 30.6% Zr, and 41.8% V by weight (33.2% Ti, 19.4% Zr, and 47.4% V by atomic composition).

Before installation into the MAX II storage ring the copper dipole vacuum chambers were prebaked and activated. The temperature was ramped from room temperature to 200 °C in 8 h. The chambers were kept at 200 °C for at least 12 h, after which the temperature was ramped down to room temperature again in 8 h. For the installation the chambers were vented with dry nitrogen gas. After installation, the chambers were activated again at 200 °C following the same procedure as during the prebake.

Currently there are three NEG-coated copper dipole vacuum chambers installed in the MAX II storage ring. To evaluate the influence of the NEG-coated dipole chambers on the pressure and lifetime in the storage ring, measurements were performed with movable aperture restriction (scrapers) and with scintillation detectors registering the bremsstrahlung radiation emanating from the dipole vacuum chambers.

TABLE I. Relative proportions of the residual gases in MAX II during operation.

Gas	Relative proportion (%)
H_2	94.6
H_2O	2.2
CO	2.6
CO_2	0.6

A. Scraper measurements

In 2003, before any NEG-coated vacuum chambers had been installed, scraper measurements were performed at MAX II to determine the acceptances and lifetimes of the storage ring.[21] Following the same procedure as in 2003, new scraper measurements were performed in connection with the installation of the last two NEG-coated dipole chambers in April 2009 in order to determine the evolution of the pressure and the lifetime before and after the installation and to compare this with the results from 2003.

The total lifetime, τ_{tot}, in MAX II is given by[21]

$$\frac{1}{\tau_{\text{tot}}} = \frac{1}{\tau_{\text{elastic}}} + \frac{1}{\tau_{\text{inelastic}}} + \frac{1}{\tau_{\text{Touschek}}}, \tag{1}$$

where τ_{elastic} and $\tau_{\text{inelastic}}$ are the lifetimes due to the elastic and inelastic scattering, respectively, of the beam electrons on the atoms of the residual gas and τ_{Touschek} is the lifetime due to the Touschek effect. Assuming a rectangular acceptance, the elastic scattering lifetime is given by[22]

$$\frac{1}{\tau_{\text{elastic}}} = cn_g \frac{2\pi r_e^2 Z^2 \langle \beta_V \rangle}{\gamma^2 \varepsilon_{AV}} \frac{1}{\pi} \times [\pi + (R^2+1)\sin(2\arctan R) + 2(R^2-1)\arctan R], \tag{2}$$

where c is the speed of light, n_g is the residual gas density, r_e is the classical electron radius, Z is the atomic number of the residual gas, γ is the relativistic factor of the electrons in the stored beam, and

$$R = \sqrt{\frac{\langle \beta_H \rangle \varepsilon_{AV}}{\langle \beta_V \rangle \varepsilon_{AH}}}, \tag{3}$$

where ε_{AV} and ε_{AH} are the vertical and horizontal acceptance and $\langle \beta_V \rangle$ and $\langle \beta_H \rangle$ are the average vertical and horizontal beta functions in the storage ring. Equation (2) is valid when the vertical acceptance is smaller than the horizontal acceptance. If the horizontal acceptance is smaller than the vertical acceptance Eqs. (2) and (3) can be used with exchanged H and V.

For MAX II in normal operating mode at full energy, γ is 2915, ε_{AH} is 5.6×10^{-6} m, $\langle \beta_V \rangle$ is 6.3 m, and $\langle \beta_H \rangle$ is 7.4 m. The relative proportions of the residual gases were determined with a residual gas analyzer (RGA), Balzers Quadstar 421, using tabulated values for the relative probabilities of ionization and relative ion currents of fragment ions.[23] The result is given in Table I. Comparing this with the result from 2003,[21] when the residual gas consisted of 96.5% H_2, 1.1%

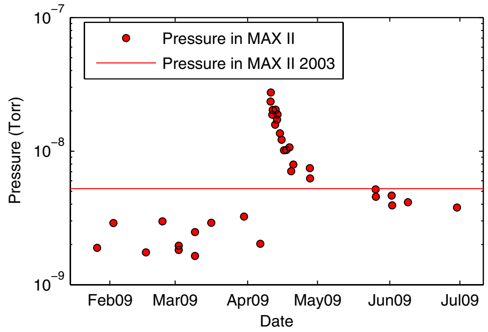

FIG. 3. (Color online) Pressure in the MAX II storage ring from February 2009 to July 2009. The solid line corresponds to the pressure in MAX II in 2003 (Ref. 21).

H_2O, 1.8% CO, and 0.6% CO_2, it can be seen that the residual gas is still dominated by H_2 and that is has largely the same content as 6 years ago. No signs of methane or other gases not pumped by NEG could be found from the RGA measurement. The RGA is situated in the straight section between cells 5 and 6.

By combining Eqs. (1) and (2) and measuring the total lifetime at different positions of the vertical scraper (and thus different vertical acceptances), a fit can be made on the data to determine τ_{elastic}. With knowledge of the relative proportions of the residual gases the residual gas density n_g and from that the pressure in the storage ring can be determined. Figure 3 shows the pressure in MAX II in normal operation mode at full energy from February 2009 to July 2009. The solid line depicts the pressure measured in 2003.[21] The stored current in the storage ring varied between different scraper measurements but was mainly in the region 140–180 mA. The installation of the two new NEG-coated copper dipole vacuum chambers in April 2009 can clearly be seen in Fig. 3. Although the pressure is not yet down to the levels it was before the April venting of cells 2 and 3, it is already lower than it was in 2003. Cells 2 and 3 were also vented during July 2008, when two NEG-coated ID chambers were installed. It took 5 months before the pressure had reduced to the low levels shown in the left half of Fig. 3, whereas the last scraper measurement in Fig. 3 was done less than three months after the April 2009 venting.

The relative proportions of the residual gas, as measured by the RGA, were not affected by the April 2009 venting. However, since the RGA is situated in the straight section between cells 5 and 6, far from the vented section, it is possible that the initial content of the residual gas after the venting contained N_2 that did not show up on the RGA. The pressure measurements for the first days after the venting could thus be somewhat imprecise compared to the other results.

Using the results from the scraper measurements $\tau_{\text{inelastic}}$ can also be determined. Since the residual gas in MAX II is dominated by hydrogen, the contribution from inelastic scattering on the electrons in the residual gas cannot be omitted when calculating $\tau_{\text{inelastic}}$.[21] Taking into account the inelastic scattering on both the residual gas nucleus and electrons, the lifetime due to inelastic scattering is given by[24]

$$\frac{1}{\tau_{\text{inelastic}}} = cn_g 4\alpha r_e^2 \left\{ \left[Z^2 \ln\left(\frac{183}{Z^{1/3}}\right) + Z \ln\left(\frac{1194}{Z^{2/3}}\right) \right] \times \frac{4}{3} \times \left[\ln\left(\frac{1}{\varepsilon_{\text{acc}}}\right) - \frac{5}{8} \right] + \frac{Z(Z+1)}{9} \left[\ln\left(\frac{1}{\varepsilon_{\text{acc}}}\right) - 1 \right] \right\}, \tag{4}$$

where α is the fine structure constant $1/137$ and ε_{acc} is the momentum acceptance of the storage ring [2% in MAX II (Ref. 25)]. Finally, τ_{Touschek} is indirectly determined from results of the other lifetimes using Eq. (1).

Figure 4 shows the product of the stored current and the lifetimes determined by the scraper measurements from August 2008 to July 2009. Added to the figure are the products of current and total lifetime for the days when MAX II was operating but no scraper measurement was done. The lines depict the products of current and lifetime in 2003.[21] The measurements of τ_{tot} and τ_{elastic} are not dependent on knowledge of the relative proportions of the residual gases, whereas $\tau_{\text{inelastic}}$ and thus τ_{Touschek} are. Due to the uncertainty of the content of the residual gas during the first days after the venting $I\tau_{\text{inelastic}}$ and $I\tau_{\text{Touschek}}$ are not shown in Fig. 4 for these days.

The beam lifetime in MAX II is limited by the Touschek effect rather than by the vacuum situation in the storage ring. This was the case in 2003 and is still valid 6 years later. In the beginning of May 2009 there were some problems with one of the standard dipole vacuum chambers in cell 1 and in June 2009 problems with the rf cavities prevented operation with full stored beam. Even with these problems the lifetime situation in MAX II is currently, less than 3 months after the installation of the two new NEG-coated dipole chambers, already similar to the situation in 2003. The main difference compared to 2003 is that $I\tau_{\text{elastic}}$ has decreased. This is explained by the fact that both the horizontal and vertical acceptances in MAX II have decreased since 2003. The horizontal acceptance has decreased from 9.6×10^{-6} to 5.6×10^{-6} m, whereas the vertical acceptance has decreased from 7.4×10^{-6} to 5.4×10^{-6} m. This is most likely due to horizontal absorbers installed upstream of the superconducting wigglers to shield the wigglers from dipole magnet synchrotron radiation and the small vertical aperture of the NEG-coated ID vacuum chambers.

The average $I\tau_{\text{tot}}$ during June 2009 was 3.7 A h which is close to the average $I\tau_{\text{tot}}$ during the past 7 years of MAX II operation at about 4 A h. In the first quarter of 2009, before the April 2009 venting the performance of MAX II was among the best since the startup of the storage ring. During a 30-day period the average stored current in MAX II was over 200 mA, the highest average current recorded.

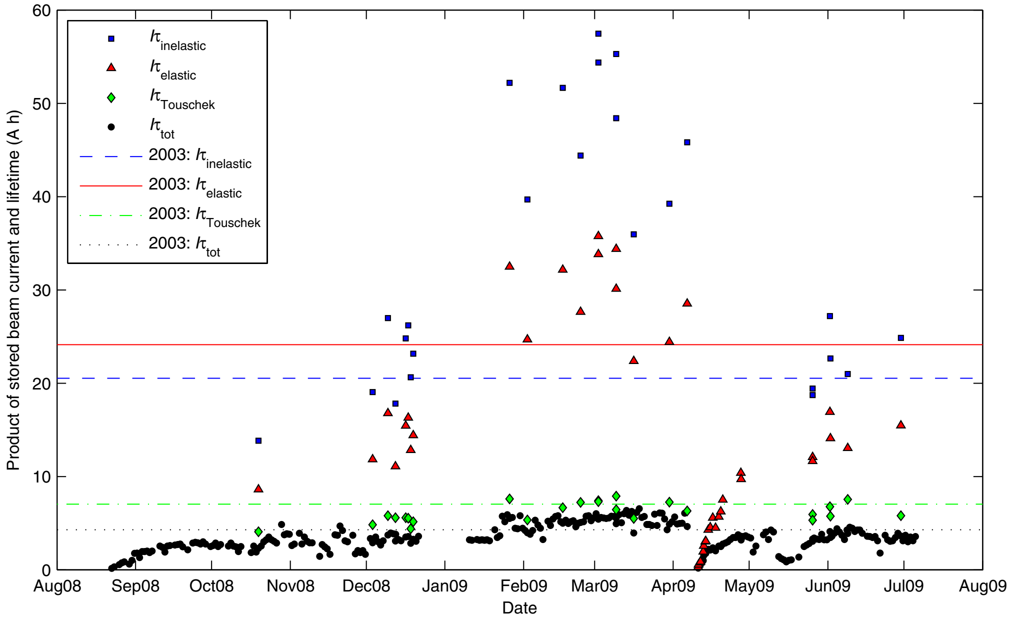

FIG. 4. (Color online) Product of stored beam current and total lifetime in MAX II from August 2008 to July 2009. Where available, the products of current and lifetime limitations due to inelastic scattering, elastic scattering, and the Touschek effect are given. The lines correspond to the products of current and lifetime in MAX II in 2003 (Ref. 21).

B. Bremsstrahlung measurements

The pressure in MAX II as seen by the stored electron beam has been determined by scraper measurements in the section above. To evaluate the performance of the NEG-coated dipole vacuum chambers it would be of interest to determine the local pressure inside or close to the dipole chambers. Unfortunately, there are no calibrated vacuum gauges connected to the MAX II vacuum system. In an attempt to study the relative change in the pressure before and after the April 2009 dipole chamber installation two $2\times 2\ \text{in.}^2$ sodium iodide (NaI) scintillation detectors were placed downstream the second dipole in cells 2 and 3, respectively. The bremsstrahlung radiation emanating from inelastic scattering on the residual gas is proportional to the pressure of the residual gas in that area. The NaI detectors were placed 3.2 m downstream of the end of the second dipole chambers in cells 2 and 3 looking at the bremsstrahlung from a 5 cm region 30–35 cm into the dipole chamber.

The count rate in the detectors per 10 s and milliamperes stored current in MAX II from March 2009 to June 2009 is shown in Fig. 5. In April 2009 the second dipole chamber in cell 2 was changed from a standard stainless steel vacuum chamber to a new NEG-coated copper chamber. The second dipole chamber in cell 3 was vented during the installation but it had the same NEG-coated copper dipole vacuum chamber both before and after the April venting. The count rates in both detectors increased after the venting. The largest difference was for the detector downstream cell 2, where the new chamber had been installed. 2 months after the venting the count rates in the detector downstream cell 2 were about 20% higher than before the venting, whereas for cell 3 they were about 60% higher. If the detectors only detected the bremsstrahlung from the dipole chambers the count rate would be proportional to the pressure. However, the detec-

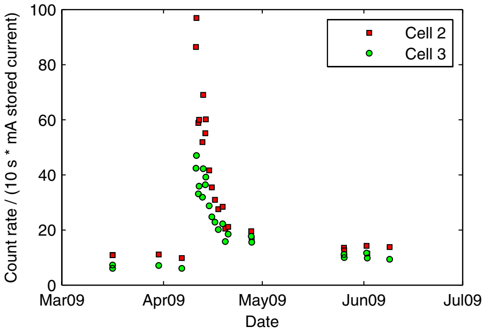

FIG. 5. (Color online) Count rate in the NaI detectors per 10 s and milliamperes stored current in MAX II from March 2009 to June 2009.

tors were also sensitive to particle losses from the Touschek effect and to the settings of the insertion devices in the ring. To minimize the influence of this the settings in MAX II were kept as identical as possible during the measurements shown in Fig. 5. However due to these uncertainties the count rates can only be seen as a very rough estimate of the relative pressure levels in the dipole vacuum chambers.

IV. CONCLUSIONS

Since 2003 four NEG-coated aluminum ID vacuum chambers and three NEG-coated copper dipole vacuum chambers have been installed in the MAX II synchrotron light source. For each standard ID vacuum chamber replaced by a new NEG-coated ID vacuum chamber one ion pump and two titanium sublimation pumps have been disconnected from the vacuum system. For each NEG-coated dipole vacuum chamber one ion pump and one titanium sublimation pump have been disconnected. Even though the cross sections of the new vacuum chambers are significantly smaller than for the old chambers and even though there are no extra pumps connected to the new chambers, the pressure and lifetime in MAX II are still similar to the values from 2003. In cell 2 of MAX II only a titanium sublimation pump and a turbomolecular pump are connected to the vacuum system and even though the NEG-coated dipole vacuum chambers are mixed with stainless steel vacuum chambers exposed to synchrotron radiation, the lifetime in MAX II, 3 months after the latest venting, is close to the average lifetime during the past 7 years. During a month in early 2009, when the vacuum system of MAX II included one NEG-coated dipole chamber and four NEG-coated ID chambers, the average stored current in MAX II was over 200 mA, the highest average current recorded for a 30-day period. Judging by the experiences from MAX II, NEG-coated vacuum chambers, including dipole vacuum chambers, do not appear to have any negative impact on the performance and operation of a synchrotron light source.

ACKNOWLEDGMENTS

The authors would like to thank F. Bodart, J.-L. Bersier, and H. Colou for their work on the coating bench at ESRF and J. Thånell and M. Nilsson for the installation of the NEG-coated vacuum chambers at MAX-lab. The authors also would like to thank M. Eriksson for the possibility to carry out this study.

[1] P. Chiggiato and P. Costa Pinto, Thin Solid Films **515**, 382 (2006).
[2] LEP Vacuum Group, Vacuum **41**, 1882 (1990).
[3] C. Benvenuti and F. Francia, J. Vac. Sci. Technol. A **6**, 2528 (1988).
[4] C. Benvenuti and F. Francia, J. Vac. Sci. Technol. A **8**, 3864 (1990).
[5] H. J. Halama and Y. Guo, J. Vac. Sci. Technol. A **9**, 2070 (1991).
[6] C. Benvenuti and P. Chiggiato, Vacuum **44**, 511 (1993).
[7] H. A. Sakaue, Y. Hirano, S. R. In, S. Yokouchi, K. Watanabe, and S. H. Be, Vacuum **44**, 523 (1993).
[8] D. J. Wang, J. R. Chen, G. Y. Hsiung, J. G. Shyy, J. R. Huang, S. N. Hsu, K. M. Hsiao, and Y. C. Liu, J. Vac. Sci. Technol. A **14**, 2624 (1996).
[9] C. Benvenuti, P. Chiggiato, F. Cicoira, and Y. L'Aminot, J. Vac. Sci. Technol. A **16**, 148 (1998).
[10] C. Benvenuti, J. M. Cazeneuve, P. Chiggiato, F. Cicoira, A. Escudeiro Santana, V. Johanek, V. Ruzinov, and J. Fraxedas, Vacuum **53**, 219 (1999).
[11] P. Chiggiato and R. Kersevan, Vacuum **60**, 67 (2001).
[12] R. Kersevan, Proceedings of the EPAC, Vienna, Austria, 2000 (unpublished), p. 2291.
[13] M. Hahn and the ESRF Vacuum Group, Vacuum **81**, 759 (2007).
[14] F. Mazzolini, J. Miertusova, F. Pradal, and L. Rumiz, Proceedings of the EPAC, Paris, France, 2002 (unpublished), p. 2577.
[15] J. D. Herbert, O. B. Malyshev, K. J. Middleman, and R. J. Reid, Vacuum **73**, 219 (2004).
[16] C. Herbeaux, N. Béchu, and J.-M. Filhol, Proceedings of the EPAC, Genoa, Italy, 2008 (unpublished), p. 3696.
[17] M. Sjöström, E. Wallén, M. Eriksson, and L.-J. Lindgren, Nucl. Instrum. Methods Phys. Res. A **601**, 229 (2009).
[18] M. C. Bellachioma, J. Kurdal, M. Bender, H. Kollmus, A. Krämer, and H. Riech-Sprenger, Vacuum **82**, 435 (2007).
[19] Å. Andersson, M. Eriksson, L.-J. Lindgren, P. Röjsel, and S. Werin, Nucl. Instrum. Methods Phys. Res. A **343**, 644 (1994).
[20] See: http://www.maxlab.lu.se/maxlab/max4/.
[21] E. Wallén, Nucl. Instrum. Methods Phys. Res. A **508**, 487 (2003).
[22] H. Wiedemann, *Particle Accelerator Physics* (Springer, Berlin, 2007), p. 325.
[23] Balzers Instruments, *Partial Pressure Measurement in Vacuum Technology* (Balzers Instruments, Liechtenstein, 1996), pp. 26–27.
[24] C. J. Bocchetta, *Proceedings to the CERN Accelerator School, CAS 98-04* (CERN, Geneva, 1998), p. 243.
[25] Å. Andersson (private communication).

PAPER II

Transverse electron beam imaging system using visible synchrotron radiation at MAX III

A. Hansson, E. Wallén, Å. Andersson.

Nucl. Instr. and Meth. A **671**, 94–102 (2012).

Nuclear Instruments and Methods in Physics Research A 671 (2012) 94–102

Contents lists available at SciVerse ScienceDirect

Nuclear Instruments and Methods in Physics Research A

journal homepage: www.elsevier.com/locate/nima

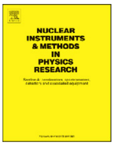

Transverse electron beam imaging system using visible synchrotron radiation at MAX III

A. Hansson*, E. Wallén, Å. Andersson

MAX-lab, Lund University, P.O. Box 118, SE-221 00 Lund, Sweden

ARTICLE INFO

Article history:
Received 23 October 2011
Received in revised form
21 December 2011
Accepted 26 December 2011
Available online 30 December 2011

Keywords:
Electron beam profile
Synchrotron radiation

ABSTRACT

The diagnostic beam line at the MAX III synchrotron light source utilizes the synchrotron radiation (SR) in the visible to ultraviolet range to form images of the transverse electron beam profile. The emission and subsequent propagation and focusing of the SR is modeled, taking into account effects such as diffraction and the longitudinally distributed SR generation. A detailed description of the setup of the beam line and method used to determine the transverse beam profile is given in the paper. In order to investigate the imaging method, a series of measurements were performed where the beam line configuration was varied to utilize different wavelengths and polarizations of the SR and different horizontal opening angles of the measurement system. A suggestion is made how to measure future small horizontal beam sizes.

1. Introduction

Synchrotron radiation (SR) is commonly used for electron beam diagnostics at accelerator facilities. The emitted SR can be used for non-destructive studies of electron beam properties such as the transverse beam profile. An overview of the different SR-based diagnostic methods used for transverse beam profile measurements is given by Kube [1]. An updated list of beam profile measurement methods in synchrotron light sources is given by Takano [2].

The most common methods used today to determine the transverse beam sizes at synchrotron light sources are pinhole cameras using SR in the X-ray range (see e.g. Refs. [3–5]) and interferometers using SR in the visible range (e.g. Refs. [6,7]). X-ray imaging methods using different X-ray focusing optics, such as a Fresnel zone plate [8] or compound refractive lenses [9], are also in use.

Another method to determine the transverse beam profile is imaging with visible to ultraviolet (vis–UV) SR. This method was used already in the early 1970's to monitor the beam profile in SPEAR [10]. With smaller beam size effects such as diffraction and depth-of-field had to be taken into account [11]. By treating these effects as separate phenomena and using approximate methods, the errors from diffraction (using Fraunhofer far-field approximation) and depth-of-field were estimated separately and corrected for. In this way the beam profiles at MAX I [12] and SURF III [13] were determined. A similar approximate approach has also been used, more recently, at the optical diagnostic beam line at CLS [14,4].

The optical resolution of the vis–UV imaging method can be improved by exploiting the wave-optics features of SR [15,16]. The emission of SR along the curved longitudinal electron trajectory and the subsequent propagation and focusing is modeled with high accuracy. Instead of treating effects like diffraction, depth-of-field and curvature as separate phenomena, they are modeled as a single phenomenon within the framework of classical electrodynamics. From these models it is possible to predict how the on-axis minimum of the vertically (π) polarized SR in the image plane will be blurred by the non-zero vertical beam size. This so-called π-polarization method was used to determine transverse beam sizes in MAX II [17,18] and SLS [19]. At SLS the smallest vertical beam size measured was 6.4 ± 0.5 μm, corresponding to an emittance of 3.2 pm rad.

A temporary visible imaging system installed in the MAX III synchrotron light source, using one of the straight section viewports, was used in the characterization of the ring [20], but it only gave rough estimates on the electron beam size. To allow for precise beam profile measurements, a new diagnostic beam line was designed and installed in 2010. This paper reports on the details of this new diagnostic beam line. Since a vis–UV imaging system has proven to be capable of measuring one of the smallest vertical storage ring beam sizes worldwide [19], it is of common interest to study the method in more depth and possibly improve it.

A short overview of the MAX III synchrotron light source is given in Section 2. Section 3 describes in detail the setup and

---

* Corresponding author.
E-mail address: anders.hansson@maxlab.lu.se (A. Hansson).

0168-9002/$ - see front matter © 2011 Elsevier B.V. All rights reserved.
doi:10.1016/j.nima.2011.12.100

components of the diagnostic beam line at MAX III. The method used to determine the transverse electron beam profile is presented in Section 4 together with some examples of beam profile measurements. In Section 5 the measurement method is investigated by measuring the electron beam profile for different horizontal opening angles of the measurement system and different SR wavelengths and polarizations.

2. MAX III

The MAX III synchrotron light source was commissioned in late 2006 and characterized in 2008 [20]. It is a third generation electron storage ring with an electron energy of 700 MeV intended for SR generation in the infrared and ultraviolet region. It has an eightfold periodicity, 36 m circumference and a design horizontal emittance of 13 nm rad. The storage ring makes extensive use of combined function magnets to obtain a compact lattice. Each unit cell contains a dipole with a defocusing gradient and two focusing quadrupoles with a sextupole component.

Five of the eight straight sections in MAX III are available for insertion devices. So far two insertion devices have been installed, an elliptically polarizing undulator and a planar undulator, providing SR in the ultraviolet region. A third beam line is currently under commissioning. It will utilize the infrared light from one of the MAX III dipole magnets.

3. The MAX III diagnostic beam line

Fig. 1 shows a drawing of the diagnostic beam line and cell 6 of MAX III as seen from the side, whereas Fig. 2 shows the beam line as seen from above. In Fig. 3 a detailed drawing of the main vacuum chamber of the diagnostic beam line, containing the optical components and baffles, is shown.

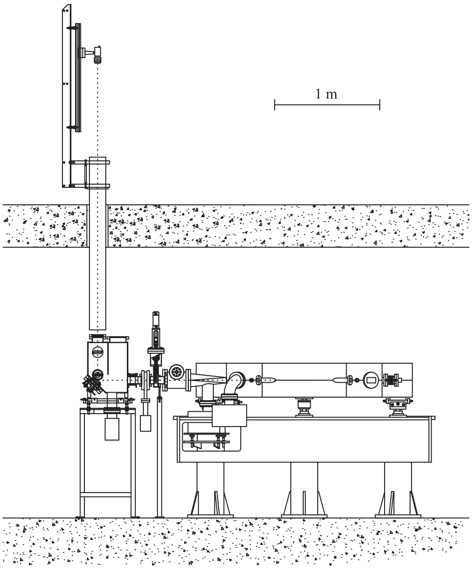

Fig. 1. Drawing of the MAX III diagnostic beam line and cell 6 as seen from the side.

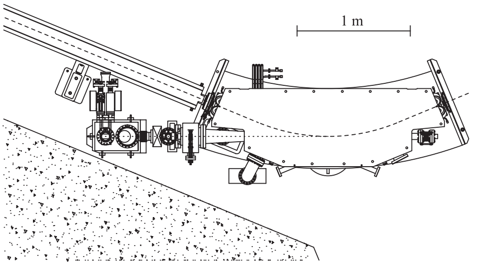

Fig. 2. Drawing of the MAX III diagnostic beam line, cell 6 and straight section 6–7 as seen from above.

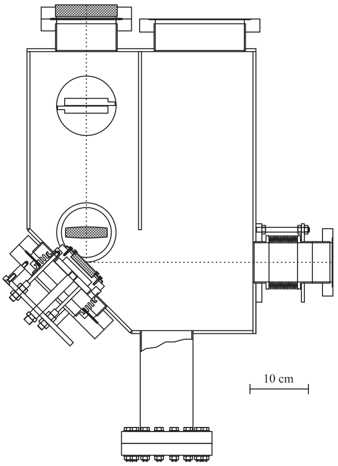

Fig. 3. Detailed drawing of the main vacuum chamber of the MAX III diagnostic beam line as seen from the side. The dashed line corresponds to the path of the center of the vis–UV SR. The SR enters from the right hand side of the drawing. The vis–UV part of the SR is reflected 90° upwards by the mirror and is focused in the lens. Horizontal baffles determine the horizontal opening angle of the measurement system. Finally, the vis–UV SR passes out of the vacuum chamber through a vacuum window in the upper part of the drawing.

The source point for the diagnostic beam line is the center of the bending magnet in cell 6 of the MAX III storage ring. The bending radius of the magnet is 1.58 m and the design values for the machine functions in the center of the bending magnet are $\beta_x = 0.27$ m, $\beta_y = 12.8$ m, $\eta_x = 0.14$ m and $\eta_y = 0.00$ m. Downstream in the beam line, the SR in the vis–UV range is reflected 90° upwards by a SiC mirror. The SR is focused in a fused silica symmetric spherical lens, after which the horizontal acceptance of the beam line is determined by movable aperture restrictions (baffles). The SR propagates out of the vacuum system through a fused silica vacuum window. An optical rail is situated on top of the MAX III roof, on which optical filters and a CCD camera are placed. The CCD of the camera is positioned at the image plane. Narrow band-pass filters and a Glan–Taylor polarizer are used to select the wavelength and polarization of the measurement.

Table 1
Positions of the components of the diagnostic beam line (maximum error).

MAX III diagnostic beam line	Position (m)
Photon origin (design)	-1.993 ± 0.004
Photon origin (measurement)	-1.980 ± 0.007
SiC mirror	-0.049 ± 0.001
Lens (center)	0.000
Baffles	0.213 ± 0.001
Window (center)	0.386 ± 0.001
Camera CCD—364 nm measurement	2.906 ± 0.010
Camera CCD—488 nm measurement	3.091 ± 0.010
Camera CCD—633 nm measurement	3.196 ± 0.010

Table 1 gives the positions of the components of the diagnostic beam line along with the estimated maximum errors. The uncertainty in camera position depends both on the measurement of its position and the determination of the image plane (see Section 4.1). The photon origin in the MAX III dipole magnet is determined both from the design drawing and from measurements of the focal length of the lens (see Section 3.1) and position of the image plane (camera CCD) for three different SR wavelengths. About 5 mm of the 13 mm discrepancy between the design and measured photon origin is explained by the stored electron orbit deviating from the design orbit. The remaining 7 mm discrepancy is within the measurement uncertainty. The measured photon origin at 1.980 m is used in the calculations and simulations.

The magnification factor of the diagnostic beam line is 1.462 ± 0.011 at 364 nm, 1.556 ± 0.011 at 488 nm and 1.609 ± 0.011 at 633 nm (maximum errors).

3.1. Optical components

To minimize the distortions of the SR wave front, the demands on the optical components are very high.

The mirror used for the diagnostic beam line originates from SLS, where a similar mirror is installed in the SLS diagnostic beam line [19]. It is made out of SiC due to the advantageous ratio of thermal conductivity to expansion of the material. Together with the water-cooled mirror holder this ensures that the mirror does not suffer thermal deformations from the SR heat load. In case any thermal deformation is suspected, even if this is not anticipated, the vacuum chamber of the diagnostic beam line is prepared for installation of a cold finger. The mirror is in thermal contact with the holder via a thin layer of gallium. The mirror is 50 mm high, 60 mm wide and has a surface flatness specification (peak-to-valley) of $\lambda/30$ at 633 nm. Due to space restrictions in MAX III the mirror reflects the vis–UV SR 90° upwards instead of sideways. Since the attenuation of the different polarization components of the SR depends on the bending direction of the mirror, the vertically (π) polarized light will be more attenuated than the horizontally (σ) polarized light at the MAX III diagnostic beam line. If π-polarized SR is the component most used for measurements, which is the case for light sources with very small vertical beam sizes, any potential mirror should reflect the light sideways instead of upwards to minimize the attenuation of the π-polarized SR.

The UV-grade fused silica symmetric spherical lens was custom made with the specifications 1.200 ± 0.024 m focal length at 500 nm, $70.0+0.0/-0.2$ mm diameter, $15.0+0.0/-0.5$ mm center thickness and a peak-to-valley surface deviation better than $\lambda/15$ at 633 nm. Measurements of the surface deviations, performed by the manufacturer, verified that surface deviations were within specifications. Measurements performed at MAX-lab determined a focal length of 1.220 m at 633 nm and 1.204 m at 488 nm, corresponding to a lens radius of 1.112 ± 0.001 m. The lens is placed in a lens holder so that it can be remotely taken in and out of the SR. The optical axis of the lens was measured to deviate by 2.4 ± 0.2 mrad from the direction of the SR.

The UV-grade fused silica window was custom made with the specifications $93.5+0.0/-0.2$ mm diameter, $20.0+0.0/-0.5$ mm thickness and a peak-to-valley surface flatness better than $\lambda/15$ at 633 nm. It was installed into a CF100 flange viewport. The surface flatness of the window was measured by the manufacturer before and after the installation into the viewport and was found to be well within specification.

3.2. Baffles and opening angles

To determine the electron beam profile (see Section 4) it is essential to know the horizontal and vertical opening angles of the beam line.

The vertical opening angle is determined by the SiC mirror. The height of the mirror is 50 mm. It is installed at a 45° angle with respect to the machine plane and the vertical light is further restricted by the mirror holder. Combined the effective mirror height is 31.5 mm, giving a vertical acceptance angle of ± 8.1 mrad. Ideally, the diagnostic beam line should accept all vertical light from the bending magnet. Simulations of the angular spectral flux of the MAX III bending magnet vis–UV SR for σ and π-polarized light show that a vertical opening angle of ± 8.1 mrad is enough to accept more than 99.8% of the vertical light. By removing the lens from the SR the intensity distribution of the SR could be studied. The vertical acceptance angle was verified to be centered better than to 0.8 mrad.

The horizontal opening angle is determined by the baffles and the mirror. The mirror is 60 mm wide, which gives a maximum opening angle of ± 15.5 mrad, which was verified experimentally. To keep clear from the edges of the mirror, the maximum baffle aperture used is 50 mm, corresponding to a horizontal opening angle of ± 13.6 mrad at 364 nm, ± 13.5 mrad at 488 nm and ± 13.5 mrad at 633 nm. The baffle aperture is controlled remotely with an accuracy better than 0.1 mm.

3.3. Optical rail with filters and CCD camera

The SiC mirror reflects the vis–UV dipole magnet SR at a 90° angle. A hole has been drilled into the MAX III ceiling to let the light pass through and an optical rail has been installed on the roof so that changes can be made to the measurement system while MAX III is running. The optical rail has been aligned with the SR to facilitate movement of the filters and CCD camera when measuring at different positions along the optical rail, i.e. at different SR wavelengths.

Since the filters are close to the camera, the surface flatness requirements on the filters are less stringent, allowing filters to be bought from off-the-shelf vendors instead of being custom made. A Glan–Taylor prism was selected as polarization filter, due to its high extinction ratio and large wavelength range. Three different laser-line filters, with central wavelength at 364 nm, 488 nm and 633 nm, and 1 nm FWHM bandwidth are used. For measurements with high current in MAX III neutral density filters are used to lower the intensity of the light.

The camera used in the setup has square pixels with a side length of 3.75 μm. The camera roll error was minimized by placing the CCD camera far off focus and aligning it with the central minimum of the π-polarized light. Far off focus the central minimum of the π-polarized light is determined by the bending plane of the dipole magnet instead of by the tilt of the electron beam. In this way the camera roll error relative the dipole bending plane was determined to be less than ± 5 mrad.

Measurements were also performed to make sure that the CCD output is linear with light intensity.

4. Determination of the electron beam profile

Ideally, the intensity profile measured by the diagnostic beam line camera would correspond to the electron beam profile at the source point scaled by the magnification factor of the system. However, that is not the case. A number of effects cause the image to deviate from the transverse electron beam intensity distribution. The narrow vertical opening angle of the SR and the horizontal aperture restrictions of the optical system give rise to diffraction effects. Additionally, the non-zero horizontal acceptance of the optical system means that the detected SR is not emitted from a point in the dipole magnet but generated along a part of the longitudinal electron trajectory in the dipole magnet. Since the longitudinally distributed source will not have a common image point, this gives rise to depth-of-field effects. The curvature of the longitudinally extended source will also affect the image.

These effects should of course be treated as a single phenomenon of SR emission, propagation and focusing, within the framework of classical electrodynamics. The Synchrotron Radiation Workshop (SRW) code [21] elegantly handles the numerical computations needed for such a treatment. The near-field SR emission by a filament electron beam passing through the bending magnet is modeled by SRW using the Fourier transform of the retarded scalar and vector potentials [22], preserving all phase information from the relativistic emission process. The subsequent propagation and focusing of the SR is modeled by SRW by applying the integral theorem of Helmholtz and Kirchoff [23] to this Fourier Transform (instead of applying it to the more common Fourier Transform of a spherical wave). As a consequence, the model includes in a natural way the diffraction effects as well as the depth-of-field and curvature effects. From the simulations it is possible to calculate the intensity distribution of the SR at the image plane.

The intensity distribution at the image plane corresponds to the image of a filament electron beam passing through the bending magnet would give rise to at the image plane (where the CCD of the camera is situated). It is called the filament-beam-spread function (FBSF). For a point source, this would correspond to the point-spread function. By deconvoluting the image detected by the CCD camera with the FBSF, using the Lucy–Richardson algorithm [24,25], the ideal image of the electron distribution is reconstructed. This ideal image can now be scaled by the magnification factor of the measurement system to determine the electron beam profile.

No assumptions on the distribution of the electrons in the beam are made in the calculations. However, at stable beam conditions, the electron beam profile can be assumed to be a two-dimensional Gaussian, which has been verified during measurements of the stored beam in MAX III. This Gaussian can be rotated due to betatron coupling and spurious vertical dispersion. By fitting a two-dimensional Gaussian to the reconstructed electron beam profile, the horizontal and vertical beam sizes (defined along the major and minor axes of the elliptical Gaussian) as well as the angular tilt of the electron beam at the source point can be determined.

4.1. Beam line model

The initial wave front is calculated at the position of the first component of the beam line (the mirror) based on the electron energy, dipole magnetic field, wavelength of the SR together with the distance to and size of the mirror. The wave front is then propagated through the lens and the baffles until it reaches the image plane. At the image plane the intensity distribution of the SR, i.e. the FBSF, is extracted for the π and σ polarized components of the SR.

The lens is modeled as a thin lens in SRW. In order not to introduce errors the distances to the lens in the model are given with respect to the principal points instead of the lens center. Another effect which has to be considered is that of monochromatic third-order optical aberrations (Seidel aberrations). Because of the small angular deviation between the optical axis of the lens and the direction of propagation of the SR, four of the five Seidel aberrations (coma, astigmatism, field curvature and distortion) are at least an order of magnitude smaller than aberrations from the manufacturing errors of the lens and can be neglected. The final Seidel aberration, the spherical aberration, is however on the same scale as the aberrations from manufacturing errors of the lens. It has thus been included in SRW as a phase error located at the same position as the lens.

While doing measurements to determine the image plane of the beam line, there were indications that the position of the image plane was different for the horizontal and vertical directions. Detailed measurements together with simulations in SRW showed that the image plane was about 10 mm closer to the lens in the horizontal direction than in the vertical direction. It is suspected that this astigmatism of the system originates from one of the optical components. In order to explain the astigmatism there would need to be a 0.1% difference in the horizontal and vertical bending radius of the lens or a bending of the mirror in one dimension with a focal length of about 900 m. It is unknown which optical component gives rise to the astigmatism, but in order to correct for it the lens is modeled in SRW to be slightly astigmatic. Beam profile measurements are typically performed in the vertical image plane and the FBSF is calculated accordingly.

4.2. Effects not included in the model

The SR is modeled to be monochromatic in the simulations. However, due to the 1 nm FWHM bandwidth of the laser line filters, this is not the case for the measured images. These chromatic aberrations will give rise to an error in the model. The uncertainty in the magnetic field (due to the defocusing gradient in the dipole), in the electron energy and in the vertical acceptance angle might also give rise to errors in the model. These four effects have been investigated using SRW. For a horizontal beam size of 101 μm the error from each of these effects is 0.1 μm or smaller. For a vertical beam size of 29 μm the corresponding errors are 0.2 μm or smaller. Compared to the spread in beam size from one measurement to the next (see Section 5) the errors are negligible for the horizontal beam size and small for the vertical beam size.

An effect that was found to slightly influence the results was errors in positioning the camera CCD relative to the position at which the FBSF was calculated (see Section 5). It is thus crucial to ensure that the camera is located at the same position at which the FBSF is calculated.

When calculating the FBSF, the optical components are assumed to be perfect. SR wave front distortions caused by imperfections, such as surface inaccuracies originating from the manufacturing of the components, are not corrected for. To facilitate high-precision measurements, it is essential that the optical components used are manufactured with a high surface accuracy.

4.3. Examples of beam profile measurements

Fig. 4 shows an example of a transverse beam profile measurement performed using σ-polarized light at a wavelength of 488 nm for a baffle opening of 20 mm (corresponding to a horizontal opening angle of ± 5.4 mrad). The measured CCD camera image is shown together with the FBSF and the resulting deconvoluted image. Fig. 5 shows a similar example, but with a baffle opening of 50 mm (± 13.5 mrad horizontal opening angle). Figs. 6 and 7 show examples of transverse beam profile measurements with π-polarized light. The measured images and the FBSFs vary significantly depending on the beam line settings. The deconvoluted images have a similar appearance, as can be seen in Figs. 4–7. This is of course expected, since the electron beam profile should be more or less identical for these images taken only a few minutes after each other.

Looking at Figs. 4–7, some wave optics features are clearly recognizable. The on-axis minimum for π-polarized light is clearly seen in the measured images in Figs. 6 and 7. For the FBSF the intensity in the minimum is zero. By using the smearing of the minimum by the finite vertical beam size it is possible to determine very small vertical beam sizes (see e.g. Ref. [19]). Another feature seen in Figs. 5 and 7 is the horizontal asymmetry of the measured images for large horizontal opening angles (large baffle apertures). This gives a clear experimental verification of the peculiar intensity distribution predicted by SRW. Because of the relatively large horizontal beam size in MAX III, the measured distribution is of course not showing the detailed fringes of the FBSF. However, for a future light source with a very small horizontal beam size, these fringes will be visible. It is the authors' suggestion, that the visibility of these fringes should be used (in a similar fashion as the π-polarization method is used for determination of small vertical beam sizes), as a sharp tool to determine horizontal beam sizes below 20 μm. An example of a future light source where such a small horizontal beam size is anticipated is the MAX IV 3 GeV synchrotron light source [26], which has recently started construction.

By scaling the deconvoluted image with the magnification factor of the system, the electron beam profile can be reconstructed. The horizontal and vertical electron beam sizes in MAX III as well as the tilt of beam ellipsis are determined by fitting a two-dimensional Gaussian to the reconstructed electron beam profile. By creating a two-dimensional Gaussian distribution, scaling it with the magnification factor of the system and convoluting it with the FBSF it is possible to create a calculated intensity distribution that corresponds to the image a certain electron beam profile would give rise to at the image plane. Fig. 8 compares the measured image from Fig. 7 with such a calculated intensity distribution. It also shows the reconstructed electron beam profile (Fig. 8(c)) and the fitted two-dimensional Gaussian distribution (Fig. 8(d)). The calculated image (Fig. 8(b)) gives a good prediction of the measured image (Fig. 8(a)). This can also be seen in Fig. 8(e), where vertical image profiles of the measured and calculated images are presented. The vertical image profiles result from integrating over 20 horizontal pixels centered on the horizontal maximum.

5. Investigation of the measurement system

To investigate the performance of the diagnostic beam line and the vis–UV imaging method, the electron beam profile was measured for different beam line settings. Fig. 9 shows the horizontal and vertical beam sizes measured at 48 different beam

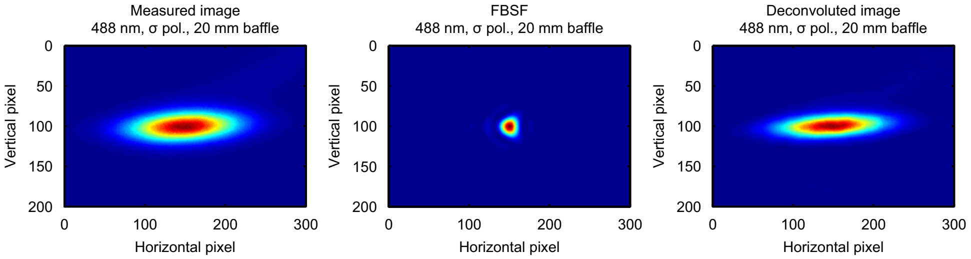

Fig. 4. Example of beam profile measurement with σ-polarized light at 488 nm. Measured image, filament-beam-spread function and deconvoluted image for baffle aperture 20 mm (± 5.4 mrad horizontal opening angle). Pixel size 3.75 μm.

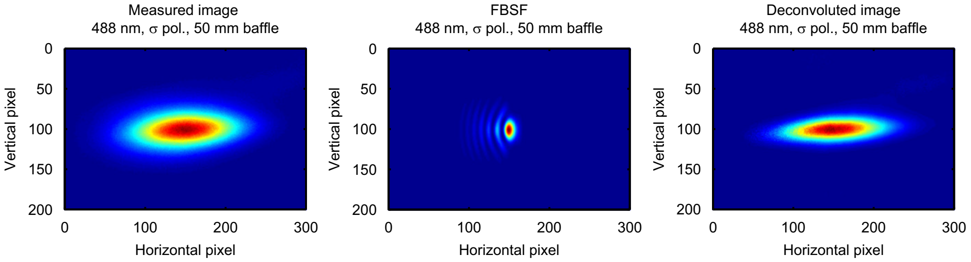

Fig. 5. Example of beam profile measurement with σ-polarized light at 488 nm. Measured image, filament-beam-spread function and deconvoluted image for baffle aperture 50 mm (± 13.5 mrad horizontal opening angle). Pixel size 3.75 μm.

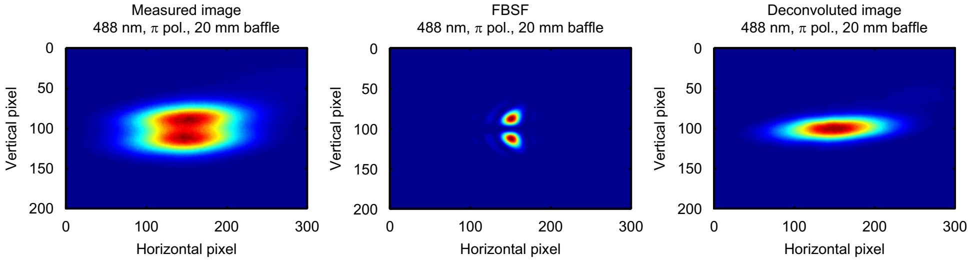

Fig. 6. Example of beam profile measurement with π-polarized light at 488 nm. Measured image, filament-beam-spread function and deconvoluted image for baffle aperture 20 mm (± 5.4 mrad horizontal opening angle). Pixel size 3.75 μm.

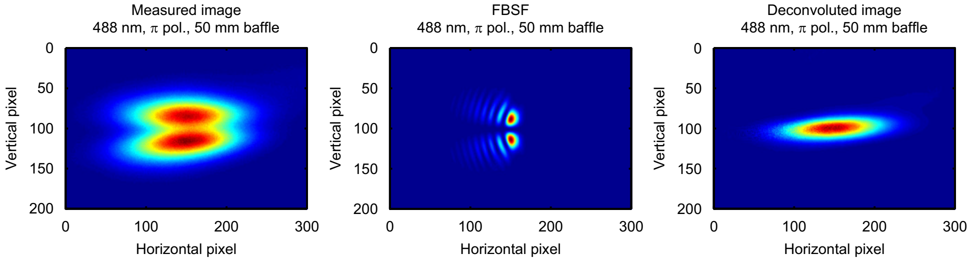

Fig. 7. Example of beam profile measurement with π-polarized light at 488 nm. Measured image, filament-beam-spread function and deconvoluted image for baffle aperture 50 mm (± 13.5 mrad horizontal opening angle). Pixel size 3.75 μm.

line settings, by first selecting the SR wavelength and then measuring at different baffle apertures and SR polarizations. For each measurement setting the horizontal and vertical beam sizes are presented as the mean and standard deviation (one sigma) of 50 images recorded and analyzed for that setting. The measurements were performed at the vertical image plane (see astigmatism in Section 4.1). The horizontal and vertical beam sizes are along the major and minor axes of the beam profile ellipse.

Assuming there are no changes in the electron beam during the measurements, the horizontal and vertical beam sizes in Fig. 9 should be independent of the measurement settings. To keep the electron beam as stable as possible, no insertion device gap changes, orbit corrections or other changes affecting the electron beam were performed during the measurements. Furthermore, the measurements were performed at a low current to keep changes of stored current to a minimum. In total, the measurements presented in Fig. 9 took around 70 min to complete. During this time the stored current in MAX III decreased from 1.7 mA to 1.6 mA. The shutter time of the camera was typically a few ms.

Combining these 2400 measurements gives a mean horizontal beam size of 101.3 μm with a standard deviation of 1.2 μm. Similarly, the vertical beam size is determined to be 28.9 ± 1.1 μm. The tilt of the beam profile ellipse is determined to be 61 ± 8 mrad. For the tilt an additional uncertainty of ± 5 mrad should be added due to the camera roll error. The above rms figures are thus including possible systematic errors between different beam line settings which would otherwise not be noted.

Some comments on the results are the following: Firstly, the manufacturing errors of the optical components are not included in the model. For different beam line settings, different areas of the optical components are exposed to the SR. The optical component surface inaccuracies will thus contribute to the difference in results for the different beam line settings. In order to correct for these distortions, the manufacturing errors would need to be properly measured and included in the beam line model. For the current setup this is too late, but for a future setup it would be recommended. Secondly, air turbulence between the vacuum exit window and the CCD camera contributes to the spread in measured beam sizes at individual beam line settings. In order to minimize the effects of air turbulence on the images, the vacuum window of the diagnostic beam line should be placed closer to the camera than is the case for the current setup. Thirdly, difficulties in finding the exact position of the image plane contributes to the spread between results for different wavelengths. A remotely controlled camera positioning, allowing faster image evaluation, would alleviate this problem.

Aside from these three possible improvements, the design of the MAX III diagnostic beam line has been found to work well. As seen in Section 4.3 the theoretical calculations agree well with the experimental observations. And, as seen in Fig. 9, there is good agreement between the measured beam sizes for all 48 different beam line settings investigated. Since it is possible to image the vis–UV SR directly onto a CCD, there is no need for a conversion via some kind of screen, which is the case for all X-ray methods. This is advantageous in view of resolving the true beam profile and simplifies the measurement system. In combination with the small number of components needed to build up a vis–UV imaging system, this makes imaging with vis–UV SR is a simple and cost-effective way to measure the electron beam profile.

6. Summary and conclusions

The MAX III diagnostic beam line utilizes SR in the vis–UV region to image the transverse electron beam profile in MAX III.

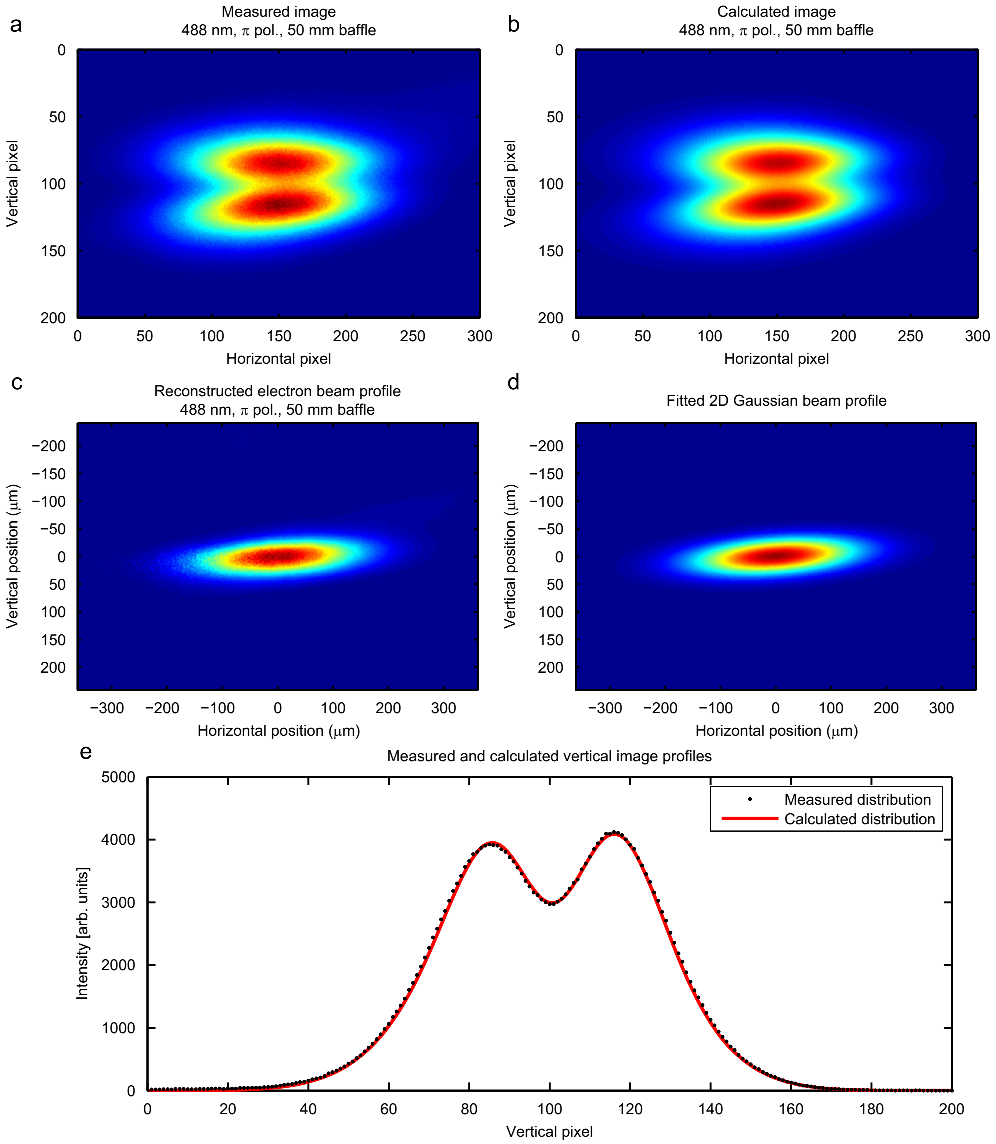

Fig. 8. Comparison between the measured and calculated image for π-polarized light at 488 nm with baffle aperture 50 mm (± 13.5 mrad horizontal opening angle). (a) shows the measured intensity distribution (same as in Fig. 7). (c) shows the reconstructed electron beam profile obtained by scaling the deconvoluted image with the magnification factor. (d) shows a two-dimensional Gaussian fit of the reconstructed electron beam profile. (b) shows a calculated image obtained by convoluting the scaled two-dimensional Gaussian with the FBSF. (e) shows the measured (dots) and calculated (solid line) vertical image profiles (integrated over 20 horizontal pixels centered on the horizontal maximum). Pixel size 3.75 μm.

By modeling the emission and subsequent propagation and focusing of the SR a FBSF is calculated for each setting of the diagnostic beam line. By deconvoluting the image recorded in the image plane with the FBSF a reconstruction of the ideal image, free from diffraction, depth of field and curvature effects, is obtained. This ideal image is then scaled by the magnification factor of the system to obtain the

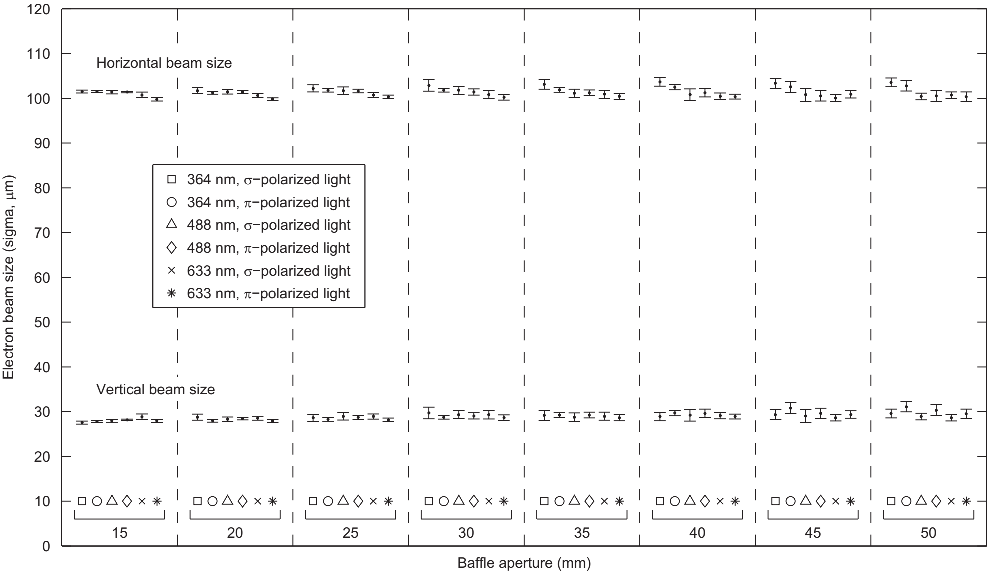

Fig. 9. Electron beam size measured for different SR wavelengths, polarizations and horizontal opening angles. For each measurement setting the horizontal and vertical beam sizes are presented as the mean and standard deviation of 50 images recorded and analyzed for that setting.

electron beam profile. Since no assumptions about the distribution of the electrons in the beam are made in the calculations, the full two-dimensional transverse electron beam profile is determined by the method. Also, in view of resolving a true beam profile, it is advantageous to work in the vis–UV region, allowing a direct imaging onto a CCD without the need of a conversion via some kind of screen, which is the case for all X-ray methods.

The appearance of the FBSF varies greatly depending on the measurement settings. The vertical double peak of π-polarized SR as well as the horizontal asymmetry for large horizontal opening angles (due to the curvature of the longitudinally distributed source) could be clearly observed experimentally, agreeing well with theoretical calculations. To investigate the performance of the diagnostic beam line, measurements were performed for 48 different beam line settings, varying the wavelength and polarization of the SR and the horizontal opening angle of the measurement system. There was good agreement between the results for different beam line settings. The measured electron beam profile was shown to have a horizontal beam size of 101.3 ± 1.2 µm and vertical beam size of 28.9 ± 1.1 µm.

A possible improvement of the setup would be to measure the surface inaccuracies of the optical components and include them in the beam line model. Also, the vacuum window should be placed closer to the CCD camera in order to minimize air turbulence. If π-polarized SR is the component most used for measurements, the mirror should reflect the light sideways instead of upwards to minimize the attenuation of the π-polarized SR.

One advantage of the beam line is the large maximum horizontal opening angle (±13.5 mrad). This makes it possible to clearly observe a horizontal asymmetry in the measured images, as predicted by the fringe pattern in the FBSF. It is the authors' suggestion, that the visibility of these fringes should be used (in a similar fashion as the π-polarization method is used for determination of small vertical beam sizes), as a sharp tool to determine horizontal beam sizes below 20 µm.

Acknowledgments

The authors would like to thank Magnus Sjöström for assisting in the scientific design of the MAX III diagnostic beam line, Håkan Svensson for the mechanical design and Bengt Sommarin for assembly and installation of the beam line.

References

[1] G. Kube, Review of synchrotron radiation based diagnostics for transverse profile measurements, in: Proceedings of the Eighth European Workshop on Diagnostics and Instrumentation for Particle Accelerators, Venice, pp. 6–10.
[2] S. Takano, Beam diagnostics with synchrotron radiation in light sources, in: Proceedings of the 2010 International Particle Accelerator Conference, Kyoto, pp. 2392–2396.
[3] P. Elleaume, C. Fortgang, C. Penel, E. Tarazona, Journal of Synchrotron Radiation 2 (1995) 209.
[4] J.C. Bergstrom, J.M. Vogt, Nuclear Instruments and Methods in Physics Research A 587 (2008) 441.
[5] C. Thomas, G. Rehm, I. Martin, R. Bartolini, Physical Review Special Topics—Accelerators and Beams 13 (2010) 022805.
[6] T. Mitsuhashi, Spatial coherency of the synchrotron radiation at the visible light region and its application for the electron beam profile measurement, in: Proceedings of the 1997 Particle Accelerator Conference, Vancouver, pp. 766–768.
[7] M. Masaki, S. Takano, Journal of Synchrotron Radiation 10 (2003) 295.
[8] S. Takano, M. Masaki, H. Ohkuma, Nuclear Instruments and Methods in Physics Research A 556 (2006) 357.
[9] G. Kube, J. Gonschior, U. Hahn, P. Ilinski, G. Priebe, H. Schulte-Schrepping, C. Wiebers, S. Weisse, C. G. Schroer, PETRA III diagnostics beamline for emittance measurements, in: Proceedings of the 2010 International Particle Accelerator Conference, Kyoto, pp. 909–911.
[10] A.P. Sabersky, IEEE Transactions on Nuclear Science NS-20 (1973) 638.
[11] A. Hofmann, F. Méot, Nuclear Instruments and Methods in Physics Research 203 (1982) 483.

[12] Å. Andersson, J. Tagger, Nuclear Instruments and Methods in Physics Research A 364 (1995) 4.

[13] U. Arp, Nuclear Instruments and Methods in Physics Research A 462 (2001) 568.

[14] J.C. Bergstrom, J.M. Vogt, Nuclear Instruments and Methods in Physics Research A 562 (2006) 495.

[15] O. Chubar, Resolution improvement in beam profile measurements with synchrotron light, in: Proceedings of the IEEE Particle Accelerator Conference 1993, pp. 2510–2512.

[16] O. Chubar, Novel applications of optical diagnostics, in: Proceedings of the 2000 European Particle Accelerator Conference, Vienna, pp. 177–181.

[17] Å. Andersson, M. Eriksson, O. Chubar, Beam profile measurement with visible synchrotron light on MAX-II, in: Proceedings of the 1996 European Particle Accelerator Conference, Sitges, pp. 1689–1691.

[18] M. Sjöström, H. Tarawneh, E. Wallén, M. Eriksson, Nuclear Instruments and Methods in Physics Research A 577 (2007) 425.

[19] Å. Andersson, M. Böge, A. Lüdeke, V. Schlott, A. Streun, Nuclear Instruments and Methods in Physics Research A 591 (2008) 437.

[20] M. Sjöström, E. Wallén, M. Eriksson, L.-J. Lindgren, Nuclear Instruments and Methods in Physics Research Section A: Accelerators, Spectrometers, Detectors and Associated Equipment 601 (2009) 229.

[21] O. Chubar, P. Elleaume, Accurate and efficient computation of synchrotron radiation in the near field region, in: Proceedings of the 1998 European Particle Accelerator Conference, Stockholm, pp. 1177–1179.

[22] L.D. Landau, E.M. Lifshitz, The Classical Theory of Fields, Pergamon, Oxford, 1975.

[23] M. Born, E. Wolf, Principles of Optics, Pergamon, New York, 1985.

[24] L.B. Lucy, Astronomical Journal 79 (1974) 745.

[25] W.H. Richardson, Journal of the Optical Society of America 62 (1972) 55.

[26] S.C. Leemann, Å. Andersson, M. Eriksson, L.-J. Lindgren, E. Wallén, J. Bengtsson, A. Streun, Physical Review Special Topics—Accelerators and Beams 12 (2009) 120701.

Paper III

Imaging of the MAX III electron beam profile using visible synchrotron radiation

A. Hansson, E. Wallén, Å. Andersson.

Proceedings of IPAC2011, San Sebastián, Spain, pp. 1332–1334 (2011).

TUPC132 **Proceedings of IPAC2011, San Sebastián, Spain**

IMAGING OF THE MAX III ELECTRON BEAM PROFILE USING VISIBLE SYNCHROTRON RADIATION

A. Hansson[*], E. Wallén, Å. Andersson, MAX-lab, Lund University, SE-22100 Lund, Sweden

Abstract

The recently assembled MAX III diagnostic beam line utilizes the bending magnet synchrotron radiation (SR) in the visible to ultraviolet range to form images of the transverse electron beam profile. Computer simulations model the generation and propagation of the SR through the beam line, taking into account effects such as diffraction, the longitudinally distributed source point and the curvature of the electron orbit. Using the diagnostic beam line, the electron beam size and the emittance in the MAX III synchrotron light source has been determined.

INTRODUCTION

Several different methods are used at synchrotron light sources to determine the transverse electron beam sizes [1]. The most common methods are pinhole cameras using synchrotron radiation (SR) in the X-ray range and interferometers using SR in the visible range. Other methods are imaging with visible to ultraviolet (vis-UV) SR and X-ray imaging using focusing optics, such as a Fresnel zone plate or compound refractive lenses.

The method used at MAX III is imaging with vis-UV SR. This used to be a common method, but other methods were developed since the optical resolution of the beam imaging with vis-UV SR seemed to be insufficient for measurements of small beam sizes. However, the optical resolution can be improved by exploiting the wave-optics features of SR together with detailed modeling of the SR emission and propagation through the imaging system [2, 3].

MAX III

The MAX III synchrotron light source was commissioned in late 2006 and characterized in 2008 [4]. It is a 3rd generation electron storage ring with an electron energy of 700 MeV intended for SR generation in the infrared and ultraviolet region. It has an eightfold periodicity, 36 m circumference and a design horizontal emittance of 13 nm rad. The storage ring makes extensive use of combined function magnets to obtain a compact lattice. Each unit cell contains a dipole with a defocusing gradient and two focusing quadrupoles with a sextupole component. Two insertion devices (ID) have been installed in the ring, providing SR in the ultraviolet region. A third beam line, which will utilize infrared light from one of the dipole magnets, is currently under construction.

MAX III DIAGNOSTIC BEAM LINE

The MAX III diagnostic beam line was designed and installed in 2010. A detailed description of the setup of the beam line and the method used to determine the transverse electron beam profile can be found in Ref. [5].

The source point of the beam line is the center of the bending magnet in cell 6 (D6) of MAX III. The vis-UV part of the SR is reflected 90 degrees upwards by a water-cooled SiC mirror. The mirror determines the vertical acceptance of the measurement system (±8.1 mrad). A fused silica symmetric spherical lens focuses the SR, whereas movable aperture restrictions (baffles) determine the horizontal opening angle. The SR propagates out of the vacuum system through a fused silica vacuum window. Close to the image plane, narrow band-pass filters and a Glan-Taylor polarizer select the wavelength and polarization of the measurement. At the image plane a CCD camera (pixel size 3.75 μm) records the intensity distribution of the SR.

DETERMINATION OF THE ELECTRON BEAM PROFILE

Ideally, the SR intensity distribution recorded by the beam line camera would correspond to the electron beam profile at the source point scaled by the magnification factor of the system. However, features like the narrow vertical opening angle of SR and the longitudinally distributed SR generation cause the image to deviate from the scaled electron beam intensity distribution. In order to reconstruct this ideal image, the measured intensity profile is deconvoluted with the image a single electron passing through the bending magnet would give rise to at the camera. By scaling the deconvoluted (ideal) image with the magnification factor the electron beam profile at the source point is reconstructed.

The image a single electron passing through the bending magnet would give rise to at the camera is called the filament-beam-spread function (FBSF). It is calculated numerically using SRW [6]. The emission and subsequent propagation and focusing of the SR through the beam line is treated within the framework of classical electrodynamics, including in a natural way effects such as diffraction, the longitudinally distributed source point and the curvature of the electron orbit.

Figure 1 shows an example of a beam profile measurement at MAX III using σ-polarized light at 488 nm. The measured CCD camera image is shown together with the FBSF and the resulting deconvoluted image. Figure 2 shows a similar example using π-polarized light.

---

[*] anders.hansson@maxlab.lu.se

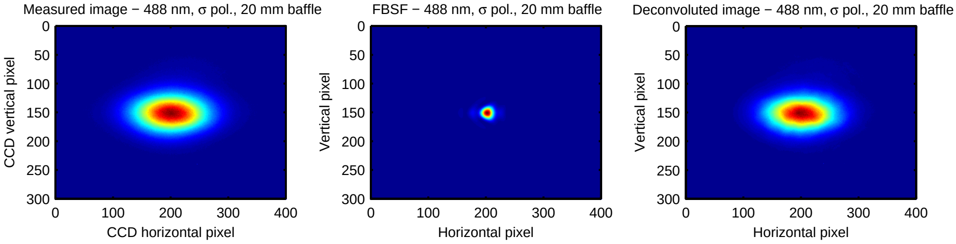

Figure 1: (Color) Example of beam profile measurement with σ-polarized light at 488 nm. Measured image, filament-beam-spread function and deconvoluted image for baffle aperture 20 mm (±5.4 mrad horizontal opening angle).

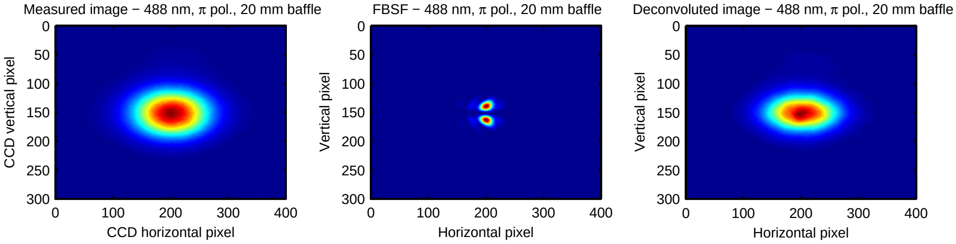

Figure 2: (Color) Example of beam profile measurement with π-polarized light at 488 nm. Measured image, filament-beam-spread function and deconvoluted image for baffle aperture 20 mm (±5.4 mrad horizontal opening angle).

MEASUREMENTS AND RESULTS

The MAX III diagnostic beam line has been used to determine the electron beam size, dispersion and emittance in the MAX III synchrotron light source. Using MATLAB LOCO [7] the machine functions, natural energy spread, momentum compaction and horizontal emittance of a fitted MAX III lattice has been determined. The details of the measurements are given below. Table 1 shows an overview of the results obtained, comparing the design values (from Ref. [4]) with results from the fitted lattice and diagnostic beam line measurements.

Electron Beam Size

The electron beam profile in MAX III is reconstructed by scaling the deconvoluted image with the magnification factor of the measurement system. The horizontal and vertical beam sizes as well as the tilt of the electron beam ellipsis are determined by fitting a two-dimensional Gaussian to the reconstructed electron beam profile. The beam sizes in MAX III are large enough to be determined both by σ and π-polarized light. 100 images were recorded with σ-polarized light and 100 images with π-polarized light at 488 nm wavelength and 20 mm baffle aperture (±5.4 mrad horizontal opening angle). The measurements (from which the images in Figs. 1–2 are taken) were performed at low current (1.5 mA) with the standard operating orbit in MAX III and all ID gaps open. The mean and standard deviation of the horizontal beam size σ_x and vertical electron beam size σ_y for the 200 analyzed images were

$$\sigma_x = 101.0 \pm 0.4\ \mu\text{m}$$
$$\sigma_y = 51.6 \pm 0.9\ \mu\text{m}$$

The performance of the diagnostic beam line has been investigated by doing a series of measurements where the beam line configuration was varied to utilize different wavelengths and polarizations of the SR and different horizontal opening angles of the measurement system [5]. Based on that investigation and experience from operating the beam line, the standard deviation of the systematic error of the measurement is estimated to be (smaller than) 2.0 μm, which gives

$$\sigma_x = 101.0 \pm 2.0\ \mu\text{m}$$
$$\sigma_y = 51.6 \pm 2.2\ \mu\text{m}$$

Fitted Lattice (LOCO)

Using MATLAB LOCO [7] a computer model of the MAX III ring was fitted to 24 sets of measurement data. Three response matrix measurements were performed, with the standard operating orbit and ID gaps open, at three different occasions. At each occasion eight different orbit changes due to changes in RF frequency were measured. By using several sets of input data the uncertainty in the fitted parameters could be estimated.

The mean and standard deviation of the natural energy

Table 1: MAX III Design and Measured Parameters.

	Design [4]	Fitted lattice	Measured
Horizontal beam size at center of D6, σ_x (μm)	-	-	101.0 ± 2.0
Vertical beam size at center of D6, σ_y (μm)	-	-	51.6 ± 2.2
Horizontal beta function at center of D6, β_x (m)	0.27	0.2731 ± 0.0056	-
Vertical beta function at center of D6, β_y (m)	12.8	13.978 ± 0.077	-
Horizontal dispersion at center of D6, η_x (m)	0.14	0.1358 ± 0.0027	0.1341 ± 0.0008
Vertical dispersion at center of D6, η_y (m)	0.00	0.0362 ± 0.0117	0.0278 ± 0.0002
Natural energy spread, σ_E/E	0.0006072	$0.00060005 \pm 0.00000013$	-
Momentum compaction, α_c	0.032559	0.032883 ± 0.000024	-
Horizontal emittance, ϵ_x (nm rad)	13	13.159 ± 0.041	13.7 ± 1.1
Vertical emittance, ϵ_y (mn rad)	-	-	0.170 ± 0.012
Coupling, κ	0.1	-	0.0124 ± 0.0013

spread σ_E/E, momentum compaction α_c, horizontal emittance ϵ_x, the beta functions β_x, β_y and dispersion η_x, η_y at the center of D6, for the 24 fitted lattices, are presented in Table 1.

Dispersion

The dispersion η_i can be determined from the orbit displacement Δi due to a shift in the RF frequency f_{RF}:

$$\eta_i = -\alpha_c \frac{\Delta i}{\Delta f_{RF}} f_{RF}$$

Using the diagnostic beam line the horizontal displacement Δx and vertical displacement Δy at the source point of the diagnostic beam line due to a shift in the RF frequency was determined to be

$$\Delta x/\Delta f_{RF} = -0.04081 \pm 0.00024 \text{ m/MHz}$$
$$\Delta y/\Delta f_{RF} = -0.00846 \pm 0.00005 \text{ m/MHz}$$

The uncertainty of the measurement is given by the uncertainty in determining the magnification factor. With f_{RF} = 99.925 MHz and using the fitted momentum compaction, the dispersion at the center of D6 is

$$\eta_x = 0.1341 \pm 0.0008 \text{ m}$$
$$\eta_y = 0.0278 \pm 0.0002 \text{ m}$$

Comparing with the fitted values for the dispersion it can be seen that the values agree, but that the accuracy is significantly better for the diagnostic beam line measurement.

Emittance and Coupling

The emittance ϵ_i is given by

$$\epsilon_i = \frac{\sigma_i^2 - (\sigma_E/E)^2\eta_i^2}{\beta_i}$$

The horizontal emittance ϵ_x and vertical emittance ϵ_y in MAX III can now be determined using the measurements of the electron beam size and dispersion function at the center of D6 together with the fitted LOCO results for the natural energy spread and the beta function at the center of D6.

$$\epsilon_x = 13.7 \pm 1.1 \text{ nm rad}$$
$$\epsilon_y = 0.170 \pm 0.012 \text{ nm rad}$$

The value used for the energy spread is the fitted natural energy spread. Since the beam size measurement was performed at a low current the actual energy spread is expected to be close to the natural energy spread. However, if there is a discrepancy the actual energy spread is expected to be larger than the natural energy spread, in which case the values for the emittance will be slightly overestimated. The measured horizontal emittance agree with the design value and with the fitted LOCO result.

The emittance coupling ratio in MAX III is

$$\kappa = \epsilon_y/\epsilon_x = 0.0124 \pm 0.0013$$

This value is significantly smaller than the design value of κ = 0.1. During standard operation a shaker connected to a strip line in the ring excites the vertical tune of the betatron oscillation in order to increase the vertical beam size.

REFERENCES

[1] G. Kube, in Proceedings of the eighth European Workshop on Diagnostics and Instrumentation for Particle Accelerators, Venice (2007) pp. 6–10.

[2] O. Chubar, in Proceedings of the 2000 European Particle Accelerator Conference, Vienna (2000) pp. 177–181.

[3] Å. Andersson, M. Böge, A. Lüdeke, V. Schlott, and A. Streun, Nucl. Instr. and Meth. A 591 (2008) 437.

[4] M. Sjöström, E. Wallén, M. Eriksson, and L.-J. Lindgren, Nucl. Instr. and Meth. A 601 (2009) 229.

[5] A. Hansson, E. Wallén, and Å. Andersson, "Transverse electron beam imaging system using visible synchrotron radiation", submitted for publication.

[6] O. Chubar and P. Elleaume, in Proceedings of the 1998 European Particle Accelerator Conference, Stockholm (1998), pp. 1177–1179.

[7] J. Safranek, G. Portmann, A. Terebilo, and C. Steier, in Proceedings of the European Particle Accelerator Conference, EPAC 2002, Paris (2002), pp. 1184–1186.

PAPER IV

Electron beam stability and lifetime at the MAX III synchrotron light source

A. Hansson, E. Wallén, Å. Andersson, J. Breunlin, G. Skripka.

Manuscript in preparation.

Electron beam stability and lifetime at the MAX III synchrotron light source

A. Hansson*, E. Wallén, Å. Andersson, J. Breunlin, G. Skripka

MAX-lab, Lund University, P.O. Box 118, SE-221 00 Lund, Sweden

Abstract

At low currents the horizontal beam size and bunch length in the MAX III synchrotron light source agree well with expected values. At higher currents, however, both the horizontal beam size and bunch length are strongly affected by longitudinal instabilities. The instabilities lead to an increase in the energy spread of the electron beam, which increase the bunch length but also the horizontal beam size through dispersion. A second passive Landau cavity has been installed in the storage ring and has been shown to dampen the instabilities. The observed bunch length and horizontal beam size is explained by the energy spread increase from the remaining instabilities and the bunch lengthening from the Landau cavities. The longitudinal bunch shape and the induced cavity voltages in the triple RF system agree well with simulations.

The electron beam lifetime in MAX III is significantly lower than the design lifetime. Vertical scraper measurements have determined the lifetime limitations in MAX III and have shown that the lifetime is Touschek limited. The low Touschek lifetime is explained by the lower than design emittance ratio and momentum acceptance. The paper also describes how a careful analysis of horizontal scraper measurement results could be used to identify and improve the horizontal acceptance and momentum acceptance of the storage ring.

Keywords: Beam lifetime, Beam size, Bunch length, Landau cavities

1. Introduction

The MAX III synchrotron light source was commissioned in late 2006 and characterized in 2008 [1]. Several issues remained for further investigation after the characterization. Among them were the low lifetime compared to the design value, an observed bunch lengthening at higher currents which suggested instability issues, and measurements of the transverse beam profile and emittance.

A diagnostic beam line that utilizes the synchrotron radiation in the visible to ultraviolet range to form images of the transverse electron beam profile was designed and installed in 2010. The imaging system and the method used to determine the transverse beam profile was described and investigated in Ref. [2]. Using the diagnostic beam line, the transverse beam profile for the normal operating settings was measured at low currents. The transverse beam sizes and emittances were determined and the horizontal beam size at the location of the diagnostic beam line and the horizontal emittance was found to agree with the design values [3]. The vertical beam size, however, was found to be smaller than design, leading to an emittance ratio smaller than design.

In this paper two of the remaining issues are addressed. Section 2 gives a short introduction to MAX III. In Sec. 3 the behavior of the transverse beam size and bunch length at higher currents is investigated, with and without a third harmonic Landau cavity. In Sec. 4 the lifetime limitations are determined and the cause of the lower than design lifetime is investigated. A summary and conclusions are given in Sec. 5. Appendix A describes the calibrations of the cavity voltages.

2. MAX III

MAX III is a 3rd generation synchrotron light source with an electron energy of 700 MeV intended for synchrotron radiation generation in the infrared and ultraviolet region. Five of the eight straight sections in MAX III are available for insertion devices. So far two insertion devices have been installed, an elliptically polarizing undulator and a planar undulator, providing synchrotron radiation in the ultraviolet region. A third beam line utilizes the infrared synchrotron radiation from one of the MAX III dipole magnets.

MAX III was also intended as a test bench for new accelerator technology. The storage ring makes extensive use of combined function magnets to obtain a compact lattice and a small 36 m circumference. It has an eightfold periodicity and each unit cell contains a dipole with a defocusing gradient and two focusing quadrupoles with a sextupole component. All magnets of the unit cell are machined into a common iron block resulting in an integrated girder-magnet design where the alignment errors are reduced to the level of machining accuracy. Based on the experiences from MAX III [1], the MAX IV synchrotron light source will use a similar compact magnet technology [4].

For the characterization of the storage ring [1], a computer model of MAX III was developed in MATLAB Accelerator Toolbox [5]. MATLAB LOCO [6] was used to fit linear optics measure-

---

*Corresponding author.

Email address: `anders.hansson@maxlab.lu.se` (A. Hansson)

ments to the MAX III model. Additional response matrix measurements and fits, using the current operating settings of MAX III, was performed for the determination of the emittance [3]. The average of these recent fits forms the basis of the currently used model. The model has been converted to a version compatible with OPA [7], which was used for the Touschek lifetime and momentum acceptance calculations in Sec. 4.

The RF system in MAX III consists of three RF cavities: one active cavity and two passive higher harmonic cavities. The main cavity operates at 100 MHz and is actively powered by a FM transmitter. A passive 500 MHz Landau cavity installed at the start-up of the ring never worked properly, possibly exciting a higher order mode when the cavity is tuned close to its operating point. It is thus detuned during normal operation. In October 2011 a new passive 300 MHz Landau cavity was installed. It is a prototype for the Landau cavities that will be used at MAX IV [4] and it is used during normal operation in MAX III. The calibration of the cavity voltages, needed in order to perform the simulations in this paper, are described in Appendix A.

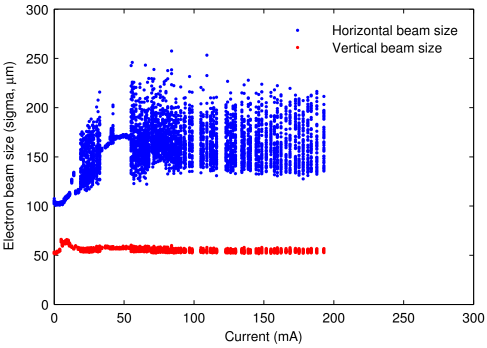

Figure 1: Horizontal and vertical beam size in the center of the dipole in cell 6 of MAX III as a function of stored current in April 2011. The 300 MHz Landau cavity was not yet installed and the 500 MHz Landau cavity was tuned out. The systematic error of the measured beam size is estimated to be ± 2 μm.

3. Stability

During the characterization of MAX III, current dependent bunch lengthening was observed [1]. The cause or nature of the instabilities was not investigated further. During the commissioning of the diagnostic beam line [2] an unstable beam size was noticed. The investigation of the imaging system was performed at low currents where the beam size was stable and reproducible from fill to fill. The emittance was determined in the same region of current [3]. In this section the focus is instead on the behavior of the beam at higher currents.

A spectrum analyzer has been used to observe the frequency spectrum of the beam. At higher currents there are plenty of longitudinal multi-bunch modes. When the instabilities are most severe, there are modes around all the RF and revolution peaks. Not only dipole modes are seen, but also higher order modes. Longitudinal modes with a distance from the revolution peak from one to eight times the synchrotron frequency have been observed on the spectrum analyzer. The higher order modes diffuse the electron density and increase the bunch length as well as the energy spread of the electrons.

No transverse modes have been observed at operating conditions. However, when increasing the RF frequency and thus decreasing the energy, the vertical chromaticity comes close to zero and transverse modes (both vertical and horizontal) have been observed on the spectrum analyzer. In these cases the vertical beam size increases dramatically and becomes unstable.

3.1. Transverse beam size

The diagnostic beam line in MAX III observes the synchrotron radiation emitted from the center of the dipole magnet in cell 6. At this location the horizontal beta function has a minimum and the vertical beta function has a maximum. The horizontal dispersion is positive everywhere in the ring, with the largest dispersion in the straights and the lowest values at the center of the dipole magnets. At low currents the horizontal beam size (one sigma) is around 100 μm and the vertical beam size (one sigma) is around 50 μm in the center of the dipole in cell 6. Figure 1 shows the horizontal and vertical beam size as a function of current in April 2011. At this time the 300 MHz Landau cavity was not yet installed and the 500 MHz cavity was tuned out. At each measured current 50 images were recorded and analyzed at a rate of three images per second and an integration time per image of around one ms. The systematic error of the measured beam size is estimated to have a standard deviation of 2 μm [2, 3]. As seen in Fig. 1, the beam clearly suffers from instabilities. An increase in the average horizontal beam size as well as a large difference in the horizontal beam size from one image to the next is apparent at higher currents. The vertical beam size is also affected by the instabilities, but the effect is smaller.

In October 2011 the new 300 MHz Landau cavity was installed. Since then it has been part of the routine operation of MAX III. Figure 2 shows the horizontal and vertical beam size as a function of current in April 2012. During the measurement the 300 MHz Landau cavity was tuned in and kept at a constant resonance frequency. The 500 MHz Landau cavity was tuned out. The measurement settings were otherwise identical to the settings used in the measurement presented in Fig. 1. With the new 300 MHz Landau cavity tuned in the beam is more stable, resulting in smaller transverse beam sizes and lower differences in the beam size from one image to the next. The longitudinal multi-bunch modes, observed with the spectrum analyzer, are also less pronounced. At lower currents, where the voltages in the passive Landau cavities are lower and there is less Landau damping, the average beam size is larger than at higher currents. Still, the difference in beam size from image to image is smaller than before the cavity was installed. The damping of the instabilities is most effective in the current range 110-250 mA, which is the main window of operation for MAX III.

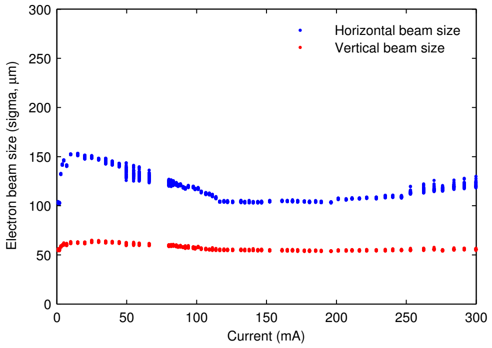

Figure 2: Horizontal and vertical beam size in the center of the dipole in cell 6 of MAX III as a function of stored current in April 2012. The 300 MHz Landau cavity was tuned in and the 500 MHz Landau cavity was tuned out. The systematic error of the measured beam size is estimated to be ± 2 μm.

Based on observations with the spectrum analyzer, the increase in transverse beam size is believed to originate from an increase in the energy spread of the beam due to longitudinal instabilities. The energy spread influences the transverse beam sizes through dispersion. The vertical change in beam size is smaller than the horizontal change, which is to be expected because of the small spurious vertical dispersion. If the transverse emittances and coupling are constant, the relation $\sigma_x^2 - \eta_x^2\sigma_\delta^2$ is also constant, where σ_x is the horizontal beam size, η_x the horizontal dispersion and σ_δ the energy spread. At low currents, where the beam is stable and the energy spread is equal to the natural energy spread, the constant can be determined. Knowing the constant, the energy spread at different currents can be determined from the horizontal beam size.

If the increase in beam size is indeed due to an increase in energy spread, the determined energy spread can be used to simulate the longitudinal bunch shape and bunch length. By comparing the simulated bunch lengths with measured bunch lengths, the assumption that the beam size increase comes from an energy spread increase can be tested.

3.2. Bunch length

At the same occasion as the transverse beam size presented in Fig. 2 was measured, part of the time the light from the diagnostic beam line was diverted to an optical sampling oscilloscope in order to measure the longitudinal bunch shape. In the sampling head of the optical sampling oscilloscope the incident light is focused and converted into photo electrons at a photo cathode. The electron path is bent by deflecting plates and swept over a slit. The electrons passing the slit generate light on a phosphor screen which is transformed into an electric signal by a photomultiplier tube. The signal was sampled with 2048 points on a 2.4 ns time axis. Figure 3 shows the measured full width at half maximum (FWHM) bunch length as a function of stored current. The total data acquisition time was about 70 seconds per measurement point. The error is estimated to be ± 3% for the measured bunch lengths. Unless otherwise noted, the error estimations in this paper are given as standard deviations.

The bunch length was also measured with a strip line. The signal from the strip line was connected to a spectrum analyzer where the frequency spectrum was measured. The envelope of the RF harmonics, taking into account the cable attenuation and the strip line frequency modulation, gives information about the bunch length. The fit to the amplitude of the RF harmonics is made simpler if the shape of the distribution is known. At low currents, where the beam is stable and the bunch shape is Gaussian, a few measurement points from the strip line are included in Fig. 3. For higher currents, where the bunch shape is not necessarily Gaussian, only measurements from the optical sampling oscilloscope are used. The error of the strip line measurement is estimated to be ± 5%.

The main cavity voltage was kept constant at 108 ± 1 kV during the entire measurement. The RF frequency was 99.925 MHz. The 300 MHz Landau cavity resonance frequency was kept constant at 299.972 ± 0.001 MHz, 197 ± 1 kHz from the third RF harmonic. The 500 MHz Landau cavity resonance frequency was kept constant at 500.328 ± 0.001 MHz, 703 ± 1 kHz from the fifth RF harmonic. The peak voltage seen by the beam in a passive Landau cavity is given by

$$V_{Landau} = R_S I F \cos\Psi \tag{1}$$

where R_S is the transit-time corrected shunt impedance of the Landau cavity (defined as $R_S \equiv V_{Landau}^2/P_{cav}$, where P_{cav} is the cavity losses), I is the stored current, F is the form factor and Ψ is the tuning angle given by

$$\Psi = \arctan\frac{2Q(f_{res} - Nf_{RF})}{f_{res}} \tag{2}$$

where Q, f_{res} and N are the quality factor, the resonance frequency and the harmonic number of the Landau cavity and f_{RF} is the RF frequency of the main cavity. Once the Landau cavity voltage amplitude, V_{Landau}, and its phase relative to the main RF are determined for both Landau cavities, the combined voltage and potential of the triple RF system are fixed as well. In this potential, the electron energy loss per turn should include the losses in the Landau cavities. The bunch shape is then given by knowledge of the relative energy spread and the momentum compaction factor [8]. However F, being the Fourier component of the bunch shape at the harmonic closest to the Landau cavity frequency, is unknown for both Landau cavities. Likewise are the phases of these components unknown. Still, it is possible to find, by an iterative process, the self-consistent solution to the problem, i.e. the bunch shape and position relative to the main RF, which fulfills Eq. 1 and gives the proper Fourier component phase for both Landau cavities.

Figure 3 shows the result of two such simulations of the triple RF system. One simulation uses the energy spread calculated from the measured horizontal beam size, and the other uses the natural energy spread. The natural bunch length is also plotted in Fig. 3. The natural bunch length is the bunch length the electron beam would have if there were no instabilities and

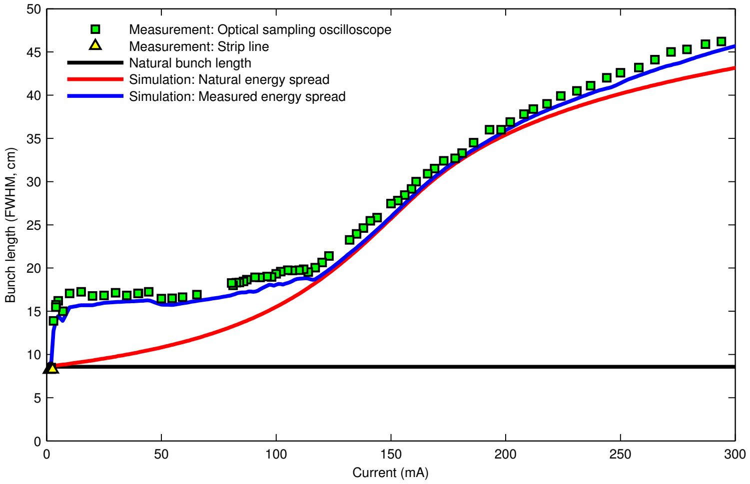

Figure 3: Bunch length in MAX III as a function of stored current in April 2012. The bunch length is measured with an optical sampling oscilloscope for the entire current range and with a strip line for the low current values where the beam shape is Gaussian. The error of the measured bunch length is estimated to be ± 3% for the optical sampling oscilloscope measurement and ± 5% for the strip line measurement. The three lines correspond to the natural bunch length and the simulated bunch length from simulations performed with the natural energy spread and with the measured energy spread.

no lengthening from the Landau cavities. The simulation with natural energy spread takes into account the bunch lengthening from the Landau cavities but not the bunch lengthening from instabilities. The simulation with measured energy spread includes both effects and should, if the assumption that the increase in horizontal beam size is due to an increase in energy spread is correct, correspond to the measured bunch length. As can be seen in Fig. 3, the measured bunch length agrees well with the simulation based on the measured energy spread. This verifies the interpretation that the beam size increase comes from an energy spread increase. Above the threshold of the instabilities and before it is damped down by the Landau cavities the instabilities give rise to a bunch length about twice the natural bunch length. The measured FWHM bunch length is systematically about 1 cm longer than the simulated bunch length. The source of this systematic error is unknown.

Figure 4 shows three examples of bunch shapes from the measurement in Fig. 3 together with the corresponding simulation based on the measured energy spread. At low currents (left-hand plot in Fig. 4) the beam is stable and the fields in the Landau cavities are low, which gives a Gaussian bunch shape and a bunch length close to the natural bunch length. At medium currents (middle plot in Fig. 4) the fields in the Landau cavities distorts the bunch shape and elongates the bunch. At high currents (right-hand plot in Fig. 4) the fields in the Landau cavities over-stretches the bunches so that two peaks are formed. In order to verify that the over-stretched bunch shape was real and not a time-averaging artifact of the optical sampling oscilloscope, measuring on an unstable beam, the bunch shape was also measured single-shot with a fast diode. Although the single-shot bunch shapes were noisy it was still clear that the over-stretched bunch shape was real.

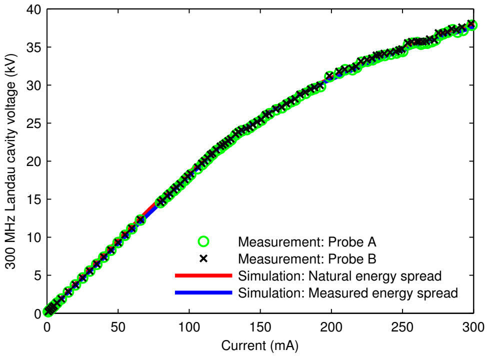

Figure 5: 300 MHz Landau cavity voltage as a function of stored current for the bunch length measurement in Fig. 3. The voltage was measured from calibrated signals from two different probes on the cavity. The error of the measured voltage is estimated to be ± 1%. Simulations were performed with the natural energy spread and with the measured energy spread.

Figure 5 shows the 300 MHz Landau cavity voltage as a function of stored current for the measurement in Fig. 3. Figure 6 shows the same for the 500 MHz Landau cavity voltage. The results from the simulations are shown together with measurements of the Landau cavity voltages from calibrated probes on the cavities (see Appendix A for details on the calibration). If

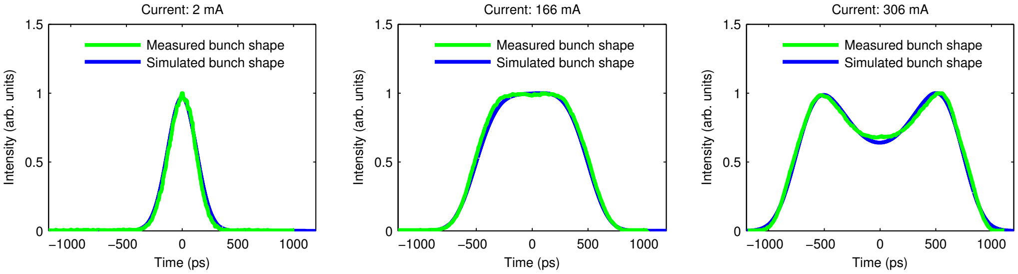

Figure 4: Three examples of measured and simulated bunch shapes from the bunch length measurement in Fig. 3. The measurement is done with the optical sampling oscilloscope. The simulation is performed with the measured energy spread. At low currents (left) the beam is stable and the fields in the Landau cavities are low, which gives a Gaussian bunch shape and a bunch length close to the natural bunch length. At medium currents (middle) the fields in the Landau cavities distorts the bunch shape and elongates the bunch. At high currents (right) the fields in the Landau cavities over-stretches the bunches so that two peaks are formed.

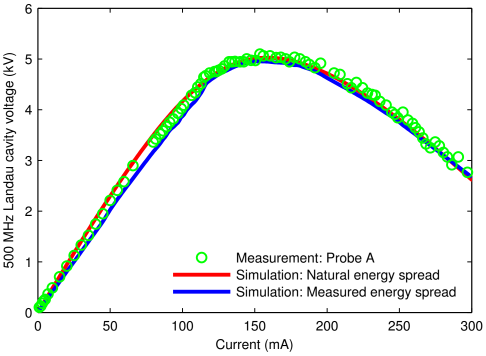

Figure 6: 500 MHz Landau cavity voltage as a function of stored current for the bunch length measurement in Fig. 3. The voltage was measured from a calibrated signal from a probe on the cavity. The error of the measured voltage is estimated to be ± 2%. Simulations were performed with the natural energy spread and with the measured energy spread.

the form factors at 300 and 500 MHz were constant the voltages in the Landau cavities would increase linearly with stored current (see Eq. 1). However, as the bunch length increases the form factors decrease. For the 300 MHz Landau cavity voltage (Fig. 5) this is seen as a slower increase in the voltage. For the 500 MHz Landau cavity voltage (Fig. 6) the form factor at higher currents decreases faster than the current increases as the bunch length grows and the bunch shape is distorted. The voltage reaches a maximum at around 150 mA and then starts to decrease for higher currents. Even though the 500 MHz cavity is tuned 703 ± 1 kHz from the fifth RF harmonic, the fields are still large enough to affect the bunch length in MAX III.

4. Lifetime

The lifetime in MAX III has never been close to the design lifetime. In order to alleviate this problem a signal generator is connected to a strip line in MAX III during normal operation and excites the vertical tune in order to increase the vertical beam size. This procedure increases the lifetime but makes the vertical beam size unstable and it is sensitive to shifts in the vertical tune due to movements of the gaps of the undulators. The measurements presented in Sec. 3 as well as the measurements presented in this section were all performed with the vertical excitation disabled.

Unless otherwise noted, the main cavity voltage for the measurements presented in this section was 108 ± 1 kV. The RF frequency was 99.925 MHz and the 500 MHz Landau cavity resonance frequency was 500.328 ± 0.001 MHz, the same settings as in the previous section. The 300 MHz Landau cavity was however tuned further out, with the resonance frequency kept constant at 300.193 ± 0.001 MHz, 418 ± 1 kHz from the third RF harmonic. The lifetime in MAX III is determined from the decay of current as measured by a DC current transformer. The error of the lifetime measurement depends on the accuracy of the DC current transformer and the current loss during the data acquisition period. The data acquisition period was 60 s and the error was estimated to be smaller than 0.3%. The error estimations are given as standard deviations.

4.1. Lifetime limitations and vertical acceptance

In December 2011, vertical and horizontal scrapers were installed in MAX III. The scrapers can be used to determine the different lifetime limitations contributing to the total lifetime in MAX III. The total lifetime in an electron storage ring is given by

$$\frac{1}{\tau} = \frac{1}{\tau_{elastic}} + \frac{1}{\tau_{inelastic}} + \frac{1}{\tau_{Touschek}} + \frac{1}{\tau_{quantum}} \tag{3}$$

where $\tau_{elastic}$ and $\tau_{inelastic}$ are the lifetimes due to the elastic and inelastic scattering of the beam electrons on the atoms of the residual gas, $\tau_{Touschek}$ is the lifetime due to electron-electron scattering and $\tau_{quantum}$ is the lifetime due to emission of synchrotron radiation.

The vertical scraper predominantly acts on electrons that have been elastically scattered on residual gas nuclei. At the position of the vertical scraper the vertical beam size is around 16 μm (one sigma). As long as the scraper is further away than 0.1 mm from the beam center the contribution of the quantum lifetime to the total lifetime is negligible. Inelastic scattering on the residual gas and the Touschek effect affects the energy of the beam electrons. If the vertical scraper affects the momentum acceptance it will also affect the inelastic and Touschek lifetime. Measurements show that as long as the scraper is 0.25 mm or further away from the beam center the momentum acceptance is not influenced. At 0.25 mm and further away, it is thus only the elastic lifetime that is affected by the vertical scraper. Also, since the momentum acceptance is not affected, the position where the scraper becomes the vertical restricting aperture determines the vertical acceptance.

The elastic lifetime for a one-dimensional vertically limiting aperture is given by [9]

$$\frac{1}{\tau_{elastic}} = c n_g \frac{2\pi r_e^2 Z^2}{\gamma^2} \left[\frac{\langle \beta_y \rangle \beta_y}{a_y^2} \right] \tag{4}$$

where c is the speed of light, n_g is the residual gas density, r_e is the classical electron radius, Z is the atomic number of the residual gas, γ is the relativistic factor of the electrons in the stored beam, $\langle \beta_y \rangle$ is the vertical beta function averaged over the storage ring, β_y is the vertical beta function at the limiting vertical aperture and a_y is the limiting vertical aperture. By combining Eq. 3 and Eq. 4 and measuring the total lifetime at different positions of the vertical scraper, a fit can be made on the data to determine the elastic lifetime and the combined inelastic and Touschek lifetime. The vertical acceptance a_y^2/β_y is constant until the scraper becomes the limiting aperture. When the scraper is the limiting aperture, a_y is the distance between the vertical scraper and the beam center and β_y is the vertical beta function at the vertical scraper. The design value for the vertical acceptance is 7.8×10^{-6} m and the design limiting vertical aperture is in the center of the dipole vacuum chamber. If the residual gas composition is known, the residual gas density can be determined from Eq. 4. This can be used to determine the inelastic lifetime. When the inelastic lifetime is known the Touschek lifetime can be separated from the combined inelastic lifetime and Touschek lifetime. This was how the lifetime limitations in MAX II were determined [10, 11].

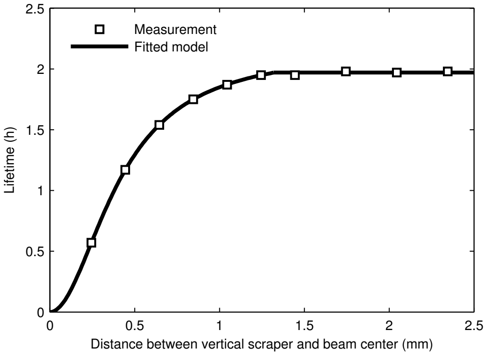

Figure 7: Vertical scraper measurement at around 300 mA stored current. Measurement of the lifetime in MAX III as a function of the distance between the vertical scraper and the beam center. The error of the measured lifetime is estimated to be smaller than ± 0.3%. The solid line corresponds to a fitted model to the measurement data.

In MAX III in normal operating mode γ is 1370 ± 10, $\langle \beta_y \rangle$ is 4.478 ± 0.001 m and the vertical beta function at the vertical scraper position is 1.37 ± 0.01 m. Figure 7 shows a measurement of the lifetime in MAX III as a function of the distance between the vertical scraper and the beam center in April 2012. The main cavity voltage was 130 ± 1 kV and the stored current was around 300 mA. The measurement was performed after the main cavity was moved (see Sec. 4.2 for details). Figure 7 also shows the fitted model. Three different vertical scraper measurements with similar settings were performed during the same day. The mean and standard deviation of the elastic lifetime for the three measurements is 22.3 ± 0.9 h and the corresponding result for the combined inelastic lifetime and Touschek lifetime is 2.18 ± 0.01 h. The vertical scraper becomes the vertical restricting aperture at 1.35 ± 0.02 mm, which gives a vertical acceptance of $1.33 \pm 0.03 \times 10^{-6}$ m, much smaller than the design acceptance. The horizontal acceptance is larger than $44 \pm 2 \times 10^{-6}$ m (see Sec. 4.2), which makes the assumption in Eq. 4 of a one-dimensional limiting aperture valid.

Unfortunately, there is no good residual gas analyzer at MAX III. For comparison, measurements on MAX II showed a vacuum dominated by H_2 with average $Z^2 = 3.4$ [11]. The situation in MAX III is likely similar. The shortest inelastic lifetime in MAX III would be for 100% H_2. The inelastic lifetime would in that case be 147 ± 8 h for the three measurements. All other residual gas compositions give a longer inelastic lifetime. Based on that information the Touschek lifetime can be determined to be 2.20 ± 0.03 h.

In Table 1 the measured lifetimes are compared to the design lifetimes. The design Touschek lifetime was 4.5 Ah for an emittance ratio of 0.10. The design vacuum lifetime (the combined elastic and inelastic lifetime) was 2.6 Ah at start-up and 5.2 Ah

Table 1: Comparison design and measured lifetimes. The design lifetimes are scaled to 300 mA stored current from [12], the measured lifetimes are for 300 mA stored current in April 2012.

	Design [12]	Measured
Total lifetime (h)	8	1.98 ± 0.01
Elastic lifetime (h)	-	22.3 ± 0.9
Inelastic lifetime (h)	-	≥147 ± 8
Vacuum lifetime (h) [a]	17	21 ± 2
Touschek lifetime (h)	15	2.20 ± 0.03
Momentum acceptance	0.020	0.0158 ± 0.0003
Emittance ratio	0.10	0.012 ± 0.001 [3]

[a] Combined elastic and inelastic lifetime

after some years of operation [12]. The larger of these two design vacuum lifetimes is used in Table 1. Table 1 also includes the measured and design values for the momentum acceptance and emittance ratio. The measurement of the momentum acceptance is described in Sec. 4.2 and the emittance ratio was determined in Ref. [3]. The measured vacuum lifetime is somewhat larger than the design vacuum lifetime, in spite of the low vertical acceptance. This suggest a better vacuum in MAX III than what was expected during the design. The measured Touschek lifetime, however, is far from the design value. At current operating conditions, the MAX III lifetime is clearly Touschek limited. The low Touschek lifetime and possible measures to increase it is discussed in Sec. 4.3.

The linear Touschek lifetime has been calculated using OPA for a fitted model of MAX III (see Sec. 2). For the settings used when measuring the lifetime limitations the calculated Touschek lifetime is 0.80 h, a factor of 2.7 smaller than the measured Touschek lifetime. The OPA calculation does not take the bunch lengthening from the Landau cavities and the increased energy spread from the instabilities into account. The energy spread and bunch length was measured during one of the vertical scraper measurements and a simulation of the triple RF system was performed. Using the measured energy spread together with the bunch shape and the small separatrix reduction resulting from the triple RF system, the Touschek lifetime was calculated using ZAP [13] to be 2.8 h, a factor of 1.3 larger than the measured Touschek lifetime.

4.2. Horizontal acceptance and momentum acceptance

At the position of the horizontal scraper the horizontal beam size is around 350 μm. For a horizontal scraper measurement, the quantum lifetime contribution to the total lifetime is negligible as long as the horizontal scraper is further away than 2 mm from the beam center. The three other lifetimes, however, all depend on the horizontal scraper position, since it affects both the horizontal acceptance and the linear lattice momentum acceptance. Still, useful information can be obtained from horizontal scraper measurements.

Figure 8 shows the horizontal aperture at the position of the horizontal scraper as a function of frequency change from the normal operating frequency. The horizontal aperture at the position of the scraper is in this context the distance between the beam center and the horizontal scraper position where an effect on the lifetime starts to appear. The measurements were performed shortly after the scrapers were installed in December 2011. The error in determining the horizontal aperture depends both on the error in determining the beam center and the error in determining the horizontal scraper position where an effect on the lifetime starts to appear. Since the MAX III lifetime is Touschek limited and the vertical acceptance is small the main effect on the lifetime from the horizontal scraper will appear when the momentum acceptance is affected. For the design apertures the horizontal scraper would, according to OPA calculations, start to affect the linear lattice momentum acceptance at 17.4 ± 0.1 mm from the beam center. The horizontal aperture as measured in Fig. 8 is clearly smaller. A dependency on the frequency can be observed. At lower frequencies the electron energy is increased since the momentum compaction is positive. Since all locations in MAX III have positive dispersion the beam will move outwards when the energy is increased. This corresponds to a smaller horizontal aperture in Fig. 8. If the frequency is increased the electron energy is lower and the beam will move towards the center of the storage ring. This corresponds to a larger horizontal aperture in Fig. 8. The behavior of the horizontal aperture suggests that a physical horizontal aperture, significantly smaller than the design value, is located someplace on the outer side of the vacuum system.

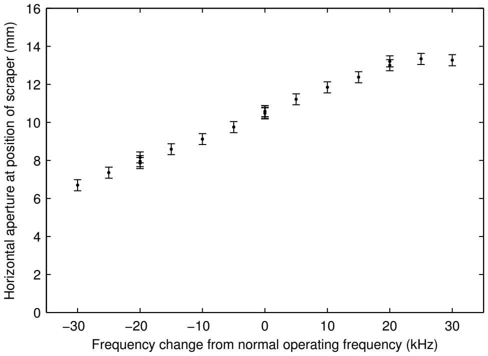

Figure 8: Horizontal aperture at the position of the horizontal scraper as a function of frequency change relative the normal operating frequency. The horizontal aperture is given by the distance between the beam center and the scraper position where an effect on the lifetime starts to appear.

At around +20 kHz the horizontal aperture does not appear to increase any further when increasing the frequency. The measurements were performed at 108 ± 1 kV main cavity voltage and around this point the Touschek scattered electrons are not lost because of the linear lattice momentum acceptance from the horizontal restricting aperture but because of the limiting RF momentum acceptance.

On the horizontal outer side of the vacuum system the smallest design apertures are given by the absorbers. Electron orbits with local orbit bumps were created in order to locate the re-

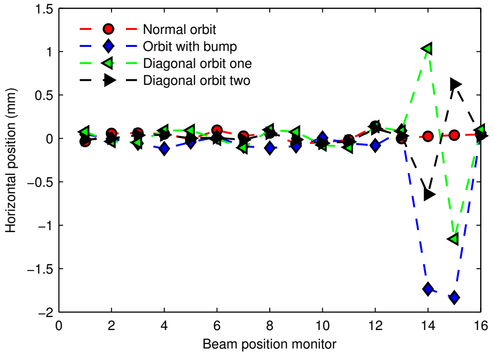

Figure 9: Horizontal beam position at the 16 beam position monitors in MAX III for four different orbits. The error of the measured beam position is estimated to be ± 0.05 mm.

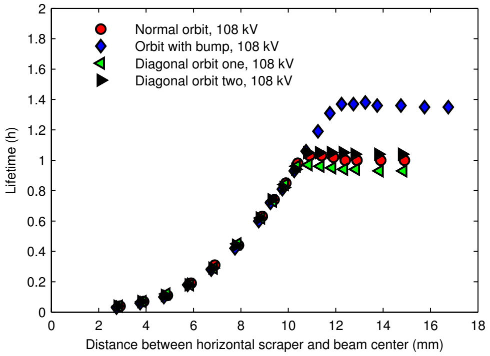

Figure 10: Horizontal scraper measurements for the four different orbits from Fig. 9. Measurements of the lifetime as a function of the distance between the horizontal scraper and the beam center. The error of the measured lifetime is estimated to be smaller than ± 0.3%. The uncertainty in the location of the beam center is estimated to be ±0.2 mm. The measurements were performed at a main cavity voltage of 108 ± 1 kV.

stricting aperture. Figure 9 shows the horizontal beam position at the 16 beam position monitors in MAX III for four different orbits. One orbit is the normal operating orbit in MAX III and the other three have different orbit distortions around the main cavity straight section. The main cavity straight section starts at beam position monitor 14 and ends at beam position monitor 15. Figure 10 shows horizontal scraper measurements for the four different orbits from Fig. 9. The lifetime is measured as a function of the distance between the horizontal scraper and the beam center. The uncertainty in the location of the beam center is estimated to be ±0.2 mm. The measurements were performed at a main cavity voltage of 108 ± 1 kV. The scraper measurement corresponding to the orbit with the local bump has a larger lifetime than the other three measurements when the horizontal scraper is far from the beam. The position at which the scraper starts to affect the lifetime is further away from the beam. This suggests that the horizontal aperture restriction is situated in the main cavity straight section. The orbit with the local bump moves the electron beam towards the inside of the ring in the main cavity straight section. The aperture restriction is thus located on the outer side of the ring, which is supported by the conclusion from the measurement in Fig. 8.

For the two diagonal orbits in Fig. 9 and 10 the scraper measurements show only small differences. The diagonal orbit two appears to lead to a slightly higher lifetime than the normal orbit which in turn appears lead to a slightly higher lifetime than the diagonal orbit one. This suggests that the aperture restriction is located close to the center of the main cavity straight section, where the diagonal orbits cross the normal orbit. Since diagonal orbit two appears to be give a higher lifetime than diagonal orbit one the aperture restriction is likely located slightly upstream the center of the main cavity straight section. Figure 11 shows a drawing of the MAX III main cavity straight section as seen from the side (top) and from above (bottom). Marked in grey in the bottom drawing is the area where the horizontal aperture restriction was suspected to be located. The main sus-

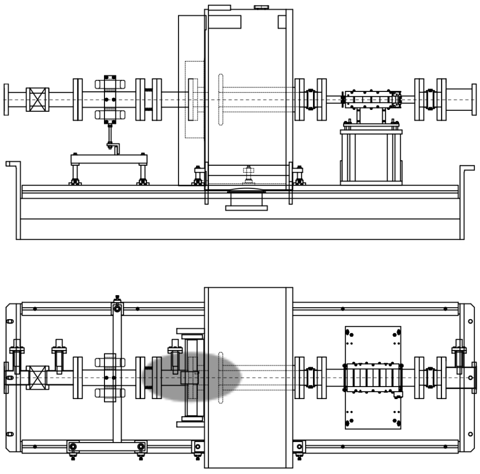

Figure 11: Drawing of the MAX III main cavity straight section as seen from the side (top) and from above (bottom). From left to right, the straight section components are an absorber, vacuum valve, absorber, skew quadrupole, bellows, absorber, the 100 MHz main cavity, bellows, the injection kicker, bellows and an absorber. On either side of the straight section, not shown on the drawing, are beam position monitors. Marked in grey in the bottom drawing is the area where the horizontal aperture restriction was suspected to be located based on the measurements in Fig. 9 and Fig. 10.

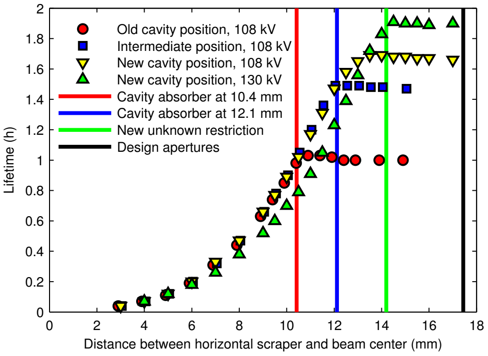

Figure 12: Horizontal scraper measurements for the old, intermediate and new cavity position. Measurements of the lifetime as a function of the distance between the horizontal scraper and the beam center. The error of the measured lifetime is estimated to be smaller than ± 0.3%. The uncertainty in the location of the beam center is estimated to be ±0.2 mm. Three of the measurements were performed at a main cavity voltage of 108 ± 1 kV and one was performed at a main cavity voltage of 130 ± 1 kV. The four lines correspond to the calculated position where the horizontal scraper would start to influence the linear lattice momentum acceptance if the cavity absorber is located at 10.4 mm, if the cavity absorber is located at 12.1 mm, for the new unknown restriction and for the design apertures.

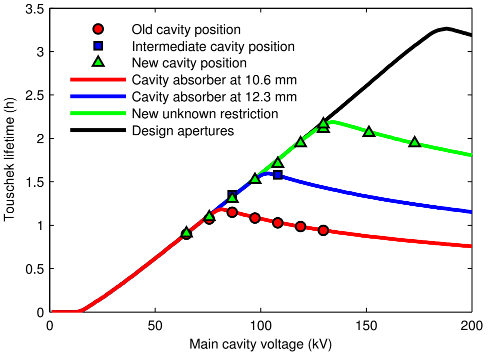

Figure 13: Measurements of the Touschek lifetime as a function of the main cavity voltage for the old, intermediate and new cavity position. The error of the measured Touschek lifetime is estimated to be ± 1% or smaller. The four lines correspond to calculations of the Touschek lifetime as a function of the main cavity voltage for the case that the cavity absorber is located at 10.6 mm, that the cavity absorber is located at 12.3 mm, for the new unknown restriction and for the design apertures.

pect was the absorber located close to and on the same vacuum structure as the main cavity.

Before the main cavity was moved, the alignment group verified the misalignment of the main cavity and concluded that the main cavity was placed roughly 5 mm too far towards the center of the ring. In January 2012 the main cavity was moved 1.4 ± 0.3 mm horizontally towards the outside of the ring. The move increased the beam lifetime and a new measurement with the local bump in the main cavity section suggested that the lifetime could be increased by moving the cavity further. A week later, the cavity was moved from this intermediate position to its current position, an additional 3.1 ± 0.1 mm towards the outside of the ring. Figure 12 shows horizontal scraper measurements at 108 ± 1 kV main cavity voltage for the old, intermediate and new cavity position, and at 130 ± 1 kV main cavity voltage for the new cavity position. For the measurements at the old and the intermediate cavity position there is a sharp edge in the scraper measurement when the horizontal scraper is moved towards the beam center and it abruptly limits the momentum acceptance instead of the cavity absorber. For the measurement at the new cavity position at 108 ± 1 kV the scraper measurement is noticeably softer, since the momentum acceptance is limited by the RF momentum acceptance until the scraper starts to influence it through the linear lattice momentum acceptance. For the measurement at 130 ± 1 kV the position where the horizontal scraper starts to limit the momentum acceptance is sharper again, which suggests there might be a new unknown restriction that limits the horizontal aperture.

In order to more closely investigate the transition from where the momentum acceptance is limited by the RF momentum acceptance to where it is limited by the lattice momentum acceptance, measurements of the lifetime as a function of the main cavity voltage were performed. Figure 13 shows the Touschek lifetime as a function of the main cavity voltage for the old, the intermediate and the new cavity position. The Touschek lifetime was obtained by subtracting the vacuum lifetime component (as determined in Sec. 4.1) from the measured total lifetime at around 300 mA stored current. The error in the determined Touschek lifetime is estimated to be ± 1% or smaller. As long as the momentum acceptance is limited by the RF momentum acceptance, the Touschek lifetime will increase when the main cavity voltage increases. When the momentum acceptance is limited by the lattice momentum acceptance, increasing the main cavity voltage will not affect the momentum acceptance. Instead, the Touschek lifetime will decrease when the main cavity voltage is increased, since the bunch length decreases and the electron density increases at higher main cavity voltages, increasing the probability of electron-electron scattering. During a transition region the momentum acceptance is limited by the RF momentum acceptance in parts of the ring and the lattice momentum acceptance in parts of the ring. The linear lattice momentum acceptance in MAX III does not vary much around the ring. For a fixed aperture restriction, the maximum value of the linear lattice momentum acceptance is around 15% larger than the minimum value and at most locations it is close to the average value. The transition region between the RF momentum acceptance and the lattice momentum acceptance is thus a limited voltage span, and the location and appearance of the transition region is largely determined by the average lattice momentum acceptance.

The lines in Fig. 13 corresponds to calculations of the linear Touschek lifetime from OPA. The calculated lifetimes have been scaled by the scaling factor 2.7 determined in Sec. 4.1. The best agreement with the measured lifetimes for the old cavity position is for calculations where the cavity absorber is located 10.6 mm from the beam center. For the intermediate cavity position the best agreement is for calculations where the cavity absorber is located 12.3 mm from the beam center. For the new cavity position the measured Touschek lifetimes suggest a new unknown restriction. If the unknown restriction is assumed to be situated at the horizontal scraper, the best agreement with the measured lifetimes for the new cavity position is for calculations where the horizontal scraper position is 14.4 mm from the beam center.

The calculations in Fig. 13 assume that the RF momentum acceptance is given by the main cavity only. The Landau cavities will however influence the RF momentum acceptance. For the settings used in the measurements the Landau cavities will decrease the RF momentum acceptance by up to 3%. Taking the effect of the Landau cavities into account and including other error sources the cavity absorber is determined to be located 10.4 ± 0.3 mm from the beam center for the old cavity position and 12.1 ± 0.3 mm from the beam center for the intermediate cavity position. For the new cavity position the horizontal scraper starts to limit the lattice momentum acceptance 14.2 ± 0.3 mm from the beam center. These results can be compared to the horizontal scraper measurements in Fig. 12. The position, according to OPA calculations, where the horizontal scraper would start to influence the linear lattice momentum acceptance if the cavity absorber was located 10.4 mm or 12.1 mm from the beam center is marked in Fig. 12 together with the new unknown restriction that corresponds to the horizontal scraper at 14.2 mm from the beam center.

The lattice momentum acceptance of the new restriction is clearly smaller than for the design apertures. It is also smaller than what could be explained by the new position of the cavity absorber. It is unknown if the new restriction is a physical or dynamic aperture. The average lattice momentum acceptance of the new restriction is however known to have a value close to the average linear lattice momentum acceptance of the horizontal scraper when it is located 14.2 mm from the beam center. Figure 14 shows the horizontal scraper at 14.2 mm and the corresponding apertures around the ring that give the same average linear lattice momentum acceptance. If there is a physical horizontal aperture restriction located somewhere in MAX III, it is located close to the line in Fig. 14.

The horizontal beta function at the location of the cavity absorber is 4.10 ± 0.06 m. The horizontal acceptance is thus $26 \pm 2 \times 10^{-6}$ m for the old cavity position and $36 \pm 2 \times 10^{-6}$ m for the intermediate cavity position. For the new unknown restriction the value of the acceptance depends on where the restriction is located. For each position in the ring, a physical restriction can however not be located closer to the beam center than the solid line in Fig. 14 since that would give a smaller average lattice momentum acceptance than the observed one. This gives a lower value for the horizontal acceptance. For the current operating settings in MAX III, the horizontal acceptance is larger than $44 \pm 2 \times 10^{-6}$ m. The design value for the horizontal acceptance is 73×10^{-6} m and the design limiting horizontal aperture is the absorber downstream the dipole magnet.

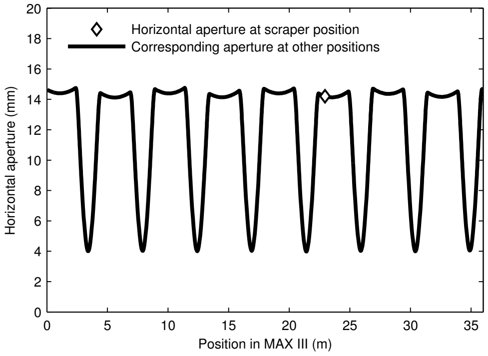

Figure 14: For the new unknown restriction, the horizontal scraper starts to limit the lattice momentum acceptance 14.2 ± 0.3 mm from the beam center. The marker shows the position of the horizontal scraper and the 14.2 mm horizontal aperture. The solid line shows calculations of the corresponding apertures around the ring that would give the same average linear lattice momentum acceptance as the horizontal scraper at 14.2 mm.

As long as the main cavity voltage is high enough the momentum acceptance is determined by the lattice momentum acceptance. The average lattice momentum acceptance is 0.0116 ± 0.0003 for the old cavity position and 0.0135 ± 0.0003 for the intermediate cavity position. For the current operating settings in MAX III, the average lattice momentum acceptance is 0.0158 ± 0.0003, whereas the design average lattice momentum acceptance is 0.020. Before moving the main cavity, the main cavity voltage was typically around 110 kV and the momentum acceptance was limited by the cavity absorber. For the new cavity position the main cavity voltage is kept around 130 kV, where the RF momentum acceptance and the lattice momentum acceptance is roughly equal, in order to give the maximum lifetime. This has increased the lifetime in MAX III by a factor of two.

4.3. Further lifetime improvements

The lifetime limitations measurement in Sec. 4.1 was performed after the main cavity was moved. Even though moving the main cavity increased the lifetime by a factor of two, the Touschek lifetime is still far from the design value (see Table 1). The design Touschek lifetime was envisaged to be achieved by a design with a Landau cavity to elongate bunches, a momentum acceptance of 0.020 and an emittance ratio of 0.10.

Because of the instabilities, the observed lifetime increase when the 300 MHz Landau cavity is tuned in appears to be smaller than expected from theory. As the Landau cavity is tuned in and the instabilities are dampened the bunch widening due to the increased energy spread disappears while the bunch lengthening due to the Landau cavity appears. During the vertical scraper measurement, the 300 MHz cavity was not tuned in as far as during the measurement in Fig. 3. By tuning in the cavity further, the Touschek lifetime can be increased by an additional 20%.

Moving the main cavity increased the momentum acceptance from 0.0116 ± 0.0003 to 0.0158 ± 0.0003. As Fig. 13 shows the Touschek lifetime could be increased by an additional 50% if the lattice momentum acceptance was determined by the design apertures and the main cavity voltage was increased to 190 kV. The FM transmitter can give enough power to increase the main cavity voltage, but in order to increase the lattice momentum acceptance further investigations are needed in order to locate the new unknown horizontal restriction.

The design emittance ratio was to be reached by increasing the coupling via a skew quadrupole located in the main cavity straight section (see Fig. 11). In normal operation the skew quadrupole is turned off, since engaging it decreases rather than increases the lifetime. When the skew quadrupole is turned off, the lattice momentum acceptance is determined by the horizontal apertures. When engaged, however, the lattice momentum acceptance has been observed to be limited by the small vertical acceptance. In order to increase the lifetime by increasing the coupling, further investigations are needed in order to locate the origin of the small vertical acceptance. Increasing the emittance ratio from the current value of 0.012 ± 0.001 to the design value of 0.10 would increase the Touschek lifetime by roughly a factor of three.

5. Summary and Conclusions

The horizontal beam size and bunch length in MAX III agree well with theoretical values at low currents. At higher currents, however, longitudinal instabilities have been observed. They affect the energy spread of the electron beam and give rise to an increase in the bunch length as well as in the transverse beam size through dispersion. From measurements of the horizontal beam size the increase in energy spread has been determined. By installing an additional Landau cavity, which elongates the bunches and provides Landau damping, the instabilities have been damped. In the current range 110-250 mA, which is the main window of operation for MAX III, the instabilities have been almost completely damped down.

The MAX III RF system consists of three cavities. The active 100 MHz main cavity and two passive Landau cavities at 300 MHz and 500 MHz, respectively. The triple RF system has been successfully simulated together with the measured energy spread to reproduce the observed bunch lengths, bunch shapes and induced cavity voltages. The Landau cavities have been observed to distort the bunch shapes and, at high voltages in the cavities, even over-stretch the bunches so that two distinct peaks are formed.

Vertical scraper measurements have determined the electron beam lifetime limitations in MAX III at 300 mA stored current. The elastic scattering lifetime is 22.3 ± 0.9 h, the inelastic scattering lifetime is larger than 147 ± 8 h, and the Touschek lifetime is 2.20 ± 0.03 h. The modelled Touschek lifetime for this case was 2.8 h. The vertical acceptance has been determined to be $1.33 \pm 0.03 \times 10^{-6}$ m, much smaller than the design acceptance 7.8×10^{-6} m.

By performing horizontal scraper measurements at different RF frequencies a horizontal aperture restriction was found to be present somewhere on the outer side of MAX III. A combination of local orbit distortions and horizontal scraper measurements pinpointed the location of the horizontal aperture restriction within less than a meter. The location of the misalignment in the main cavity straight section was verified by measurements by the alignment group. From measurements and calculations of the Touschek lifetime as a function of the main cavity voltage, the aperture restriction in the main cavity straight section was determined to be located 10.4 ± 0.3 mm from the beam center. Horizontal scraper measurements verified this conclusion. The main cavity was moved in two steps, which increased the average lattice momentum acceptance from 0.0116 ± 0.0003 to 0.0158 ± 0.0003 and the horizontal acceptance from $26 \pm 2 \times 10^{-6}$ m to larger than $44 \pm 2 \times 10^{-6}$ m. Still, the acceptance values are smaller than the design average lattice momentum acceptance of 0.020 and the design horizontal acceptance of 73×10^{-6} m, pointing at a new unknown horizontal restriction. The increase in momentum acceptance from moving the main cavity increased the lifetime in MAX III by a factor of two.

The measured Touschek lifetime of 2.20 ± 0.03 h at 300 mA, determined after the movement of the main cavity, is significantly smaller than the design Touschek lifetime of 15 h at 300 mA. If the new horizontal restriction could be located the lattice momentum acceptance might be increased to the design value, which would increase the Touschek lifetime up to 50%. If the measured emittance ratio of 0.012 ± 0.001 was increased to the design emittance ratio of 0.10, roughly an additional factor of three could be gained in Touschek lifetime. In order to increase the emittance ratio by increasing the coupling, the origin of the small vertical acceptance must first be located, since the small vertical acceptance starts to limit the lattice momentum acceptance when the coupling is increased.

Acknowledgements

The authors would like to thank P. Fernandes Tavares for cross-checking the triple RF simulations, L. Malmgren, R. Nilsson and P. Lilja for discussions and assistance with the RF measurements, F. Lindau for assistance with the laser injection system, B. Sommarin and P. Garsztka for measuring the main cavity misalignment and S. C. Leemann, M. Sjöström and M. Eriksson for fruitful discussions.

Appendix A. Calibration of the cavity voltages

In order to perform many of the measurements and simulations described in this paper it is essential to know the voltages of the three cavities in MAX III. None of them were calibrated when this measurement series began. Below, the calibration of the main cavity voltage and the Landau cavity voltages are described. Error estimations are given as standard deviations.

Appendix A.1. 100 MHz main cavity voltage calibration

The 100 MHz main cavity is a capacitance loaded cavity with a shunt impedance of 3.4 ± 0.2 MΩ [1]. Watt meters were connected to directional couplers on the coaxial line feeding power

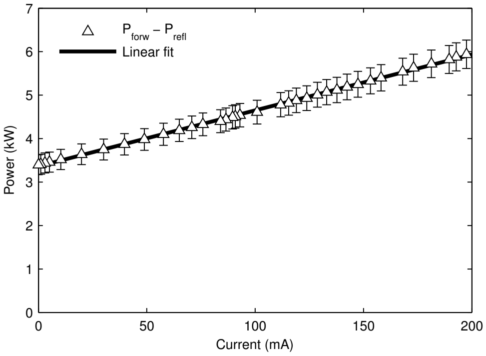

Figure A.15: Measurement of the forward power minus the reflected power as a function of stored current. The main cavity voltage is kept constant during the measurement. The solid line corresponds to a linear fit of the measurement data.

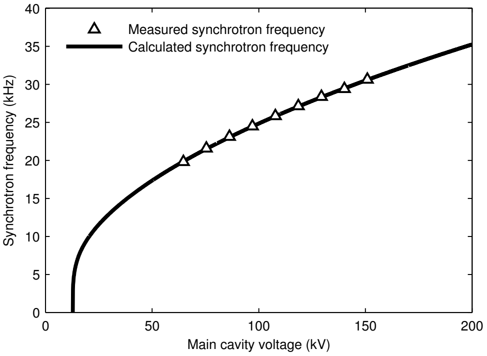

Figure A.16: Measurement of the synchrotron frequency as a function of the main cavity voltage at low currents. The error of the measured synchrotron frequency is estimated to be ± 0.2%. The solid line corresponds to the calculated synchrotron frequency.

from the FM transmitter to the main cavity. In this way the forward power to the cavity and the reflected power from the cavity could be measured. The error in the measured power was estimated to be ± 5%. When there is beam in the storage ring part of the power sent to the cavity drives the electron beam and another part is lost in the cavity walls. The voltage in the main cavity is given by

$$V_{RF} = \sqrt{P_{cav} R_S} \tag{A.1}$$

where P_{cav} is the cavity losses and R_S is the shunt impedance. The cavity losses can be determined from the relation

$$P_{forw} - P_{refl} = P_{cav} + \frac{IU_0}{e} \tag{A.2}$$

where P_{forw} is the forward power to the cavity, P_{refl} is the reflected power from the cavity, I the stored current, U_0 the energy loss of the electrons per turn and e is the electron charge. By measuring the forward and reflected power, with no beam in the storage ring, while varying the output power from the FM transmitter several values of the cavity losses were obtained. From these values the corresponding main cavity voltages were determined using Eq. A.1 and a vector voltmeter, used to measure the main cavity voltage, was calibrated. The estimated error of the calibration is ± 4%.

Figure A.15 shows a measurement of the forward power minus the reflected power as a function of stored current. The main cavity voltage, and thus the cavity losses, was kept constant during the measurement. From a linear fit to the measurement data, taking into account the estimated error in the measurements of the forward and reflected power, the energy loss of the electrons per turn is determined to be 12.9 ± 0.8 keV/turn. The theoretical value is 12.8 keV/turn. The insertion devices were kept open during the measurement and the Landau cavities were tuned out.

In order to verify the calibration of the main cavity voltage and possibly improve it, calculated values of the synchrotron frequency were compared to measurements. Figure A.16 shows measured and calculated values of the synchrotron frequency as a function of the main cavity voltage. The measurement was performed at a low current in order to make sure the Landau cavities do not affect the synchrotron frequency. By comparing the measured and calculated synchrotron frequency the estimated error of the main cavity voltage calibration can be reduced from ± 4% to smaller than ± 1%.

Appendix A.2. 500 MHz Landau cavity voltage calibration

The voltage in a passive Landau cavity is given by Eq. 1 and Eq. 2. If the resonance frequency of the Landau cavity is tuned so that it is identical to a higher harmonic of the RF frequency the tuning angle becomes zero and the voltage in the cavity is given by

$$V_{Landau} = R_S I F \tag{A.3}$$

The 500 MHz Landau cavity is a pillbox type cavity and its resonance frequency is tuned by changing its temperature or by inserting a plunger. The Q-value of the cavity was measured with a spectrum analyzer and determined to be 21720 ± 50 at the normal operating resonance frequency and 21900 ± 50 at the calibration resonance frequency. The shunt impedance, R_S, of the cavity was determined by multiplying the measured Q-value with results for transit-time corrected R_S/Q obtained from simulations using SUPERFISH [14] and COMSOL. In this way, the shunt impedance was determined to be 3.14 ± 0.02 MΩ at the normal operating resonance frequency and 3.17 ± 0.02 MΩ at the calibration resonance frequency.

The cavity is equipped with two probes that couple to the generated fields in the cavity. Figure A.17 shows a calibration measurement of the 500 MHz Landau cavity Probe A signal strength as a function of the 500 MHz Landau cavity voltage. The solid line corresponds to a linear fit of the measurement data, giving the calibration coefficient. The resonance

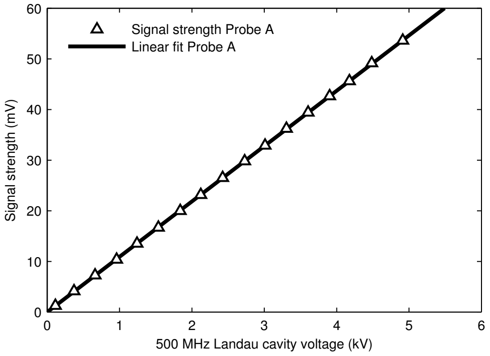

Figure A.17: Measurement of the signal strength of the 500 MHz Landau cavity Probe A signal as a function of the cavity voltage. The error of the measured signal strength is estimated to be ± 0.5%. The solid line corresponds to a linear fit of the measurement data.

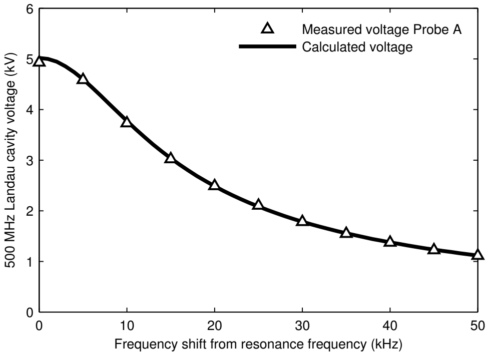

Figure A.18: Measurement of the 500 MHz Landau cavity voltage as a function of the frequency difference between the fifth harmonic of the RF frequency and the 500 MHz Landau cavity resonance frequency. The error of the measured voltage is estimated to be smaller than ± 1%. The solid line corresponds to the voltage calculated using Eq. 1 and Eq. 2.

frequency of the cavity was tuned to the fifth harmonic of the RF frequency, so that the voltage in the cavity was given by Eq. A.3. The main cavity voltage was constant during the measurement in order to keep the form factor constant. The calibration was performed by varying the stored current, while keeping it low enough to keep the Landau cavity voltage limited and the bunch shape, and thus the form factor, determined by the main cavity voltage. The error in the calibration coefficient is estimated to be smaller than ± 1%.

Figure A.18 shows a measurement of the 500 MHz Landau cavity voltage as a function of the frequency difference between the fifth harmonic of the RF frequency and the 500 MHz Landau cavity resonance frequency. The measurement was performed in order to verify that the resonance frequency of the 500 MHz Landau cavity was tuned to the fifth harmonic of the RF frequency and that the behavior of the cavity voltage was understood. The shift in frequency was done by keeping the 500 MHz Landau cavity resonance frequency constant while changing the RF frequency. The main cavity voltage was kept constant during the measurement and the difference in stored current at the start and at the end of the measurement was negligible. The solid line in Fig. A.18 corresponds to the Landau cavity voltage calculated using Eq. 1 and Eq. 2.

Appendix A.3. 300 MHz Landau cavity voltage calibration

The 300 MHz Landau cavity is a capacitance loaded cavity and its resonance frequency is tuned by changing its temperature, by inserting a plunger or by changing the capacitance through mechanical deformation of one of the side walls. The Q-value of the cavity was measured with a spectrum analyzer and determined to be 20430 ± 40 at the normal operating resonance frequency and 20490 ± 40 at the calibration resonance frequency. The shunt impedance of the cavity was determined by multiplying the measured Q-value with results for transit-time corrected R_S/Q obtained from simulations using SUPERFISH and COMSOL, giving a shunt impedance of 5.36 ± 0.03 MΩ at the normal operating resonance frequency and 5.37 ± 0.03 MΩ at the calibration resonance frequency.

The cavity is equipped with two probes that couple to the generated fields in the cavity. The calibration of the 300 MHz Landau cavity voltage was performed in a similar way as for the 500 MHz Landau cavity (see Appendix A.2). A minor difference is that the resonance frequency of the 300 MHz Landau cavity was not exactly on resonance during the measurement, but located about 0.4 kHz away from the third harmonic of the RF frequency. The calibration results were analyzed accordingly. Figure A.19 shows a calibration measurement of the 300 MHz Landau cavity Probe A and Probe B signal strength as a function of the 300 MHz Landau cavity voltage. The solid lines correspond to linear fits of the measurement data, giving the calibration coefficients. The error in the calibration coefficient is estimated to be smaller than ± 1%.

Figure A.20 shows a measurement of the 300 MHz Landau cavity voltage as a function of the frequency difference between the third harmonic of the RF frequency and the 300 MHz Landau cavity resonance frequency. The voltage is measured both from Probe A and Probe B. The solid line corresponds to the voltage calculated using Eq. 1 and Eq. 2.

[1] M. Sjöström, E. Wallén, M. Eriksson, L.-J. Lindgren, The MAX III storage ring, Nuclear Instruments and Methods in Physics Research A 601 (2009) 229–244.

[2] A. Hansson, E. Wallén, Å. Andersson, Transverse electron beam imaging system using visible synchrotron radiation at MAX III, Nuclear Instruments and Methods in Physics Research A 671 (2012) 94–102.

[3] A. Hansson, E. Wallén, Å. Andersson, Imaging of the MAX III electron beam profile using visible synchrotron radiation, in: Proceedings of IPAC2011, San Sebastián, Spain, pp. 1332–1334.

[4] S. C. Leemann, Å. Andersson, M. Eriksson, L.-J. Lindgren, E. Wallén, J. Bengtsson, A. Streun, Beam dynamics and expected performance of Sweden's new storage-ring light source: MAX IV, Physical Review Special Topics - Accelerators and Beams 12 (2009) 120701.

[5] A. Terebilo, Accelerator toolbox for MATLAB, 2001. SLAC-PUB-8732.

[6] J. Safranek, G. Portmann, A. Terebilo, C. Steier, MATLAB-based LOCO, in: Proceedings of EPAC 2002, Paris, France, pp. 1184–1186.

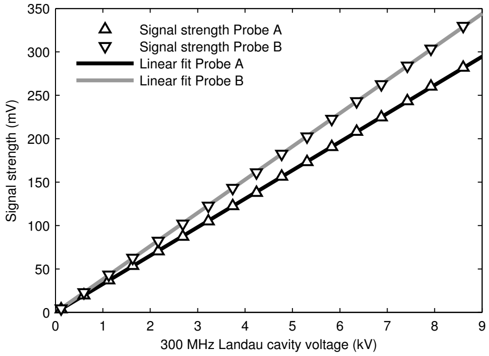

Figure A.19: Measurement of the signal strength of the 300 MHz Landau cavity Probe A and Probe B signal as a function of the cavity voltage. The error of the measured signal strength is estimated to be ± 0.5%. The solid lines correspond to linear fits of the measurement data.

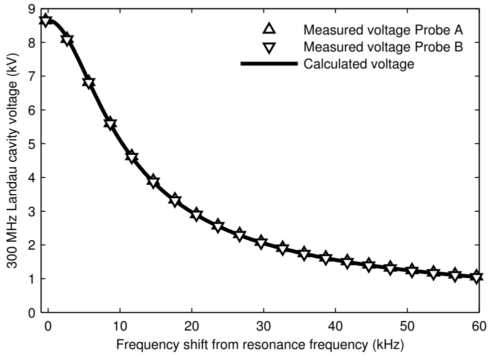

Figure A.20: Measurement of the 300 MHz Landau cavity voltage as a function of the frequency difference between the third harmonic of the RF frequency and the 300 MHz Landau cavity resonance frequency. The voltage is measured both from Probe A and Probe B. The error of the measured voltage is estimated to be smaller than ± 1%. The solid line corresponds to the voltage calculated using Eq. 1 and Eq. 2.

[7] A. Streun, OPA, code and documentation available at http://people.web.psi.ch/streun/opa.

[8] A. Hofmann, S. Myers, Beam dynamics in a double RF system, 1980. CERN-ISR-TH-RF-80-26.

[9] J. L. Duff, Current and current density limitations in existing electron storage rings, Nuclear Instruments and Methods in Physics Research A 239 (1985) 83 – 101.

[10] E. Wallén, Aperture and lifetime measurements with moveable scrapers at MAX II, Nuclear Instruments and Methods in Physics Research A 508 (2003) 487–495.

[11] A. Hansson, E. Wallén, M. Berglund, R. Kersevan, M. Hahn, Experiences from nonevaporable getter-coated vacuum chambers at the MAX II synchrotron light source, Journal of Vacuum Science & Technology A: Vacuum, Surfaces, and Films 28 (2010) 220–225.

[12] Å. Andersson, M. Bergqvist, M. Eriksson, L. Malmgren, L. Thånell, The 100 MHz RF system for MAX-II and MAX-III, in: Proceedings of EPAC 2002, Paris, France, pp. 2118–2120.

[13] M. S. Zisman, S. Chattopadhyay, J. J. Bisognano, ZAP user's manual, 1986. LBL-21270.

[14] J. H. Billen, L. M. Young, Poisson/Superfish, 1996. LA-UR-96-1834.